Brunel University London

Doctoral thesis

Multiple beams Yb:fibre laser welding process for Grade 2205 duplex stainless steel

Author:
Maxime Bolut

Supervisors:
Prof. Peter Hobson
Dr. Katherine Cashell

A thesis submitted in partial fulfilment of the requirements for the degree of Doctorate of Philosophy in the

Department of Mechanical and Aerospace Engineering

March 2018

Abstract

This thesis describes the development of a Yb:fibre laser welding process for Grade 2205 duplex stainless steel (DSS) using a multiple beam approach.

Grade 2205 DSS can be found in many structural applications, and in particular in the UK, for the manufacturing of intermediate level nuclear waste (ILW) containers made of 3 and 6 mm thick plates. To ensure good weld integrity, Yb:fibre laser welding was the choice of welding process used for these nuclear containers. The existing welding practice requires filler wire feed to maintain the microstructure in the weld. However, filler wire adds cost and complexity to the process which often leads to high failure rate. For this reason, the possibility of removing the requirement for filler wire is very attractive. One possible way of doing this is to tailor the laser beam's energy distribution delivered to the workpiece to influence the material's cooling rate and therefore the resulting microstructure in the weld.

In this study, tailored energy distributions were achieved by impinging multiple beams onto the work-piece, which were produced using either a beam splitter module (dual beam) or a diffractive optical element (DOE). Experiments included welding trials using a single beam, dual beam and diffracted beam. In all experiment, the temperature during welding was recorded, and the resulting weld microstructure was analysed through metallography assessment, point counting, Vickers hardness testing and corrosion testing. In addition, electron backscatter diffusion (EBSD) imaging and energy-dispersive X-ray spectroscopy (EDX) have also been carried out on selected samples. These techniques offer in-depth analysis of the crystal size, orientation, shape, and phase which define the weld properties.

Process optimisation using single beam at welding speed of 1 to 1.5 m/min showed that the use of pure nitrogen shielding gas during welding improved the austenitic microstructure by up to 15% when compared with welding shielded with pure argon gas. The weld nevertheless resulted in ferrite phase volume fraction which was over the acceptable threshold of 70% necessary for its long-term corrosion performance.
Dual beam welding of 3 mm plates achieved the reduction of the ferrite phase volume fraction within the desired range (30-70%). These results were supported by the improvement of the corrosion test outcome in comparison with single beam results.
The DOE used in this study was characterised and a bespoke welding head allowing quick access to the optics was designed and manufactured. Results with 6 mm plates showed a local reduction of the ferrite volume fraction around 60% at the weld cap.

In conclusion, the investigation in this doctorate study showed that autogenous single beam welding of grade 2205 DSS is possible providing a slow welding speed and that the undesirable ferrite volume fraction excess can be reduced to an acceptable amount by using a tailored energy distribution.

Acknowledgements

This PhD was a personal challenge but also an excellent opportunity to satisfy my curiosity and gain knowledge while working in the dynamic and multi-cultural company that is TWI. It gave me the chance to interact and work with amazing people that influenced me on many aspects and that I am thankful to have met. I cannot properly thank them all, as the acknowledgements would be longer than the actual thesis, but for all the ones I missed, be sure that you will stay with my memories of these five nice years that I spent in Cambridge.

Many thanks to Choon Yen Kong for his guidance and his confident attitude. I always admired his calm in stressful situations and his relentless efforts and imagination to solve all kinds of issues, always with an exuberantly positive state of mind. Thanks to Jon Blackburn for his trust and management skills, and for giving me the opportunity to present TWI work abroad. Their contributions to my training, inclusion and development at TWI were valuable.

A million thanks as well to my Brunel academic supervisors. Peter Hobson and Katherine Cashell were not only very helpful for the guidance and corrections of this thesis with amazingly fast responsiveness, but they were also a mental support and great teachers to guide me through this experience.

I would also like to acknowledge my colleagues that were part of my PhD's success, even if the list is not exhaustive. Sullivan Smith made phase diagram and material solidification easy for me and on a completely different topic, he was a great running coach, helping me to push beyond what I thought I was capable. Tony Pramanik was the sweetest colleague I ever worked with, and with Fiona Snell they turned many gloomy days into good ones. Andy Wilson and Chris Allen were my living Wikipedias, Paola De Bono was always kind to me, Ali Khan and Paul Hilton enlightened me about laser processing and shared with me a plethora of colourful stories and scientific anecdotes. All the technicians were very supportive, and Matt Spinks taught me pretty much everything technical I needed to conduct my experiments. Thanks all of you for your help, support and the good vibes that contributed to make the workplace so enjoyable.

The acknowledgements would not be complete without a special thanks to my loved one, family and friends outside of work that gave me the support, focus and confidence to get to this stage.

Thanks to Maria Jose Perez Garcia for staying by my side during this time and for her good heart. Your love, patience and smile helped me to get through. I love you.

To Sabrina Blackwell and Clement Bhur for giving me the motivation to pursue a PhD, to Daniel Bacioiu and Irene Garrote Moreno for the good times living together, to Xian "Effy" Meng and François Guerraz and all of them for being kind and inspirational friends.

Merci aussi à mes parents et ma soeur qui ont toujours beaucoup compté pour moi et qui ont toujours été la quand j'en ai eu besoin.

Declaration

I declare that this thesis is the result of my own research except as cited in the reference. The thesis has not been accepted for any degree and is not concurrently submitted in candidature of any other degree.

Maxime Bolut

List of publications

The publications directly arising from this research are the following:

1) M. Bolut, C. Y. Kong, J. Blackburn, K. A. Cashell, and P. R. Hobson, "Yb-Fibre laser welding of 6 mm duplex stainless steel 2205," Phys. Procedia, vol. 83, pp. 417–425, 2016.

2) M. Bolut, C. Y. Kong, P. R. Hobson, K. A. Cashell, and J. Blackburn, "Laser beam welding of duplex stainless steel with a diffractive optical element to locally reduce high ferrite content," in 39th MATADOR Conference Laser, 2017, NOT YET PUBLISHED.

The author also published on experiments done with a diffractive optical element but on a different topic:

3) C. Y. Kong, M. Bolut, J. Sundqvist, A. F. Kaplan, E. Assuncao, L. Quintino, and J. Blackburn, "Single-pulse conduction limited laser welding using a diffractive optical element," Phys. Procedia, vol. 83, pp. 1217-1222, 2016.

List of abbreviation

ANOVA	ANalysis Of VAriance
ASTM	American Society for Testing and Materials
BCC	Body-Centred Cubic
BPP	Beam Product Parameter
BS	British Standard
BSI	British Standards Institution
CGH	Computer-Generated Hologram
CW	Continuous Wave
DOE	Diffractive Optical Element
DSS	Duplex Stainless Steel
EBSD	Electron Backscatter Diffraction
EDX/EDS	Energy-Dispersive X-ray Spectroscopy
FCC	Face-Centred Cubic
FFT	Fast Fourier Transform
FL	Focal length
GMAW	Gas Metal Arc Welding
GTAW	Gas Tungsten Arc Welding (same as TIG)
HAZ	Heat Affected Zone
HOE	Holographic Optical Element
ICALEO	The International Congress on Applications of Lasers & Electro-Optics
IFTA	Iterative Fourier Transform Algorithm
ILW	Intermediate Level (nuclear) Waste
ISO	International Standards Organisation
LASER	Light Amplified by Stimulated Emission of Radiation
MAG	Metal Active Gas

MEMS	Micro-Electro-Mechanical Systems
MIG	Metal Inert Gas
NA	Numerical Aperture
Nd:YAG	Neodymium-doped Yttrium-Aluminium-Garnet
PAW	Plasma Arc Welding
PREN	Pitting Resistance Equivalent Number
RSM	Response Surface Methodology
SCC	Stress Corrosion Cracking
SEM	Scanning Electron Microscopy
SLM	Spatial Light Modulator
SM	Single Mode
SME	Small and Medium Enterprises
TEM	Transverse Electromagnetic Mode
TIG	Tungsten Inert Gas (same as GTA or GTAW)
TWI	The Welding Institute
YAG	Yttrium-Aluminium-Garnet
Yb:Fibre	Ytterbium-Doped Fibre

Content

Chapter 1: Introduction

1.1 Introduction

Many of the fundamental principles of the laser were developed in the 1950's, and the first laser was built in 1960 [1]. The first laser cutting of metal was performed in 1967 at TWI by A. Sullivan with a CO_2 laser [2] and from then on this technology has been a competitor to other techniques within welding and other mechanical processes. Further development brought new lasers with other wavelengths down to ultraviolet such as the excimer laser. UV-lasers have played a significant role to reduce the size of electronic components through UV-lithography making it possible to fit a cell phone in our pocket. Higher power (kW order), better beam quality (a value that describes how well the laser can be focused) and lower costs gave rise to new possibilities in almost every context of science and production.

In manufacturing laser is used for a great variety of material processes such as cutting, welding, drilling, soldering, cladding, marking, etc. Laser processing methods have many advantages compared with mechanical approaches. By concentrating high energy through very narrowly focused light beam, the processing of very fine structure is possible without the mechanical stress of blades or drills and result in high-quality work. In addition, high processing speed is usually achieved with a laser. The non-contact nature of the laser tool is also advantageous in the field of nuclear decommissioning, e.g. cutting of irradiated components.

For fusion welding, laser beam, plasma, and electron beam welding are the only known methods allowing for deep penetration of metal. Plasma welding has a limited usefulness compared to electron and laser beam because of its low maximum power and limited focus ability. Electron and laser beam can deliver much higher intensity through a much smaller processing spot. However, the electron beam requires for the process to be performed in a vacuum chamber. The possibility for laser welding to be operated in a room atmosphere quickly gave the laser its own niche. This niche is continuously growing in the market with a long list of joining and welding technologies used for assembly in the industry.

This research aims to develop a novel Ytterbium-doped fibre (Yb:fibre) laser welding process for duplex stainless steel (DSS), overcoming the limitations of current laser welding methods. The new process focuses on the tailoring of the laser beam's spatial energy distribution. Multiple beam approaches are investigated to control the cooldown of the material and influence the formation of the desired microstructure and thus remove the need for a filler wire. Figure 1.1 depicts the ideas and steps of this dissertation's core research chapters.

This chapter highlights the importance of fibre laser technology and the new advantages that can be achieved with a beam splitter or diffractive optical elements (DOEs). The material of interest, grade 2205 DSS, is described with its typical applications. The fibre laser welding challenges of grade 2205 DSS are summarised to highlight the use of tailored energy distributions as a solution. Thereafter, a brief overview of the thesis layout is presented.

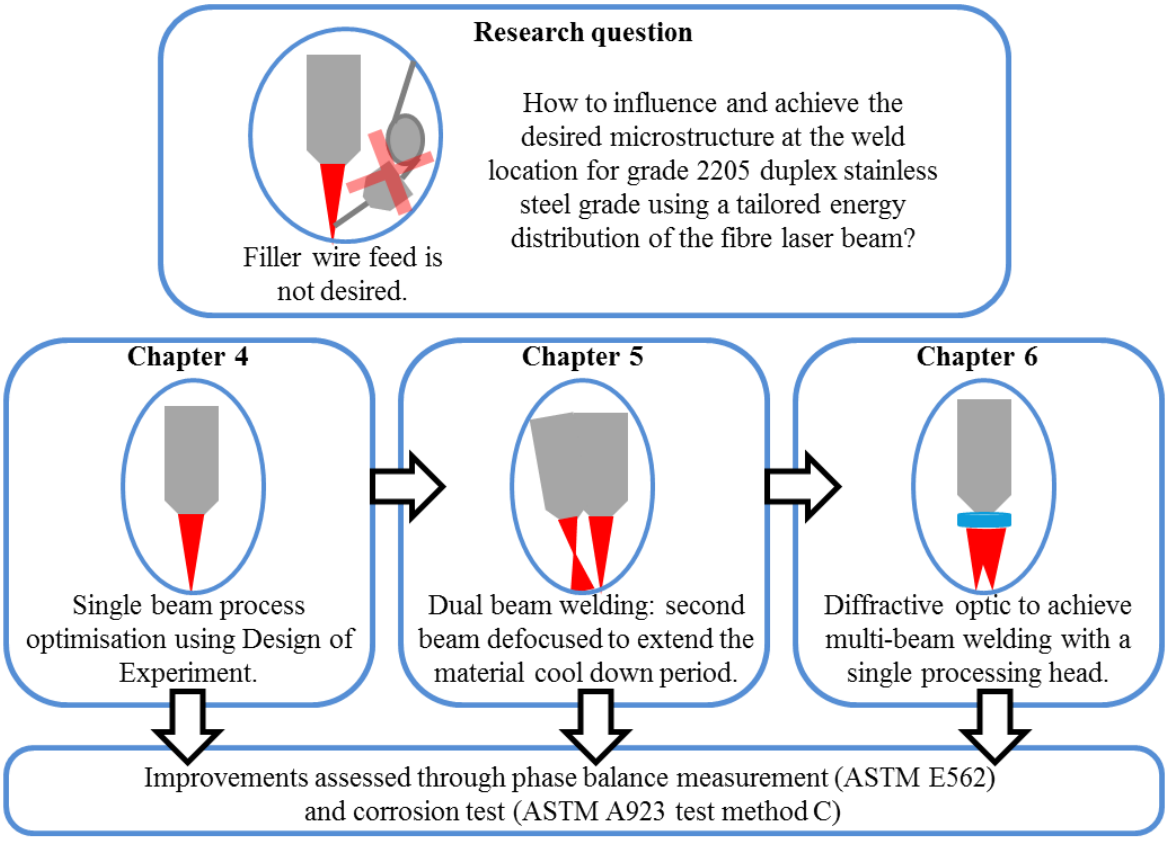

Figure 1.1: Core research chapters of this dissertation

1.2 Fibre lasers in material processing industries

The acronym LASER, which stands for Light Amplification by Stimulated Emission of Radiation, describes a device that creates and amplifies a narrow frequency of light with low divergence and whose photons are coherent spatially and temporally; i.e. they propagate with the same phase and wavelength in the same direction. The acronym which was coined by Gould in 1959 [3] shortly before the first laser beam was observed, is now commonly used as a noun, attesting the wide-spread interest in this technology in today's world. The properties of the laser beam are ideal for focusing the light wave to a very concentrated point, increasing its intensity greatly. In 1962, Schwarz and DeMaria [4] and Bahun and Eng-Quist [5] rapidly realised the potential for using the laser beam for material applications such as cutting, drilling welding and surfacing processes. The first industrial application in 1967 was to drill a hole into diamonds [6]. The operation was conducted with a ruby laser and took 15 minutes instead of 24 hours, compared with conventional mechanical drilling. The same year, the first gas-assisted laser cut was demonstrated at TWI by Houlcroft and Sullivan [2]; a 2.5 mm thick stainless steel plate was cut at a speed of 1 m/min under oxygen with a 300 W CO_2 laser, as shown in Figure 1.2 A. As a comparison, current CO_2 lasers can cut stainless steel plates which are 20 mm in thickness at the same cutting speed using a 4 kW system. Further laser cutting developments have included automated remote cutting/welding in multiple directions (as shown in Figure 1.2 B) and hand-held cutting using fibre lasers, as presented in Figure 1.2 C.

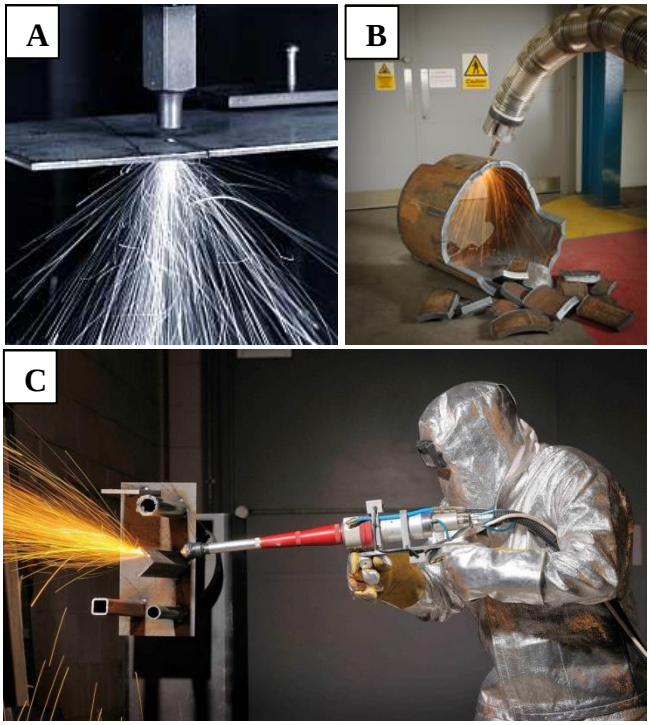

Figure 1.2: (A) The first oxygen assisted gas laser cutting performed in May 1967 [2]**; (B) Fibre laser automated snake arm cutting a 1,3 m diameter stainless steel dissolver vessel; (C) The first hand-operated laser cutting demonstration in March 2013**

Currently, high power lasers (here referred to as lasers with output powers over 1 kW) are essential tools in many manufacturing industries. They are widely used in the automotive sector for roof seams joining, door welding, the welding of tailored blanks, three-dimensional cutting of hydroformed parts, annealing of door springs and marking of polymeric and metallic components. The aerospace industry uses lasers for high-quality welding of critical components, and the nuclear industry uses lasers for high-quality hermetic sealing of radioactive waste storage containers. Many other industries also use this technology for everyday commodities. A few examples include laser welded razor blades, refrigerator doors, washing machine drums and kitchen sinks [7].

In recent years, laser welding has been viewed as an attractive alternative to the more traditional arc-based welding processes, mainly because of its higher processing speed and its versatility. Recent progress in fibre laser technology has made it possible to combine good beam quality and high energy stability [8], producing welds with significantly lower heat input than another welding process such as Tungsten Inert Gas (TIG) welding. Other benefits include lower distortion, reduced heat affected zone (HAZ) and fewer weld defects. Therefore, consistent weld profiles with deep root penetration can be achieved, resulting in negligible weld porosity [9]. As a result, the market for laser material processing has been growing and is worth billions of pounds, as presented in Table 1.1 [10][11].

Table 1.1: All industrial laser material processing revenues

Revenue (US $M)	2013	2014	2015	2016
Marking	$335.0	$347.5	$543.1	$560.2
year-to-year growth		4%	56%	3%
Micro materials	$597.0	$611.3	$894.8	1.105.0
year-to-year growth		2%	46%	23%
Macro materials	$1,554.4	$1,671.6	$1,428.0	1,492.1
year-to-year growth		8%	-15%	4%
Total	$2,486.4	$2,630.4	$2,865.9	$3,157.3
year-to-year growth		6%	9%	10.2%

Among the different laser systems for material processing, fibre lasers for metal cutting and joining operations represented 41% of the total industrial laser revenues in 2016 [12]. Fibre laser technological advancement, lower purchasing cost and increased versatility are driving the fibre laser market. Its share of the existing market continues to increase while new markets and applications are also continuing to emerge. Most of the recent studies on process development that have helped the maturation of this technology focused on process parameter optimisation but few have investigated the multiple beam approach or the transformation of the laser beam's spatial energy distribution by the optical system. The research presented in this thesis explored the possibility of changing the laser beam's spatial energy distribution at the workpiece using a beam splitter and a diffractive optical element (DOE). This approach is intended to enable laser welding of DSS where a single beam process has failed.

1.3 Tailored energy distributions

In the context of this thesis, the term 'tailored energy distribution' refers to a specific spatial arrangement of the laser beam's energy distribution delivered at the workpiece that differs from a conventional Gaussian or top-hat beam distribution. One way of changing the energy distribution at the workpiece is to use multiple laser welding heads or DOEs. Examples of the different energy distributions used in this research are depicted in Figure 1.3. These types of distribution may offer more control over the thermal gradient at the weld location and therefore influence the microstructure formation of some metal.

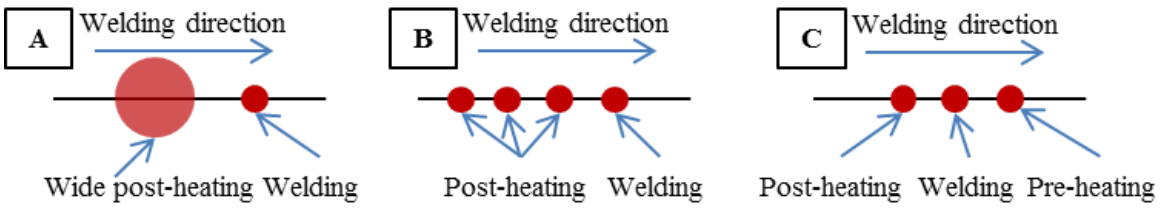

Figure 1.3: Different energy distribution tested in this research

In this research, a beam splitter module in which an incoming beam from the laser source was split equally into two was used. By using the adjustment of the mounting fixture such as the separation distance from the process heads and the defocus position it was possible to achieve the energy distribution presented in Figure 1.3 A. More complex distributions and larger numbers of beam spots can be produced using the special optics known as DOEs that use the principle of diffraction to transform an incident beam into the desired output. The diffractive optic is inserted just before the focusing lens in a standard optic setting for laser welding. Multiple beam configurations shown in Figures 1.3 B and C were attempted using a DOE in Chapter 6. The main advantages of using a DOE over a beam splitter module for the multiple beam approach are the reduction of optical components needed and a simpler set-up with the additional flexibility of the beam configurations that can be achieved.

1.4 Grade 2205 duplex stainless steel

The material of focus of this study was grade 2205 DSS, which is the most commonly available in the duplex family of stainless steels. It first emerged in the 1970's when improved electric arc furnaces made it possible to lower the carbon content and reduce impurity levels, compared with the more widely-used austenitic grades. Since the 1990's, DSS has been increasing in popularity compared with austenitic stainless steel, owing to its improved weldability, better strength properties and expanding availability. The material is relatively lightweight compared to other stainless steel (material density 7800 kg/m^3), has high strength (tensile strength of around 700 MPa) and good corrosion resistant properties (pitting resistance equivalent number (PREN) of around 35) making it an excellent material choice for applications in harsh environments. In addition, international pressure for environmental preservation has increased the need for long-term structural integrity of key applications in important industrial sectors such as oil and gas, marine, nuclear and construction. In response, bridges made of grade 2205 DSS instead of conventional painted carbon steel have been built around the world, such as the iconic pedestrian bridge in San Diego (first duplex steel bridge in the USA in 2011) and the Meads Bridge in Bristol, UK (Figure 1.4). Another example of a critical application for grade 2205 DSS is an intermediate nuclear waste container which is typically used in the UK and is made from 3 and 6 mm thick panels (Figure 1.5).

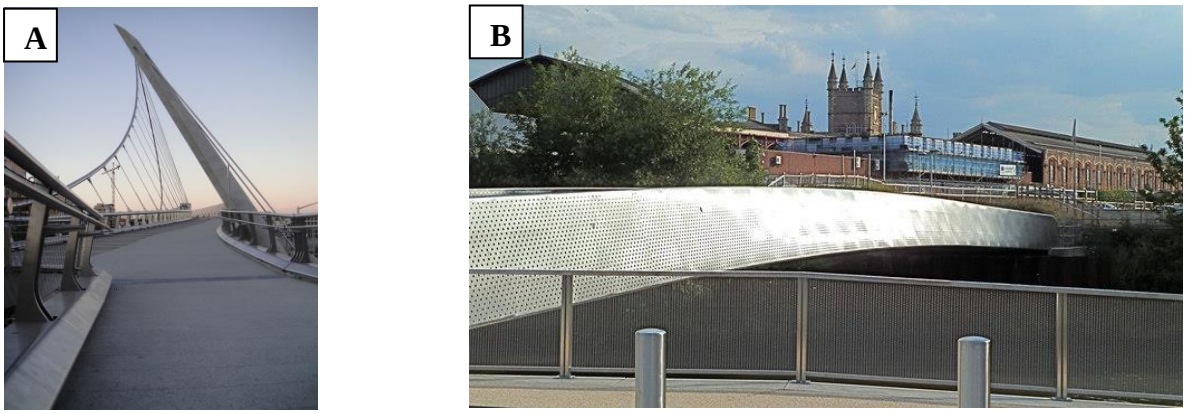

Figure 1.4: (A) Pedestrian bridge in San Diego; (B) Meads bridge in Bristol

Figure 1.5: Intermediate nuclear waste container made of grade 2205 DSS
Courtesy of Graham Engineering, BB9 8SY Nelson, UK

The welding technique used in the manufacturing of these containers requires careful consideration. Heat input and other welding parameters can lead to intermetallic precipitation detrimental to the material properties or unbalance the content of ferrite and austenite phase. An unbalanced weld resulting in excess of ferrite can reduce the resistance to pitting corrosion for instance.

Laser welding is considered as a viable process for this type of applications/material as low heat input can prevent material distortion and welding speed can reduce manufacturing cycle times. Nevertheless, maintaining the phase balance at the weld location remains challenging as the fast cooldown associated with laser welding lead to ferrite excess. The common industrial approach to weld grade 2205 DSS with laser requires an expensive filler material over alloyed with nickel (i.e. ER2209). The reason for using a filler material during laser welding is to prevent undercut, improve gap bridging and to maintain the phase balance of the material. However, it adds costs and reduces the flexibility of the welding process because of the increased complexity, lower speed and higher failure rate.

This research studied the possibility of using a tailored energy distribution single-pass laser welding approach to achieve high productivity and weld quality. It contributed to a greater understanding, confidence and control from the laser welding process applied to grade 2205 DSS.

1.5 Motivations

The research motivation was to determine if it is possible to remove the requirement for filler materials during the Yb:laser welding process of grade 2205 DSS (with thicknesses of 3 and 6 mm that are typically used in the nuclear sector) to decrease the cost and reduce the complexity of the process. The first part of this research was the benchmarking of single beam autogenous Yb:laser welding of grade 2205 DSS. The second part was to test a dual beam approach with a dual head set up to potentially improve the phase balance or broaden the process window for acceptable weld profile dimensions. Finally, testing a diffractive optic that reproduces a similar energy distribution developed previously developed was the last stage of this research. The aims and objectives are re-defined at the end of Chapter 2 (literature review).

1.6 Thesis structure

Chapter 2 presents a review of the literature, categorised into three major topics. Firstly, the properties of grade 2205 DSS are presented. Then, fibre laser welding technology is described, and laser-matter interaction during welding is covered. The critical parameters and concepts later used in the experimental chapter are reviewed. Finally, tailored energy distribution techniques are presented and evaluated. A review of these techniques reveals an overlooked approach of tailored energy distribution for temperature control during welding.

Chapter 3 presents the approach and methodology adopted to answer the research question. The materials and techniques used are presented and justified. The equipment is characterised, and the precision and accuracy of measurement are discussed.

Chapter 4 describes the optimisation and benchmarking of the single beam Yb:fibre laser welding process of grade 2205 DSS without filler wire. Two material thicknesses of 3 and 6 mm are studied.

In all the following chapters the same materials (grade and thicknesses) were used and all the welding techniques presented were carried out autogenously (without filler wire)

Chapter 5 presents the results of dual beam Yb:fibre laser welding studies obtained using a dual welding head set-up.

Chapter 6 presents the results of welds made with a 3-spots DOE. The optic selected is discussed and characterised. The welds using the 3-spots DOE are then compared to those made using single and dual beam techniques. In this chapter, a brief trial of another DOE (4-spots) used for the welding of 3 mm thick grade 2205 DSS is also reported.

Chapter 7 is the concluding chapter, comparing the different techniques and answering the questions stated in the aims and objectives (Chapter 1 Section 5).

There are two appendices included at the end of this thesis which provide more information on the principles of laser sources (Appendix 1) and manufacturing processes for diffractive optics (Appendix 2).

Chapter 2: Literature Review

2.0 Introduction

The scope of this research ranged from laser welding process, tailored energy distribution and fusion of duplex stainless steel (DSS). Readers may not be familiar with all of these topics, and therefore this literature review covers the relevant background and previous research into these three topics; ultimately, to highlight the context in which the research question falls.

Firstly, the essential features of grade 2205 DSS are described, including its microstructure, its properties and the relevant applications that motivated this research. An assessment of the typical welding processes used for this grade is also presented, with particular attention given to laser welding, whose adoption may be advantageous in an industrial context. This is followed by a review of fibre laser welding and the key features which are relevant to this thesis. The technology and advantages of Yb:fibre lasers and the keyhole welding process are highlighted. The scope for development regarding laser welding of DSS is evaluated, and tailoring the energy distribution of the laser beam is presented as a potential solution for improving the welding of grade 2205 DSS since it can influence the melt pool and the thermal dynamics of the weld. Finally, the different solutions for modifying the energy distribution of the laser beam delivered at the workpiece are reviewed with a particular focus on diffractive optics and their advantages. The-state-of-the-art of this relatively new technique, when used with laser welding, is exposed, highlighting the promises of this technology. The literature ends with a short conclusion summarising the context of the work and the identified gaps in existing research.

Part 1: Duplex stainless steel

2.1 Duplex stainless steel

It is not an understatement that stainless steels are used widely in our daily lives [13]. From inexpensive items such as cutlery, cans and water buckets, to high-end items such as cars, planes and space engines, stainless steel is ubiquitous. Nevertheless, not everything is known about the material science of stainless steel alloys, and there is still significant research being undertaken to develop new stainless steel alloys and their manufacturing processes.

Stainless steel, which has been engineered for better oxidation resistance than carbon steel, contains at least 10.5% chromium content and less than 1.2% carbon. The thin chromium-rich oxide layer (1-5 nm) forming naturally at the steel surface considerably reduces the anodic dissolution reaction (a phenomenon known as passivation) and provides excellent corrosion resistance to the material. Also, with the oxygen in the air, the chromium oxide layer can reconstruct itself in areas that have been slightly damaged mechanically. Resistance to corrosion without the need of protective coatings is the main advantage of stainless steel but there are several other ones such as its attractive appearance, wide range of surface finishes, ease of cleaning, hygienic, non-magnetic properties and wide range of service temperature (from -50°C to 980°C for short use and up to 300°C for long-term exposure). There are many different types of stainless steel, comprising nearly 200 different grades which are included in the European standards. These grades can be divided into five families depending on their chemical composition. These families are austenitic, ferritic, martensitic, precipitation-hardened and DSS. Within these groups, DSS represents the largest growth trend regarding production and consumption (for the last two-decades) [14], with a significant number of new applications [15]. Compared with austenitic stainless steels, DSSs have higher resistance to pitting and stress corrosion cracking (SCC), and they exhibit greater toughness and better weldability than ferritic stainless steels. The duplex structure is made of ferrite and austenite phases as illustrated in Figure 2.1 and combines the advantages of both structures. The excellent material properties regarding corrosion resistance and strength, resulting from an equally balanced ferrite/austenite microstructure, have led to an increase in the popularity and attractiveness of DSS.

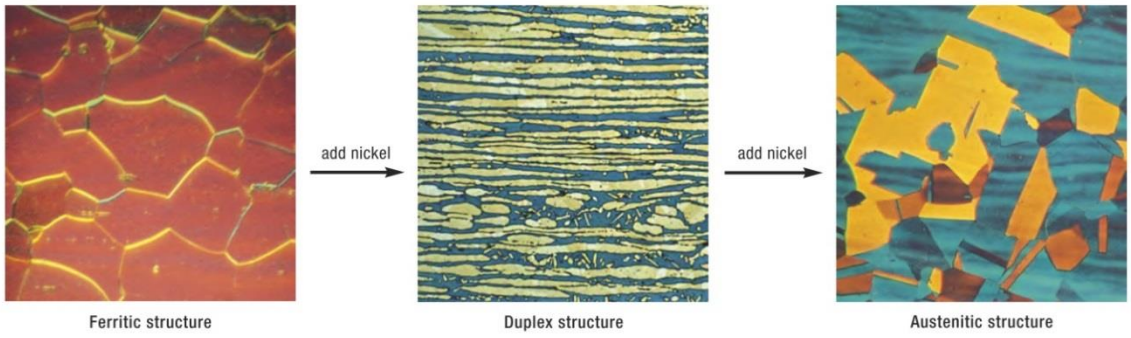

Figure 2.1: Different structure of stainless steel [16]

2.1.1 Grade 2205 duplex stainless steel

The most commonly used grade of DSS is grade 2205 (also known as UNS S31803, UNS S32205 and 1.4462), as it combines high material strength with good wear resistance and excellent resistance to pitting and SCC and is competitively priced. Grade 2205 DSS has much higher yield strength (450 MPa) than typical austenitic stainless steel and allows a reduction in thickness to give similar mechanical properties compared with equivalent designs in common 300 series austenitic grades [17]. Moreover, it is more price-stable than other types of stainless steel owing to its relatively low nickel content, which tends to fluctuate in price considerably.

Two main allotrope phases of iron are present in the parent material: gamma austenite (γ) having a face-centred cubic (FCC) structure and delta ferrite (δ) having a body-centred cubic (BCC) structure (alpha ferrite being the ferrite formed from austenite phase in austenitic metal [18]). Optimum properties are achieved when the microstructure presents a nearly equal proportion of austenite and ferrite phase [19][20][21]. Here, only the most significant alloying additions are briefly discussed to understand their role in the resulting microstructure and therefore their impact on the material properties.

Chromium is the main alloying element in percentage by mass, added mostly to improve the localised corrosion resistance, as it is responsible for passivation. Chromium is a ferrite phase stabiliser, and there is a limit to the amount that can be added, as a high percentage enhances detrimental precipitations such as sigma or chromium nitride. These phases are often associated with a reduction of the corrosion properties and ductility [19].

Another ferrite phase stabiliser is molybdenum, an element that increases the pitting and crevice corrosion resistance in chloride solution as it suppresses active sites via formation of an oxy-hydroxide or molybdate ion [19][22].

Nickel is an austenite stabiliser, and its addition is there to counterbalance the ferrite stabilising effect of chromium and molybdenum. It is also a critical element in ensuring good pitting corrosion resistance properties [23]. The level of nickel needed to maintain about 40 to 60% of ferrite will depend primarily on the chromium content of the given duplex. As depicted in Figure 2.2, the absence of nickel leaves the stainless steel microstructure fully ferritic while an excess of nickel can lead to an austenitic microstructure.

Nitrogen addition is interesting as it raises the temperature at which austenite starts to form when the metal goes from liquid to solid state. The ternary Fe-Cr-Ni phase diagram presented later in Figure 2.4 shows the effect of additional nitrogen in the microstructure.

The alloying elements above are also used to characterise the DSSs into groups according to their pitting resistance equivalent number (PREN). This number is calculated using an empirical formula in which the favourable effect of particular alloying elements upon the pitting corrosion resistance is taken into consideration. The commonly used formula to classify DSSs is given by equation 2.1[19]:

$$PREN = \%Cr + 3.3 \times \%Mo \times 16 \times \%N \qquad \text{Equation 2.1}$$

Grade 2205 DSS has a typical PREN of 35, a much higher PREN than any ferritic stainless steels or 300 series of austenitic stainless steels. Studies have highlighted that around an equal proportion of ferrite and austenite phase in grade 2205 DSS exhibited the highest resistance to pitting corrosion [24]. Several other studies on similar grades or super DSSs showed that an increase of the ferrite phase above the volume fraction of 49 to 62.5% (depending on the grade) was linked to a decrease of the pitting resistance[21][25][26].

2.1.2 Applications of grade 2205 duplex stainless steel

As mentioned before, DSSs have higher resistance to pitting and SCC when compared with austenitic grades and exhibit greater toughness and better weldability than ferritic stainless steels. Accordingly, they are widely used in various chemical, petrochemical, food, power, transportation, pulp and paper industries as well as oil refineries.

Grade 2205 DSS is used in a variety of applications such as transmission lines in the oil and gas sectors, heat exchangers in power plants, offshore structural components for marine infrastructure, and plays a major role in water treatment facilities. Norm EN 10312 from DIN (Deutsches Institut für Normung or German Institute for Standardization) recommend grades 1.4362 (Grade 2304 DSS) and 1.4462 (grade 2205 DSS) preferably for systems of water distribution and storage.

In the UK, grade 2205 DSS is commonly used for intermediate level nuclear waste (ILW) containers made of 3 and 6 mm thick flat panels [27] (as depicted in Figure 2.2). This latter application was partly motivating the research since the UK nuclear industry requires tens of thousands of these containers to be manufactured as nuclear facilities in the UK are decommissioned. The manufacturer of these ILW containers (Graham Engineering, BB9 8SY Nelson, UK) was also looking for an improved laser welding process for large volume production.

Figure 2.2: Intermediate nuclear waste containers
Courtesy of Graham Engineering, BB9 8SY, Nelson, UK

ILW does not produce significant heat but still emits radiation. They may require long-term storage, as for Sellafield (CA20 1PG Seascale, UK), and to be stored for up to 150 years at site before transporting to a permanent geological disposal facility (GDF) for a further 350 years. Corrosion resistance is, therefore, a critical requirement for the container. In addition,

they should meet the basic mechanical requirements of static loading, impact loading and stiffness.

2.1.3 Welding of grade 2205 duplex stainless steel

In production, the phase balance of DSS is achieved through solution heat treatment, but after welding, it can be profoundly modified depending on the weld thermal cycle. Some studies have reported that the microstructural changes during welding, as the material melts, have a profound impact on the structural performance [20][28]. The ferrite-austenite transformation during welding, leading to the final phase balance, is dependent on the material composition and the cooling rate.

Grade 2205 DSS solidifies primarily in the fully ferritic phase, and this is followed by the time-dependent formation of the austenite phase through solid-state transformation (i.e. nucleation) [19]. The ferrite-austenite transformation during welding, leading to the final phase balance is, therefore, a function of the thermal history. Figure 2.3 shows the solidification path of grade 2205 DSS through the iron-chromium-nickel ternary phase diagram. After welding, at the fusion zone, further cooling initiates the formation of austenite, nucleating at the ferrite grain boundaries. Austenite starts to form below the ferrite solvus temperature, which is dependent on the weld metal composition. Depending on the ferrite grain size and cooling rate, austenite forms intergranularly as widmanstatten or intragranular plates. The precipitation of austenite is a diffusion-controlled process, whereby the diffusion of nitrogen and carbon is the controlling process and, as such, the cooling rate is a major determinant of the extent of transformation. The time-dependent precipitation occurring during cooling as depicted in Figure 2.4.

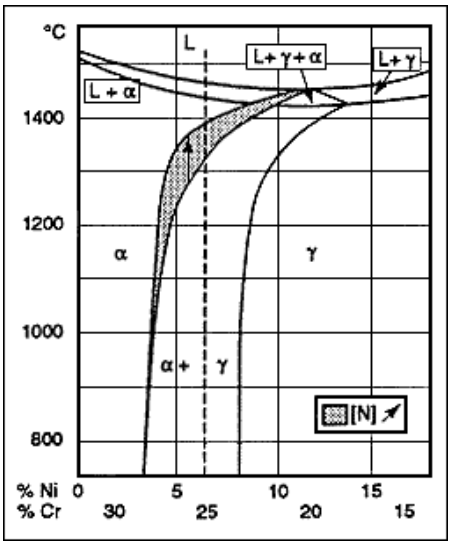

Figure 2.3: Fe-Cr-Ni phase diagram representing typical DSS compositions [16]

Welds resulting in a low ferrite content (< 30%) can reduce the resistance to stress corrosion cracking (SCC), whereas a high ferrite content (> 70%) can reduce the toughness and the resistance to pitting corrosion [24][29]. Within the range of 30 to 70% of ferrite in the weld, these detrimental reductions in toughness, pitting resistance and SCC resistance are less significant [30]. Therefore, the cooling rate plays an important role in achieving the necessary

mechanical properties and corrosion resistance, which has to be controlled to allow the higher content of austenite to form. The target is to produce a weld containing a balanced 50% austenite and 50% ferrite phase. The offshore standard for submarine pipelines, for instance, stipulates that the ferrite content shall be within the range 30-65% [31].

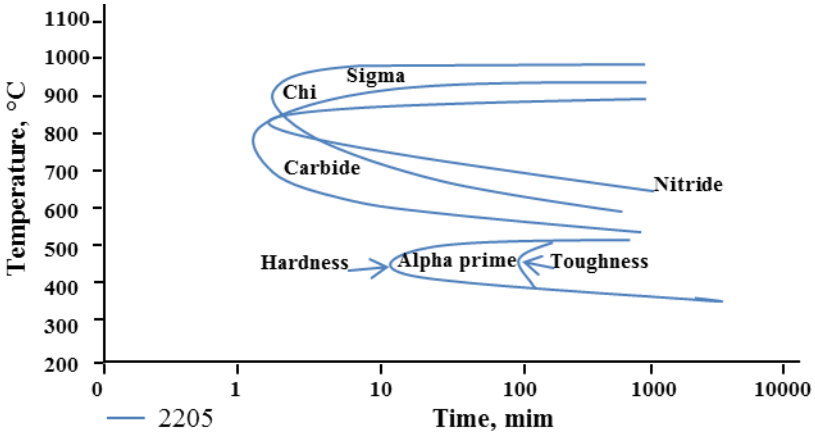

Figure 2.4: Time temperature diagram of Grade 2205 DSS [19]

Established welding techniques using high heat inputs such as tungsten inert gas (TIG) and gas metal arc welding (GMA) result in a relatively slow cooling process which promotes the ferrite-austenite transformation resulting in a more favourable phase balance. However, such conditions also tend to produce wide heat-affected zones (HAZ), coarse-grained weld deposits as well as an increased tendency toward precipitation of brittle intermetallic phases. Most of the detrimental precipitation in the weld occurs when the temperature is maintained at high temperature for a prolonged time (as depicted in Figure 2.4) which can be the case of conventional arc-based welding processes if the interpass cooldown is not respected [19][32]. Production of intermetallic phases and embrittlement, constitute a significant risk, markedly reducing both toughness and corrosion resistance [33]. For instance, the sigma phase (Cr-rich phase), can cause considerable reduction in plasticity and impairment in corrosion resistance[34], [35]. These impairments form at temperatures between 550 and 1000°C for the sigma and chi phases and at a lower temperature from 350 to 550°C for the embrittlement. They start to form if the temperature is held for a couple of minutes. Hence these risks are mostly for heat treatments and certain types of arc welding with high heat input over a large area combined with a slow process.

On the other hand, relatively low heat-input processes such as laser welding can avoid the formation of most of the harmful precipitation, reduce material distortion and give a narrow HAZ with a finer grain microstructure. However, the laser welding process is not entirely free from detrimental precipitation as studies reported that during welding, as the ferritised microstructure cools rapidly, the ferrite becomes supersaturated in nitrogen, resulting in a competition between chromium nitride and austenite precipitation [36] [37]. Intergranular nitrides (Cr_2N rods or CrN plates) result in degradation of the mechanical and corrosion properties of the welded joint [37]. Hexagonal nitride Cr_2N and cubic nitride CrN can also be found in the weld HAZs. Promoting the growth of austenite phase is therefore critical to

absorb the nitrogen that has a low solubility in the ferrite phase and therefore avoiding the detrimental precipitation to happen.

DSS is a prominent and widely used grade in many engineering applications that required welding, but there are still issues. The formation of undesirable precipitates, increased distortion level and residual stresses with multi-pass welding are the concerns for high energy arc process (GTAW/TIG, GMAW) while the high ferritisation in the weld remains the principal problematic with low energy arc process such as plasma arc, electron and laser welding. As pointed out in a recent review on the effect of welding processes of DSS, more research perspective to this area is required [38].

2.1.4 Welding processes comparison for duplex stainless steel

The need to manufacture in large volumes impacts on the economics of production, necessarily driving the unit cost down if parts are to be manufactured at a realistic price, but quality must be maintained as suitable for service. Designs using DSSs usually require long-term corrosion performance alongside other criteria such as impact performance and strength. There is, therefore, a need for research to evaluate existing welding processes capable of producing relatively low cost, structures in stainless steels that meet high-level quality requirements and operate at high speed to meet productivity requirements and also result in low distortion [39].

Arc welding processes such as conventional metal inert gas (MIG), controlled deposition MIG and TOPTIG^{TM} might show promise for applications but need further work to demonstrate their relative capabilities for producing high-quality welds with controlled heat input in stainless steel components. These processes also require multiple passes for thicker sections (>5 mm) and the high heat input applied to thin sections usually results in high levels of distortion. Typical welding speed for arc welding are below 0.5 m/min while for laser welding it is approximately an order of magnitude higher.

Arc welding processes can be coupled with a laser to form a hybrid laser- arc welding process [40]. However, these combinations, are not an attractive choice for welding thin materials and in continuous production, even if hybrid laser welding techniques increase heat input and have been reported to give wider welds and better response to nitrogen additions to the shielding gas for 1-2 mm thick duplex steel [41]. Hybrid laser-arc welding processes are quite complex as the parameters of both the arc and laser processes, and the interactions between the two processes have to be optimised. In practice they are relatively rarely adopted by industry for this reason. Another drawback is that hybrid laser welding, when using a consumable electrode (wire addition), may give excessive weld metal reinforcement for butt welded thin sheet and that for 8 mm and 13.5 mm thick material, the filler metal may not reach the weld root with a single pass [41][42]. In addition, MAG hybrid welding has a tendency to spatter formation, and advanced pulsed power sources are required for thin material applications.

Finally, other available approaches are laser welding processes on their own. They are capable of producing welds at high speeds with the potential for low distortion and are also

worthy of consideration for the welding of DSS. The features of laser welding processes such as increasing productivity and achieving full automation are fundamental requirements for cost-effective design. In addition, laser processing is an attractive technology for industry, as its versatility for multiple material processes (welding, cutting, surfacing, hardening, drilling) makes it very flexible depending on the work needed.

Welding of DSS with low a heat input process (for example, electron and laser beam) has been the subject of numerous papers all pointing out the excess of ferrite resulting at the weld location due to the fast cooling rate associated with these technologies [28][43][44]. The current solution for laser welding DSS involves filler wire (i.e. ER2209) over alloyed with nickel, as this element is very effective in promoting austenite formation [43]. However, wire addition adds costs to the process, increases its complexity and reduces its flexibility. Welding should be controlled in a way that leads to a cool-down period which is sufficiently slow to enable between 30 and 70% austenite formation and yet fast enough to limit the size of the HAZ and avoid damaging precipitation.

The following part presents the laser technology and more specifically the ytterbium-doped fibre laser along with the key concept of laser welding.

Part 2: Yb:fibre laser welding

2.2 Laser technology

Yb:fibre lasers fundamentally work in the same way as all other lasers: a population of atoms or molecules are brought into a higher state of energy, and the relaxation of some atoms or molecules to a lower level of energy will release a photon emission. This will, in turn, stimulate the relaxation of other excited atoms/molecules producing an avalanche effect of photon emission all having the same phase and direction of the incident one. The principle of the laser is shown schematically in Figure 2.5. A laser usually consists of two reflectors forming a cavity, in which light bounces back and forth, and is amplified through a gain medium pumped or excited by an external source.

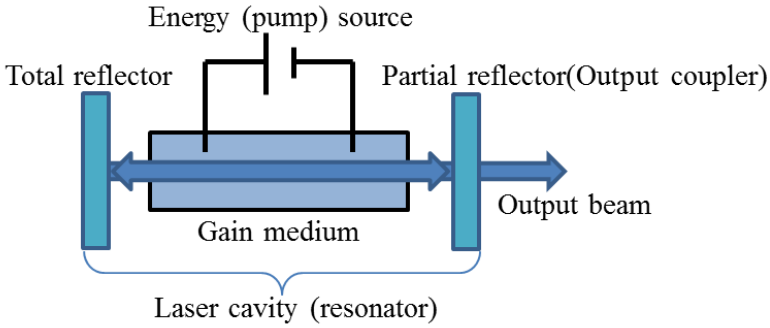

Figure 2.5: Laser schematic

The simplest form of a cavity consists of two highly reflecting mirrors at each end of the gain medium. For the photons to be in phase with each other, the length (L) of the optical resonator must be a natural number (n) multiple of half the wavelength (λ) of the electromagnetic radiation.

$$L = n\,\lambda/2 \qquad \text{Equation 2.2}$$

The back mirror reflects the light entirely, while the front one leaves a fraction of the desired light to pass through. The external energy source, known as the pump, is there to create the population inversion for the light to be amplified in the gain medium. Incident photons interacting with excited atoms or molecules lead to their multiplication, a process known as the lasing effect.

Ultimately, the laser light properties depend on the design, quality and integration of the different laser components such as the gain medium, the pump and the resonator. The resulting operating mode, wavelength emission, maximum rated power and beam quality are then the key factors to take into account for the industrial use of a laser.

2.2.1 Yb:fibre laser sources

This section gives particular attention to the type of laser used in this research, the Ytterbium-doped fibre laser (Yb:fibre) source.

First laser emission with fibre was demonstrated in early 60's and then revisited in the 70's. A primary interest in this technology came later in the 80's in the context of optical fibre telecommunication since the emission of some rare earth doped lasers fall in the third communication window (~1.55 µm).

The use of rare-earth-doped fibre lasers for materials processing applications has risen significantly over the past decade, especially Ytterbium doped fibres, which is the current fibre gain medium of choice [45]. The development of Yb:fibre lasers has led to a range of laser sources available with tremendous power outputs up to 100kW, outstanding beam qualities (as good as 0.33 mm.mrad), and excellent wall-plug efficiencies (~ 40%). This success is due in large part to the fibre's geometry, which provides considerable resilience to the effects of heat generation in the core, and facilitates efficient conversion from relatively low-brightness diode pump radiation to high-brightness laser output [45].

The schematic of a Yb:fibre laser is shown in Figure 2.6, each part is then discussed in the following sub-sections.

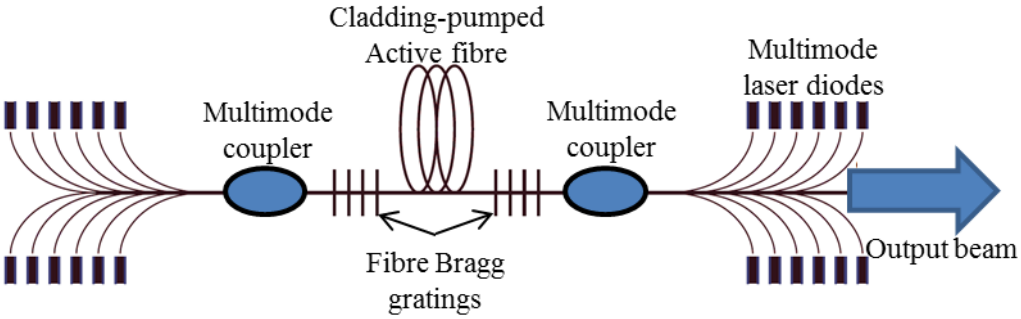

Figure 2.6: Yb:fibre laser schematic

2.2.1.1 Gain medium

The gain medium is a critical part of a laser as it determines the emitting wavelength λ, one of the key parameters for laser material processing as is it directly relates to the energy absorbed by the material. Lasers are usually named after the gain medium used in their design. Typically, a device made from coils of ytterbium-doped multi-clad fibre with an emission wavelength of 1.07–1.08 µm is used. Alternatively, it may be thulium doped with a wavelength of 1.8–2.0 µm or erbium doped with a wavelength of 1.54 – 1.56 µm [8], although, these are relatively rare for materials applications.

2.2.1.2 Pump

In any laser, to excite the gain medium to achieve the population inversion, pumping is necessary. Optical pumping refers to the use of a flash-lamp, arc lamp, or other light sources to excite the gain medium whose energy is transmitted in a photon form. The pump plays a central role in the laser power consumption and therefore the resulting wall-plug efficiency (which is mostly expressed in percentage terms of energy consumed versus the laser energy

output). As an example, flash lamp pumps were replaced by diodes in Nd:YAG and Yb:YAG laser systems doubling or tripling the wall plug efficiency. With increasing environmental issue awareness and the price of the electricity, the wall-plug efficiency is a parameter not overlooked by industry. In this regards, Yb:fibre outperforms most other industrial laser systems with the exception of the diode laser system. Nevertheless, diode laser systems suffer from low beam quality, limiting their application to surface processing or thin sheet welding.

2.2.1.3 Cavity and emission

The front mirror is partially reflective and works as the aperture of the laser source. For Yb:fibre laser sources, the principle is the same, but the mirrors are replaced by fibre Bragg gratings attached (spliced) to the fibre. A fibre Bragg grating consists of periodic layers of different materials with different refractive indexes inside the fibre. Each layer's interface contributes to a Fresnel reflection. The refractive indexes and the distance separation between layers are such that the reflected waves are in phase so they can add up constructively and almost total reflection at the design wavelength can be achieved if the grating is sufficiently long (millimetre order). Intensity of the light builds up in the medium.

Light amplification in a laser medium is accompanied by a decrease in the population at the upper level leading to an adjustment of the gain until the gain saturation. This mechanism adjusts the gain to a value where it just balances the losses in the cavity so that steady oscillations can result. The steady state oscillation or ability of a laser system to maintain a beam with constant output power level is then reached. This mode of operation is referred to as continuous-wave (CW), although this mode may be modulated and/or ramped up/down with the help of a shutter.

Lasers can also operate in pulsed a mode and emit light in a series of single energy bursts of a defined duration. The shorter the duration of a pulse at a given energy, the higher the peak power will be. Among the methods to generate pulsed lasers, the two most popular used for material processing are Q-switching and mode locking. Both are achieved by placing either an active element (such as acousto-optic or electro-optic modulator) or a passive element (such as a saturable absorber) in the cavity [46]. Typical output values of an active Q-switched Nd:YAG laser may be around 100 mJ pulse energy, 10-1000 Hz repetition rate and around 10 ns pulse duration. Mode locking methods can produce ultrashort pulses in the region of picoseconds or femtoseconds. Ultrashort pulses will not be further discussed here, as they are not relevant for welding; Q-switched lasers for material processing are typically used for, micromachining, cutting, drilling, laser marking, and femtosecond lasers find applications in micro-ablation and processing of medical instrument or prosthesis.

2.2.1.4 Power output

A description of the spatial distribution of light within the cavity of the laser is called a mode. The power per unit cross section of the laser beam is the intensity, and the way it is distributed depends on both the mode or combination of modes running in the laser cavity and on how those modes are distorted by the presence of apertures, refractive index gradients of optical elements used, imperfect optical surfaces and other perturbing influences [47].

Boundary conditions in the cavity lead to the formation of standing longitudinal electromagnetic waves. Constructive and destructive interferences between these longitudinal waves give rise to the formation of an electromagnetic radiation field pattern transverse to the longitudinal waves. This is referred to as Transverse Electromagnetic Mode ($TEM_{n,m}$, where the integers m and n indicate the number of zero fields in a particular direction). Laser beams with a higher TEM are harder to focus to a small spot than a laser beam with a low TEM because higher TEM are larger [48]. The advantage of higher TEM or multi-mode laser (cohabitation of several modes) is that they can extract more power as the TEMs occupy a larger volume in the gain medium and therefore can interact with more of the active medium. However, keeping the laser oscillating only in its lower mode $TEM_{0,0}$, also known as the fundamental mode or diffraction limited mode, leads to the best beam quality possible which can be beneficial for selected industrial applications. $TEM_{0,0}$ is the most straightforward mode and its intensity distribution, *I*, as a function of the radius, *r*, from the central axis can be theoretically described as a Gaussian function, see Equation 2.3 and Figure 2.7.

$$I(r) = I_0 e^{\frac{-2r^2}{\omega_0{}^2}} \qquad \text{Equation 2.3}$$

Where I_0 is the axial irradiance and ω_0 is the beam waist's radius. A Gaussian beam radius is defined as the radius where its irradiance is $1/e^2$ of the peak irradiance.

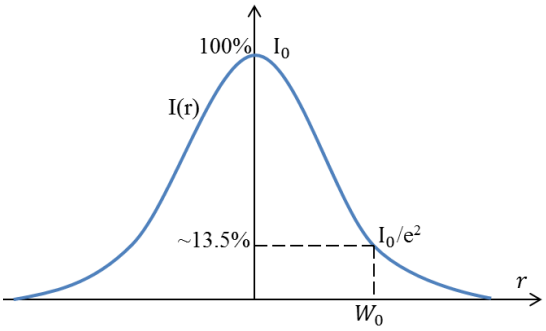

Figure 2.7: Intensity plot of a Gaussian function

According to Equation 2.3, the diameter is the portion of the laser beam that contains 86% of the total energy of the beam.

Light inside the fibre propagates by total internal refraction (TIR) and if the core of the fibre is small enough (depending on the wavelength traveling inside), the fundamental mode $TEM_{0,0}$ (although for fibre, modes are usually expressed in terms of "Linear Polarisation" the fundamental one being LP_{01}) can be propagated alone. For Yb:fibre lasers, the core diameter of single-mode operation is between 10-30 µm. Advantages of the single-mode fibre laser are the excellent beam quality (BPP is related to the diameter of the core fibre) and a high peak intensity (Gaussian energy distribution, $TEM_{0,0}$). State-of-the-art Yb:fibre single-mode laser systems can deliver up to 10 kW output powers.

Several modes can propagate at the same time with a larger diameter core fibre. For Yb:fibre lasers, powers over 10 kW are achieved by combining the output from several single-mode fibre lasers, and power above 100 kW has been produced [49] [50]. Nevertheless, a broader core (50-300 µm for Yb:fibre) leads to a lower BPP (4-12 mm.mrad), and the dispersion at the output is translated by a wider energy distribution with a flattened peak intensity [51].

2.2.1.5 Beam delivery

As powerful a laser system can be, it is not effective without a finely tuned beam delivery system. The laser beam emitted from the cavity needs to be re-directed to a specific location. Depending on the configuration, the beam delivery system can include components such as mirrors, lenses, and optical fibres arranged to precisely guide the laser beam to its final destination.

A typical industrial installation of a Yb:fibre laser source, will include beam delivery by an optical fibre. The purpose of this optical fibre is not to support the lasing action, but to deliver the beam from the laser source to where the beam is required. However, the laser beam exiting the delivery fibre will have large divergence, and typically requires a series of lenses first to collimate, and then focus the laser beam down into a spot size suitable for industrial laser materials processing applications. A schematic of a simple collimating/focusing lens system is shown in Figure 2.8.

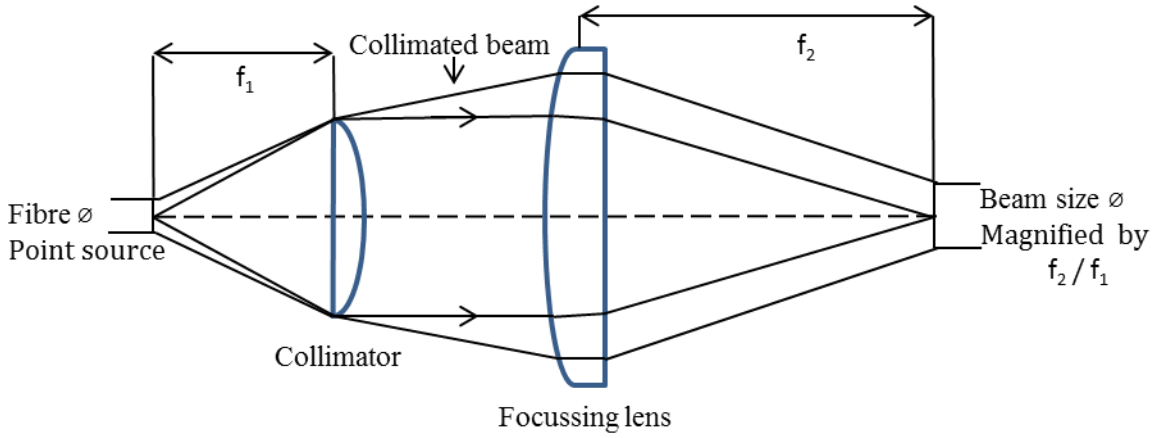

Figure 2.8: Dual lens system

If the fibre end (fibre core) is filled by the laser beam (which is the case with step index fibres), its image formed on the workpiece in the focal plane is given by the relation of ray tracing optics in Equation 2.4.

$$Beam\ size = \emptyset\ fibre\ core \times \frac{\text{focal length focusing lens}}{\text{focal lengthcollimator}} \qquad \text{Equation 2.4}$$

This formula holds in the approximation of a thin lens. The ratio between the focal length of the focusing optics (f_2) and the one of the collimator (f_1) is the magnification ratio.

Along the propagation direction of light, the laser beam diameter converges to a minimum. This point is called the beam waist, and its radius is referred to as ω_0 (in mm). The angle θ formed by the increase in beam diameter as the laser beam propagates through space is called the beam divergence angle and it is expressed in mrads.

Diffraction is unavoidable due to the wave nature of light, and for any given optical system the diffraction phenomenon will dictate the theoretical limit of its performance. Therefore, if a collimated beam of diameter *D* is focused by lens of focal length *f* that does not introduce

any aberration, the theoretical diffraction limited spot size or beam waist $\omega_0(th)$ is given by Equation 2.5 and Figure 2.9 depicts the enounced parameters:

$$\omega_0(th) = \frac{2\,\lambda\,f}{\pi\,D}\,M^2 \quad [48] \qquad \text{Equation 2.5}$$

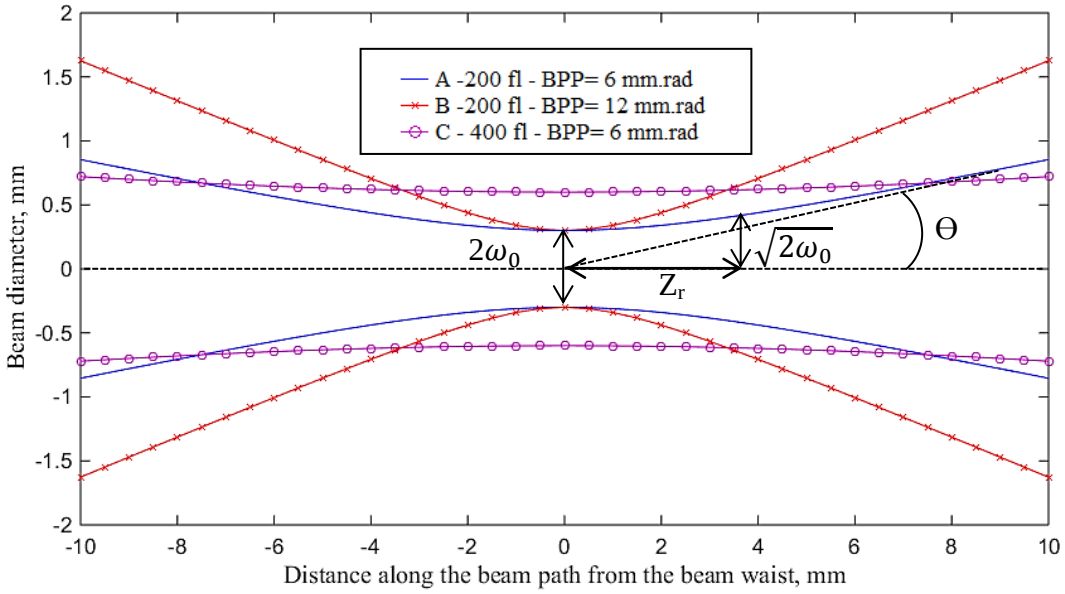

Figure 2.9: Beam propagation with different focal lengths and BPP

The product $\theta \times \omega_0$ is defined as the beam product parameter (BPP). Its measurement is given by standard ISO11146 [52]. Theoretically the lowest BPP for a perfect Gaussian beam is equal to λ/π. The ratio between a real beam focus-spot diameter and the focus-spot diameter that would be produced by a theoretically perfect beam is called the beam quality and is denoted by an M^2 value [53]. For CO_2 lasers, the beam quality is often stated in terms of M^2 while the beam quality for Yb:fibre lasers beam is typically expressed in terms of its BPP value. A small value of BPP equates to a good beam quality. The notion of beam quality is essential as it expresses how small a beam can be focused and the smaller the beam size (with a certain power), thereby giving higher power densities and enabling certain materials processing applications [54].

The most widely mathematical description of the laser modes comes from solving the wave equation in scalar approximation. The mathematical solutions give an elegant formulation for the beam radius ω along the propagation direction z and the power density in cylindrical coordinates. The theoretical beam radius along the Z-axis given by Equation 2.6:

$$R(Z) = \omega_0\sqrt{1 + \left(\frac{Z}{Z_R}\right)^2} \qquad \text{Equation 2.6}$$

The beam waist or beam radius ω_0 is found as the focal point (narrowest beam waist, Equation 2.5). The Rayleigh range Z_R describes the distance it takes, along the propagation direction, for the area of the cross-section to be doubled (which means for the beam radius to

be extended by a factor $\sqrt{2}$). Theoretical Z_R (for a Gaussian beam propagating in free space along the Z axis) is given by Equation 2.7:

$$Z_R = \frac{\pi {\omega_0}^2}{\lambda} \qquad \text{Equation 2.7}$$

Z_R describes the distance it takes, along the Z axis, for the area of the cross-section to be doubled and therefore gives a practical characterisation of the beam divergence.

2.2.2 Laser welding

Laser welding consists of focusing a laser beam with enough power on substrate's surface to melt and/or vaporise the metal. Many metals including steel, stainless steel, aluminium alloys, titanium alloys, and nickel alloys can be laser welded, but also non-metallic materials like ceramics, composites and plastics may also be laser welded.

Figure 2.10 shows a sequence of laser-matter interactions, with increasing energy densities. The focused laser beam interacts with the material. The energy absorbed can lead to a phase change of the substrate (gaseous, liquid) creating a liquid melt pool and potentially a keyhole (if the laser intensity reaches several MW/cm^2). The melt pool is then propagated along the solid interface fusing the original seam between the components to be joined. There are two forms possible of laser welding, one is conduction limited welding (involving the melting of the substrate), and the other one is keyhole welding (involving the vaporisation of the substrate). They are depicted in Figure 2.11.

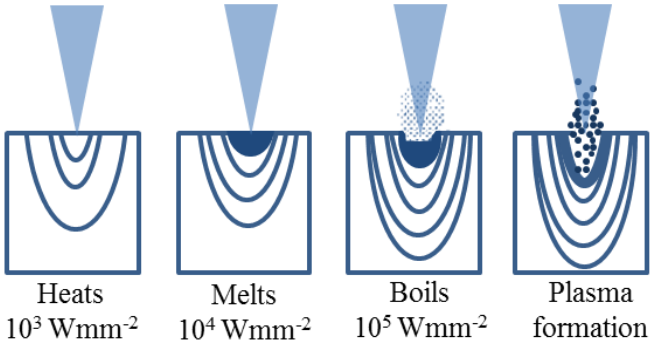

Figure 2.10: Sequence of absorption

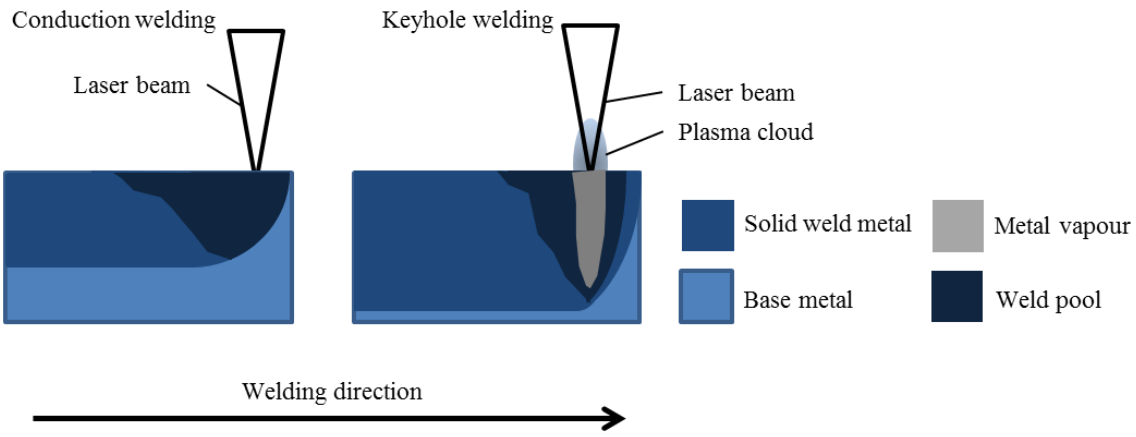

Figure 2.11: Conduction and keyhole welding

A summary of advantages of keyhole fibre laser welding is presented in Table 2.1 [55].

Table 2.1: Advantages of keyhole laser welding

Characteristics	What makes it possible	Advantage in industry
Low heat input	• Laser beam can be narrowly focused • High speed possible	✓ Narrow HAZ ✓ Minimal thermal distortion ✓ High aspect ratio (width:depth) ✓ Possibility for simpler clamping
High-speed process	• Laser beam can be narrowly focused • High power • Efficient energy transferred to the workpiece	✓ High productivity ✓ Possibility for longer weld seams increasing component stiffness
Flexibility	• Operate at atmospheric pressure • Non-contact process • Autogenous process • Fibre optic delivery of laser beam • Easy robotic automation	✓ No component size limitations ✓ Complex welding geometry possible ✓ Variety of joint configurations possible (Butt, lap, T-butt etc.)
Repeatability	• Excellent equipment reliability • Easy robotic automation • Laser beam is not affected by magnetic fields	✓ Accurate, reliable welding process

2.2.2.1 Keyhole laser welding

In the case of keyhole welding, the workpiece is not only melted, but the centre of the melt pool is vaporised, leading to deeper weld penetrations. Keyhole welding requires a very high power beam to create a full penetration. Vaporisation of metallic substrates can occur at applied intensities as low as 10^2 W/mm^2 if the interaction time is sufficient. However, applied laser intensities exceeding 10^5 W/mm^2 are often used to achieve vaporisation of the surface's materials. Typically, a 5 to 10 kW laser beam is focused down to a small spot of around 0.2 to 0.8 mm in diameter, which is required to evaporate the material and form the vapour capillary known as the 'keyhole'. As shown in Figure 2.12, a keyhole surrounded by a hollow column of molten material is formed in the core of the weld, and the vapour column's pressure keeps it open. As a result, the laser light is efficiently absorbed as it is subject to many reflections off the keyhole's walls (Fresnel absorption). Consequently, the effect of absorptivity and hence the laser wavelength becomes less important the deeper the hole. Conduction and convection in the liquid transfer heat to the material increasing the molten volume.

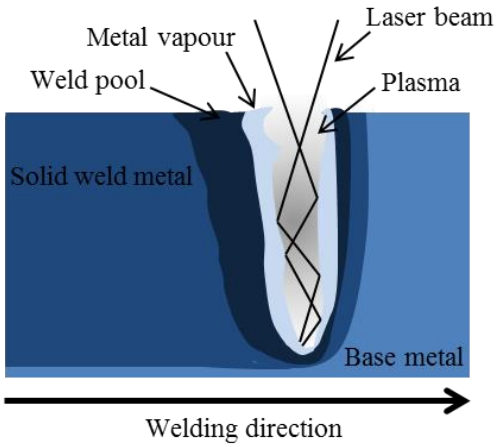

Figure 2.12: Sketch of a keyhole

During welding, the relative motion of the beam moves the keyhole through the seam leaving a fused zone behind. At power densities of around 10^7 w/cm^2 and higher (in metals and with CO_2 radiation) some of the electrons in the vapour become ionised. These free electrons can also absorb energy directly from the incoming laser beam, resulting in higher temperatures, more ionisation and increased absorption. Plasma of ionised metal vapour, which can absorb laser light and emit blackbody radiation, is formed. As long as the power density is sufficient to sustain it, the plasma will be a net contributor to the process. At even higher power densities, the vapour column leaves the keyhole, forming a cloud over its opening. This plasma cloud (or plume) is fed by the partial absorption of the incident laser beam through the Inverse Bremsstrahlung mechanism, decreasing the energy entering the keyhole and reduce the penetration. In such situations, the laser wavelength will regain importance because the inverse Bremsstrahlung absorption coefficient is directly proportional to the square of the laser wavelength [56]. Short wave radiations are less absorbed by the plasma, and in fact, with a Yb:fibre laser, the plume is considered as a hot metal vapour rather than plasma as the ionisation is at best weak [57].

2.2.2.2 Improving the keyhole welding process

In order to improve the keyhole laser welding process for higher absorption of the laser beam and deeper penetration, several parameters can be modified [58]. They are divided into categories, the parameters directly relate to the laser system itself, the material being welded and finally the welding process parameters. Table 2.2 summarises these factors.

Table 2.2: Properties influencing absorption

Laser Properties	Material Properties	Process Parameters
Power density	Composition	Welding speed
Wavelength	Surface quality (oxide layers, dust, etc.)	Beam position
Polarization	Temperature	Beam size
Angle of incidence	Roughness	Shielding gas

Laser properties are mostly intrinsic to the laser system and can rarely be changed without permanent modification of the system. Material properties are also set in term of composition, but the roughness or surface quality is usually taken into account during the

manufacturing process. Dirt, dust or grease can contaminate the weld or challenge the stability of the keyhole during welding. Research shows that with high power Yb:fibre lasers, the edge surface roughness has a large effect on absorption, due to the multiple reflections it causes. Bergström et al. [59] recorded, by reflectance measurements, a trend of increasing absorptance for increasing roughness above Sa 1.5 µm for stainless steels and above 6 µm for low-alloyed steels (Sa is the areal roughness parameters). Nevertheless, in many industrial processes where the laser system and material composition are set, and the process parameters remain the principal leverage to optimise the welding process. In addition, the process parameters are closely related to the dynamic behaviours of the keyhole and the melt pool which will also affect the weld profile and joint quality [60].

High welding speed can cause spatter due to the difficulty of the molten material to flow around the keyhole. At low welding speed, porosity can be formed from bubbles generated from the tip of the keyhole [61]. Power density and high brightness, which is defined as the power density in the spot per solid angle in the cone of the focused beam, have been pointed out as a key factor for achieving deep penetration in stainless steel [54][62]. The beam size and position are other parameters influencing the weld profile and presence of potential defects such as cracking, humping or porosity. In this regard, the use of multiple beams technique has been investigated in the last decade to address weld defects caused during single beam welding. A number of studies pointed out this approach as a potential solution to avoid cracking [63], porosity [64] or influencing certain phase formation [65].

2.2.3 Yb:fibre laser welding of grade 2205 duplex stainless steel

In the first part of the literature review, the industrial use of grade 2205 DSS has been put into context, highlighting the need for research on developing a manufacturing process with a focus on the phase balance conservation to maintain the material properties. The potentials of Yb:fibre laser are high in term of weld quality and high productivity.

It has been reported that welding trials carried out using an IPG YLR 20000 Yb:fibre laser achieved full penetration in 15 mm thick plates of grade 2205 DSS at 10.9 and 8.56 kW for welding velocities of 1.0 and 0.5 m/min, respectively [66]. Nevertheless, the main drawback of keyhole welding of DSS is the high cooling rate due to the low heat input, which can cause an unfavourable phase balance in the weld metal. As mentioned in section 2.1.4, low heat input results in high percentage of ferrite at the weld [28][43][67] thus impeding the weld quality in term of corrosion properties [19][20][24][28][29][30][31]. Therefore, the addition of over-alloyed filler metal or even post-weld annealing is required. Filler wire is costly and difficult to implement as it introduces many more variables to control (feeding rate, wire diameter, positioning etc.) and post-weld heat treatments, in addition to considerably lower the productivity, are not always possible.

Research on optimising autogenous laser welding process parameters for stainless steel including grade 2205 DSS have been mostly done with a CO_2 laser or a Nd:YAG [28][68]. Results pointed out the excess of ferrite, the benefits of using nitrogen gas as shielding to favour austenite formation and recommended a high power density with the beam waist being

in the vicinity of the workpiece's top surface. A pulsed Nd:YAG laser welding approach on 2 mm thick sheets resulted in low welding speed, very high ferrite content and significantly increased hardness [69]. CO_2 and Nd:YAG laser technologies are nevertheless different from modern Yb:laser fibre that offers a more efficient utilisation of the laser energy into the welding process. Current research using Yb:fibre lasers to weld grade 2205 DSS is rare. Recent research has confirmed the advantages of nitrogen shielding gas to improve the phase balance [70], but ferrite content at the weld location was still above 70%.

As a reminder, grade 2205 DSS solidifies primarily in a fully ferritic state followed by a solid-state transformation to austenite. The final phase balance is therefore controlled by the cooling rate of the workpiece.

Capello et al. used a CO_2 laser without filler wire to weld 5mm thick grade 2205 DSS with a processing power of 5.6 kW and a reference welding speed of 2.1 m/min [71]. Then, the same laser was used for a re-heating pass after welding. The surface treatment was made in defocus position at lower power 1.2 to 2.15 kW and very slow speed from 0.06 to 0.18 m/min. As a result, the estimated ferrite fraction at the weld cap was reduced from 80% to 58%. This work demonstrated that by a subsequent laser pass it was possible to modify the weld cap ferrite to austenite ratio. The technique is extremely time consuming and therefore not desired in industry for large volume application.

Approaching the issue with a similar idea but implemented in one welding pass, Westin and Fellman have tried a combination of different welding techniques. A lasers beam (CO_2, Nd:YAG and Yb:fibre) followed by either GTA or GMA with and without filler wire were used to influence the cooling rate and promote the formation of austenite [72]. Although this comparative study was carried out on grade 2201 and filler wire was used for most of the welds, the combination of an Nd:YAG laser followed by a GTA process decreased the ferrite content of the weld to 62%, compared with 81% for a weld made with Nd:YAG laser alone. Such a technique remains difficult to implement in industry because of the many parameters to control and the close contact needed between the GTA torch and the workpiece limits the flexibility of the process to weld complex paths. Nevertheless, the manipulation of the power distribution at the weld location, in this case, two different disjointed heat sources, seems to be able to influence the microstructure of the weld and could be a solution as well for grade 2205 DSS. A laser beam with a tailored energy distribution providing post-weld heating with only one pass and one laser would potentially be an effective solution. With a titanium alloy metal, for instance, Shen et al. reported that a dual beam laser welding allowed the desired formation of O phase at the weld location thanks to a cooling rate decrease when compared to single beam welding [65].

The subsequent, and final, part of this literature review, therefore, presents different ways the spatial energy distribution of the laser beam, i.e. the laser beam's intensity profile, can be modified when delivered to the workpiece.

Part 3: Tailored energy distributions

2.3 Changing the energy distribution

As stated previously, changing the energy distribution of the laser beam to control temperature gradient, the weld pool morphology and the weld profile would potentially offer more control over the welding process of grade 2205 DSS. This section presents some commercially available solutions for tailoring the spatial energy distribution of laser beams, with a particular focus on diffractive optics.

A laser beam is an electromagnetic radiation and cannot be modified without altering its wave-front. 'Beam shaping' in the context of this thesis consists of altering an incoming beam by transforming either or both the scale and the intensity distribution (irradiance profile) of a laser. There are two possibilities for changing the energy output of a laser: either by making modifications in the laser system itself (changing the cavity length or mirrors, precision etching of the fibre end in case of a fibre laser) or by adding an optical system in the delivery optics. The former is possible but presents numerous drawbacks with the permanent arrangement, and only limited numbers of simple energy distributions are possible. In addition, the cost for a custom-made laser would be relatively high, and beam profiling by fibre end shaping, such as etching of the end of an optical fibre by chemical, electrochemical or photochemical methods, has not yet been reported at high powers (>1kW).

Thus, a desirable solution would be an optical system outside of the laser beam delivery system, offering multiple options from simple to complex energy distributions. The simplest way of doing this would be to use an aperture. Aperturing consists of placing a mask with a desired shape on the beam path. However, this solution leads to energy losses. The wasted energy can produce excessive heat and damage the surrounding optical components. Also if the aperture size is the same order of the beam wavelength, diffraction occurs, and the desired result is not achievable. Another approach to change the beam's energy distribution at the focal plane is to use an optic or a set of optics referred to as beam shaper [73]. In general, the appropriate beam shaper is inserted just before the focusing lens. In some cases the focusing lens can even be integrated into the beam shaper optic, providing a focused, shaped spot. The two types of beams shapers are field mappers and beam integrators.

Field mappers are optic or set of optics that redistribute the input beam at the targeted plan by refracting the incident beam. Commonly used field mappers are prism, π-shaper or axicon lenses. The latter is a specialised type of lens which has a conical surface and images a point source into a line along the optic axis or transforms a laser beam into a ring.

The other types of beam shaper are beam integrators; an array of mirrors or optics that break up the input beam which later assembles at the targeted plan. As an example, spatial light modulators (SLM) based on liquid crystal microdisplays have been used with a nanosecond pulsed laser for marking thin metal sheet with complex two-dimensional patterns [74]. SLMs

are commercially available products in the form of a programmable microarray that will change the laser phase that after reflection will form the desired pattern at the workpiece. Similar examples are diffractive optics that can be transmissive. The surface of a diffractive optics lens has local changes of the diffraction order size (i.e. same size order as the incoming wavelength) that split the incident laser beam and redirects the fragments at the focal point to form a specific pattern also through the principle of interference and phase control.

A similar idea to the array of mirrors to change the energy distribution of the laser beam is to drive mirrors at high angular deflections in longitudinal and transverse directions, enabling high-speed scanning of the laser beam at the work-piece [75]. Typically used for high-speed welding but capable of producing effectively a tailored energy profiles if high enough frequency is used, this commercially available device is known as a galvanometric scanner or just scanner. Nevertheless, the intensity of the beam is not modified, and this technique is merely producing a quasi-static energy distribution at the targeted plan.

Finally, another solution is to use multiple laser sources. Either by using different lasers as Katamaya did with a 16 kW disk laser coupled with another 10 kW disk laser to improve the penetration depth during welding [76] or using a beam splitter module to redistribute the laser power of a single laser source into two welding heads. Dual beam techniques are commonly referred as twin beams or tandem technique.

2.3.1 Advantages and limitations, the choice of diffractive optics

Table 2.3 summarises the different methods, and their limitations, for laser welding with tailored spatial energy distribution.

Conventional optics like field mappers have high efficiency and a wide range of useful wavelengths, but only a limited range of energy distributions are available. Refractive beam shapers for material processing with high power single mode and multimode lasers are available in the form of π-shaper, but they have limited possibilities for shaping the beam; explicitly: flat top, inverse gauss and super gauss are possible. Line or square shaped spots can be obtained with additional optics adding to the bulkiness, complexity and giving alignment challenges [77]. Prism and axicon lens show the same drawback when it comes to design flexibility. There are also limitations in the manufacturing of these optics, as the radius of curvature of the surface cannot be too small. Furthermore, the achievable spot sizes of refractive beam shapers are above the diffraction limit [78].

Beam integrators in the forms of adaptive or flexible mirrors also have limitations. Intracavity flexible mirrors are complicated to integrate and often results in a re-design of the laser system itself [79]. Adaptive mirrors mounted outside the laser system have been used to enhance the absorption of a CO_2 laser beam on a substrate by controlling the focus, beam waist and divergence [80]. Nevertheless, the change of energy distribution is very small and limited.

Beam integrators in the form of lenslets or mirror arrays are among the commercially available techniques. However, the periodic structure and the overlapping of beamlets

produce interference effects especially with highly coherent light [81]. Thus, these products present limitations with a highly coherent laser. They have been primarily developed for a laser with poor beam quality (M^2>10). Besides the tight manufacturing tolerances for the individual microlenses and possible misalignment in the array, the relatively high costs for mounting are the major drawbacks [81]. Commercial products such as SLMs can produce a wide range of spot pattern and energy distribution arrangement but this technology is not ready yet for keyhole laser welding of steel as the maximum power that can be withstood is 100 W [82].

While galvanometric scanners have been proven as a useful tool for experimenting with tailored energy, the technology requires high capital investment and skilled operator to program and carry out welding. The processing head is also limited by the power it can withstand.

Multiple beam technique with a beam splitter module would be a useful tool for evaluating different tailored energy distributions, but the implementation in industry would not be practical and would require additional investment and a bulky head set-up.

Diffractive optics are more interesting in this regards as they are more readily integrated without an elaborate set-up. Typically made of fused silica, a material that has a high laser radiation resistance, the diffractive structure can be realised within a thin layer (micrometres or less) hence resulting in a thin and lightweight plate even with very large apertures. Consequently, very compact systems can be designed. It is also possible not to overlay the effect of focusing in the diffractive optic. This makes it possible to do experiments with different focusing optics, thus reducing the need for different costly diffractive optics. Theoretically, any pattern of energy distribution can be generated. Nevertheless, the use of diffractive optics in laser welding has been limited due to their complexity to design. Research and experiments are needed to find the energy requirement, and sophisticated modelling computations are necessary to design the diffractive optics. In addition, the making requires expert manufacturer. A primary barrier which is preventing the uptake of diffractive optics is that there is no straightforward and cost-effective way of determining the necessary tailored energy distribution for the end-user application. Some research [83] [84] has been carried out and the costs and knowledge to determine the energy distribution represent a barrier for the small and medium-sized companies (SMEs).

Table 2.3: Current methods, and their limitations, for laser welding with a tailored energy distribution

Categories	Process	Description	Limitations in producing Tailored Energy Distributions	Reference
Beam integrators	Spatial light modulator	Liquid crystal microdisplays	• Modulate the phase only	[81][82]
	Diffractive optics	Transmissive or reflective optic with discrete phase changing steps at their surface inserted in the processing head	• Efficiency can be limited depending on the type of diffractive optics • Wavelength-dependent • Relatively high cost, depending on the type diffractive optics	[85] [86]
Field mappers	Π-shaper	Assembly of refractive optics	• Bulky and very simplistic energy distributions available • Relatively high cost, as dedicated process head is required	[77]
	Prism and axicon lens	Refractive optic	• Limited number of very simplistic energy distributions available • Change in the energy distribution require precise changes in the optic alignment • Beam delivery system is bulky containing multiple optical elements	[87]
Multiple laser heads	Conventional beam splitting	A module taking the fibre laser and redirecting two fibres	• Limited power split possible (usually only 50/50) • Relatively high cost	
Scanner	Galvanometer driven laser beam scanner	High-speed scanning of the laser beam at the work-piece by driving mirrors at high angular deflections	• Very high capital cost; typically €80-150k • Highly skilled engineer required to program the scanner for new geometries • Calibration required at regular intervals • Beam delivery system is bulky and significantly heavier than standard heads, resulting in increased manipulation requirements • Expensive spare parts (typically ~€1-3k for cover slides) • Multi-spot sequential welding approach results in tombstoning defects in electronic assemblies	[75]
	Adaptive or flexible mirrors	Mirror with a variable curvature	• Modify only the focus and the beam divergence • Permanent or semi-permanent arrangement; changes in the energy distribution require precise changes in the optic alignment.	[79] [80]

2.3.2 Diffractive optics

The term diffractive optics refers to optical elements that operate principally on the mechanism of diffraction and that take the place of conventional refractive elements. Diffractive optics can be used to generate complex two and three-dimensional energy distributions without the need for any moving components [86]. The term diffractive optical element (DOE) which is one type of diffractive optics among others is nonetheless too often used to cover other types, if not all diffractive optics. To be rigorous in the terminology and avoid confusion, the diffractive optics are classified by either their structural aspects or their optical functionalities. This classification is also chronological and is presented in Figure 2.13 [85].

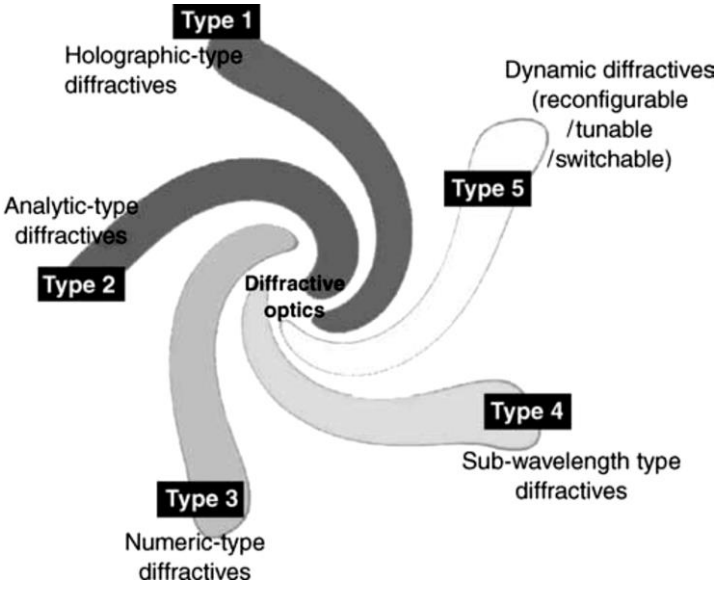

Figure 2.13: Types of diffractive optics

In this research, as discussed in Section 1, the focus was on fibre-delivered high power laser sources. For this reason, only Type 2 and 3 diffractive optics are reviewed further. Sub-wavelength diffractive elements (Type 4), such as nano-optical or photonic crystals, are operating at low power and their applications are not related to beam shaping. Dynamic diffractive (Type 5) refers to all the technologies used to implement reconfigurable, tuneable or switchable optical functionalities such as SLM.

2.3.2.1 Holographic Optical Elements (HOEs)

Holographic optical elements (HOEs) refer to the traditional optical holographic recording of volume-phase holograms (in phase modulation materials) or surface-relief holograms (in photoresist materials). This is an optic generated by the interference of two wavefronts to produce a component that will be used to act as an optical component. The recording of a hologram for high power applications is theoretically possible using conventional optical holographic techniques, but in the visible region only. Therefore, as there is no suitable material for recording in the infrared region, where Yb:fibre lasers are operating, HOEs are not a suitable method for tailoring the spatial energy distributions of lasers relevant to this

research. It could be argued that the hologram can be recorded in the visible region and replayed in infrared, but this would lead to geometrical aberrations [88].

2.3.2.2 Diffractive Optical Elements (DOEs)

DOEs refer mostly to elements that can be designed or optimised using analytic methods such as ray tracing (as is done in most optical CAD tools), or by solving an analytic equation (as is done for Fresnel lenses or gratings) [85]. These are the most common diffractive optics. To generate a simple pattern (several spots corresponding to diffraction order), the principle is based on diffraction grating: the period Λ of the repeated structure determines the angular separation between the orders. A small period creates large angular separation, while a large period results in closely spaced output beams. For a better understanding, Figure 2.14 below shows a laser light passing through a diffraction grating. Full angle θ_f and separation angle θ_s are depicted. The separation between the spot is denoted by d (measured from centre to centre) and the length of the spot array by D while *m* is the order of diffraction.

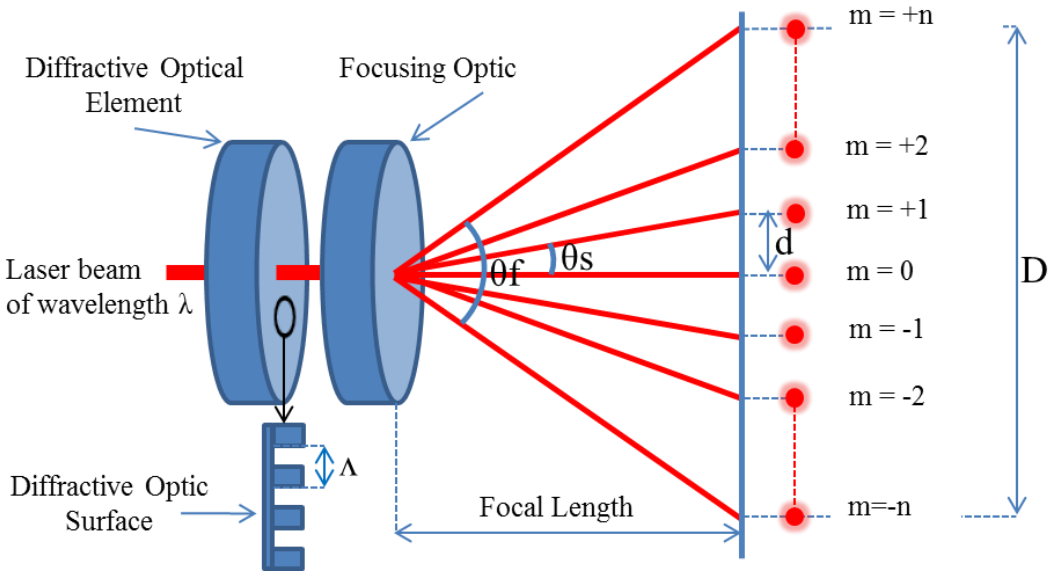

Figure 2.14: Diffraction grating parameters of interest

The angle $\theta_s m$ of each output beam of order *m* relative to the zero-order beam is given by the grating Equation 2.8:

$$\theta_s m = \sin^{-1}\left(\frac{m\lambda}{\Lambda}\right) \qquad \text{Equation 2.8}$$

The relation between d and θ_s is given by a simple trigonometric formula taking the focal length into account:

$$d = Focal\ Length \times tan\ \theta_s \qquad \text{Equation 2.9}$$

Although the grating equation determines *where* the light is directed, it does not determine the relative power directed into each of the diffracted orders. This power distribution is dictated by the shape and nature of the surface profile within a single grating period.

The angular separation between the diffracted spots directly relates to the periodic structure ʌ of the grating as seen in equation 2.8. The relative power directed into a particular order (diffractive efficiency) is determined by other factors such as the number of levels (here it is a binary grating), the phase depth and the duty cycle. These factors are described and depicted in Figure 2.15.

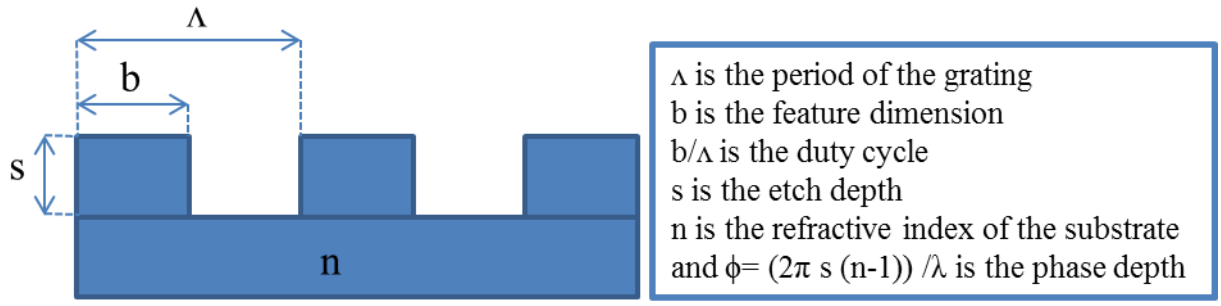

Figure 2.15: Important factor of a binary level DOE

The diffraction efficiency of the different orders can be calculated for various values of etch depth, duty cycle and refractive index. Diffractive optics for 1 µm wavelength laser sources are typically made of fused silica (n = 1.45), and the duty cycle is usually fixed at ½ (fifty-fifty) for better efficiency. The relative intensity in different orders is then calculated depending on the etch depth. The exact formula comes from the calculation of the diffractive pattern in the far field (Fraunhofer approximation) in the scalar theory of diffraction. Mathematically a planar wavefront passing through the grating can be described as a function (the convolution of the comb function and a rectangle function multiplied by a phase term), and the diffracted order in the far field is (mathematically) the Fourier transform of this function [85], [86].

2.3.2.3 Computer-Generated Holograms (CGHs)

CGHs refer mostly to elements that cannot be designed or optimised by analytic methods, and that require stochastic iterative optimisation procedures and algorithms. These elements can implement more complex optical functions than analytic-type diffractive but have limitations (the amount of CPU power required, the need to rasterise the element in the design process). They are increasingly used in industry. These diffractive optics types are of high interest as they offer the ultimate design flexibility and great diffraction efficiencies are available.

A type of CGH is known as kinoform. This diffractive optic whose phase-controlling surfaces are smoothly varying (phase changes in range 0-2π). The kinoforms are highly efficient devices (compared to other types of holograms), with efficiencies over 90%. The kinoform can force the extraneous diffracted orders into a single diffracted order, with the result that the maximum amount of incident energy is converted into the required output profile. The kinoform consists of an array of pixels each assigned a different phase level. Each pixel can be thought of as a point source of a spherical wave-front, emitting with controlled phase retardation. These wave-fronts combine in the focal plane to generate the required image. To design the optic knowing the intensity light profile from the laser source, the first challenge is to calculate the multi-level phase pattern of the diffractive optic which will generate the

desired energy distribution. Computer computations are necessary, and several algorithms have been developed. The Iterative Fourier Transform Algorithm (IFTA) is one of the common methods for the calculation of such elements. The Grechberg-Saxton IFTA is the most widely used for the kinoform [89]. Knowing the desired pattern intensity, the algorithm will find the phase pattern that will generate it by first producing a random phase pattern and then modifying it through a closed loop till it gets the desired one. Fast Fourier transform (FFT) and FFT^{-1} are used to link the phase pattern and the distributed energy in the far field plan. The flow chart of the Gerchberg-Saxton algorithm is shown in Figure 2.16.

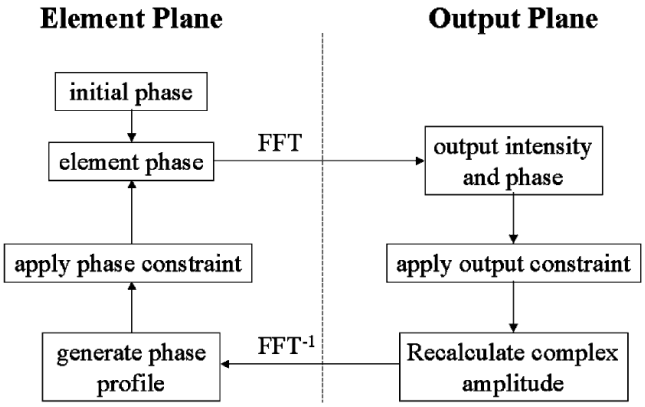

Figure 2.16: A schematic representation of the Gerchberg-Saxton algorithm

The second challenge is to transform the multi-level phase pattern into a variable depth level surface relief. The maximum depth (d_{max}) required should impose a 2π phase shift on the illuminating radiation. If a transmissive diffractive setup is used, the required depth of structures in a DOE or CGH can be calculated from equation 2.10 [86]:

$$d_{max} = \frac{(2^N - 1)\,\lambda}{2^N\,(n_{Mat} - n_{air})} \qquad \text{Equation 2.10}$$

Where 2^N is the number of discrete steps having been selected, and N is the number of etching steps (number of masks required). The refractive index of the material used for the DOE and the refractive index of the medium surrounding the optic (air, 1.0003 at room temperature) are denoted n_{mat} and n_{air} respectively. If the diffractive optic is manufactured in fused silica (n_{mat} = 1.45), the required maximum depth for 2^N = 256 steps becomes 2,43 µm for a fibre laser with λ = 1,075 µm. If a reflective solution is used instead, the required depth will be half the wavelength of the beam. The halving of the wavelength is due to light being delayed both on the way in and out of the reflective structure.

2.2.3 Diffractive optics used in laser processing

Diffractive optics are widely used in low power applications, generally in the visible region, for applications such as optical interconnects, multiple focusing and image processing. However, their effective use in high-power laser applications has been mainly limited to fibre coupling**,** beam splitting, beam sampling and Gaussian to flat top conversion**.**

DOE's have been used successfully in applications such as hardening [90], multiple point soldering [83] (see Figure 2.17), simultaneous cutting and welding of polymers and conduction welding [91].

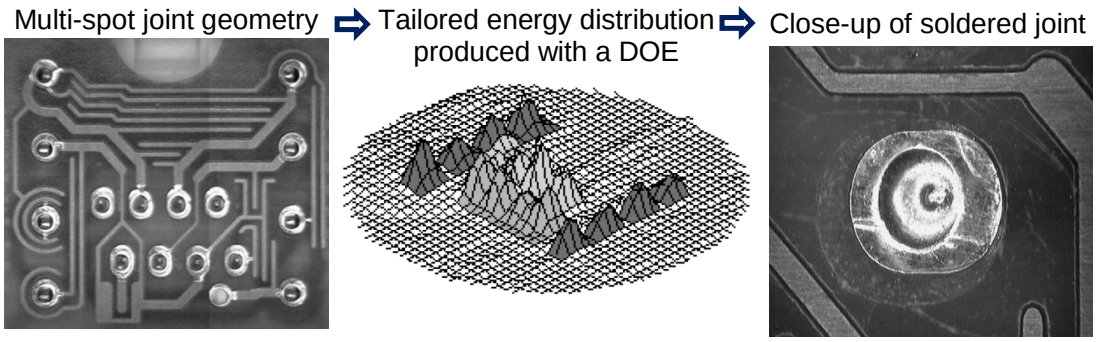

Figure 2.17: Multi-spot soldering with DOE and CO_2 laser [83]

Regarding laser welding, researchers have shown that the size of the weld pool can be controlled [92], that the weld toe can be smoothed and that a tailored energy distribution can reduce the grain size [93]. Having said that, little information is available related to welds produced using DOE, and the weld pool activities during welding.

For CO_2 lasers, a feasibility study using a DOE was reported in 1996 [94] followed by a demonstrative application in 1999 [95] where a kinoform DOE was used for multipoint soldering. In 2009 a kinoform DOE was used to control the grain size structure during a direct metal deposition process with a CO_2 laser at a maximum power of 1.2kW [93], and in 2010 a kinoform (named holographic optic element in the paper) was used to control the melt pool depth, and consequently microstructure of a nickel-based laser deposit during conduction welding of stainless steel with a CO_2 laser [96]. The resulting microstructures of nickel-based deposits when using a Gaussian energy distribution (top) and an off-set rugby post tailored energy distribution (bottom) is shown in Figure 2.18.

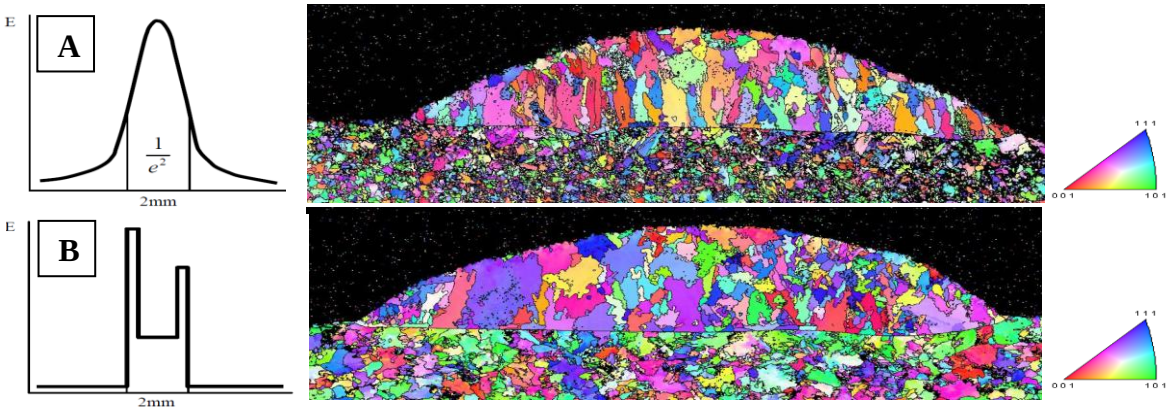

Figure 2.18: (A) Gaussian distribution and (B) rugby post distribution obtained with a DOE with the resulting nickel-based deposit structure after welding

For Nd:YAG lasers, J.B Hammond et al. used a diffractive optic in the form of a diffractive grating in 1999 to investigate the effect on welding dissimilar materials [97]. The materials; grade 1060 aluminium, grade 316 stainless steel and Inconel 718 were chosen because of

their significant differences in material properties and their use in aerospace applications. Because of the different melting point, absorptivity and thermal conductivity of these materials, the idea was to power split the Nd:YAG incident beam in two with an asymmetric repartition of the power. Ratios of 10:1, 2.5:1 and 1:1 were evaluated. Though the authors claimed to have demonstrated better results with the asymmetric split beam results, little explanation was given, and no mechanical testing was carried out.

Finally, studies with Yb:fibre lasers are even scarcer. Beam shaping was used with a 10kW IPG Yb:fibre laser during keyhole welding to weld and smoothen the weld in one pass [98]. The beam shaper was a custom-made zinc sulfide (ZnS) optic with three tilted optical surfaces having sharp transitions between them and the light was focused with a copper parabolic mirror. In this experiment, the desired tailored energy distribution was known (a main beam of 0.5 mm with 67% of the total power followed by two transverse beams of 6 mm sharing the remaining 33% of the total power 10 mm behind) and the optical system was designed with ray tracing software (Zemax). The final optic is a real piece of clever craftsmanship, but this approach is not viable when the energy distribution is not known or when more complex energy distribution is desired. Additionally, In 2014, keyhole welding with a single mode IPG Yb:fibre laser on thin sheet of mild steel (grade DC01) and stainless steel (grade 304) was performed with a 3 and 7 spots DOE to extend the size of the melt pool [92]. Processing power was kept relatively low (< 1.5 kW), but all the laser spots were forming a keyhole and were transverse to the welding direction thus extending the dimension of the resulting weld to fit the requirements of a given welding task.

In conclusion, very few studies reporting the use of diffractive optics to tailor the spatial energy distribution for laser welding can be found in the literature despite the wide range of potential applications. The use of diffractive optics with Yb:fibre laser has been proven and the efficiency reported showed that the optic could withstand high power in the kW order. Using a diffractive optic in the form of a DOE beam splitter or kinoform for keyhole welding of DSS should be possible.

2.4 Summary

Grade 2205 DSS is the most popular grade of DSS due to its good compromise between price and material properties. The dual phase balance of austenite and ferrite that compose it are of prime importance to maintain the material properties. This is particularly the case for its superior corrosion performance, making it a prominent candidate material for applications in harsh environments or where long-term material integrity is required. In the UK, ILW containers are being manufactured from Grade 2205 DSS using conventional arc-based techniques. When undergoing fusion welding, the resulting phase balance of the weld will depend upon the thermal cycle of the weld. While existing arc-based processes maintain a suitable phase balance; the high heat-input leads to distortion and costly rework.

Laser welding is an industrially accepted technology across a wide range of sectors; as a result of its ability to produce high-quality welds at high throughput and with low distortion.

Of the available laser types for welding, high beam quality fibre-delivered lasers, such as Yb:fibre lasers are an attractive option for manufacturing ILW containers.

Nevertheless, studies on laser welding of grade 2205 DSS have highlighted that the rapid thermal cycles experienced by the weld zone result in excess ferrite in the weld metal, affecting its corrosion performance. A potential solution to maintain the weld phase balance while using Yb:fibre laser is to use an over nickel alloyed filler wire, thereby enhancing austenite formation. This solution is not desirable because of the cost, complexity and higher failure rate involved in wire-fed laser processes. An autogenous laser welding process would be cheaper and less complex to implement.

Beam shaping techniques have been reviewed, and it has been identified that diffractive optics have enormous potential in industrial laser material processing. Demonstrating the use of diffractive optics (DOE or CGH) for materials requiring in-process pre/post-weld heat treatment will be a step forward for many applications. Indeed, diffractive optics can increase the flexibility and simplify the application of laser welding and potentially help SMEs that require a high degree of flexibility to serve a broad range of markets. To allow the user to change diffractive optics for various jobs, without the need of laser background and technical skills, research and development for the specific optic design are required. This is particularly costly, and experiments with a split beam arrangement may, therefore, be more flexible for developing an application.

2.5 Aims and objectives

The research motivation was to determine if it is possible to remove the requirement for filler materials during the laser welding process of grade 2205 DSS to decrease the cost and reduce the complexity of the process.

The aims are summarised as follows:

- Establish the feasibility of autogenous single beam welding of grade 2205 DSS with thicknesses of 3 and 6 mm that are typically used in the nuclear sector. Determine the key process parameters on the resultant weld quality and the dynamic behaviour of the welding process.
- Determine whether a dual laser beam can be used for reducing the ferrite excess at the weld location.
- Select and characterise a diffractive optical element (DOE) that emulates an optimised dual laser beam.
- Confirm the possibility of using DOE during keyhole laser welding.
- Determine whether the DOE based approach can reduce the ferrite excess at the weld location.

Chapter 3: Research methodology

3.1 Introduction

This chapter details the overall research approach, the experimental set-ups conducted on laser-welded duplex stainless steel, the characterisation techniques used, and the data collected for subsequent analysis. Three different experimental sets are detailed; specifically: single beam welding, dual beam welding, and welding with a diffractive optical element (DOE). For each experiment, temperature measurements were made during welding, the ferrite content in the weld was measured, electron backscatter diffraction (EBSD) imaging of the weld was performed, and the chemical composition of the different phases present in the weld were analysed. The aims of this chapter are to:

- Outline the approach taken to answer the research question.
- Detail the material and equipment used, along with the characterisation techniques employed to understand the limitations and the precision of the different measurements.
- Present the set-up and procedures used to guarantee the experiments repeatability of future research.
- Justify the standards, techniques and characterisation used in this study.

3.2 Approach

The research approach was driven by an intensive experimental programme. Key process parameters were identified using statistical techniques and assessed through mechanical, metallurgical and corrosion testing. The analysis of the results has focused on the quantitative assessment of the weld's phase balance as well as a qualitative assessment of the geometric weld profile and weld penetration.

The first stage of this research consisted of benchmarking the process of single beam autogenous Yb:fibre laser welding of grade 2205 DSS of different thicknesses. This was to identify the baseline process parameters for future comparison with different energy distributions. The second stage was the development of a tailored energy distribution using a dual beam approach with a beam splitter and two welding heads. Finally, an evaluation of welds produced using a DOE partially matching the dual beam energy distribution completed the experiment performed.

3.3 Characterisation of the material

3.3.1 Grade 2205 duplex stainless steel composition

In all experiments, grade 2205 DSS was used. It is covered by the standards presented in Table 3.1.

Table 3.1: Steel denomination

Designation			Standards		
Name in the thesis	**EN (Euro Norm) name**	**EN number**	**UNS**	**BS**	**ISO**
Grade 2205 DSS	X2CrNiMoN22-5-3	1.4462	S32205/S31803 wrought product	BS EN 10088-2	4462-318-03-I

UNS, or Unified System Numbering, is the accepted alloy designation system in North America for wrought and cast alloy products. For grade 2205 DSS, S32205 is the same as S31803 certification with two additional requirements:

- Nitrogen in the 0.14-0.20% range; and
- The absence of detrimental intermetallic phases when tested with ASTM A 923 standard test method.

BS EN 10088-2 (originally published in 1995 and revised in 2014) [99] is the material standard for stainless steel sheet, plate and strip for general purposes. The chemical composition of grade 2205 DSS given in that standard is shown in Table 3.2:

Table 3.2: BS EN 10088-2 standard chemical composition of grade 2205 DSS [99]

Designation		**Chemical composition % by mass max unless stated**									
Steel name	Steel #	**C**	**Si**	**Mn**	**P**	**S**	**N**	**Cr**	**Mo**	**Ni**	Others
X2CrNiMoN 22-5-3	1.4462 2205	0.030	≤1.00	≤2.00	0.035	0.015	0.10/ 0.22	21.0/ 23.0	2.50/ 3.50	4.5/6.5	-

The actual chemical composition of 3 and 6 mm thick DSS plate used in this report was analysed through optical emission spectroscopy (OES) during this study. The results are given in tables 3.3 and 3.4 for 3 and 6 mm plate, respectively, in % by mass:

Table 3.3: Actual composition of grade 2205 DSS (3mm thickness)

C	**Si**	**Mn**	**P**	**S**	**Cr**	**Mo**	**Ni**	**Al**	**As**	**Co**
0.022	0.35	1.42	0.024	<0.002	22.2	3.08	5.7	0.02	<0.01	0.13
Cu	**Nb**	**Sn**	**Ti**	**V**	**W**	**N**				
0.24	<0.01	<0.005	<0.005	0.07	<0.05	0.18				

Table 3.4: Actual composition of grade 2205 DSS (6mm thickness)

C	**Si**	**Mn**	**P**	**S**	**Cr**	**Mo**	**Ni**	**Al**	**As**	**Co**
0.019	0.27	1.83	0.019	<0.003	22.7	2.90	5.55	0.02	<0.01	0.04
Cu	**Nb**	**Sn**	**Ti**	**V**	**W**	**N**				
0.15	<0.01	<0.01	<0.01	0.05	<0.04	0.16				

As presented in these tables, the actual composition of the test materials met the requirements of BS EN 10088-2 [99]. The dimensions of the plates used were 3 × 300 × 135 mm, and 6 × 200 × 150 mm.

Immediately prior to laser welding, the material surfaces were cleaned using a Scotch-Brite™ pad and then an acetone wipe to avoid contamination in the weld or uneven absorption of the laser beam. For square-edge butt welding, a vertical mill was used to machine the plate.

3.3.2 Laser equipment and beam delivery

3.3.2.1 Laser source and delivery fibre

An IPG YLS 5000 Yb:fibre laser source was used for all the welding trials. This laser emits electromagnetic radiation at 1070 ± 10 nm, which was delivered to the processing head through a flexible optical fibre with a core diameter of 150 µm (giving a BPP of 5.5 – 6 mm.mrad).

3.3.2.2 Processing head and optics

The flexible optical fibre was attached to the processing head containing the collimating and focusing optics. When used, the diffractive optic was fitted in the processing head just before the focusing lens, as shown schematically in Figure 3.1. For the dual beam experiments, two separate but nominally identical processing heads were used. In all cases, the focusing lens was protected from potential damage caused by fumes and spatter using an air-knife and a semi-consumable infrared transparent cover slide between the lower surface of the focusing lens and the work-piece.

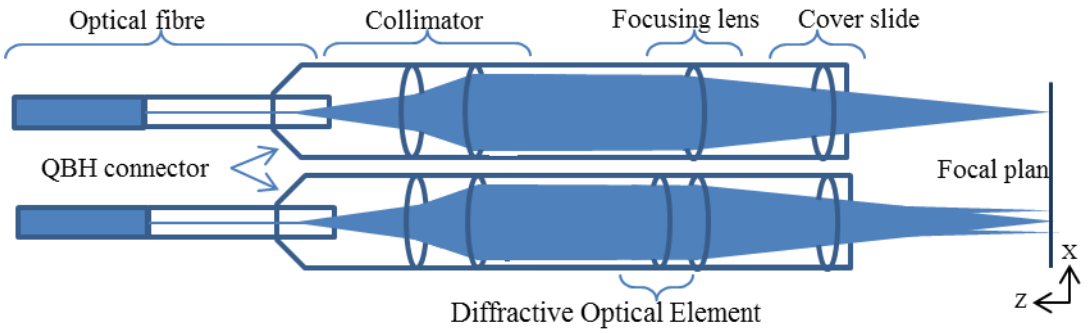

Figure 3.1: Schematic of processing head unit

Table 3.5 summarises the three optical set-ups during the experiment with the IPG YLS 5000 laser.

Table 3.5: Welding head characteristic

Parameters	Optical setting		
Fibre core diameter, µm	150		
Collimator focal length, mm	100.00	120.00	100.00
Raw beam diameter, mm	16.00	19.20	16.00
focusing lens focal length, mm	200.00	300.00	400.00
Nominal beam waist, mm	0.300	0.375	0.600
Focusing cone half angle, degree	2.29	1.83	1.15
Rayleigh length, mm	3.75	5.86	15.01
Spot power density, W/mm^2	71×10^3	45×10^3	18×10^3

3.3.2.3 Beam splitter

In all of the dual beams experiments, a beam splitter module (Optoskand 2-9420x01, FFS 2way QB-QB), Figure 3.2, was used to split the energy from one fibre into two fibres, each carrying half of the total power requested. The equipment did not allow a variable power split between the two fibres, nor did it allow the switching on or off of one of the beams. The maximum handling power of the beam splitter was 5 kW.

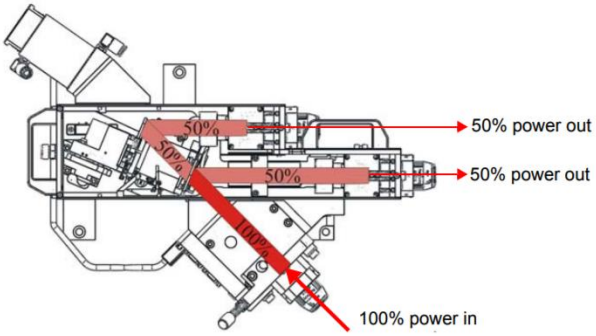

Figure 3.2: Beam splitter module schematic

3.3.3 Diffractive optics

Two different diffractive optics, more precisely diffractive optical elements (DOEs) type, were used in the experimental work.

3.3.3.1 3-spots diffractive optic element

A 3-spots transmissive DOE grating type (8 level) made of fused silica and designed for a wavelength of 1070 nm matching the laser used was sourced from Holo/Or Ltd., a diffractive optic manufacturer. The theoretically expected pattern in term of power split between the three spots is shown in Figure 3.3. The grating period of the DOE was 25 µm which leads to a separation angle of 2.44° at the laser operating wavelength. With focusing optics of 200 mm focal length (FL), the distance (*d*) between the diffracted orders was 8.52 mm. With the spots aligned to the welding direction, the first spot (+1 order) acted as pre-heating, the middle one (zero order) as the welding beam and the last spot as post-heating (-1 order).

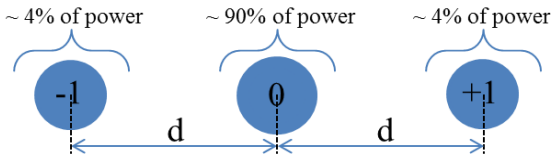

Figure 3.3: Pattern of 3-spots DOE

Both sides of the optic had an anti-reflective coating. Higher orders of diffraction redirecting less than 2% of the total power are not shown in Figure 3.3. The power redistributed in the different orders is dependent on the DOE's refractive index (n), the etch depth and the duty cycle (ratio between the width of the etched structure and the grating period). In this case, the DOE made of fused silica (n = 1.45) had a duty cycle of ½ (fifty-fifty) and an etching depth of 0.241 µm giving a diffraction efficiency of 90% for the zero order and 4% for ± 1 orders. Figure 4 below shows the predicted characteristics of the chosen DOE:

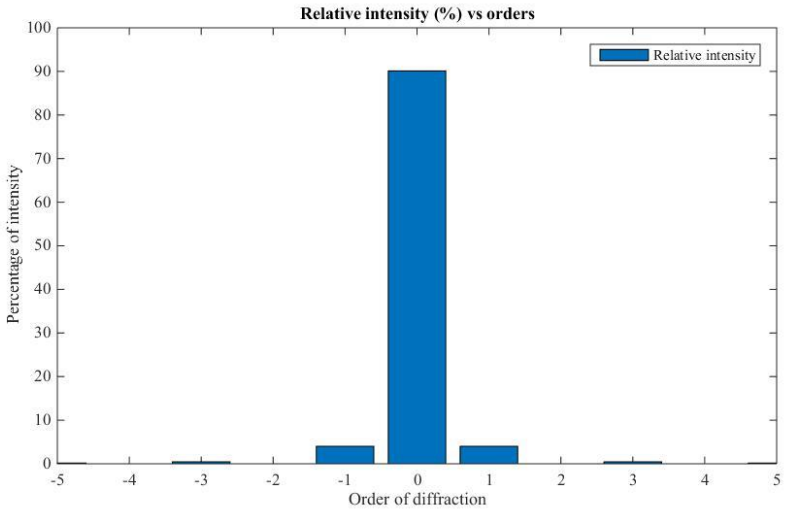

Figure 3.4: Intensity distribution of diffracted order as designed for the 3-spots DOE

3.3.3.2 4-spots diffractive optic element

A second DOE, producing four spots, was also used. The transmissive DOE was also a 8 level gratings made of fused silica, designed for a wavelength of 1070 nm, and sourced from Holo/Or Ltd. The theoretically expected pattern in term of power split is shown in Figure 3.5:

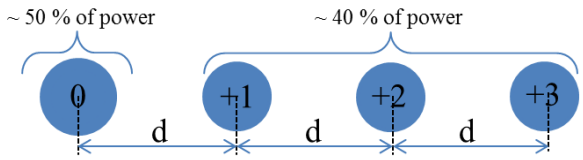

Figure 3.5: Expected pattern of the 4-spots DOE

Several other spots preceding and succeeding the first and last spot are also present and correspond to higher orders of diffraction. Around 10% of the power is distributed between these unwanted spots with a maximum of 3.70% of the total power redistributed in each beam. The DOE manufacturer Holo/Or Ltd. designed the normalised intensity distributed in each order, as shown in Figure 3.6.

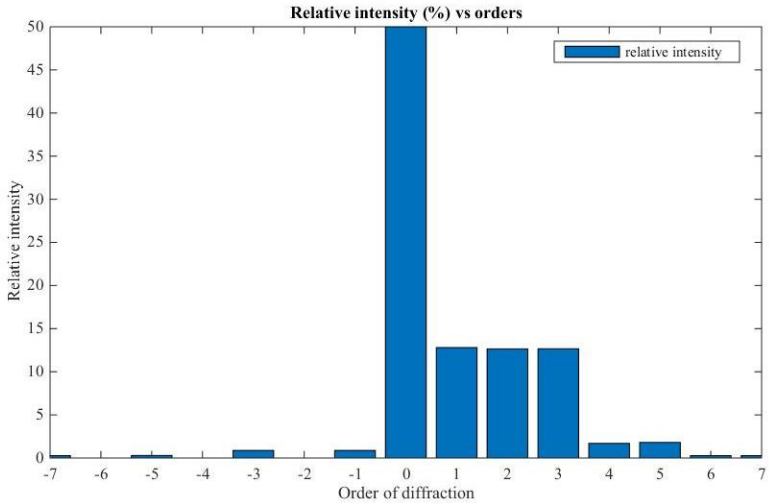

Figure 3.6: Intensity distribution of diffracted order as designed for the 4-spots DOE

The diffractive optic had an anti-reflective coating on both sides. The grating period was 53.500 µm leading to a diffraction angle of 1.146 ° at an operating wavelength of 1070 nm.

3.4 Laser welding process and procedure

Many important aspects have to be taken into account when developing a laser welding process. First, there are the choices of the optical setting, welding head and the motion control system to be used. These technical choices will depend on the material to weld (dimension, shape, and grade), the type of desired weld, and the position it will be welded. In addition, the laser welding has exacting tolerance requirements on the part preparation (surfaces, edges and cleanliness), part placement (sub-mm location of joint) and fit-up (sub-mm requirements on gap and step), which also influences the choices of optical components to use. Safety for the operator is an essential aspect as laser beam/laser reflexion, and spatters can result in severe skin burns and eye damage/blindness if appropriate security measures are not in place. The equipment also requires safety precautions such as cooling, emergency stop or video monitoring. The mindmap shown in Figure 3.7 shows these aspects in view of the current study.

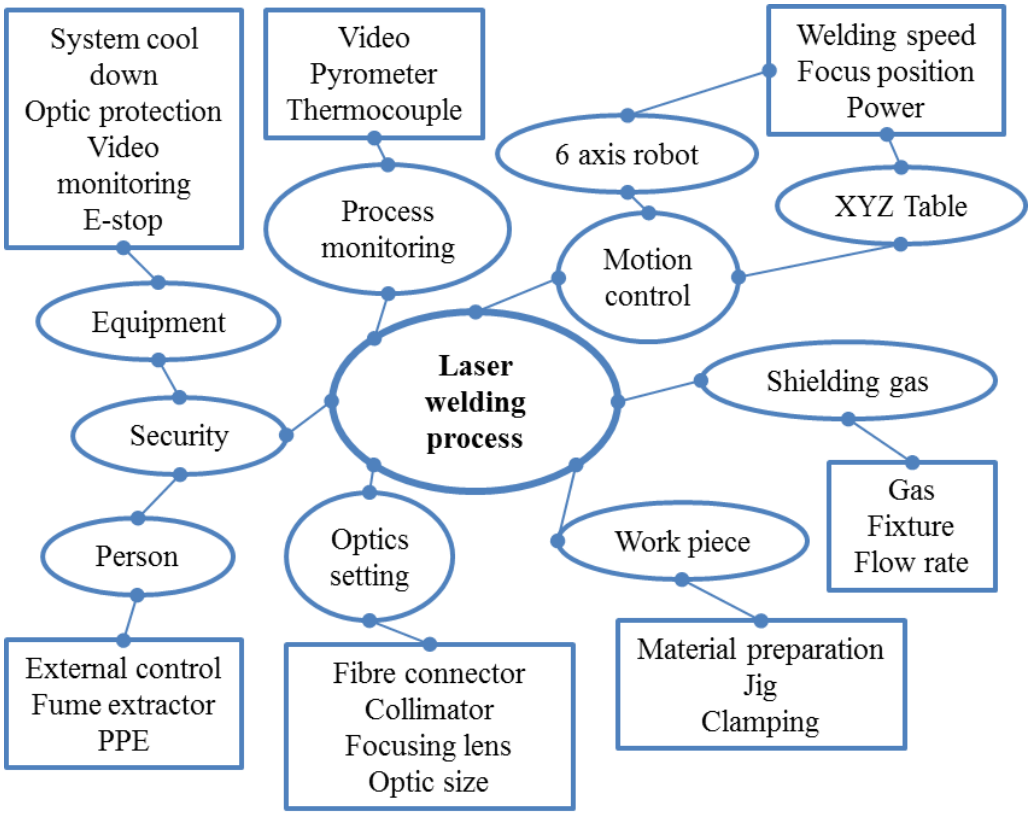

Figure 3.7: Mindmap for laser welding process

This section discusses the verification of spot size and power before welding, the welding process in term of set up, the measurements taken during welding, and the techniques for the weld characterisation. Sources of systematic and random error are also discussed.

3.4.1 Beam waist and focus position

Characterisation of the laser beam in term of its beam waist, BPP and Rayleigh length were measured according to the guidance and requirement of ISO 11462 [53].

To identify with accuracy where the focal point (beam waist) is located, the caustic was measured with the Prometec UF-100 beam profiler by sampling the beam along the z-axis. Each measurement correlated to a welding head position along the z-axis, allowing the focal point (i.e. position of minimum beam waist) to be easily identified. Where the beam waist was made coincident with the top surface of the workpiece, this position was referred to as the zero focus position. Otherwise, the distance between the focusing optic and a plate painted in black was set with a ruler to be at zero focus and marked by a 1-millisecond release of the laser at 500 W. Several other markings were made, each corresponding to an increased or decreased height of the welding head position by 1 mm. The position of the welding head corresponding to the smallest beam marking was retained as the zero focus position, and the focus position uncertainty was therefore estimated at ± 1 mm. Figure 3.8 shows an example of a marked plate with a sketch of different focus positions corresponding to the marking.

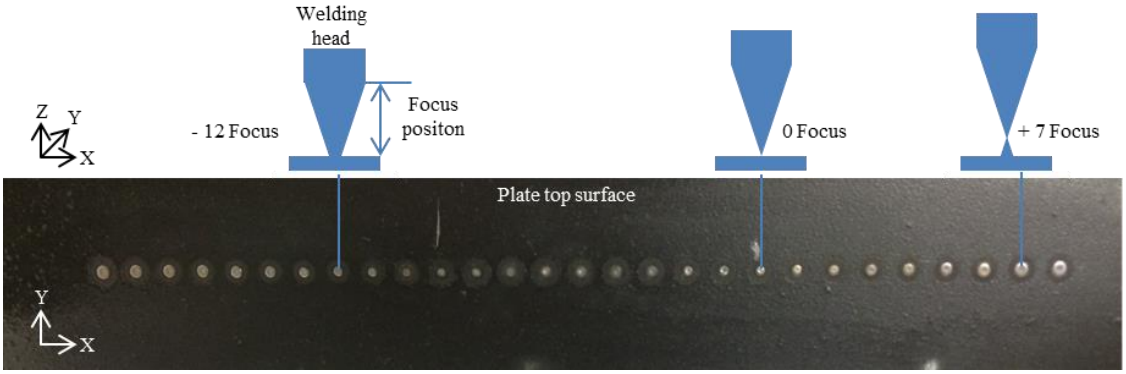

Figure 3.8: Painted plate subject to laser marking corresponding to different focus position

3.4.2 Power measurement

The laser power is requested through the LaserNet software controlling the laser. The power display by the software is obtained by a feedback of measured internal back reflection due to coupling losses in the fibre.

The power display by the laser software was then compared to the power measured at the workpiece (i.e. after any delivery optics). An Ophir power meter, model 10K-W-BB-45, was used. The correlation between the power measured at the workpiece and the power display by the laser system was found to be 99.4%, confirming the reliability of the laser system power display. It was nevertheless noted that for requested power below 2 kW the actual power delivered to the workpiece was slightly lower. Power requested below 10% (500 W) was not stable. Figure 3.9 shows the percentage difference as a function of the requested power.

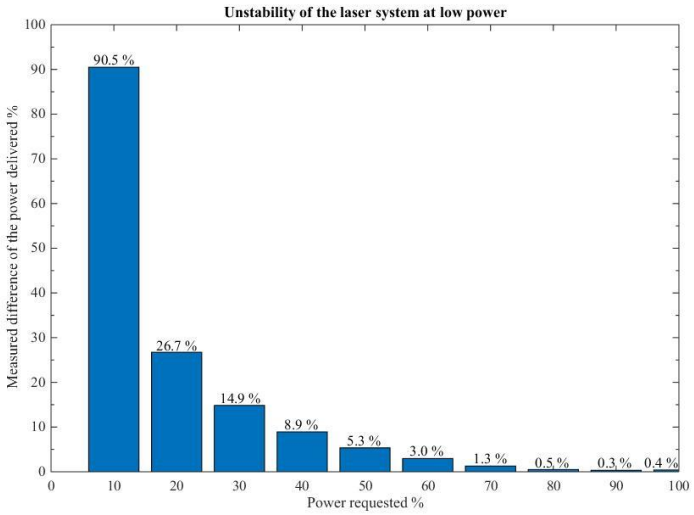

Figure 3.9: Comparison of the power requested, and that delivered to the test piece

3.4.3 Single beam set-up

Figure 3.10 shows a schematic overview of the set-up, as well as the actual welding head used for the experiments.

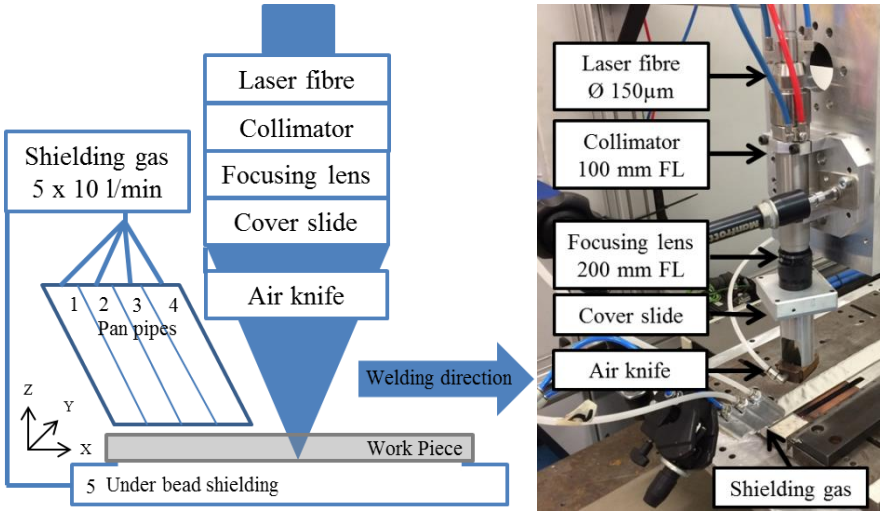

Figure 3.10: Single beam set up sketch and the actual lab set up

The variable parameters used in the single beam experiments were:

- Set of collimator and focusing lenses;
- Focus position [-8 to +4 mm];
- Welding speed [1 to 5 m/s];
- Power [1 to 4.5 kW]; and
- Shielding gas [Pure argon or pure nitrogen].

3.4.4 Dual beam set-up

Figure 3.11 shows a schematic overview of the set-up, as well as the actual welding head used for the experiments. Figure 3.12 shows the resulting two spots at the workpiece and the parameters investigated.

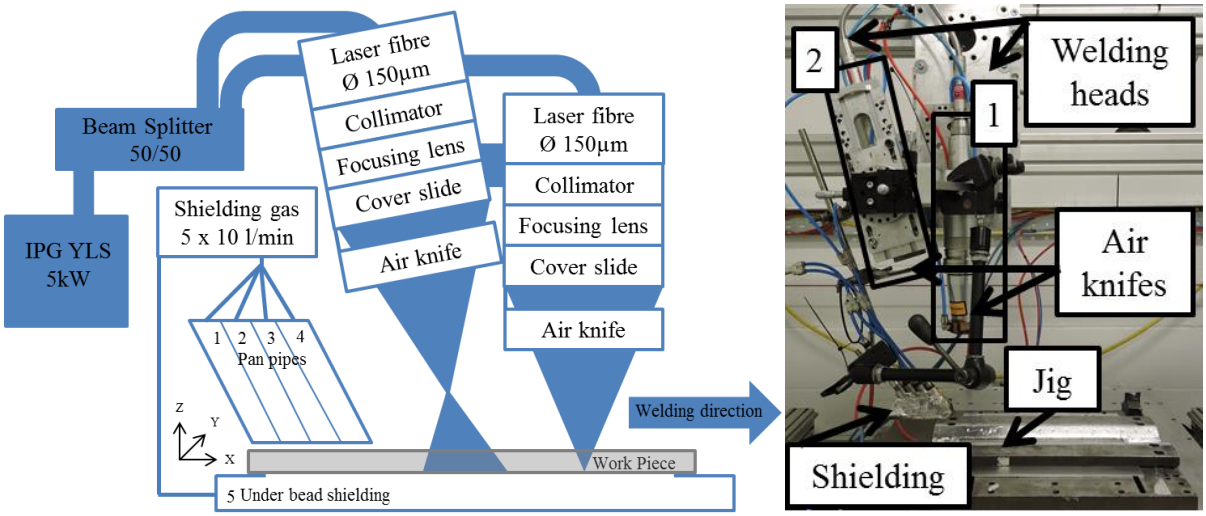

Figure 3.11: Dual beam set up sketch and the actual lab set up

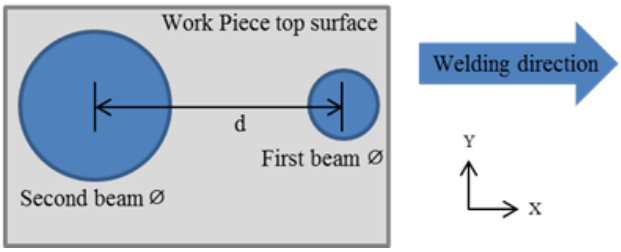

Figure 3.12: Parameters investigated

The variable parameters used in the dual beam experiments were:

- Focus position of the second welding head (directly related to second beam spot diameter) [0 to +250 mm]; and
- Separation between the two beams [0 to 22 mm].

The focus position uncertainty of the defocused beam was assumed at ± 1 mm and therefore the uncertainty on the second beam size diameter is estimated at ± 1 mm.

The distance between the spots was measured using a guided laser diode going through the heads. Actual measurements were also made on a marked piece of metal which the laser beam was released onto. The uncertainty for the distance separation is estimated at ± 1 mm.

3.4.5 DOE set-up

Figure 3.13 shows the set up using a DOE optic.

The parameters investigated were:

- Focus position [-4 to 0 mm];
- Welding speed [1 to 2 m/s]; and
- Power [2 to 5 kW].

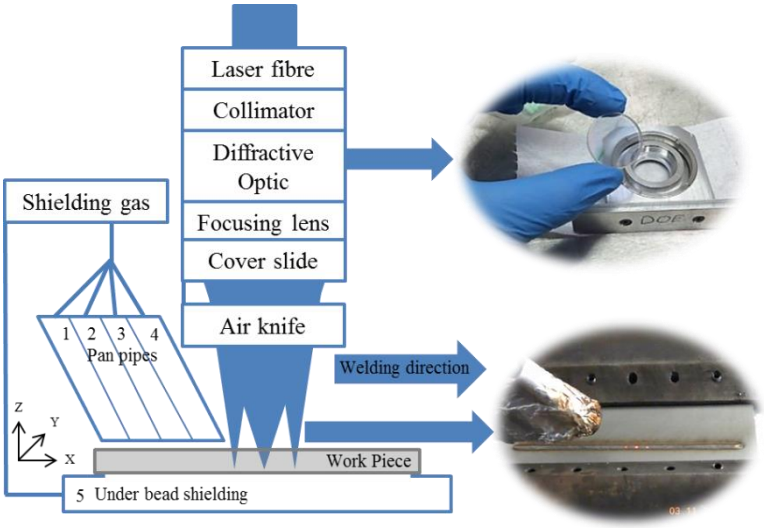

Figure 3.13: DOE set up sketch

A special welding head was designed at TWI for easy access to the diffractive optic. This processing head was used for most of the experiments involving DOEs, but not all. When not used, the same housing for the focusing lens was used to hold the DOE. Since the same collimators and optics were used from one experiment to another, this is not believed to have had an impact on the laser welding process. Figure 3.14 presents the designed head and the manufactured head used in the experiments.

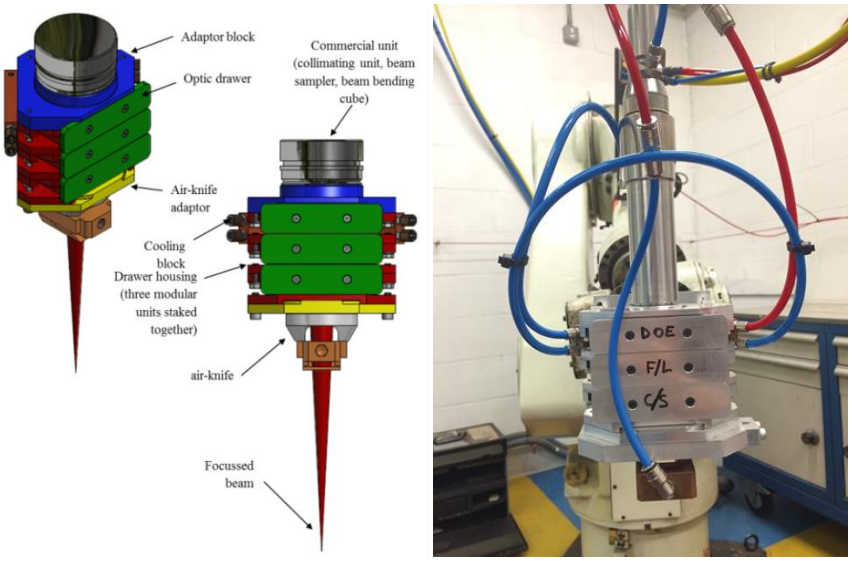

Figure 3.14: Welding head for DOE design and actual head

3.4.6 Mounting, clamping and shielding

In all experiments, the process heads were mounted either on a six-axis Kawasaki robot (model FS060L with DT Control) or an Aerotech XYZ table (model A3200). The six-axis robot has submillimetre position accuracy (0.1 mm) on the axes that have been used, meaning that negligible changes to the focal position or tilting of the head have been introduced during welding. For the Aerotech table, the workpiece moves relative to the welding head. Figure 3.15 presents the two pieces of equipment.

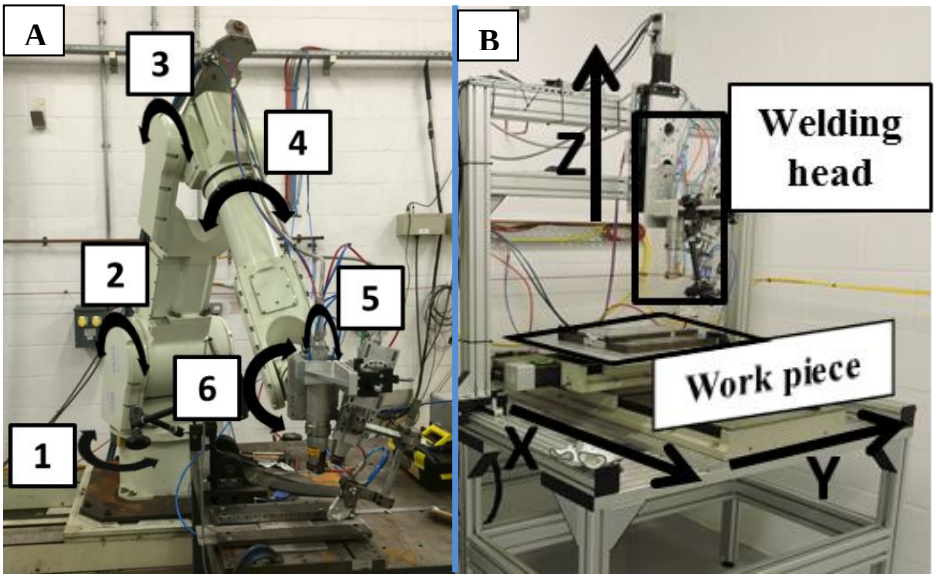

Figure 3.15: (A) 6 axes Kawasaki Robot (axes labelled from 1 to 6) and (B) Aerotech table

All welding trials were performed autogenously in the PA position (flat position) as covered by ISO 6947:2011 [100].

The same steel clamping jig was used for all of the experiments. Top-down clamps were systematically used for beads on plate and butt welds. The jig had an efflux channel as depicted in Figure 3.16. The efflux outlet was essential to avoid a build-up of gas pressure in the efflux channel which could influence the welding process.

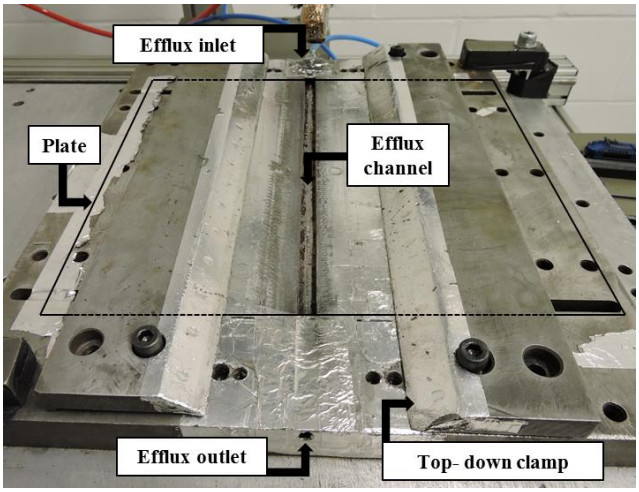

Figure 3.16: Jig and clamping used for all experiment

In all welding trials, the top bead was shielded by a flow of nitrogen or argon gas through four 10 mm diameter stainless steel tubes, arranged in a panpipe arrangement, at a rate of 10 l/min each. The weld underbead was shielded at a rate of 10 l/min, using an efflux channel insert in the base of the butt welding jig.

3.4.7 Temperature recording

To monitor the temperature change during welding at the weld location and particularly the cool down in the 1200 – 800°C window; several techniques were investigated. Two different methods of temperature monitoring were used in this research; monochromatic pyrometry, and thermocouple measurements.

The temperature changes in the sample during welding were measured using a Lumasense infrared pyrometer (model IMPAC IPE 140). The pyrometer has an uncertainty of 0.3% of measured value in °C, with a 1-second sampling rate. The temperature readings were taken at a fixed location (generally at the middle or first third of the total weld's length), at a distance of 300 mm away from the material surface. The sampling interval was 10 ms, which was the shortest available. Due to hardware limitations, the maximum temperature recorded was 1000 ˚C. The emissivity setting was set at 70% for all tests.

To measure the cooling rate, the closest temperature to 1000˚C (Temp1, Time1) and 800˚C (Temp2, Time2) were taken. Then, based on these readings, the cooling rate in the 1000-800˚C interval could be readily determined. Temperature measurement at the surface was challenging regarding the alignment as the melt pool size was of the order of millimetres in dimension. Also, the emissivity of the grade 2205 DSS plate was dependent upon its temperature, thereby affecting the temperature measurement. The technique was still relevant for comparison.

Another technique was investigated to avoid the dynamic emissivity issue and to determine the heat flow inside the weld. Type K thermocouples were attached 5 mm away from the intended position of the weld on top and bottom of the metal plate. They were attached via electromagnetic discharge. This technique is fast, and the equipment is portable. However, it is challenging to accurately position the thermocouple, partly due to the dexterity required (steady hand) and partly due to the thermocouple tip size (minimum size is in the order of millimetres). The actual distance from the beam path was 5 ± 1 mm. Temperatures were recorded using PicoLog software [101] that displays directly the graph temperature vs time. This technique was not selected for further use because of the difficulties to keep the thermocouple attached and the impossibility of putting the thermocouple at the weld location.

3.5 Weld characterisation

3.5.1 Visual observation

Oxidation, spatter, weld surface cracks, incomplete penetration, undercut, lack of fusion and sagging can be assessed by visual inspection. Figure 3.17 shows an example of an oxidised weld (1) compared to an adequately shielded weld (2). On weld (2), the steady solidification lines left by the melt pool solidification confirm a continuous flow of the melted material, and it is further evidenced by the absence of spatter.

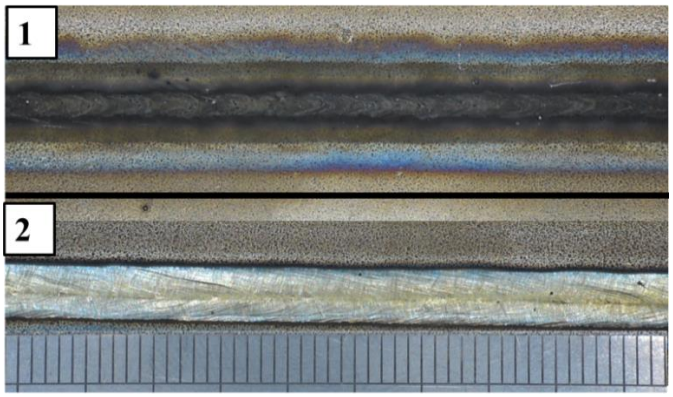

Figure 3.17: Rejected weld 1 and sound weld 2

3.5.2 Porosity

To reveal the potential presence of sub-surface porosity in the weld, x-ray imaging was used. Imaging was done on 50× films using a Comet 450 kW x-ray source set at a 1000 mm FFD (focus to film distance). For both 3 and 6 mm plate, an emission of 100 kV was set. The procedure was covered by the standard ISO 17636 [102]. All X-ray imaging had a wire type image quality indicator (IQI) of 13 meaning that smallest element readily visible in the area under inspection was 0.20 mm. Determination of the IQI was done according to ISO 19232-1 [103]. An example of x-ray imaging is given in Figure 3.18.

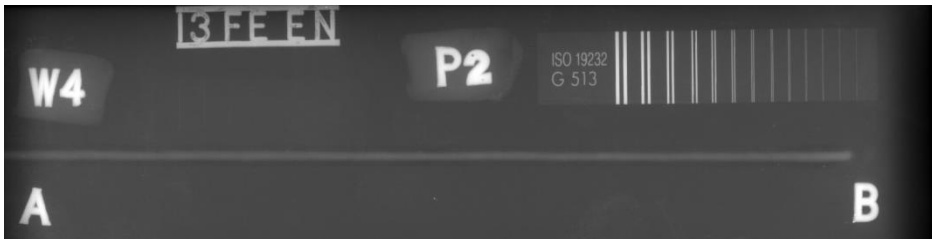

Figure 3.18: Example of X-ray imaging of a weld

3.5.3 Micrograph imaging

Welded samples were cross-sectioned and then etched with either 40% KOH (potassium hydroxide) or 20% H_2SO_4 (sulphuric acid) prior to microscope imaging. Imaging and scaling were performed through an Olympus microscope (model BX41M) with a magnification up to 1000×, and post-imaging measurements were made with ImageJ software (version 1.51d) [104]. The error coming from the scaling of the image (microscope labelled scale) is estimated at 1% by the microscope manufacturer leaving a precise measurement of ± 0.01 mm for images scaled at 1 mm and ± 0.02 mm for images scaled at 2 mm.

Selected samples were cross-sectioned and mounted with thermosetting phenol formaldehyde resin. A 0.25-micrometre diamond paste was used for the final polish, and the samples were etched with a different solution. This process is summarised in Table 3.6.

Table 3.6: Polishing and etching of the different imaging requirement

Test	Polishing	Etching	Observation/recommendation
Imaging, weld profile measurement	Down to ¼ µm and O-PU finish	Sulphuric acid for 20 sec at 3.5 V	Sulphuric acid highlights weld region, HAZ and is suitable for high contrast image
Point count	Down to ¼ µm and O-PU finish	KOH solution for 20-30 sec at 3.5 V	KOH etching gives colour to the phases but over etching makes point count inapplicable
EBSD	Down to ¼ µm and a finer finish	No etching	Highest polishing quality is fundamental to obtain results

3.5.4 Weld profile

Principal weld dimension reported in future Chapter are depicted in figure 3.19.

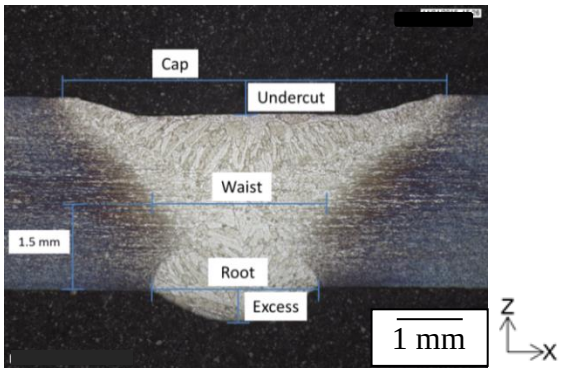

Figure 3.19: Weld profile feature

The weld profiles were characterised according to BS EN ISO 13919-1 [105] which provides guidance on quality levels for imperfections of steel welded with electron and laser beam. The weld profiles presented in this thesis were characterised according to this standard. Excessive weld metal and undercut were measured to assess the quality level of the welds. The extract in Figure 3.20 shows the quality level of excessive weld metal and penetration.

No	Imperfection, designation	ISO 6520 reference	Remarks	Limits for imperfections for quality levels		
				moderate D	intermediate C	stringent B
11	Excess weld metal	502	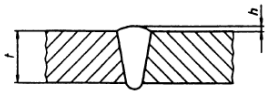 To be applied for reinforcement on weld side.	h ≤ 0,2 mm + 0,3 t or 5 mm, whichever is the smaller	h ≤ 0,2 mm + 0,2 t or 5 mm, whichever is the smaller	h ≤ 0,2 mm + 0,15 t or 5 mm, whichever is the smaller
12	Excessive penetration	504	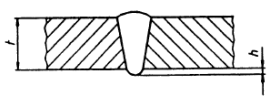 Used for root run for joints welded from one side.	h ≤ 0,2 mm + 0,3 t or 5 mm, whichever is the smaller	h ≤ 0,2 mm + 0,2 t or 5 mm, whichever is the smaller	h ≤ 0,2 mm + 0,15 t or 5 mm, whichever is the smaller

Figure 3.20: British standard extract [105]

3.5.5 Ferrite volume fraction

The percentage of ferrite phase (ferrite volume fraction) was a critical parameter for assessing the weld quality since it is directly related to the resulting corrosion and mechanical properties of the weld. The ferrite content of a test set of welds and parent material samples was evaluated using different techniques presented in the following sub-sections. They were namely: point counting, Fisher digital Feritscope® MP30, EBSD imaging, and computer image analysis.

The point count technique was found to be the most reliable and accurate technique providing certain parameters were kept constant during the process (i.e. the same operator, equipment and etching). The digital Feritscope was found reliable (similar result with other techniques) and accurate (standard deviation of 2 for ten measurements) to measure the ferrite content in the parent material only, providing the measurement was done on a polished surface. EBSD imaging gave a reliable and accurate ferrite content measurement, providing a very fine sample preparation, but the acquisition time (several days) was prohibitive to use this method systematically. Automated computer image analysis of the microstructure with a trainable algorithm or thresholding method was too experimental and not reliable enough. The difference of up to 15% of the ferrite content was found in the same image of the microstructure depending on the programme setting.

3.5.5.1 Point count

The point count technique consists of observing the microstructure on a screen with a superposed grid of points. Only the points covering the ferrite phase are counted. Several areas (fields) of the microstructure are covered. The average ferrite count per field relative to the number of points in the grid gives the volume fraction of ferrite (i.e. the ferrite content in %).

Sample etched with 40% KOH solution to colour the different phases were put under a digital microscope. The point count was carried in accordance to ASTM E562-02 [106], i.e. counting 32 fields with a 25 point grid at 1000× magnification. The point count was carried out at different locations: at the weld cap, waist and root as shown in Figure 3.21.

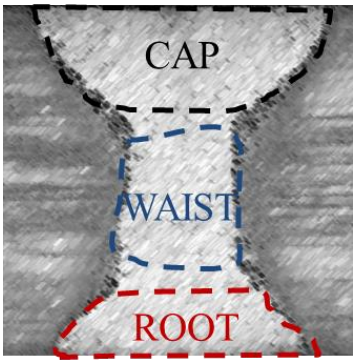

Figure 3.21: Area of point count

For each area, 32 fields were randomly selected for point count. The final result for an area is the average of the 32 ferrite point counts. The attached incertitude (margin of error) is

calculated for the result to be given at 95% level of confidence. The formula is given by Equation 3.1 [106].

$$\bar{\mathbf{x}} \pm \boldsymbol{Z} \times \frac{\boldsymbol{s}}{\sqrt{\boldsymbol{N}}} \qquad \text{Equation 3.1}$$

Where $\bar{x}$ is the mean value of the 32 point counts, Z is the Z-value for the 95 confidence level given by statistical table (2.131 in this case), s is the standard deviation for the ferrite fraction of the 32 fields (the dispersion between the 32 independent counts within an area), and N is the number of samples (i.e. 32). As an example, if the ferrite content is found to be 70% and the margin of error is 3%, then there is a 95% probability that the true ferrite content (the true population mean) is between 67 and 73%.

Nevertheless, the accuracy of point count can be influenced by many factors such as the quality of the sample preparation, the grid density, and the magnification of the substrate, and the operator interpretation of the microstructure. Quality of sample preparation is critical for the operator to distinguish precisely the different grain and their boundaries. KOH etching for 30 seconds with 3.5 volts gave the best contrast results and was preferred to sulfuric acid etching, which does not give colour to the different phases. Grid density (5 × 5) and magnification (1000×) were kept constant for all point count following standard specification. Point count of a test set carried by two different operators revealed a consistent discrepancy of 9.3% between them. Operator B always found nearly the same fraction of Operator A's results, as the dispersion of the differences between them was only 2.5%. The method is therefore reliable for qualitative estimation if the operator remains unchanged. The author of the present thesis (Operator A) carried all the point count presented to ensure reliable comparisons.

3.5.5.2 Ferrite scope

The Fisher digital Feritscope® MP30 is a non-destructive equipment to measure quasi instantly ferrite content through magnetic induction (eddy current). The Feritscope® is attached to a probe wrapped in a coil. A low alternating current flows through the coil and generates an alternating magnetic field in the ferritic sample when the probe is in contact with the sample. Ferrite is a magnetic phase while austenite is not. Alternative voltage results from the interaction of the magnetic field and the coil. As the voltage magnitude is a function of the ferrite content in the sample, Fisher Feritscope® measurement gives the ferrite number (FN). The ferrite number is the result of measurement methods standardisation, and it does not correlate linearly with the ferrite content in the sample. The ferrite content is electronically calculated and displayed by the Fisher Feritscope®, but the result has ± 16% accuracy when compared to the manual point count method. This does not tell which method is more accurate, but it already introduces a non-negligible discrepancy between the two methods. Both methods are not interchangeable. Due to the small weld region, Feritscope® measurements were found to be impracticable as the probe was bigger than the weld itself. Results were found to be inconsistent, and up to 55% difference with point count was registered. The Feritscope® was still a precise tool to measure the ferrite content in the base metal albeit consideration of the surface finish must be taken into account (surface has to be polished).

3.5.5.3 EBSD

Electron Backscatter Diffraction (EBSD) is a technique for quantitative microstructure analysis in the scanning electron microscope (SEM). The general equipment set-up is displayed in Figure 3.22 A. EBSD provides a range of sample characterisations such as phase, crystal orientation, texture, grain statistics and strain condition. Sample preparation is critical for imaging and accuracy. In this work, samples were polished to a quarter micron finish followed by a colloidal silica OP-U polishing for 5 minutes. The sample was then inserted into the vacuum chamber and tilted at 70°. The resolution step was 0.78 microns. When the SEM beam strikes the sample and Bragg's law is fulfilled, diffracted electrons form a set of paired large angles, which correspond to each diffraction plan. These electron backscatter patterns are formed on the phosphor screen of the EBSD detector and are known as Kikuchi bands, Figure 3.22 B. The phosphor screen converts the response into photon to reproduce the pattern on a Charged Coupled Device (CCD) camera. The resulting digitised image can be automatically analysed and indexed. Kikuchi bands directly indicate the orientation of the crystal and can be used to identify the specific crystal structure which generated it. In this case ferrite (BCC structure) and austenite (FCC structure), the different phases can be efficiently detected. There are no chances for inaccurate detection (ferrite detected instead of austenite or vice versa) as Kikuchi bands for this two phases are sufficiently different. Therefore, the ferrite content analysis was precise, but the relatively long acquisition (over 70 hours) for a small area of the weld (less than 2 × 2 mm) prohibited this technique being used systematically in the reported work. EBSD technique was nevertheless used for phase detection. EBSD technique was nevertheless used for phase detection.

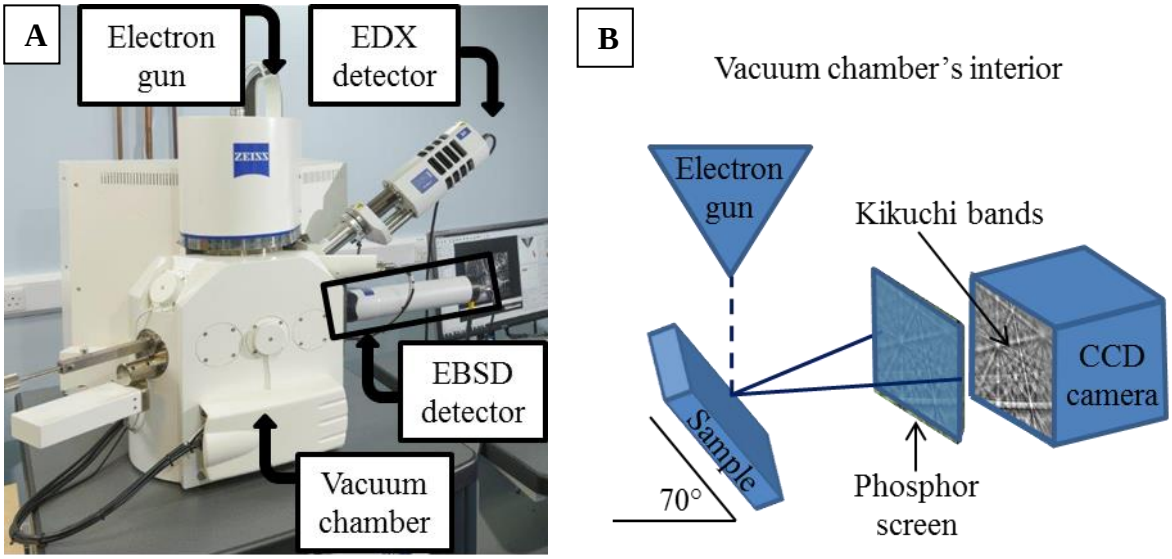

Figure 3.22: (A) SEM equipment and (B) schematic of EBSD detector

3.5.6 Phase imaging

The microstructure of the weld can be revealed through simple polishing and etching steps. By etching the microstructure, the ferrite-austenite phase boundaries become visible. Optical microscope observations starting at a nominal 10× magnification show the acicular austenite formation within the ferrite grain. Estimation of the phase balance can be achieved by a point

count technique, but no information can be obtained on the orientation of the grains. EBSD orientation imaging mapping can give this information.

3.5.7 Chemical analysis of the phases

The ferrite and austenite chemical composition were analysed at different locations in the weld and parent material. The energy dispersive x-ray spectrometry technique (EDX, sometimes referred as EDS) was used. For each measurement, 3 grains of the same phase were analysed at a micro scale and averaged. The chemical analysis was done to identify and quantify eventual elemental partition between the different phases of austenite and ferrite.

3.5.8 Corrosion

ASTM A923 test method C for duplex steel [107] is one of the most cost-effective testing methods for detection of detrimental intermetallic phase, and it is also the method used for evaluating the corrosion resistance of the welded panel for nuclear waste containers [16]. The presence of intermetallic phases and chromium nitride, in an excessively ferritic phase balance, are detected as a loss of pitting resistance. Welded samples were immersed for 24 h in a ferric chloride solution (approximatively 6% $FeCl_3$ per weight with a 1.3 pH). To qualify, the calculated corrosion rate of the tested sample shall not exceed 10 mdd (Milligrams per square Decimeter per Day). The calculation is as follows:

$$\text{mdd} = \frac{\text{weight loss (mg)}}{\text{sample area (dm}^2\text{) x time (days)}} \quad [13] \qquad \text{Equation 3.2}$$

Mdd is the unit to report a loss in mass in a unit which includes both area and time. To convert in $mm.y^{-1}$ (mm per year) Equation 3.3 is used.

$$\text{mm.y}^{-1} = \text{mdd} \times \frac{0.0365}{\rho} \quad [13] \qquad \text{Equation 3.3}$$

Where ρ is the density of the metal in $g.cm^3$ and its value for grade 2205 DSS is 7.85 $g.cm^3$.

The main issue of these units is that they are based on two assumptions that may not be true:

- The corrosion has occurred at a constant rate through the test period, which is rarely the case since most of the attacks tend to diminish with time.
- The corrosion has proceeded uniformly over the whole surface, which is rarely the case since the attacks develop from locally initiated pits.

Nevertheless, the pass or fail ASTM A923 test is recommended and used in industry for the targeted application. Comparative results can tell if a weld presents better corrosion properties than another one. Samples of size 50 × 25 mm were cross-sectioned from the weld as seen in Figure 3.23, polished to 120 grit to remove scale or spatters and then weighed. This was followed by a 24-hour immersion in a ferric chloride solution in a thermostated bath at 22 °C. Samples were finally inspected to find the pitting and weighed once again to measure the mass loss and calculate a theoretical corrosion rate. For baseline comparison, the parent material, free of weld, was also tested.

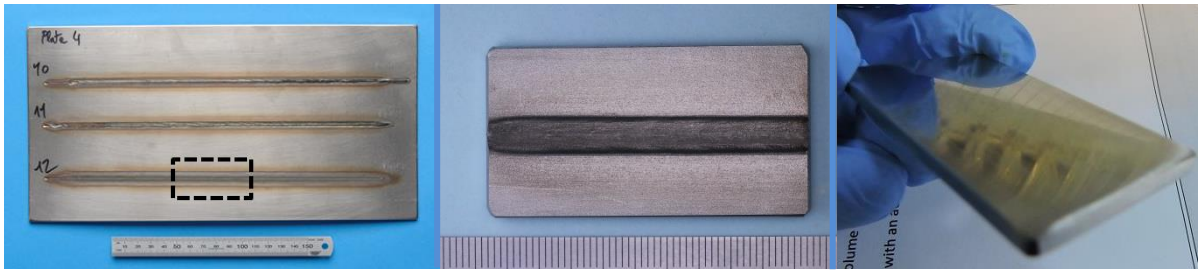

Figure 3.23: Sample preparation for ASTM A903

3.5.9 Hardness

A number of samples were tested for hardness. The test method selected was a Vickers hardness test following the BS EN ISO 6507-1 standard [108]. Several measurements were made at the cap, waist and root of the weld along a parallel line to the surface. A Vickers microhardness tester with a load on the indenter of 200 g was used for this purpose.

Chapter 4: Single beam autogenous Yb:fibre laser welding of grade 2205 duplex stainless steel

4.1 Introduction

The first stage of this research was to evaluate the single beam Yb:fibre laser welding process of grade 2205 duplex stainless steel without the use of filler wire (i.e. autogenous welding). The benchmarking of the process provided the basis for comparison with the tailored energy distribution processes presented later in Chapters 5 and 6. Autogenous Yb:fibre laser welding process was developed for two thicknesses of grade 2205 DSS (6 and 3 mm), and the results are presented separately by thickness. Firstly, Section 4.2 reviews the overall experimental approach and Section 4.3 gives general observations common for both thicknesses. Finally, Section 4.4 presents the results for 6 mm thick plates and Section 4.5 for the 3 mm plates.

4.2 Experimental programme

4.2.1 Approach

Process parameters were developed for the welding of 6 and 3 mm thick grade 2205 DSS. Welding speed, power and focus position were varied in a controlled manner. Different optical configurations leading to different spot sizes were also evaluated. In addition, as suggested in the literature [70], [109]; pure nitrogen shielding gas was compared with argon gas that is usually used with arc welding [110]. Finally, the effects of varying the process parameters on the resulting weld were evaluated. Pyrometer and thermocouple were used to measure the cooling rate during welding. X-ray imaging was used to detect weld defects such as cracks or porosity. Samples were cross-sectioned for weld profile measurement and metallographic examination. The point count technique covered by ASTM E562 standard was used to measure the resulting phase balance at the weld location. Chemical analysis of austenite and ferrite phases at different weld location was carried out on selected samples using EDX semi-quantitative method. Grain orientation was observed using EBSD technique. The Vicker hardness test and ASTM A923 test method C were performed on selected samples to evaluate the hardness at the weld and the corrosion resistance properties.

4.2.2 Equipment and material

In this chapter, the IPG YLS 5000 Yb:fibre laser was used and mounted on the Aerotech 3-axis table. The jig, clamps, pyrometer and Prometec beam profiler used are the ones described in Chapter 3. For all experiments, the optical fibre had a 150 µm core diameter and the Optoskand 100 mm focal length (FL) collimator was used.

4.2.3 Experiments

Single beam welding on 6 mm thickness plates consisted of 50 melt runs and two butt welds carried with different process parameters. Two different focusing lenses of 200 and 400 mm FL were tested, leading to nominal spot sizes of 300 and 600 µm, respectively.

Single beam welding of 3 mm thickness plates consisted of 20 melt runs and six butts welds performed with different process parameters. Only the 200 mm FL focusing lens was used.

4.3 General observations

4.3.1 Cracking and porosity

Fifty radiographs and fifty cross-sections (at 1000× magnification) of welds were examined. No welding defects or porosity were observed. This is partly due to the good crack resistance of the material and partly the welding conditions selected. On the X-ray imaging of 6 and 3 mm thick plates, as shown in Figure 4.1, the constant shade of the welds demonstrate an equal penetration along it confirming the stability of the process. Both images were taken with a 2-minutes exposure at 100 kV. Both images had a wire type image quality indicator of 13 meaning that smallest element readily visible in the area under inspection was 0.20 mm. Refer to Section 3.5.2 for more details on procedure and standards.

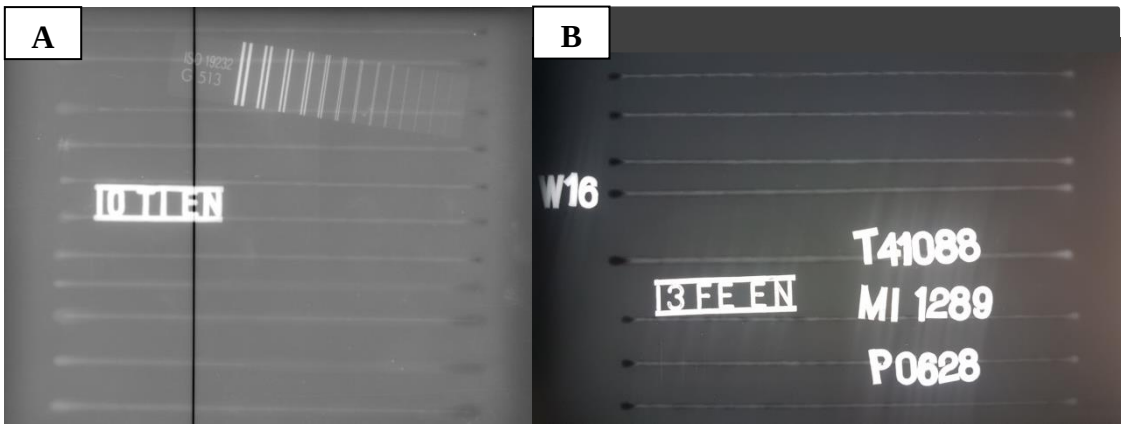

Figure 4.1: (A) X-ray imaging of 6 mm thick welded plate and (B) 3mm thick

4.3.2 Issue with spatters

Spatters were observed during all welding. Figure 4.2 shows a recorded video (25 fps) snapshot of a melt run on a 6 mm plates done with 4.5 kW at -4 mm focus at 1 m/min.

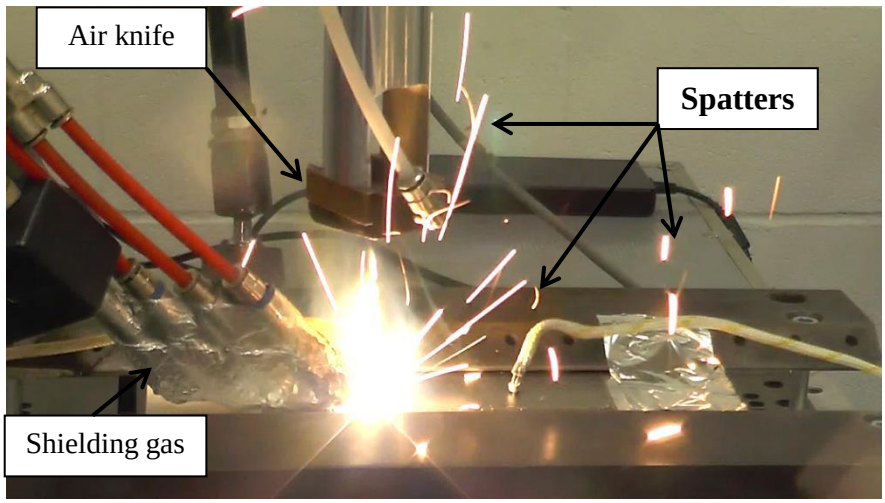

Figure 4.2: Spatters during welding

When welding with a short stand-off distance at low speed (< 1m/min), spatters can damage the cover slide protecting the optic. These damaged areas can then absorb or deflect the incident beam leading to energy loss. Figure 4.3 shows a damaged cover slide and the

resulting lack of penetration in the weld. It was found that by tilting the welding head by 5˚ was sufficient to mitigate such damage to cover slide. The head was tilted only when the focus position was set below -4 mm and for welding speed below 1 m/min.

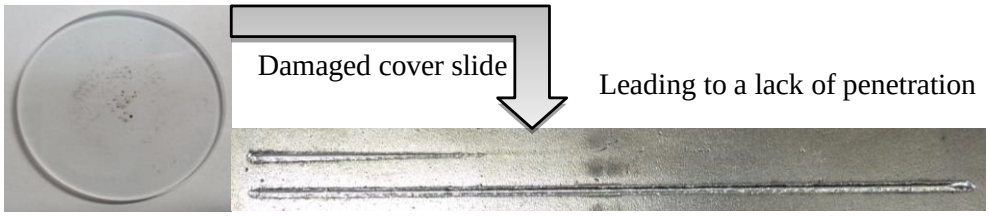

Figure 4.3: Damaged cover slide resulting in power losses

4.3.3 Shielding gas

Shielding gas is necessary during welding of grade 2205 DSS to protect the melt pool from contamination and surface oxidation, as shown in Figure 4.4, weld 1. Two different gases, pure nitrogen and pure argon, were used. Both resulted in clean welds which were free from visible oxidation Figure 4.4, weld 2 and 3, but argon shielded welds resulted in an average of 15% higher ferrite content than welds produced in the same condition with nitrogen gas shielding, see Table 4.1. The ferrite contents are given with their 95% confidence interval. These results confirm that there is a significant advantage in using nitrogen shielding to promote austenite in the phase balance, in agreement with findings elsewhere [70]. Nitrogen shielding is believed to compensate for the losses of nitrogen in the melt pool caused by the welding process (e.g. plume, spatter) [70]. For this reason, nitrogen was used in subsequent work. The gas was used without being mixed with argon as other research investigating different mixture ratio had shown that best results are obtained with pure nitrogen [109].

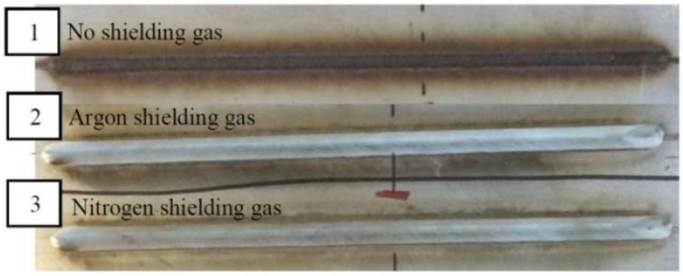

Figure 4.4: Visual inspection of welds with different shielding gases

Table 4.1: Effect of shielding gas on phase balance

	Parameters				**Ferrite content (%)**	
Weld type	Power (kW)	Welding speed (m/min)	Focus position (mm)	Shielding gas	Cap	Root
Melt runs 3mm	2.5	1	-4	Ar	86.9 ± 4.1%	86.5 ± 4.1%
	2.5	1	-2	Ar	93.0 ± 2.7%	87.5 ± 4.4%
	2.5	1	-4	N	73.1 ± 5.9%	70.4 ± 4.5%
	2.5	1	-2	N	74.9 ± 5.7%	76.0 ± 4.2%
Butt weld 6 mm	4.5	1.25	-4	Ar	86.3 ± 3.4 %	80.5 ± 2.6%
	4.5	1.25	-4	N	71.6 ± 4.2 %	67.5 ± 3.4%

4.4 Results and discussion of 6 mm plates experiments

4.4.1 Comparison of welding with different spot sizes

4.4.1.1 Beam characterisation

Both of the focusing lenses, of 200 and 400 mm FL, were used with a 100 mm FL collimator and gave a theoretical spot size of 300 and 600 µm respectively. Beam profiles were characterised with the beam profiler, and the results are summarised in Figures 4.5 to 4.8. The three-dimensional beam shapes at focus are presented in Figures 4.5 and 4.6. The beam radius ω(z) was measured along the direction of light propagation (Z-axis), giving the caustic show in Figure 4.7 and 4.8. r86%(z) is the beam radius taking into account the $1/e^2$ definition, i.e. the portion of the laser beam that contains 86% of the total beam energy. From these data, the Rayleigh range Z_R was found. To measure the beam profile parameter (BPP), ISO 11146 [53] recommends that about half of the measurement points must be more than two effective Rayleigh lengths away from the beam focus. This was not possible in practice with the 400 mm FL lens since its Rayleigh range of 16.7 mm demanding measurements from + 30 to - 30 mm along the Z-axis. When largely defocused, the space requirement for a measurement exceeded the Prometec beam profiler capability. Nevertheless, the 4.9 ± 0.5 mm.mrad BPP for the 400 mm FL focusing lens and the 5.3 ± 0.5 mm.mrad BPP for 200 mm FL focusing lens were close to the typical 5.5 mm.mrad BPP given by the manufacturer. The measurements match the theoretical values and confirm these relationships:

- The shorter the focal length, the smaller the beam waist ω_0.
- The shorter the focal length, the higher the divergence and therefore the shorter the Rayleigh range. In fact, the angular divergence θ of the beam is inversely proportional to the beam waist ω_0.

300 µm spot size

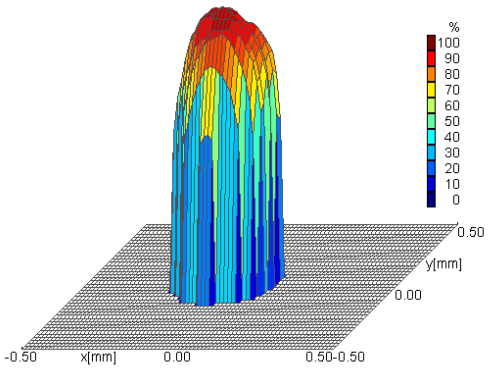

Figure 4.5: Beam profile of the IPG YLS-5000 Laser with the 86% def (200 FL)

600 µm spot size

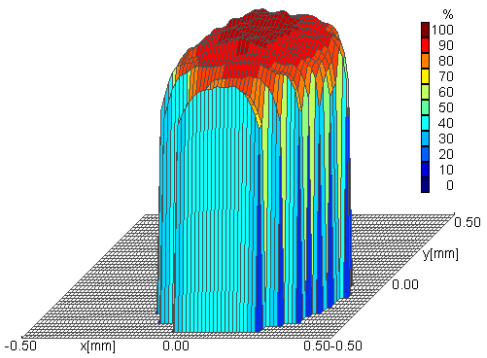

Figure 4.6: Beam profile of the IPG YLS-5000 Laser with the 86% def (400 FL)

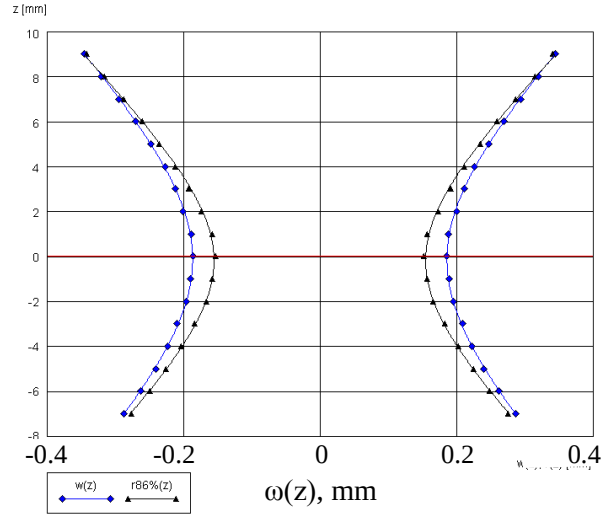

Results	Value	Value (86% def)	Unit
ω_0	0.186	**0.155**	mm
θ	0.032	**0.034**	rad
Z_R	5.87	**4.59**	mm
M^2	17.5	**15.5**	None

Figure 4.7: Caustic of the 5 kW IPG Laser with a 200 mm FL focusing lens

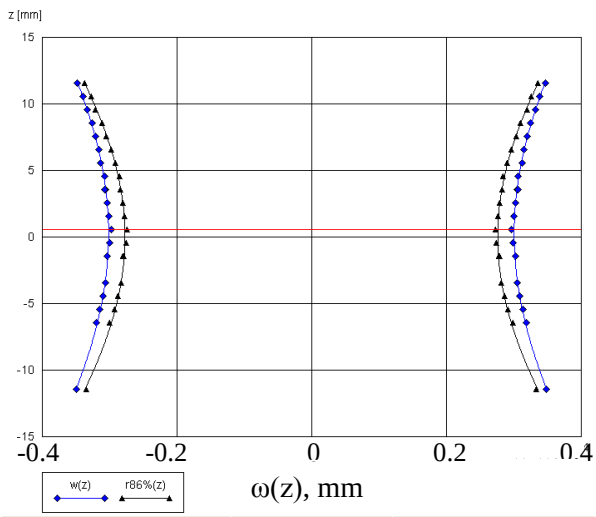

Results	Value	Value (86% def)	Unit
ω_0	0.301	**0.277**	mm
θ	0.015	**0.017**	rad
Z_R	19.81	**16.65**	mm
M^2	13.43	**13.5**	none

Figure 4.8: Caustic of the 5 kW IPG Laser with a 400 mm FL focusing lens

For both beams, a slight difference in size between the radius in the X and Y-axes was observed. The top view of the 3D caustic representation (Figure 4.9) helps to visualise that matter.

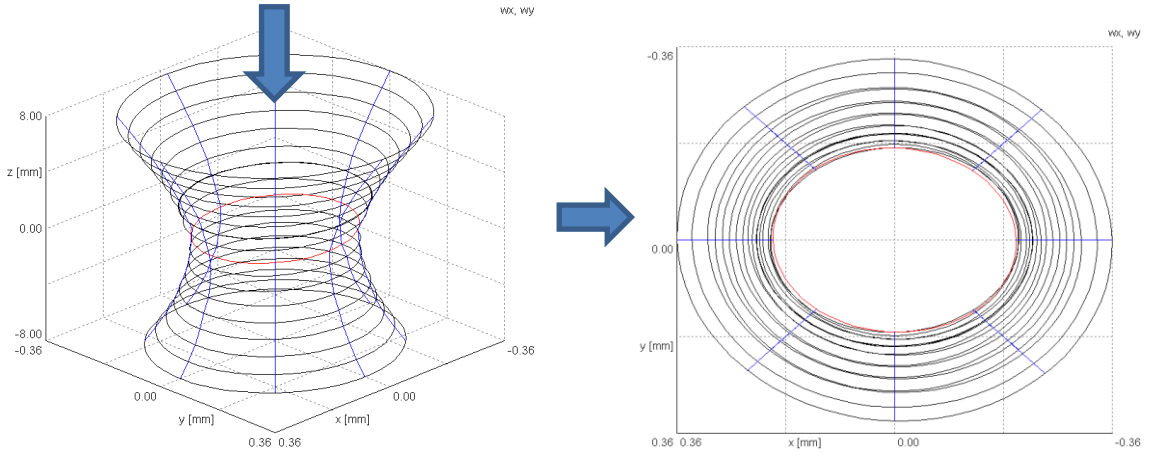

Figure 4.9: 3D caustic of the laser beam

ISO 11146 [53] defines a circular power density distribution as one where the power density distribution has a ratio between the minimum and maximum beam widths which is greater than 0.87. This was the case for the 600 µm spot size, but the 300 µm spot has a ratio of 0.84, making it elliptical. Nevertheless, this slight difference in radius symmetry along the direction of propagation is assumed to have no impact on the weld.

The power distribution at the output of the fibre depends on the modes propagating in the fibre and the quality of the optics used. The fundamental mode is described by a Gaussian profile as it is observed for a single-mode fibre laser. For a multimode laser, where the fibre guide is a graded index type, the modes are integrated, and power density is equally distributed at the fibre end. Therefore, power distribution in the focal plane, which is the image of the fibre end, should be a top-hat profile. It was indeed observed, that in the vicinity of the focal plane, the power distribution of the beam obtain with 400 mm FL focusing lens is better described by a top-hat than a Gaussian distribution. This statement is more arguable with the 200 mm FL focusing lens, but observation elsewhere pointed out the same results [51]. Table 4.2 shows the weld profiles of the 600 µm spot size in focus described by a top-hat ($\chi^2 > 95\%$) and in the far field described by a Gaussian ($\chi^2 > 95\%$). The χ^2 was calculated in Excel by comparing the coordinate of the measured beam profile against a top hat or the expected Gaussian function.

Table 4.2: Beam profile in focus and far field

Beam profile in the focal plan	Beam profile in far field
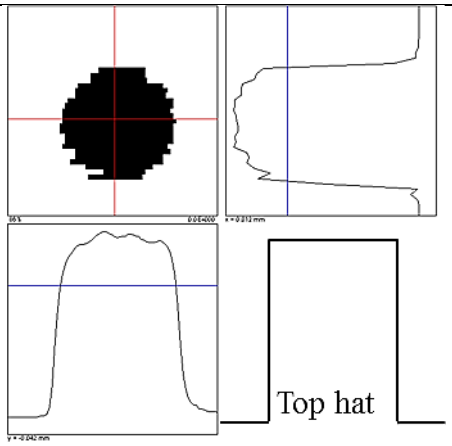	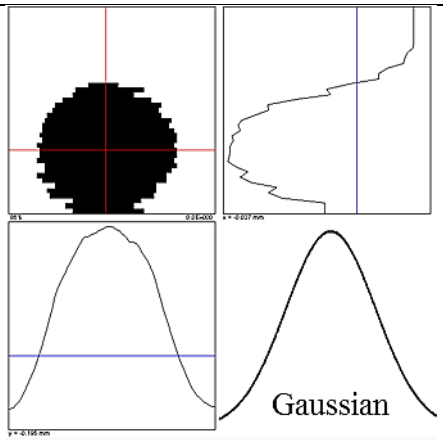
Z= 0	Z = - 11 mm

4.4.1.2 Welding observation

The laser was set as described in Section 3.4.3 and 3.4.6 with pure nitrogen as shielding gas. Minimum power and maximum speed to obtain full penetration were established with the two focusing optics. For comparison, the short focal length lens was used in a defocus position to give a measured spot size at the material interface that was equal to the one given by the long focal length lens at focus position. Results are given in Table 4.3.

Table 4.3: Full penetration with a different spot size

Optics focal length	Spot size at focus	Focus position (mm)	Spot size at the material interface (X-axis)	Fastest speed for full penetration at 5 kW	Lowest power for full penetration at 0.5 m/min
200 mm	300 µm	0	300 µm $_{measured}$	3.5 m/min	2.5 kW
200 mm	300 µm	-3	384 µm $_{theory}$	3 m/min	2.75 kW
200 mm	300 µm	-5	600 µm $_{measured}$	2 m/min	3.5 kW
400 mm	600 µm	0	600 µm $_{measured}$	1 m/min (Partial penetration)	3.5 kW (Partial penetration)

It can be seen that small spot size provides higher speed and lower power for full penetration. This is in accordance with research elsewhere, pointing at the benefits of higher power density at the material interface with a good BPP [54].

It was observed that the 600 µm spot size, when using the 400 mm FL focusing lens, could not achieve full penetration for all the length of the melt run. A plume built up and reduced the laser absorption leading to a collapse of the melt pool. An air knife blowing nitrogen gas was set horizontally just above the melt pool during welding. This air knife suppressed the plume, and the full penetration was stable, but the disturbance caused by it did not allow the shielding gas to protect the weld from oxidation.

Finally, it was interesting to see that two spots equal in size but given by different optics at different focus did not give the same welding result. In recent years, researchers have tried to characterise a laser process through fundamental laser mater interaction parameters that are independent of the optics used [111]–[113]. These parameters are the average power density, the interaction time and the specific point energy. If the average power density (power/spot size) is calculated for a beam spot in focus (top-hat power distribution) it relates closely to reality but for a slightly defocused beam which power distribution is in-between a top-hat and a Gaussian the power averaging does not describe reality correctly, and the relevance of this parameter does not hold anymore. In Table 4.4 are the different power densities of a 600 µm spot size given by the 200 mm FL focusing lens in a defocus position and by the 400 mm FL focusing lens in focus.

Table 4.4: Beam's power distributions with different optics and focus positions

200 mm focal length optic: beam spot at -5 mm focus	**400 mm focal length optic: beam spot at 0 mm focus**
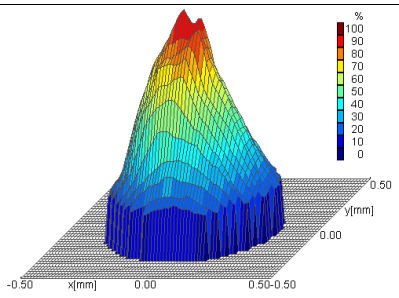	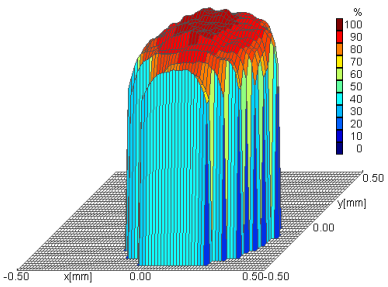
Spot size measured: 600 µm	Spot size measured: 600 µm

A longer Rayleigh length is desirable for processing thick material as it provides more robust vertical position tolerances of the workpiece. Small spot size is nevertheless more critical for higher precision and speed, and finally, the 200 mm FL focusing lens was chosen for the rest of the experiment as the more intense plume formed by the wider spot size (formed by the 400 mm FL focusing lens) was an issue for achieving full penetration.

4.4.2 Process window for full penetration

Using the 200 mm FL optic and the set up described in Section 3.4.3 using pure nitrogen shielding gas, the window for full penetration was established. Results are shown in Figure 4.10. The maximum welding speed to obtain a full penetration with the maximum power available of 5 kW was 3.5 m/min. The processing power was nevertheless fixed at 4.5 kW for latter comparison with experiments carried out with the 3-spots DOE (chapter 6). At this power core welding speed was ~1 m/min as lower speeds are not desirable for industry and because spatters have more chance to damage the optics. Welding parameters tested were welding speed from 0.8 to 2.2 m/min and focus positions from -8 to +4 mm.

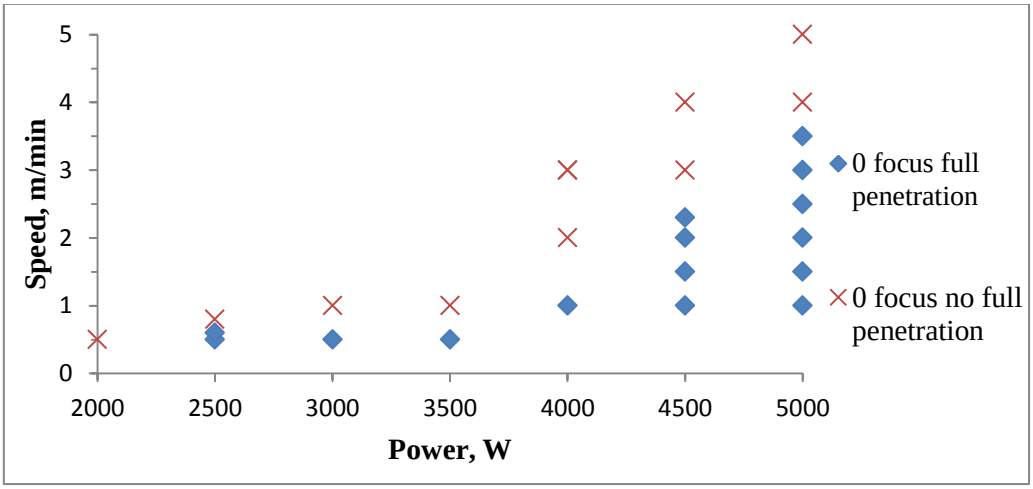

Figure 4.10: Window process for full penetration with a 300 µm spot size

4.4.3 Weld profile

Selected representative cross sections are presented in Figure 4.11, exhibiting wide top bead and full penetration without undercut. The fully penetrating weld had a high aspect ratio (penetration depth/the weld width). The symmetrical weld about the axis of the laser beam suggested a steady fluid flow during welding and explained the absence of humping defects.

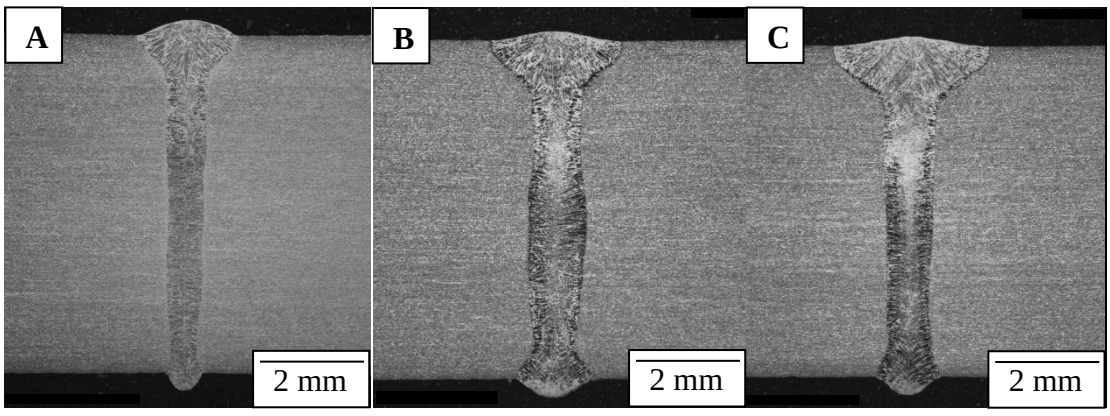

Figure 4.11: Welds at 4.5kW at different processing speed and focus position: (A) 2.2 m/min at -2 mm focus; (B) 1.5 m/min at -2 mm focus; (C) 1.5m/min at -8 mm focus

Dimensional measurements are summarised in Table 4.5. The standard BS EN ISO 13919-1 [105], which provides guidance on the quality levels for imperfections of steel welded with electron and laser beams, does not include information on the width of the weld cap or the

weld root which is required for a good weld as weld dimensions are usually dependent on the particular application. However, it was found that welding at speeds of 2 m/min or higher resulted in a narrower root of less than 1 mm in width, which is not desired by the industrial manufacturer of the nuclear waste container. Weld caps were larger at slower welding speed varying from 3 to 2 mm in width and weld roots were in average 1 mm narrower. As a general observation the smaller the heat input the narrowest the weld's waist. The maximum excess of metal was found to be 0.2 mm on the weld cap and 0.3 mm in the weld root. The standard BS EN ISO 13919-1 allows up to 5 mm of weld excess for stringent quality (Level B).

Table 4.5: Welds profile measurements for single beam welding of 6 mm plates

Parameters		**Dimensions (mm)**				
Welding speed (m/min)	Focus position (mm)	Cap	Excess metal cap	Waist	Root	Excess metal root
1	-4	3.3	0.32	1.24	1.94	0.05
1	-2	2.76	0.21	1.36	2.09	0.07
1	0	2.54	0.21	1.45	2.14	0.05
1.25	-4	2.59	0.18	1.12	1.25	0.06
1.25	-2	2.43	0.18	1.18	1.57	0.04
1.25	0	2.30	0.16	1.05	1.61	0.08
1.5	-4	2.56	0.12	1.00	1.29	0.17
1.5	-2	2.17	0.20	0.95	1.39	0.18
1.5	0	2.03	0.16	0.98	1.49	0.31
2	-6	2.37	0.24	0.76	0.67	0.33
2	-4	2.28	0.23	0.81	0.81	0.24
2.2	-2	1.92	0.30	0.67	0.69	0.32

The focus position had an impact mostly on the weld cap width with a maximum difference of 0.8 mm observed between -4 and 0 mm focus position at constant speed. Yet, the relatively low level of laser beam divergence compared with the material thickness limited the effect of the focus position (in the -4 to 0 mm range) on the waist and root width.

4.4.4 Temperature measurement

4.4.4.1 Heat diffusion

In these tests, the narrow high power laser beam, combined with a welding speed of 1 to 2.2 m/min, led to very low heat input (i.e. in the range of 0.1 to 0.3 kJ/mm compared to typical values of between 0.5 and 2.5 kJ/mm for the arc welding process). Figure 4.12 shows the microstructure of the narrow HAZ for a typical sample at two magnification levels. A sharp transition in terms of crystal structure (shape and size) between the parent material and the weld was observed, suggesting a relatively fast cooling time due to the low heat input. It also suggests that there was a very contained heat flow at the weld location.

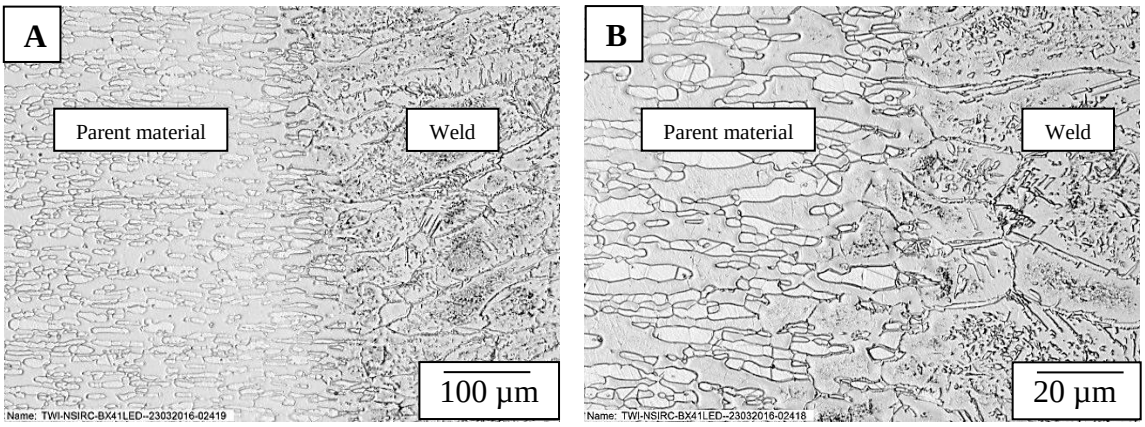

Figure 4.12: (A) HAZ at 100× magnification; (B) HAZ at 500× magnification

Type K thermocouples were placed at four different locations along the weld, 5 mm away from the weld centre line. They were placed on both sides of the plate at the start and finish of the weld as shown in Figure 4.13.

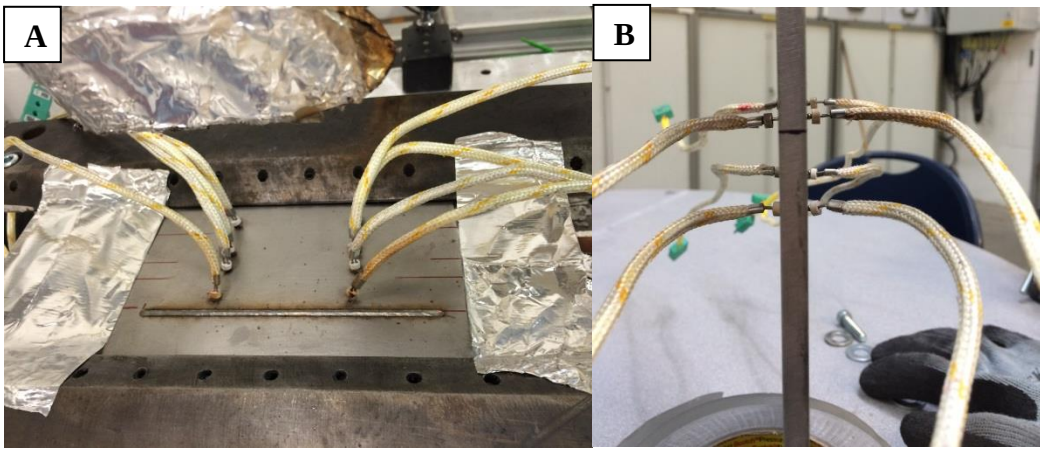

Figure 4.13: Thermocouples attached to the welded plate (A) top view and (B) side view

Similarities between recordings of the two sides of the plate suggested a balanced heat flow. The maximum temperature recorded oscillated from 200 to 300 ˚C depending on the thermocouple location. Figure 4.14 shows the typical measurements observed with a thermocouple. Knowing that melting temperature of grade 2205 DSS is 1450 ˚C, it indicates a steep declining gradient of temperature when moving away from the weld. For information, the thermal conductivity of grade 2205 DSS is estimated at 20 $Wm^{-1}K^{-1}$ [114], which is half of the value for carbon steel and one order of magnitude below the thermal conductivity of iron. The well-contained heat was already suggested by narrow HAZ. The thermocouple approach for measuring the cooling rate was not appropriate as using a capacitor-discharge machine to attach the thermocouples was lacking in accuracy. Thermocouples placed inside the weld or closer to the weld either detached or melted during welding.

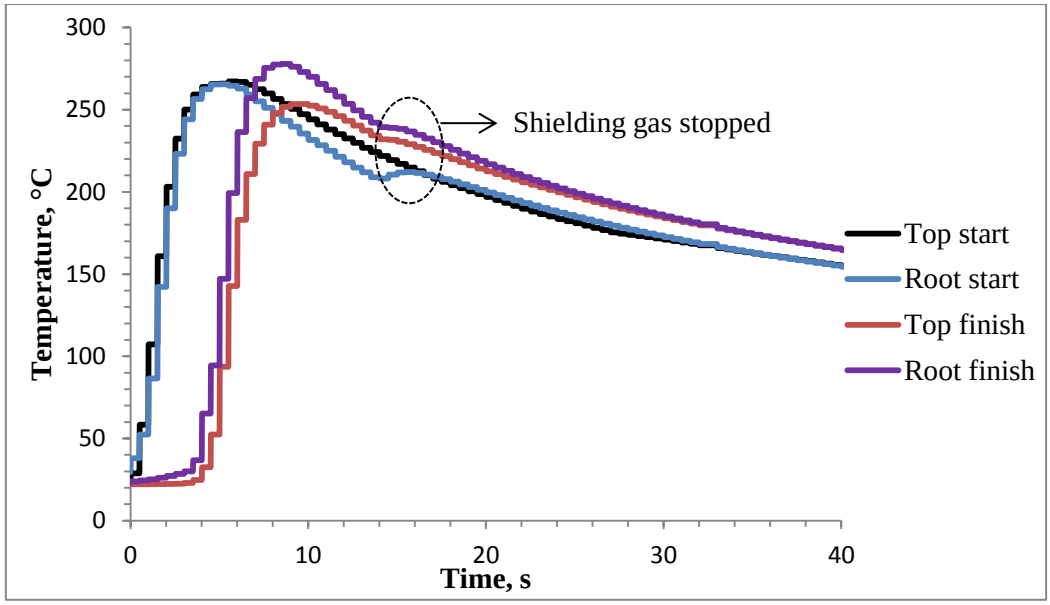

Figure 4.14: Thermocouple measurements for a weld at 4.5kW, 1 m/min, -4 mm focus

4.4.4.2 Surface cooling rate

The pyrometer technique was more flexible to measure the changes in temperature during welding but only at the weld cap. Also, due to limitations in the equipment available, it was difficult to obtain absolute temperatures as the pyrometer operated with a single infra-red sensor, which was unable to compensate for dynamic changes in emissivity between the liquidus and solidus phase. The pyrometer was nevertheless a useful tool for comparing qualitatively the effect of key parameters considered in this study. Figure 4.15 presents a typical example of melt run measurements at 4.5 kW, -4 mm focus and two different speeds. The temperature rose very sharply to the pyrometer saturation, followed by a steep cooling rate.

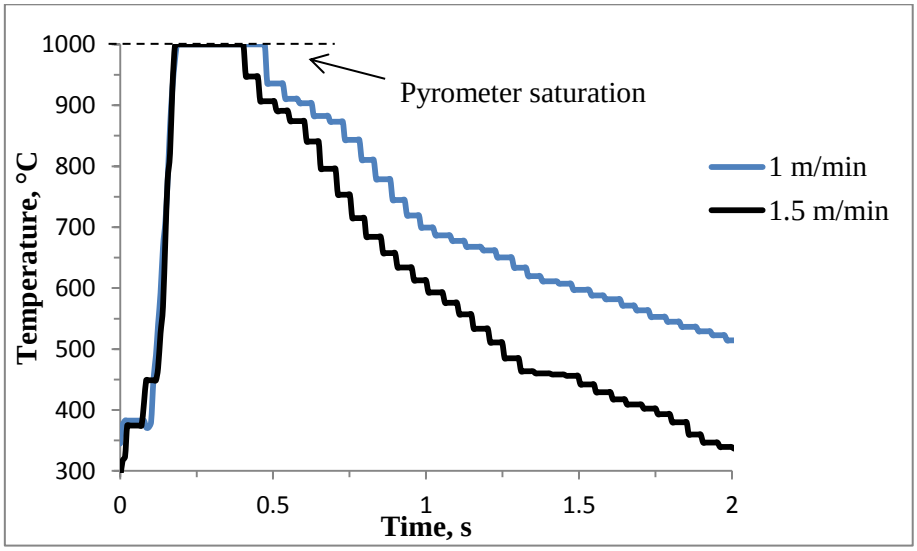

Figure 4.15: 6 mm grade 2205 DSS typical cooling curves

Results of measured cooling rates are presented in Table 4.6; an averaging was done on four measurements for each welding speed. In all melt-runs, fast cooling rates exceeding 500 °C/s were measured, and it was observed that lower welding speed at same power led to slower cooling rate. Shielding gas temperature was measured to be 10 ˚C.

Table 4.6: Averaged cooling rate

Welding speed (m/min)	Heat input (J/mm)	Time in the 1000 -800 ˚C interval (s)	Corresponding cooling rate (˚C/s)
1	270	0.36 ± 0.01 s	550 ± 50 °C/s
1.5	180	0.25 ± 0.01 s	800 ± 50 °C/s

The different cooling rates measured are nevertheless close to each other as the variation range of the most influent parameter (welding speed) was small (1 or 1.5 m/min). Figure 4.16 shows how close the cooling curves are.

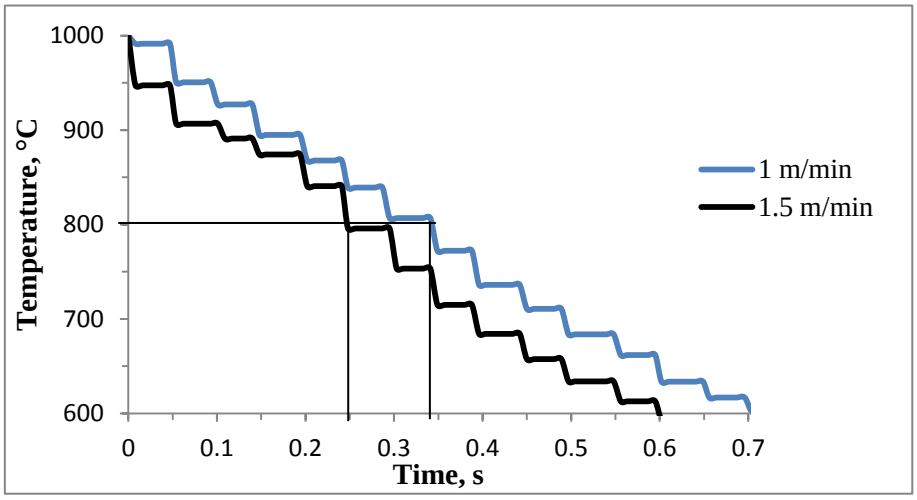

Figure 4.16: 6 mm grade 2205 DSS cooling curves in the 1000-600 ˚C interval

All welded plates returned to a temperature below 100 ˚C in less than 5 minutes (even with the highest heat input 300 J/mm) giving no chance for carbide precipitation or 450 ˚C embrittlement to happen. The fast cooling prevents the detrimental precipitation of chi, sigma, and carbide phases, [19]. Regarding Cr_2N precipitation, It was observed by Liao [115] that with low cooling rate (123 °C/s), the density of Cr_2N precipitate is lower, but their size are bigger when compared to higher cooling rate (250 °C/s). Extrapolating these results, with very high cooling rates (~500-800 °C/s) measured with laser welding it is possible to find a high density of very small Cr_2N precipitate in the HAZ. Cr_2N have not been observed at a 1000× magnification but might be there as their size can be of the nanometer order.

As the typical cooldown of the weld surface is significantly less than the time required for precipitations to occur, see Figure 4.17, there is scope to extend the cooldown.

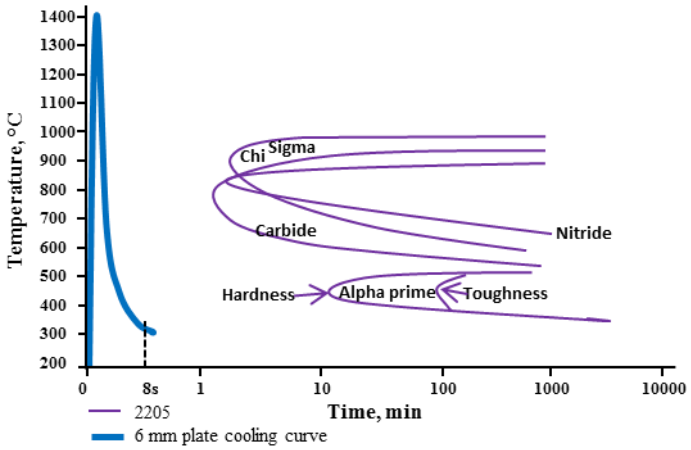

Figure 4.17: Time temperature diagram of grade 2205 DSS [19]

4.4.5 Heat input, focus position and resulting microstructure

The pyrometer peak temperature limit of 1000 ˚C was a barrier to relate the process parameter influence on the cooling rate clearly and therefore the phase balance. Nevertheless, the impact of welding speed and focus position on the phase balance was established by a set of experiments and a direct measurement of the resulting phase balance.

4.4.5.1 Microstructure change

Microstructures of welds were examined using the optical metallographic method as described in Chapter 3. Figure 4.18 shows phases present in the parent material before welding and at the weld cap after welding.

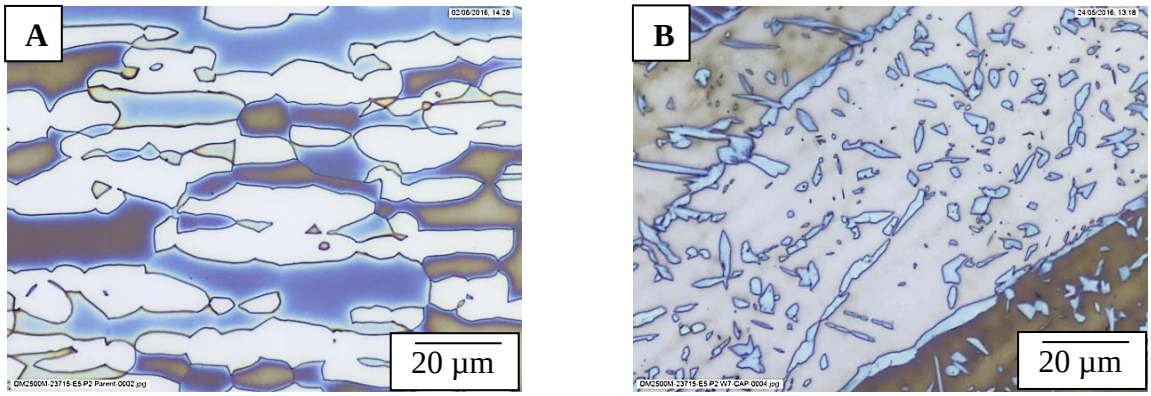

Figure 4.18: Microstructure at 1000× magnification at (A) base metal and (B) weld cap

The parent material had a volume fraction of ferrite and austenite roughly equivalent (54.6 ± 4.3% of ferrite) with equiaxed grains of roughly the same size, as shown in Figure 4.18 A. At the weld location the austenite grains formed along the grain boundaries of the large ferrite in allotriomorphic form (Figure 18 B). This is because austenite tends to nucleate at the ferrite grain surfaces, forming layers which follow the grain boundary contours. Few Widmannstätten austenite side plate structure were present. Intragranular austenite grains in acicular (needle shape) and idiomorphic (roughly equiaxed shape) forms were observed, as presented in Figure 4.18 B. These direct nucleations of austenite on the inclusion are by nature in chaotic ordering and can potentially increase the material toughness. Austenite grain

sizes sampled at the cap area on several welds were found to be less than 3 µm in width. This estimation was consistent for all sampled welds made with autogenous single beam welding. Ferrite grains were much larger and longer than in the parent material. Figure 19 B is the crystal orientation map derived from electron backscatter and it shows the grain arrangement, and orientation in a weld made at 4.5 kW and 1 m/min processing speed (Figure 4.19 A).

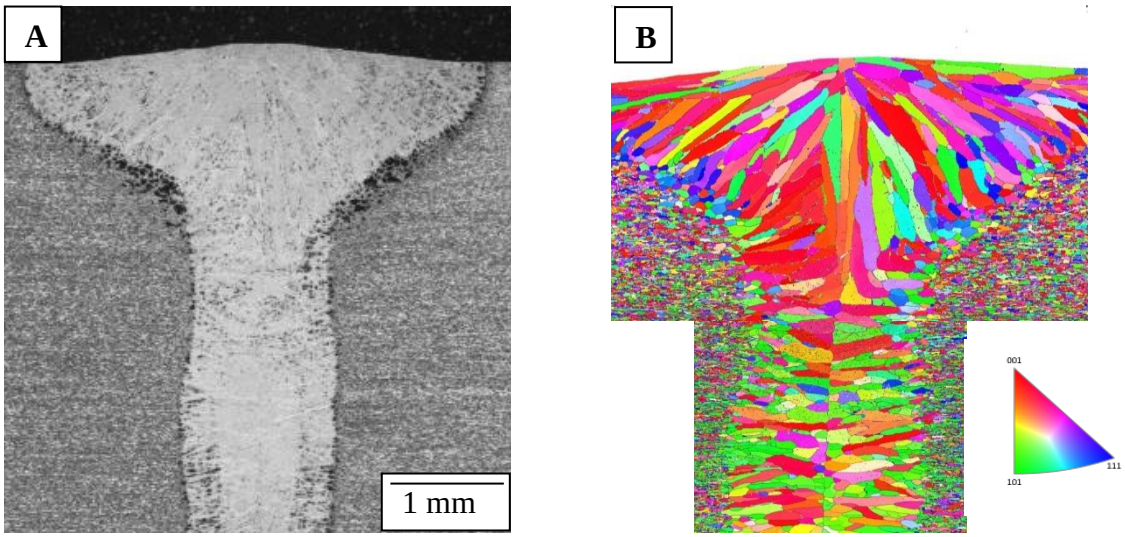

Figure 4.19: (A) Weld micrograph and (B) Crystal orientation map

The material solidifies primarily in the delta ferrite phase. The grains form from existing crystals (i.e. grains in parent material) and grow away from the heat sink, following the gradient from high to low thermal conductivity. In other terms, these columnar grains are growing from cold to hot area, and the growth rate is driven by the thermal gradient. The bigger the grain, the faster the cooling rate. The large columnar grains in the weld revealed by the EBSD imaging, in comparison with the grain size of the parent material, is evidence of the fast cooling rate of the laser welding process. The apparently smaller equiaxed grains visible in the middle of the weld are more certainly tips of columnar grains forming at an angle to the cross-section. Cross sections are 2D imaging of a 3D process.

4.4.5.2 Chemical composition

The micro-chemical composition of the phases present at the cap, waist, and root locations were determined by an EDX microprobe fitted to the scanning electron microscope (SEM). The resulting analysis of EDX at these locations and the parent material performed on γ-austenite and δ-ferrite islands are summarised in Table 4.7. The partition coefficient K is the amount of each element in the ferrite phase with respect to that in the austenite phase ([element weigh % in δ] / [element weigh % in γ]). Therefore, the ferrite stabilising elements should have a partition coefficient greater than one while austenite stabilising elements should have a coefficient lower than one. This elemental partition is clear for the parent material were the elemental distribution between ferrite and austenite had well developed according to the equilibrium conditions established during the manufacturing process (usually a solution annealing at 1050 °C). In the weld metal, on the contrary, the partitioning moved closer to unity, most likely because the fast cooling established previously hindered the

diffusion of the elements in solution. This is particularly true for chromium, nickel and molybdenum.

Table 4.7: Chemical analysis

	Phase	Si	Mo	Cr	Mn	Ni
Parent	γ	0.3	2.5	21.3	2.1	6.5
	δ	0.3	3.6	24.0	1.9	4.3
		K = 1	**K = 1.5**	**K = 1.1**	**K = 0.9**	**K = 0.7**
Single beam						
Single beam 0.5 mm from surface	γ	0.4	2.9	22.7	2.0	5.3
	δ	0.3	3.1	22.9	1.8	5.2
		K = 0.8	**K = 1**	**K = 1**	**K = 0.9**	**K = 1**
Single beam 3 mm from surface	γ	0.3	3.0	22.8	1.8	5.5
	δ	0.3	3.3	22.7	1.9	5.4
		K = 1	**K = 1.1**	**K = 1**	**K = 1.1**	**K = 1**
Single beam 5.5 mm from surface	γ	0.4	3.2	22.7	1.9	5.5
	δ	0.3	3.2	22.6	2.0	5.3
		K = 0.8	**K = 1**	**K = 1**	**K = 1**	**K = 1**

4.4.5.3 Design of Experiment

A qualitative approach was used to determine the process parameters (i.e. focal length of focusing lens, power, welding speed and focus position) to achieve a full penetration weld. In addition, a Design of Experiment approach was used to quantify the impact of changes in different weld parameters on the microstructure. Design of Experiment is a useful tool for optimising processes and has been extensively used in other fields [116].

A response surface methodology (RSM) was chosen to quantify the effect of welding speed and focus position on the resulting ferrite content in the weld. RSM purpose is to find via statistical software (in this case Design-Expert 8.0.7) a suitable approximation between the mentioned process parameter (input) and the resulting ferrite content at the weld (quantitative response).

Welding speed and focus position were varied in a controlled way relative to a set of core value (1.5 m/min;-2mm) and the ferrite percentages describing the ferrite volume fraction of the resulting welds at the cap, middle and root location were fed back into the Design-Expert 8.0.7 software as the responses.

As the power was limited to 4.5 kW (for future comparison with diffractive optic), the welding speed was varied from the minimum desired speed of 1 m/min and the speed of 2 m/min, close to the maximum value for full penetration at this power. Test points slightly out of these ranges were also tested for the robustness of predictive trend or model. The focus position was varied from -8 to +4 mm. The parameters tested are represented in Figure 4.20. The centre points are the core parameters, the axial points represent the extreme values (low and high) for each factor, and the factorial points are the variation of both factors at the same time compare to the centre points.

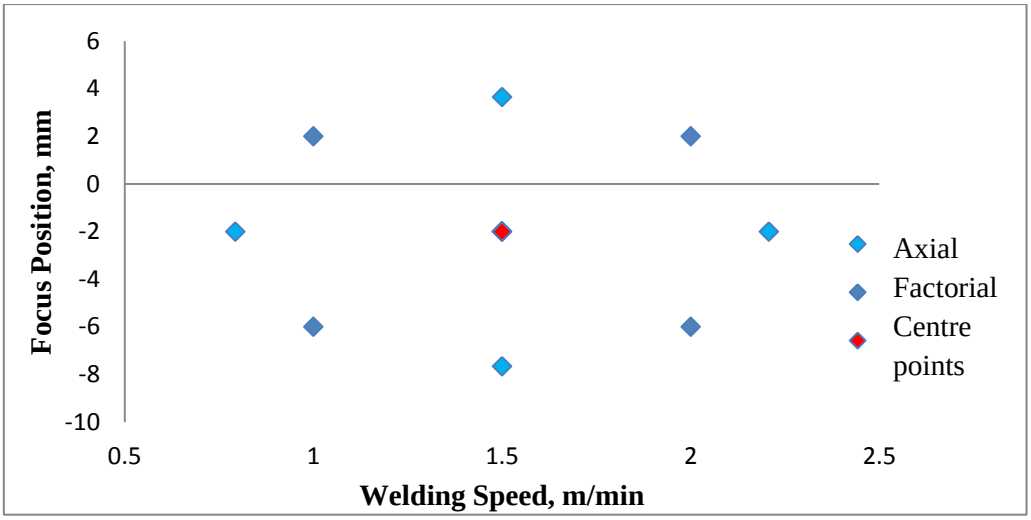

Figure 4.20: Cubic centred response surface test points

4.4.5.4 Phase balance results

Although several measurement techniques have been intended and compared (see Section 3.5.5), the phase balance was measured using point count as described in Section 3.5.5.1. Table 4.8 presents the test results including the percentage of ferrite at three locations: weld cap, waist and weld root.

Table 4.8: Design of Experiment: Process parameters and ferrite content

Process parameters		**Ferrite content (%)**				
Welding Speed (m/min)	Focus position (mm)	Cap	Waist	Root	Average ferrite at the 3 locations	Standard deviation of the 3 locations
0.8	-2	66.6 ± 4.4%	69.6 ± 3.6%	66.9 ± 3.5%	67.7 ± 3.8%	1.4
1	-6	67.9 ± 5.0%	75.0 ± 4.2%	73.6 ± 4.2%	72.2 ± 4.5%	3.1
1	2	67.4 ± 3.6%	69.8 ± 3.8%	72.2 ± 4.2%	69.8 ± 3.9%	2.0
1.5	-8	77.8 ± 3.7%	77.7 ± 4.0%	75.4 ± 5.0%	77.0 ± 4.2%	1.1
1.5	-2	75.4 ± 3.8%	81.6 ± 3.5%	67.1 ± 5.0%	74.7 ± 4.1%	5.9
1.5	-2	76.3 ± 4.5%	83.1 ± 3.0%	78.4 ± 3.8%	79.3 ± 3.8%	2.8
1.5	-2	79.4 ± 3.6%	84.0 ± 3.4%	76.8 ± 4.3%	80.1 ± 3.8%	3.0
1.5	4	73.8 ± 3.8%	84.8 ± 3.5%	86.1 ± 3.2%	81.6 ± 3.5%	5.5
2	-6	81.1 ± 3.8%	86.2 ± 3.1%	82.1 ± 4.9%	83.1 ± 3.9%	2.2
2	2	80.1 ± 4.1%	88.9± 2.6%	76.1 ± 4.6%	81.7 ± 3.8%	5.4
2.2	-2	82.1 ± 3.4%	85.1 ± 3.1%	74.3 ± 4.1%	80.5 ± 3.5%	4.6

4.4.5.5 Analysis

Design-Expert software gave a model of the process parameter impact on the ferrite content at the weld cap, waist and root. An analysis of the variance (i.e. ANOVA analysis) gave for each process parameter the value of "Prob<F". A value less than 0.05 indicates that the process parameter is significant while a value greater than 0.1 is considered to be negligible. It was found for each response (ferrite content at the cap, waist and root) that:

- The focus position is an insignificant factor ("Prob<F">0.33).
- The welding speed is a significant factor ("Prob<F"<0.0001).

This linear regression model was found to best fit the experimental ferrite content results with a 0.01% chance that the model can occur due to noise. The welding speed and ferrite content are linearly correlated with high welding speed leading to high ferrite content. Figure 4.21 shows the regression model with the 95% confidence level error interval (shown as the dotted lines) of welding speeds and the resulting ferrite content. This correlation is due to the decreasing heat input and therefore faster cooling rate as the welding speed increases. The same trend is highlighted in Figure 4.22 when plotting the heat input against the ferrite content at the three weld locations.

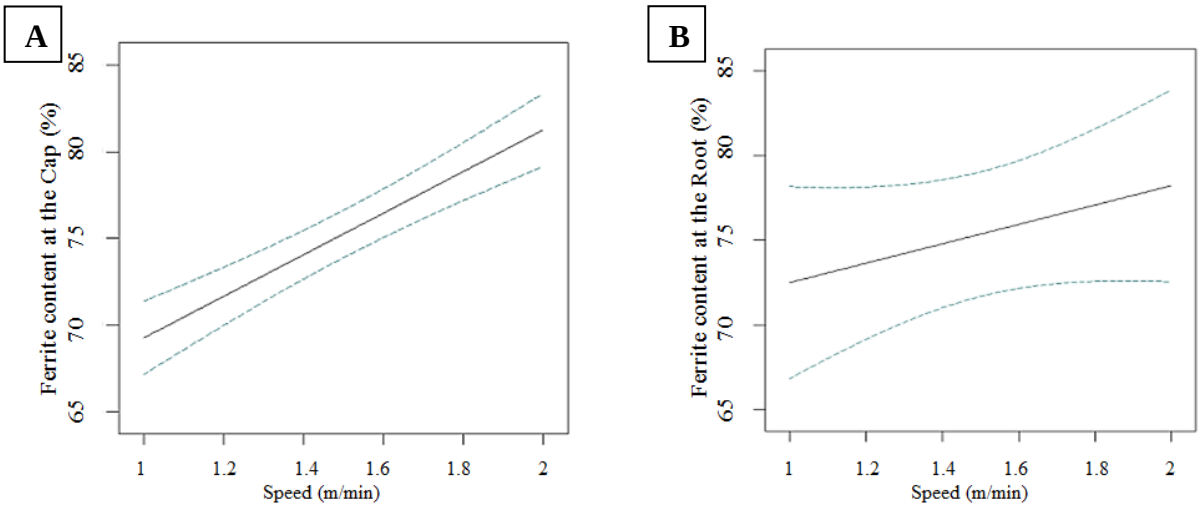

Figure 4.21: (A) Predicted ferrite content for weld cap and (B) for weld root

The same trend is highlighted in Figure 4.22 when plotting the heat input against the ferrite content at the three weld locations. Heat input is defined as the ratio between the power and the welding speed. As the power was fixed at 4.5 kW, the heat input and welding speed are entirely proportional. The errors bars are the attached incertitude of the ferrite phase measurements obtain with the point count technique.

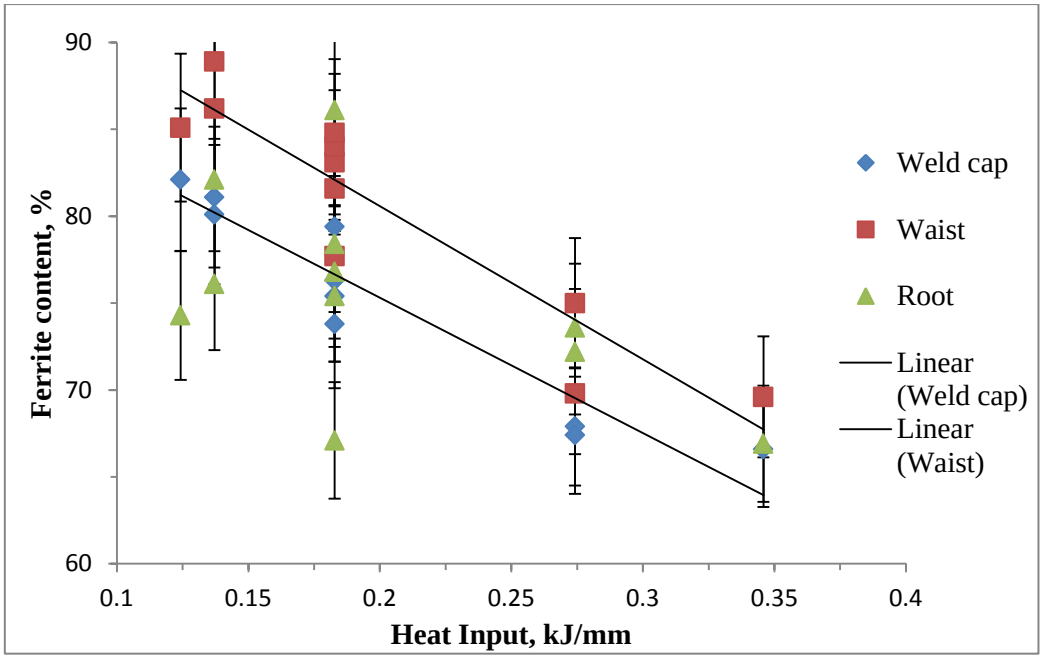

Figure 4.22: Heat input and phase balance

Finally, the ferrite content was found to be high, exceeding the upper allowed limit of 70% in most cases. The process window predicted for achieving ferrite content below 70% at the cap, middle and root is independent of the focus position (from -8 to +4 mm) but requires a welding speed below 0.5 m/min to increase the heat input.

4.4.6 Corrosion

ASTM A923 Test method C [107] was performed on selected coupons as described in Section 3.5.8. Parent metal and butt welds made either with argon or nitrogen shielding gas were tested. Butt welds were made at 4.5 kW at 1.25 m/min at -4 mm focus. The test method, consisting in measuring the weight loss of sample due to a 24h immersion into a ferric chloride solution (6% $FeCl_3$ per weight with a pH of 1.3), is validating or not the acceptance of the weld in term of corrosion resistance, i.e. tested sample shall not exceed 10 mdd (Milligrams per square Decimetre per Day). The test was carried on test samples as welded and prepared as it was observed that a substantial difference exists between the two. The standard recommends polishing the sample before the test down to a 120 grit for a better identification of pits as agreed by many laboratories performing similar corrosion test [117].

The results are presented in Table 4.9. For baseline comparison, the parent material was tested. It showed almost no weight loss (0.1 mg) nor any sign of initiated pit. This was expected due to the excellent corrosion resistance properties of the material. The butt weld shielded with nitrogen (at 4.5 kW, 1.25 m/min welding speed and -4 focus) passed the test with a tiny weight loss recorded. These welds had an average of 72% ferrite content at the cap and 67.5% at the root. The butt welds which used argon shielding gas failed the test with a 59.2 mdd corrosion rate recorded when the maximum permitted by the test is 10 mdd. Micrograph analysis showed that the cap microstructure of these samples were mostly ferritic with almost no austenite as shown in Figure 4.23 and 4.24. The average point count of ferrite

phase at the cap was 86.3% (see Table 4.1). Severe pitting crevices were also observed on the samples as depicted in Figure 4.25 and 4.26.

Table 4.9: Corrosion test of butt welded 6 mm grade 2205 DSS with autogenous single beam

Description	Specimen size (mm)	Surface area (cm^2)	weight loss (mg)	corrosion rate in (mdd)	corrosion rate in ($mm.y^{-1}$)
Parent material – no weld					
No preparation	48.7 × 24.9 × 6.0	33.06	0.4	1.21	5.60×10^{-3}
Polished on both side	49.3 × 27.8 × 5.8	36.35	0.1	0.27	1.28×10^{-3}
Polished on both side	51.2 × 25.4 × 5.7	34.74	0.1	0.29	1.34×10^{-3}
Single beam butt weld					
Samples polished on both side					
Nitrogen shielding	50.3 × 24.8 × 5.6	33.36	0.4	1.20	5.58×10^{-3}
Nitrogen shielding	52.1 × 26.2 × 5.6	36.07	0.5	1.39	6.45×10^{-3}
Argon shielding	51.8 × 23.6 × 5.7	33.05	19.6	59.31	2.76×10^{-1}
Argon shielding	52.1 × 26.1 × 5.6	35.95	21.3	59.24	2.75×10^{-1}

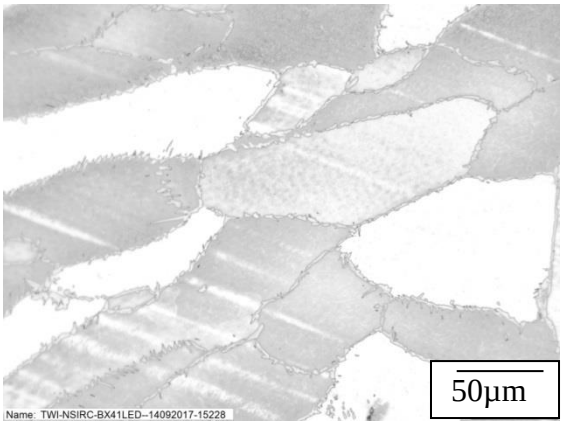

Figure 4. 23: Cap magnification 200×

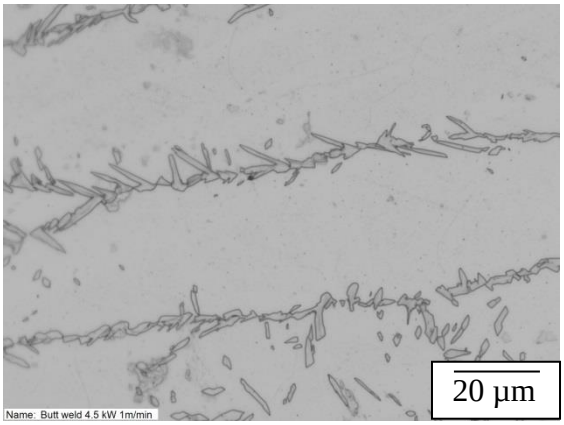

Figure 4.24: Cap magnification 500×

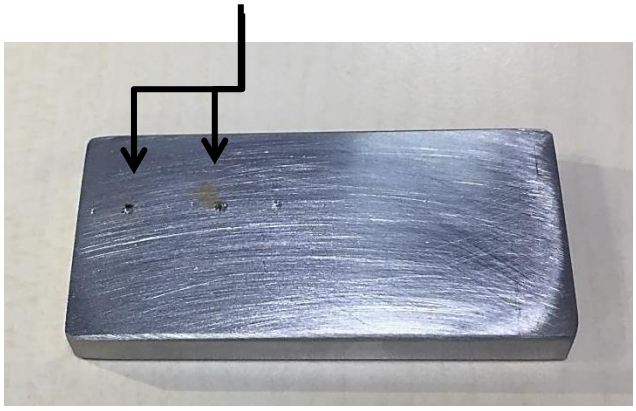

Figure 4.25: Sample showing pitting

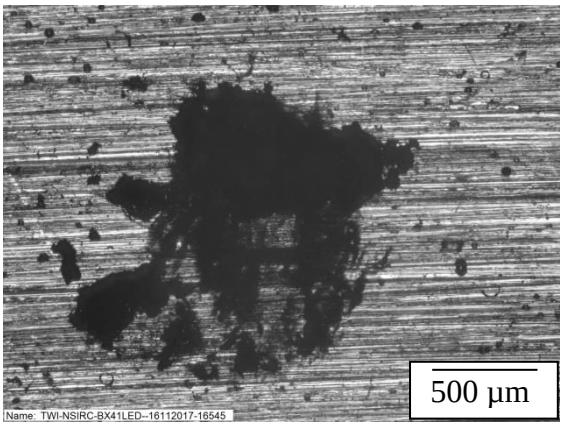

Figure 4.26: Pitting magnification 25×

4.5 Results and discussion of 3 mm plates experiments

4.5.1 Process window for full penetration

Based on previous work and experience carried at TWI on this material the core parameters developed for full penetration with an acceptable weld aspect ratio (minimum waist around 1 mm and maximum cap around 3 mm) had a processing power between 2 to 3.5 kW, welding speed between 1 to 1.5 m/min at focus position of -4 mm.

4.5.2 Weld profile

From visual observation, welding speeds from 1 to 1.5 m/min produced welds with a top bead (cap) of sufficient width, i.e. >2mm. Melt runs at 2 m/min welding speed resulted in narrow welds deemed unsuitable for most applications even though a full root penetration was achieved. Butt joints were successfully produced at 1 and 1.5 m/min. Cross-sectioned micrographs of weld made at 1 m/min show wide cap and full penetration, as it can be observed from Figure 4.27.

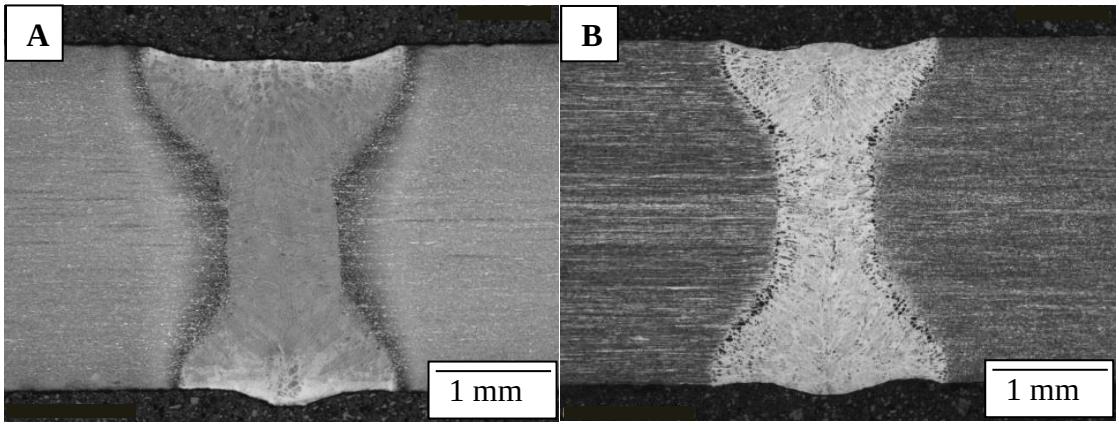

Figure 4.27: Butt welds at 1m/min with -4 mm focus and nitrogen gas shielding (A) at 2.5 kW and (B) 3.5 kW

The symmetrical weld about the axis of the laser beam also suggested a steady fluid flow during welding. The presented welds matched BS EN ISO 13919-1 criteria for stringent quality. The dimensions of the weld profiles are given in Table 4.10. All welds were made at a welding speed of 1m/min.

Table 4.10: Welds profile measurements for single beam welding of 3 mm plates

Weld Parameters			**Dimensions (mm)**		
Power (kW)	Focus position (mm)	Shielding gas	Cap	Waist	Root
2.5	-4	Ar	2.61	0.94	2.12
2.5	-4	N	2.40	0.95	2.00
2.5	+4	N	2.61	1.42	2.16
2.5	-4	N	2.19	0.96	1.89
3.5	-4	N	1.84	0.86	2.03

Focus position seems to influence the weld shape, a positive focus leading to a wider waist. Nevertheless, the dimensions of the weld shapes are similar for the cap and the root. Same process parameters show consistent results, suggesting a consistent and repeatable process.

No noticeable differences in the weld profile have been found when using argon over nitrogen.

4.5.3 Temperature measurement

4.5.3.1 Heat diffusion

The welding process established for 3 mm thickness plates had the same magnitude of heat input as with the 6 mm plates. A sharp transition in term of crystal structure between the parent material and the weld was also observed, as depicted in Figure 4.28.

A sharp transition of crystal structure (shape and size) between the parent material and the weld was observed, suggesting a relatively fast cooling time due to the low heat input. It also suggests that there was a very contained heat flow at the weld location.

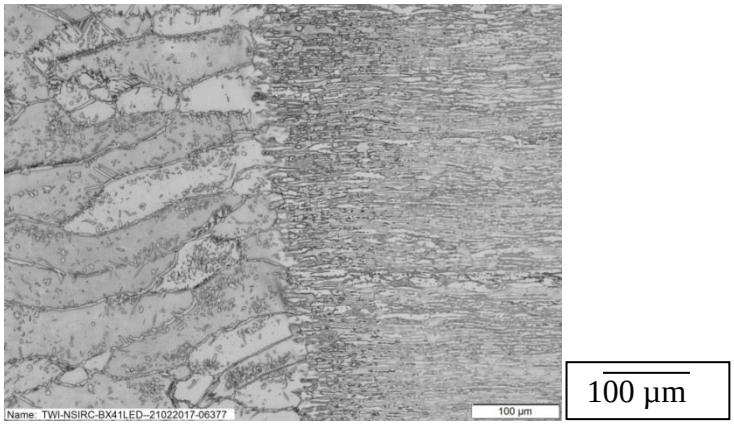

Figure 4.28: HAZ of a butt weld made at 2.5 kW, 1 m/min, -4 mm focus. 100× magnification

Thermocouples (type K) were also used to measure the temperature at the top and bottom of the weld. They were placed in the same way as the with 6 mm plates as described in subsection 4.4.4.1.The maximum temperature recorded varied from 200 to 300 ˚C depending on the thermocouple location. Figure 4.29 shows the thermocouples measurement for a weld made 3.5 kW at 1.5 m/min. Results are very similar to the one recorded for the 6 mm plate welded at 4.5kW at 1m/min, although the heat input here is almost half (140 J/mm for this weld against 270 J/mm for the weld on the 6 mm plate).This is probably because the 3 mm plates were smaller in size compared to the 6 mm plates, restricting the heat to a smaller volume. Nevertheless, all welded plates returned to a temperature below 100 ˚C in less than 5 minutes giving no chance for carbide precipitation or 450 ˚C embrittlement to happen.

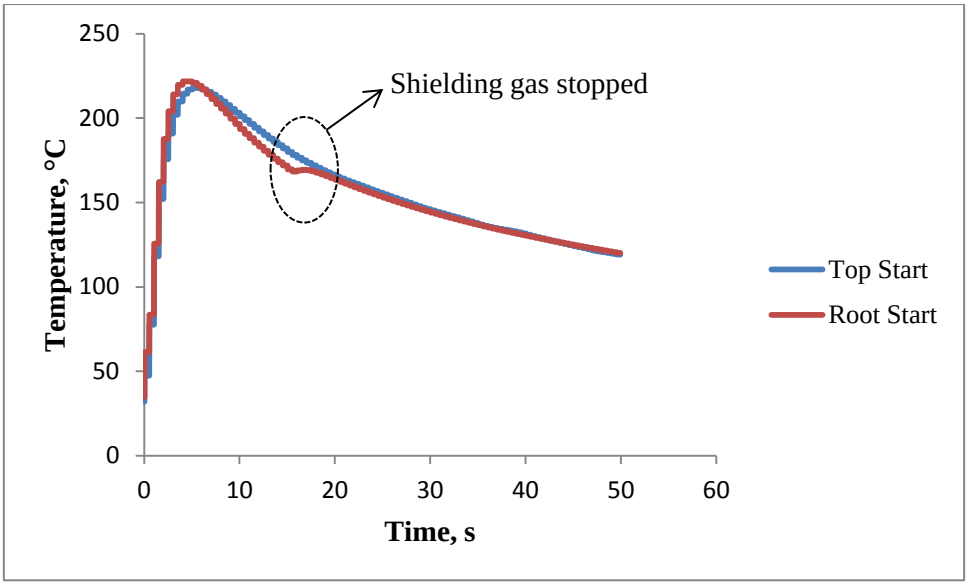

Figure 4.29: Thermocouple measurements for a weld at3.5kW, 1.5 m/min, -4 mm focus

4.5.3.2 Surface cooling rate

With the pyrometer surface temperature at the weld were recorded, usually in the middle of the melt run. Figure 4.30 shows the typical cool down for the weld performed at 1 m/min at -4 mm focus.

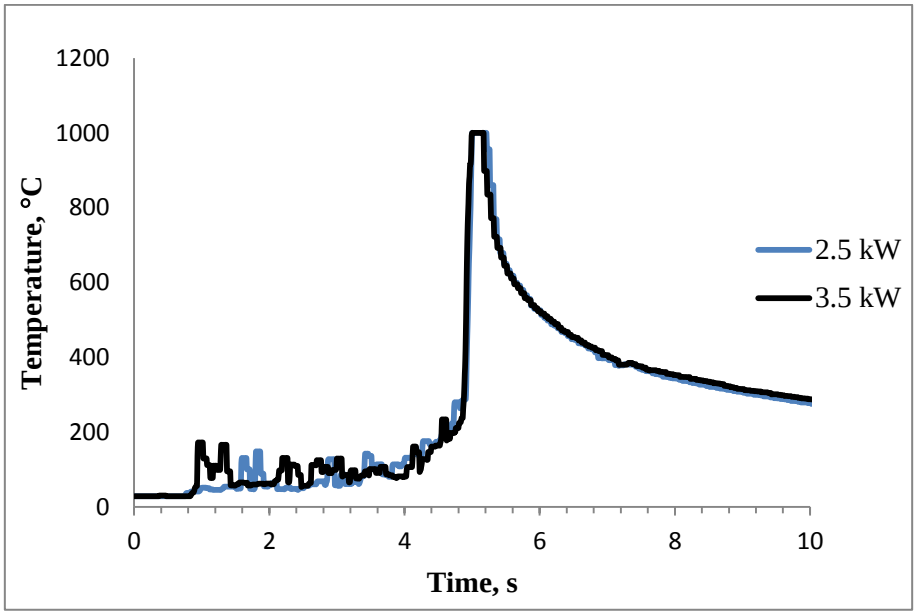

Figure 4.30: 3 mm surface cooling curves of butt welds made at 1 m/min, -4 mm focus

Higher power did not extend the cooldown significantly when compared to weld at lower power with the same welding speed. Heat input is the factor influencing the cooldown of the material, but welding speed seems to have a more predominant influence than the processing power. An averaging was done on four measurements for each welding speed (all at -4 mm focus position), and results are presented in Table 4.11. Heat input of 140-150 J/mm lead to similar cooling rate with the 3 and 6 mm thick plates.

Table 4.11: Averaged cooling rate of welded 3 mm grade 2205 DSS

Power (kW)	Welding speed (m/min)	Heat input (J/mm)	Time in the 1000 - 800˚C interval (s)	Cooling rate corresponding (˚C/s)
2.5	1	150	0.28 ± 0.05 s	800 ± 50
3.5	1	210	0.27 ± 0.05 s	750 ± 50
3.5	1.5	140	0.22 ± 0.05 s	900 ± 50

4.5.4 Heat input and resulting microstructure

4.5.4.1 Microstructure change

In Figure 4.31, as observed with 6 mm plate the same difference from the parent material and welded metal is noted. The parent material presents a balanced proportion of austenite grain in a ferritic matrix with a ferrite content of 45.3 ± 4.3% The austenite grains were slightly elongated in the direction of the cold rolling process that the metal underwent during its manufacturing. In the fusion zone, the proportion of phase is lost, and grain sizes are different. Larger ferrite grain can be observed along with the allotropomorph austenite formed at the grain boundaries as seen in Figure 4.31 B and Figure 4.32. The butt weld was made at 2.5 kW, 1 m/min and -4 mm focus position.

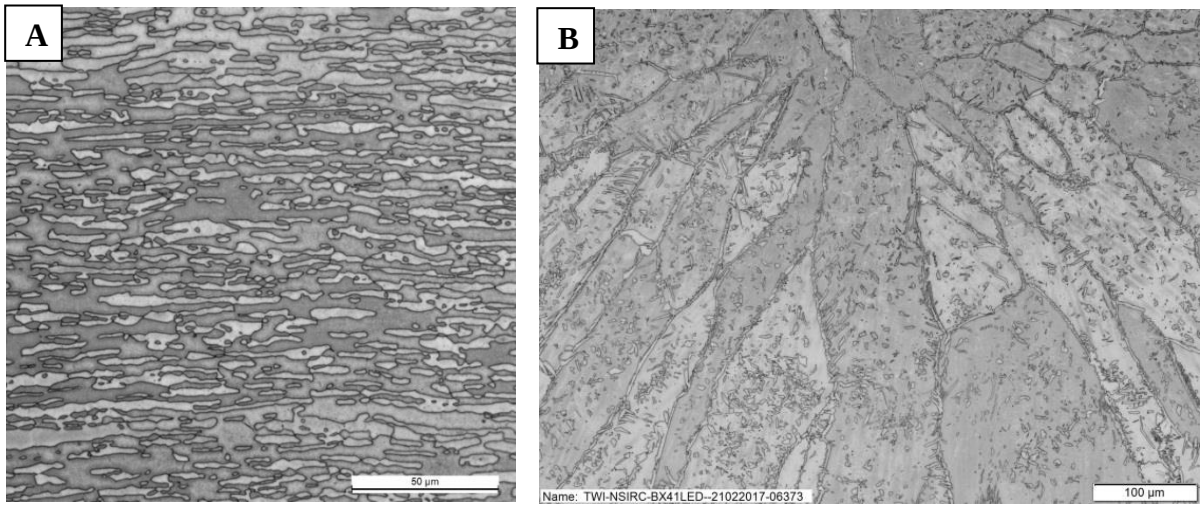

Figure 4.31: (A) Parent material at 200 × and (B) weld cap at 100 × magnification

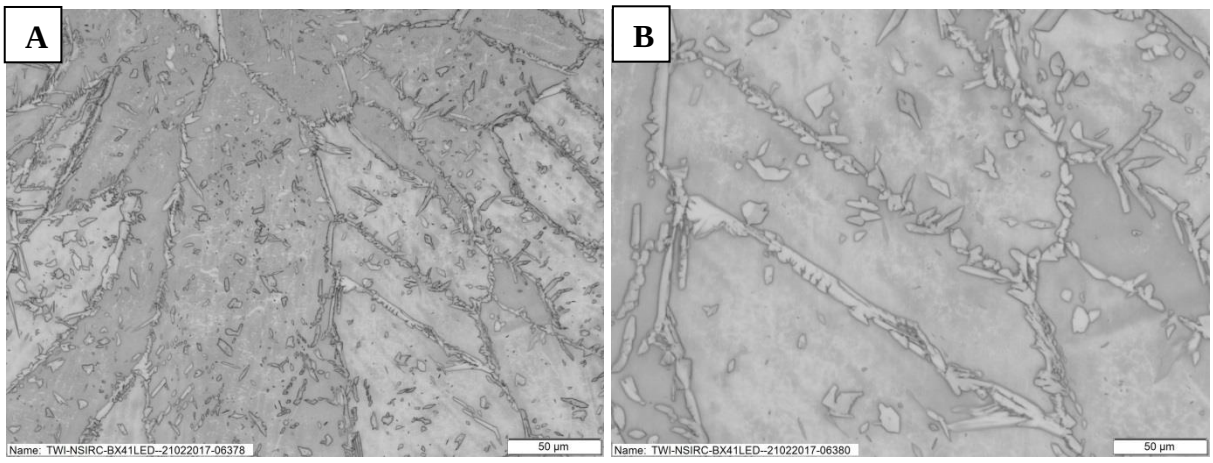

Figure 4.32: Weld Cap at (A) 200× and (B) 500× magnification

When looking closely at the cap, for instance, it can be seen that few acicular intragranular austenite precipitated within the ferrite. The lack or the low density of austenite within the ferrite grain can favour the detrimental chromium nitride precipitation. Nitrogen that has a low solubility in the ferrite phase has to diffuse over a greater distance before being absorbed by austenite.

4.5.4.2 Phase balance results

The cross-sectioned samples were point counted to determine the amount of ferrite and austenite phases in the microstructure. The results of point count are presented in Table 4.12. Ferrite volume fraction of the parent material was found to be 45.3 ± 4.3% with the point count technique (average of 4 different zones) and 43.8% with the Fischer™ Ferritescope. It was almost 10% lower than the 6 mm parent material. From this fact it was expected to obtain ferrite content at the weld with a ferrite volume fraction 10% lower than weld with 6 mm plate. This is the case if we consider that the heat input of 0.15 kJ/mm for the welding of 3 mm plates led to ferrite content around 70% when it led to ferrite content around 80% for the 6 mm plates.

Table 4.12: Ferrite content of welded 3 mm grade 2205 DSS with autogenous single beam

Parameters			Ferrite content (%)	
Weld type	Power (kW)	Focus position (mm)	Cap	Root
Butt weld	2.5	-4	73.0 ± 2.8%	75.0 ± 2.9%
Butt weld	3.5	-4	71.0 ± 3.1%	72.4 ± 3.0%
Melt run	2.5	-4	73.3 ± 3.3%	65.3 ± 4.5%
Melt run	2.5	-4	74.8 ± 4.5%	73.1 ± 4.6%
Melt run	2.5	-2	76.3 ± 3.4%	74.4 ± 4.5%
Melt run	3.5	-4	70.9 ± 4.3%	69.5 ± 3.7%
Melt run	3.5	-2	72.9 ± 2.8%	68.1 ± 4.9%

4.5.4.3 Chemical composition

The micro-chemical composition of the phases present at the cap (0.5 mm below the surface), waist (1.5 mm below the surface), and root locations (2.5 mm below the surface) were determined by an EDX microprobe fitted to the scanning electron microscope (SEM). The resulting analysis of EDX at these locations and the parent material performed on γ-austenite and δ-ferrite islands are summarised in Table 4.13 and graphically presented in Figure 4.33. Results are given in %weight with the partition coefficient K. The composition of ferrite and austenite phase in the parent material are presented in Figure 4.34. The values for the partition coefficients are consistent with data on the same and similar duplex grades [71].

As explained before in Section 4.4.5.2, the elemental partitioning in the parent material is observed with a higher content of nickel and manganese in the austenite phase (austenite stabiliser elements) and a higher content of chromium and molybdenum in ferrite phase (ferrite stabiliser elements). On the contrary, no substantial partition between ferrite-stabilising and austenite-stabilising elements occurred in the weld metal. This is due to the rapid cooldown of the weld established previously.

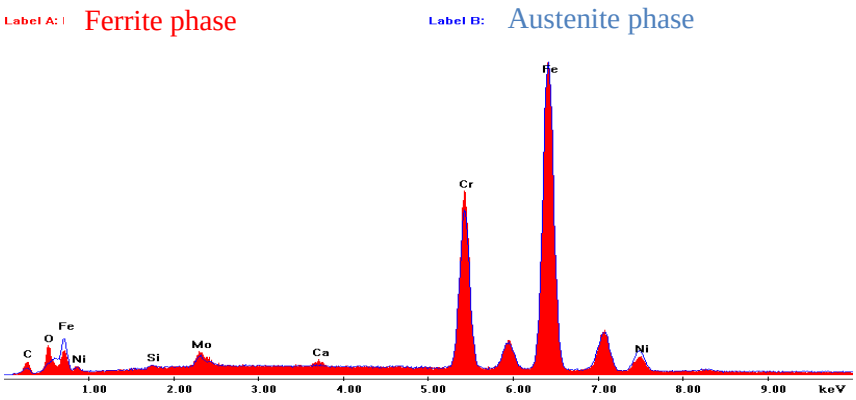

Figure 4.33: Ferrite-Austenite chemical composition

Table 4.13: Chemical analysis of a butt weld made a 2.5 kW, 1 m/min, -4 focus

	Phase	Si	Mo	Cr	Mn	Ni
Parent	γ	0.4	2.4	20.7	1.5	6.6
	δ	0.6	3.2	22.5	1.3	4.9
		K = 1.3	**K = 1.3**	**K = 1.1**	**K = 0.9**	**K = 0.7**
Single beam						
Single beam 0.5 mm from surface	γ	0.8	3.2	21.7	1.4	5.8
	δ	0.6	3.1	21.8	1.3	5.5
		K =0.8	**K = 1.0**	**K = 1.0**	**K = 1.0**	**K = 0.9**
Single beam1.5 mm from surface	γ	0.8	3.3	21.6	1.4	5.7
	δ	0.7	3.2	21.7	1.3	5.3
		K = 0.8	**K = 1.0**	**K = 1**	**K = 1.0**	**K =0.9**
Single beam 2.5 mm from surface	γ	0.8	3.3	21.7	1.3	5.6
	δ	0.6	3.1	21.8	1.3	5.3
		K = 0.8	**K = 0.9**	**K = 1.0**	**K = 1.0**	**K =0.9**

Ferrite and austenite phases do not differ much in composition because substitutional elements do not have time to partition significantly during welding. Nevertheless, a slight chromium depletion is noted in the δ ferrite phase present at the weld compared to the base metal.

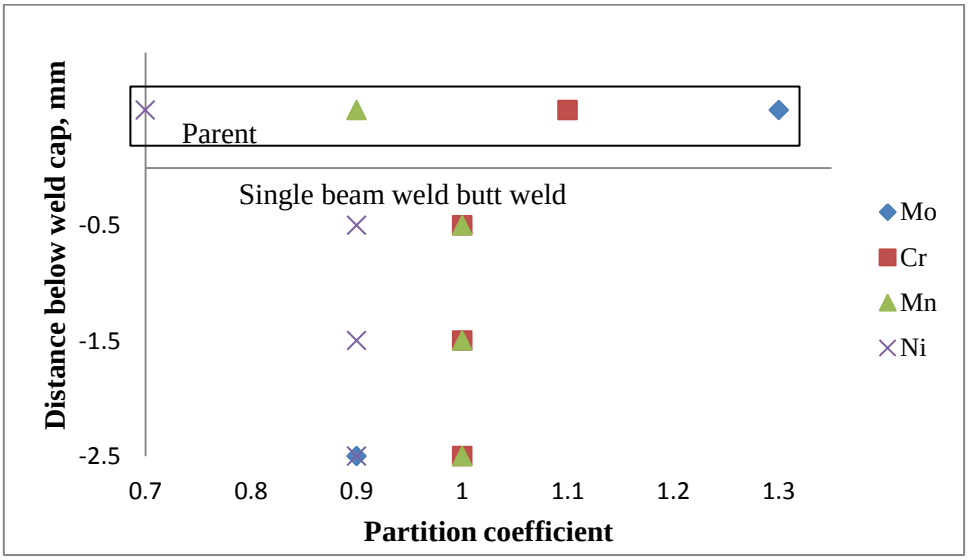

Figure 4.34: Chemical partition in parent material and single beam weld

4.5.5 Hardness

Changes in ferrite content and grain sizes usually translate to changes in hardness. Comparing with research elsewhere [28], [71], [118], [119] laser welded DSS tend to have an increased hardness at the weld location. Results obtained with the Vickers microhardness showed this trend and are presented in Table 4.14. A hardness limit in the fusion zone is sometimes recommended in the industry to provide a safe and conservative limit to mitigate against potential hydrogen embrittlement. Limit of around 350-380 HV is usually chosen [120],[121].

Table 4.14: Microhardness of single beam at 2.5 kW, 1 m/min, -4 mm focus

	Hardness (HV)		
Location	Cap	Waist	Root
Parent metal	264	-	265
Parent metal	286	-	260
Parent metal	288	-	253
HAZ	273	-	257
Fusion boundary	265	-	269
Weld metal	283	-	281
Weld metal	276	289	282
Centre weld metal	307	290	289
Weld metal	291	298	273
Weld metal	298	-	291
Fusion boundary	279	-	251
HAZ	285	-	268
Parent metal	257	-	267
Parent metal	269	-	254
Parent metal	248	-	255
Average parent	**Average cap**	**Average waist**	**Average root**
264 HV (std 12)	291 HV (std 11)	292 HV (std 4)	283 HV (std 6)

It was difficult to carry out the separate microhardness measurements for ferrite or austenite grains owing to the tiny size of the austenite grain.

4.5.6 Corrosion

The ASTM A923 Test method C was performed on selected samples as described in section 3.6.8. Parent metal and butt weld made at 2.5 kW at 1 m/min at -4 mm focus were tested. The results are presented in Table 4.15.

Table 4.15: Corrosion test of butt welded 3 mm grade 2205 DSS with autogenous single beam

Description	**Specimen size (mm)**	**Surface area (cm^2)**	**weight loss (mg)**	**corrosion rate in (mdd)**	**corrosion rate in ($mm.y^{-1}$)**
Parent material – no weld					
Polished on both side	50.5 × 25.9 × 2.7	30.28	0.1	0.33	1.54×10^{-3}
	52.0 × 27.7 × 2.8	32.72	0.1	0.31	1.42×10^{-3}
Single beam butt weld					
No preparation	50.7 × 26.1 × 3.0	31.07	9.4	30.25	1.41×10^{-1}
Polished on both side	50.9 × 26.0 × 2.5	30.31	1	3.30	1.53×10^{-2}
Polished on both side	50.6 × 26.1 × 2.6	30.40	0.5	1.64	7.65×10^{-3}

The parent material (sample without weld) experienced a quasi-null weight loss (0.1 mg). Unpolished welded sample was very close to the corrosion test threshold to fail (mdd >10). This is probably due to spatter or scale around the weld that dissolved during the test. Weld samples were also polished on both sides according to the standard to avoid this bias. They passed the corrosion test yet with an mdd value 5 to10 times superior to the parent material.

4.6 Concluding remarks

4.6.1 For the 6 mm plates single beam experiments

The beam profiles of the laser beam with different optics have been established: the power density is better described by a top-hat profile in the focal plan, but in the far field it approaches a Gaussian energy distribution. This power distribution must be considered when comparing two beams obtain with different optics at different focus position.

The shorter focal length optic of 200 mm was preferred to a 400 mm because of smaller spot size. Higher speed and lower power were possible for full weld penetration. Nevertheless, the process window for a full penetration weld is narrow. Power was fixed at 4.5 kW, and speeds were varied from 1 to 1.5 m/min. Nitrogen shielding gas was preferred to argon shielding gas to promote austenite and reduce the ferrite content.

Grade 2205 DSS is readily weldable as no crack or porosity was observed up to the magnification of 1000×, but autogenous Yb:fibre laser welding led to an excess of ferrite (> 70%) at the weld location. This was due to high cooling rates over 500 °C/s measured, leading to a fast cooling time of the material that hinder the formation of austenite. Nevertheless, the fast cooling time prevents detrimental precipitation.

The heat input (here, the welding speed) is the primary factor affecting the phase balance. Changing the focus position from -6 to +4 mm had no measurable impact on the phase balance.

4.6.2 For 3 mm plates single beam experiments

Butt joints of 3 mm thick plates were successfully welded at speed slower than 2 m/min at 2.25 kW. Bead-on-plate showed top and root bead around 2 mm width and free from the surface and internal defects.

No filler material was used in the current experiment, and welded samples show no undercut, blow hole or porosity. Nitrogen shielding gas was found to promote austenite formation in preference to Argon gas.

The ferrite content was over 65% at weld cap. Taking into account the 5% error and the 10% standard deviation (the degree to which the local measurement of ferrite content differ from the mean of the 32 measurements done within a sample) the ferrite content is exceeding this acceptable range of 30-70% of ferrite.

Chapter 5: Autogenous dual beam Yb:fibre laser welding of grade 2205 duplex stainless steel

5.1 Background

Previously investigated in Chapter 4 was the autogenous (without filler material) Yb:fibre laser welding process of grade 2205 duplex stainless steel. Two thicknesses of respectively 3 and 6 mm were investigated. Results showed that the high cooling rate, mostly influenced by the welding speed, hindered the growth of austenite and promoted a ferrite excess at the weld. Consequences of the high ferrite content were translated into a hardness increase at the weld and higher corrosion rate of the material. Nitrogen shielding was found to be advantageous over argon shielding to promote the growth of austenite and partly reduce the unwanted excess of ferrite. Acceptable process parameters in term of spot size, welding speed, processing power and focus position were established for both thicknesses.

In this chapter, a dual beam approach is proposed to influence the austenite formation at the weld and reduce the ferrite excess. Autogenous dual beam Yb:fibre laser welding process was developed for 3 mm thick grade 2205 DSS and intended for the 6 mm thick plates of the same grade. Section 5.2 reviews the overall experimental approach; Section 5.3 presents the results for 3 mm thick plates and Section 5.4 presents the results for the 6 mm thick plates.

5.2 Experimental programme

5.2.1 Approach

The core idea was to replicate the process parameters developed in the previous chapter with one welding head to make the weld, and a second welding head trailing the first one to provide a re-heating. The second welding head was in defocus position leading to a large spot size (mm order) with a lower power density than the welding beam. The second beam purpose was to decrease the material high cooling rate and influence the formation of austenite at the weld. The tilt angle of the second welding head was kept as low as possible (17° for all experiments) as laser beam with angles closer to the normal incidence presents a greater absorption coefficient.

For the 3 mm plates, a tailored energy distribution (i.e. separation between the two beams and power density of the second beam) was first developed based on observation from welds made with a single beam and a dual beam set up. The tailored energy distribution was tested on melt runs and actual butt welds with a thorough examination of one of the resulting weld. Positive results in term of the ferrite excess reduction lead to a set of experiments developed to optimise the dual beam welding parameters.

To deliver the laser power to the two welding heads, the beam splitter module described in Chapter 3 Section 3.3.2.3 was used, and therefore the maximum power possible to deliver per head was 2.5 kW. This was adequate to design tailored energy distributions for the dual beams welding of 3 mm plates, but it was a limitation for the dual beams welding of 6 mm plates since 2.5 kW is not enough to initiate a full penetrating weld. Dual beams welding trial were still intended on the 6 mm plates with both focused beams superposed. The distance

between the two beams was then iteratively augmented till the cut-off point for full penetration.

Temperature measurements were recorded during welding with the Impact pyrometer. Most of the samples were cross-sectioned for weld profile measurement and metallographic examination. The point count technique covered by ASTM E562 standard was used to measure the resulting phase balance at the weld location. ASTM A923 test method C was performed on selected samples to evaluate the corrosion resistance properties of the weld.

5.2.2 Equipment and material

In this chapter, the IPG YLS 5000 Yb:fibre laser was used. The beam splitter described in Section 3.3.2.3 was used to redirect two optical fibres having a 150 µm core diameter to two welding heads. As the set up could not hold the 100 mm FL collimator, the set of optics used in Chapter 4 were changed. Each head was equipped with an Optoskand 120 mm FL collimator and a 300 mm FL focusing lens. The resulting spot size diameter in the focal plan was therefore 375 µm. For the experiment on 6 mm plates, the six-axis Kawasaki robotic arm described in Section 3.4.6 was used. The initial experiments on 3 mm plates were carried with this robotic arm but the welds part of the design of experiment were carried and on the Aerotech three-axis table. The jigs, clamps, pyrometer used are the ones described in Section 3.4.6. Figure 5.1 shows the two welding heads mounted on the six-axis Kawasaki robotic arm.

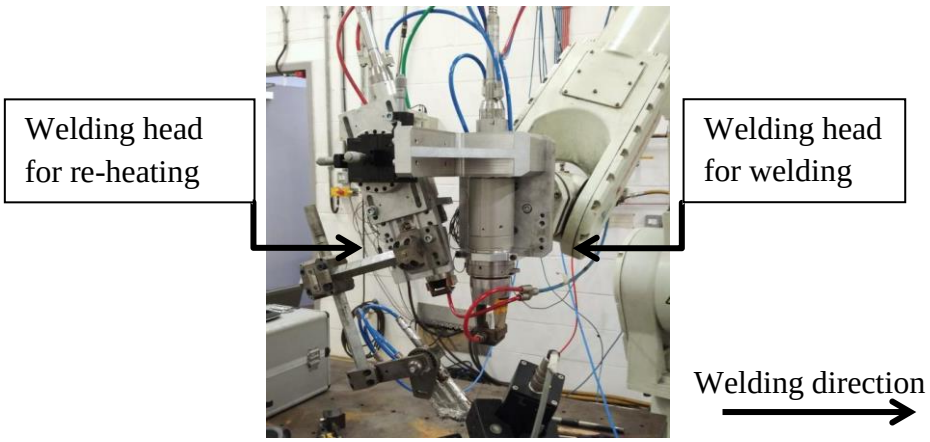

Figure 5.1: Dual beam set up

5.2.3 Experiments

Dual beam welding on 3 mm thickness plates consisted of a first evaluation of 11 melt runs to optimise the process parameters followed by a selection of four set of parameters transferred to butt weld. The effects on the weld of changing the separation and defocus position of the second beam were investigated.

Dual beam welding on 6 mm thickness plates consisted of a series of 15 melts runs. The power limitation of a maximum of 2.5 kW delivered by the welding head was a major impediment to initiate the keyhole. Both the welding and re-heating beam had to be very close to each other to achieve full penetrating weld, and the experiment focused on the effects of varying the separation between the beams.

5.3 Results and discussion of 3 mm plates experiments

5.3.1 Experimental trials

Welding speed was fixed for all experiments and was set as 1 m/min as a higher speed would have increased the cooling rate and ferrite content as it was established in Chapter 4. In addition, low welding speed is usually not desired for industries producing in large volume as it directly impacts the productivity. In the particular case of manufacturing the nuclear waste containers in the UK, the manufacturer Graham Engineering.Ltd is looking for a processing speed equal or above 1 m/min [122].

The focus position is given as the distance between the actual focus point and the material surface. The laser beam of the first spot stayed at a fixed - 4 mm focus; this choice was made to allow comparison with previous experiments.

A second beam was set in a defocus position (+ Z mm) at a nominal centre-to-centre distance *d* from the first beam as depicted in Figure 5.2.

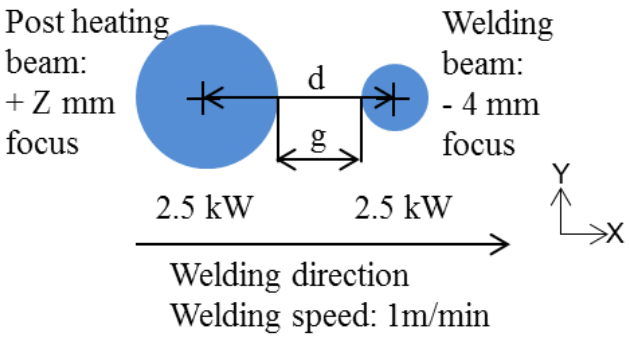

Figure 5.2: Parameters for dual beam welding

The core parameters for the second beam were chosen to have a gap distance *g* (as described in figure 5.2) in between the two beams equivalent to a 0.5 s time delay when welding at 1 m/min. From single beam pyrometer measurements, it was observed that the melt pool was staying around 0.3 s above 1000 ˚C before going back to this temperature. This was taking another 0.3 s for the material to cool down to 800 ˚C. Re-melting of the material (~ 1450 ˚C) is not desired as all the austenite will be transformed back to ferrite. On the other hand, an extension of the molten state of the material in the 1200 – 800 ˚C range is desirable for the austenite formation. The re-heating beam was then defocused at 145 mm position giving a nominal spot size of 9.3 mm to have a low power density around 15 W/mm^2 to avoid a re-melting of the material. The core parameters are summarised in table 5.1.

Table 5.1: Initial core parameters for dual beams welding trial

Parameters		**1st beam**		**2nd beam**		**Separation**		
Power (kW)	Welding speed (m/min)	defocus position (mm)	spot size (mm)	defocus position (mm)	spot size (mm)	d (mm)	g (mm)	Time delay between beam (s)
5	1	- 4	0.45	145	9.3	14	9.1	0.55

These core parameters were repeated three times to estimate the variance when using statistical analysis. From these core process parameters, the 2^{nd} spot variables (defocus position and distance separation *d*) were varied in a controlled way (symmetrical to each other). Figure 5.3 shows the parameters tested with the resulting welds profiles and Table 5.2 reviews in details the parameters tested. The statistical software Design-Expert 8.0.7 was then used to analyse the weld profile dimensions and the ferrite content data using a response surface methodology (RSM). RSM purpose is to find a suitable approximation of the relation between a quantitative response (in this case the weld dimensions and the ferrite content) and a set of input variable (in this case the process parameters).

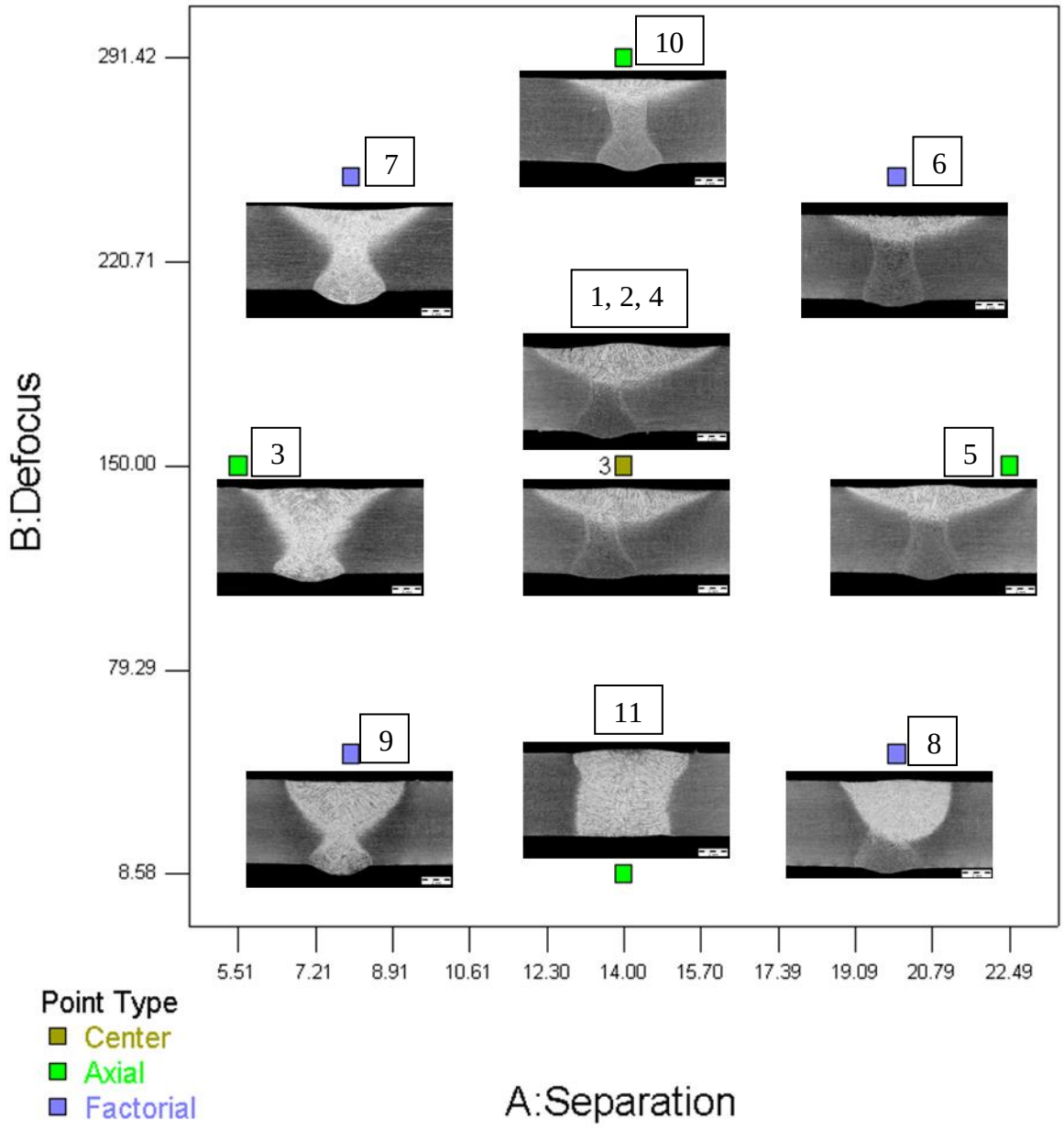

Figure 5.3: Design of experiment

Table 5.2: Details of parameters

Weld#	2nd head defocus position (mm)	2nd beam spot size (mm)	2nd beam Power density (W/mm^2)	Distance separation d (mm)	Gap between beam (mm)	Time delay between beam (s)
(1)	145	9.3	36.8	14	9.1	0.55
(2)	145	9.3	36.8	14	9.1	0.55
(3)	145	9.3	36.8	5.5	0.6	0.04
(4)	145	9.3	36.8	14	9.1	0.55
(5)	145	9.3	36.8	22.5	17.6	1.06
(6)	250	16	12.4	20	11.8	0.71
(7)	250	16	12.4	8	-0.2	-0.01
(8)	50	3.2	310.8	20	18.2	1.09
(9)	50	3.2	310.8	8	6.2	0.37
(10)	285	18.2	9.6	14	4.7	0.28
(11)	8.6	1	3183.1	14	13.3	0.80

5.4.2 First results

No welding defects or porosity were observed under radiograph and cross-section micrographs at 1000× magnification. This is partly due to the excellent crack resistance of the material and partly the welding conditions selected.

The top surface of the dual beam welded sample presented a surface free from oxidation with a smooth finish (Figure 5.4). Table 5.3 presents the weld's profile measurement.

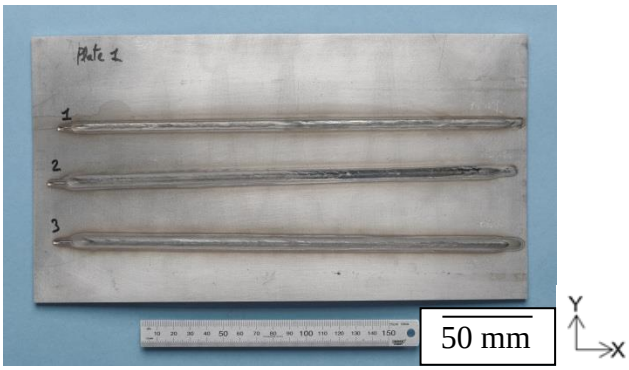

Figure 5.4: Top surface

Table 5.3: Welds profile measurements for dual beam welding of 3 mm plates

Weld#	Dimensions (mm)		
	Cap	Waist	Root
(1)	12.99	1.96	4.70
(2)	13.58	1.93	4.72
(3)	10.69	2.82	5.09
(4)	12.84	2.29	4.84
(5)	12.88	2.20	4.66
(6)	10.43	2.64	4.45
(7)	10.29	2.29	5.29
(8)	7.8	4.53	4.66
(9)	8.71	2.58	4.60
(10)	9.47	1.86	4.74
(11)	8.26	6.47	6.65

The dimension of the waist is not meaningful as the weld profiles differ significantly from each other and do not all present a glass-hour shape profile. Most importantly are the dimension of the cap and the root to consider the weld quality. All melt runs showed a root above 4.5 mm in length which is desirable as it shows that the full penetration is stable and not at the edge of an incomplete penetration. Dimensions of the root for all melt runs were very close to each other with a maximum gap of 2 mm and a standard deviation of 0.6 mm for the presented data. This suggests that the variation of parameters related to the re-heating beam had a limited impact on the root dimension. The cap dimensions were also large enough. Large weld caps are usually associated with lower residual stress than narrower caps. Here, the dimensions of the caps were varying significantly (maximum gap of 5.8 mm with a standard deviation of 2 mm). Compare to single beam weld profile (see Table 4.10 in Chapter 4), the cap and root dimension of dual beam welds were significantly larger.

Ferrite content at the cap, waist and root were measured for each weld and results are presented in Table 5.4. The ferrite content at the waist is only indicative as the different weld waists were too different in shapes and therefore not clearly delimited for point count.

Table 5.4: Ferrite measurements

Weld #	**Distance separation (mm)**	**Defocus position (mm)**	**Ferrite content (%)**		
			Cap	Waist	Root
(1)	14	145	60.5 ± 5.1%	54.1 ± 5.6%	45.6 ± 4.2%
(2)	14	145	60.5 ± 4.0%	57.1 ± 4.8%	48.4 ± 3.4%
(3)	5.5	145	50.5 ± 6.4%	56.5 ± 4.1%	50.3 ± 5.3%
(4)	14	145	57.9 ± 6.1%	55.4 ± 6.0%	44.5 ± 4.7%
(5)	22.5	145	62.8 ± 6.0%	53.6 ± 6.0%	49.3 ± 7.2%
(6)	20	250	65.5 ± 5.1%	55.9 ± 4.8%	53.5 ± 6.8%
(7)	8	250	64.1 ± 6.2%	58.8 ± 4.4%	54.5 ± 7.4%
(8)	20	50	72.1 ± 3.5%	54.9 ± 5.9%	51.9 ± 4.0%
(9)	8	50	57.5 ± 4.0%	60.6 ± 4.4%	55.4 ± 6.3%
(10)	14	285	65.5 ± 4.9%	59.5 ± 4.7%	56.4 ± 3.9%
(11)	14	(8.6) 15	49.5 ± 6.7%	55.8 ± 5.6%	54.8 ± 5.5%

Design-Expert software provided a model of the process parameter impact on the weld cap dimension and the ferrite content at the root. Analysis of the variance (ANOVA) was used to determine the statistical significance (F value) of individual terms and the most suitable regression model. For both analyses, no response transformation was needed to reduce the residual, and a reduced quadratic model was identified as the best regression in both cases. Table 5.5 and 5.6 detailed the terms and the statistical significance of the models. A model for the process parameters impact on the waist (dimension and ferrite) and root dimension were not meaningful for the reasons mentioned before. A model for the ferrite content at the cap would have been interesting, but the software could not identify a significant regression with an acceptable lack of fit for the set of data. This is probably because the ferrite contents were too scattered. Identifying the influence of the parameter for the weld cap dimension and the root ferrite content was nevertheless a good clue to extract refined process parameter for the second part of the trial.

Table 5.5: Reduced quadratic model for the cap dimension

Source	Sum of squares	Degree of freedom	Mean square	F value	Prob > F	Effect
Model	55.09	4	13.77	10.15	0.0077	Significant
A-Defocus	7.45×10^{-3}	1	7.45×10^{-3}	5.49×10^{-3}	0.9433	Not significant
B-Separation	0.29	1	0.29	0.21	0.6624	Not significant
AB	2.85	1	2.85	2.10	0.1975	Not significant
A^2	51.14	1	51.14	37.68	0.0009	Significant
Residual	8.14	6	1.36			
Lack of fit	7.86	4	1.97	13.87	0.0684	Not significant
Pure error	0.28	2	0.14			

The model F-value of 10.15 implies the model is significant. There is only 0.77% that the model could occur due to noise. Value of Prob >F less than 0.0500 indicates the model terms are significant and value greater than 0.1000 indicates the model terms are not. In this case, A^2 is a significant model term. The lack of fit value is not significant relative to the pure error. Non-significant lack of fit is good as it means the model fits the data well within errors.

Table 5.6: Reduce quadratic model for the ferrite root

Source	Sum of squares	Degree of freedom	Mean square	F value	Prob > F	Effect
Model	150.61	4	37.65	18.78	0.0015	Significant
A-Defocus	1.09	1	1.09	0.54	0.4884	Not significant
B-Separation	24.72	1	24.72	12.33	0.0127	Significant
A^2	141.96	1	141.96	70.81	0.0002	Significant
B^2	22.52	1	22.52	11.23	0.0154	Significant
Residual	12.03	6	2			
Lack of fit	3.94	4	0.99	0.24	0.8926	Not significant
Pure error	8.09	2	4.04			

The model F-value of 18.78 implies the model is significant. There is only a 0.15% chance that a model F-value this large could occur due to noise. The model terms B, A^2 and B^2 are significant.

Diagnostic checks were performed to ensure that the proposed model linking the process parameters to the resulting welds dimension or ferrite content was fixed and not random and meeting the ANOVA assumptions. For instance, externally studentized residuals were plotted for each weld and if the scatter of results about the axis was contained within the red bars (Figure 5.5 A and 5.6 A), this meant that no welds were found to have a higher degree of influence or leverage over the model. Externally studentized residual is a mathematical operation to identify an outlier, a data point whose response does not follow the general trend of the rest of the data.

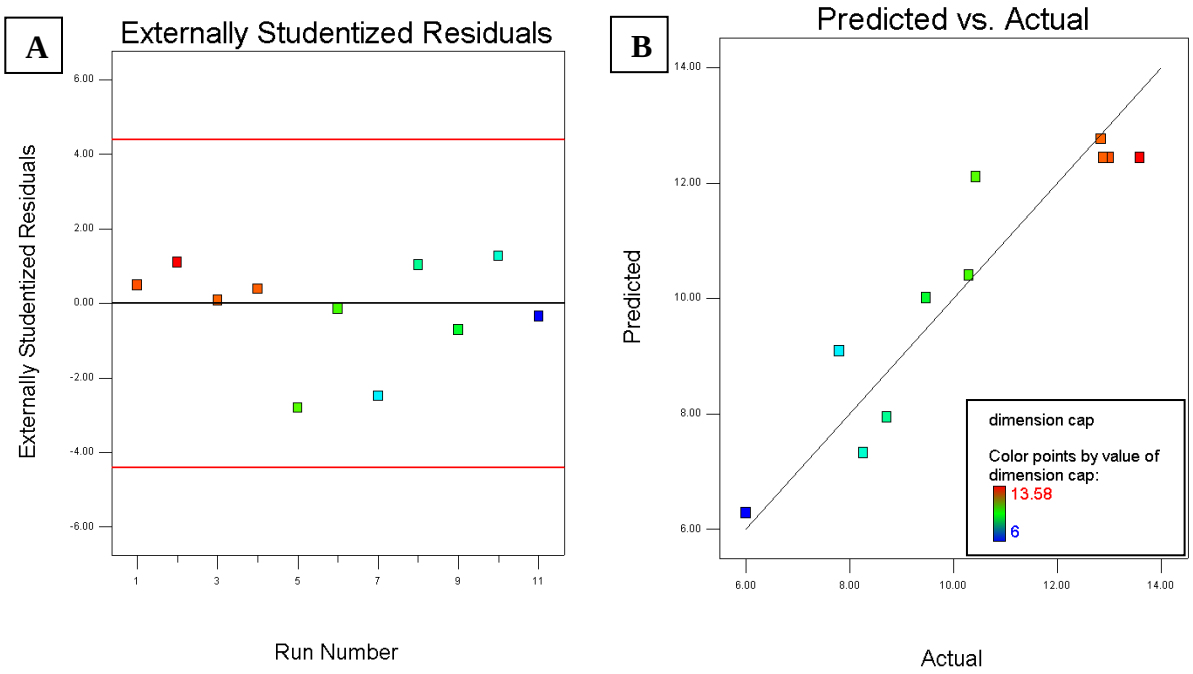

Figure 5.5: Plot for the cap dimension model of (A) externally studentized residuals and (B) Predicted Vs Actual

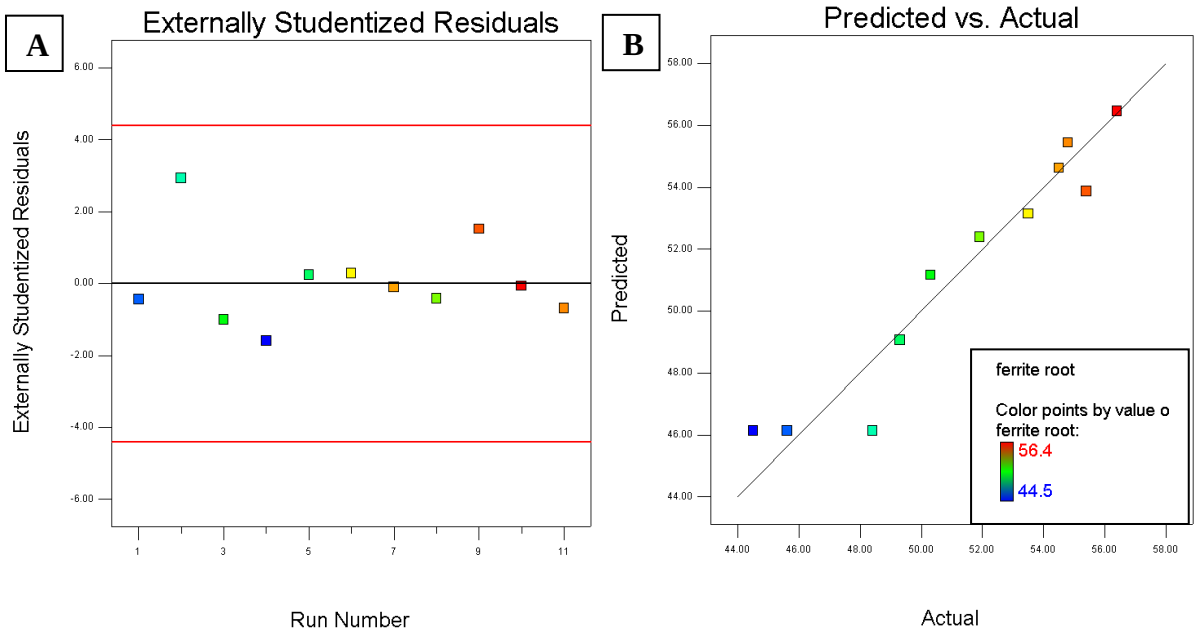

Figure 5.6: Plot of the ferrite content at the root model of (A) externally studentized residuals and (B) Predicted Vs Actual

Finally, the contour graph of the predicted value for the weld dimension and the ferrite content at the root are plotted and presented in Figure 5.7 and 5.8 respectively. To combine a large cap with low ferrite content at the root and avoiding the parameters that led to a high ferrite content at the cap the distance separation should be around 10 mm and the defocus position around + 130 mm.

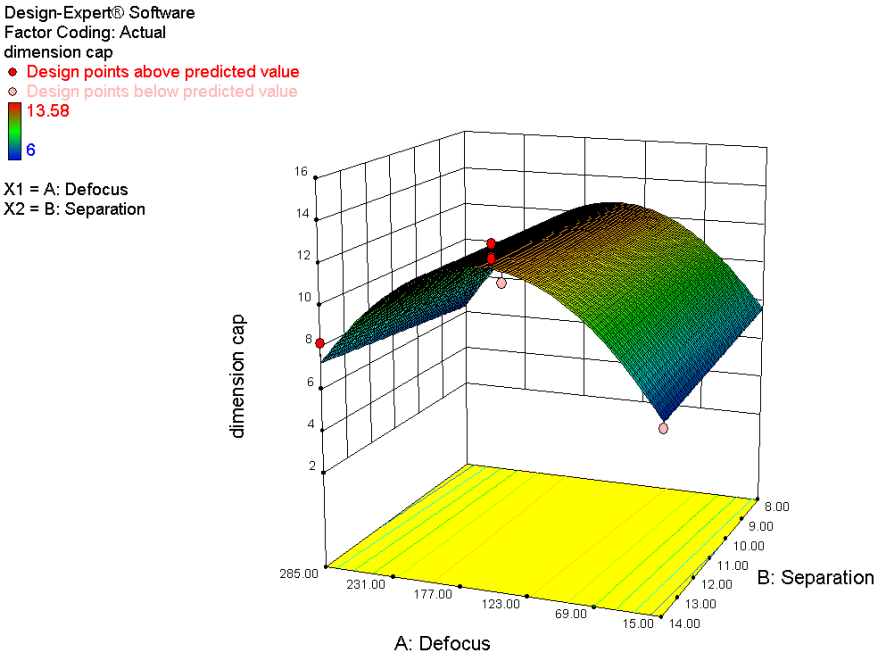

Figure 5.7: Contour graph of the process parameter effect on the weld cap dimension

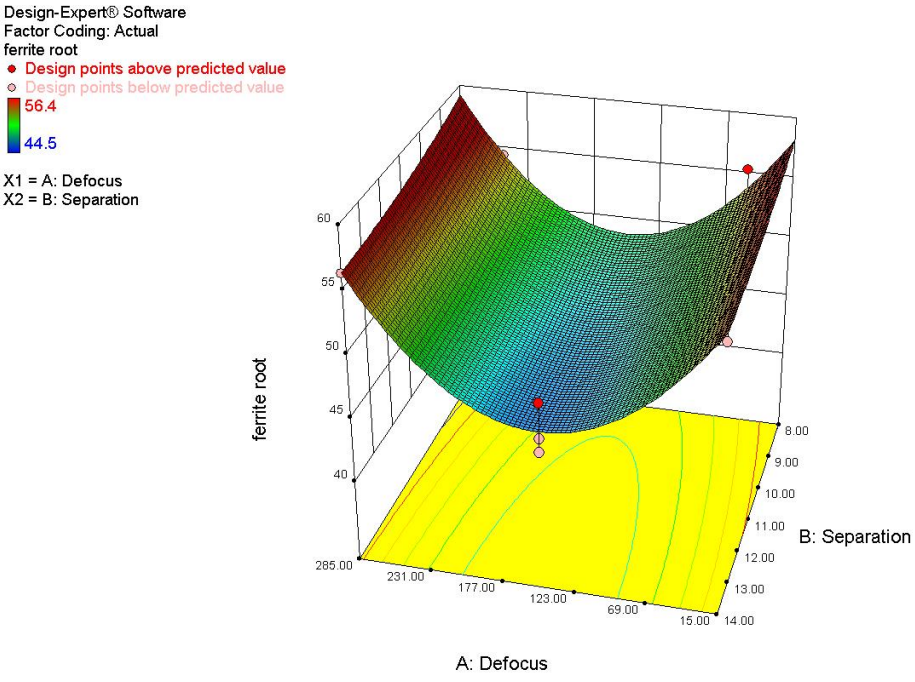

Figure 5.8: Contour graph of the process parameter effect on the weld root ferrite content

5.3.1 Selected parameters

The second beam focus was set at +93 mm or +125 mm defocus position, giving nominal spot sizes of respectively 6 and 8 mm in diameter. The nominal centre-to-centre distance *d* between the beams (see Figure 5.2) ranged from 8 to 11 mm. Table 5.7 summarises the spot size resulting from different focus positions.

Table 5.7: Details of parameters selected for dual beam welding

Weld#	2nd head defocus position (mm)	2nd beam spot size (mm)	2nd beam Power density (W/mm^2)	Distance separation *d* (mm)	Gap *g* between beam (mm)	Time delay between beam (s)
16B	93	6	88.4	8	4.8	0.29
17B	93	6	88.4	10	6.8	0.41
20B	125	8	49.7	9	4.8	0.29
21B	125	8	49.7	11	6.8	0.41

Selected parameters for weld 21B (2nd beam at +125 mm focus position with a separation distance d of 11 mm) were tested at different power (total power). Figure 5.9 shows the cross sections of the melt run carried at 4.5 and 2.5 kW. Table 5.8 shows the resulting weld dimension and ferrite content at the different location:

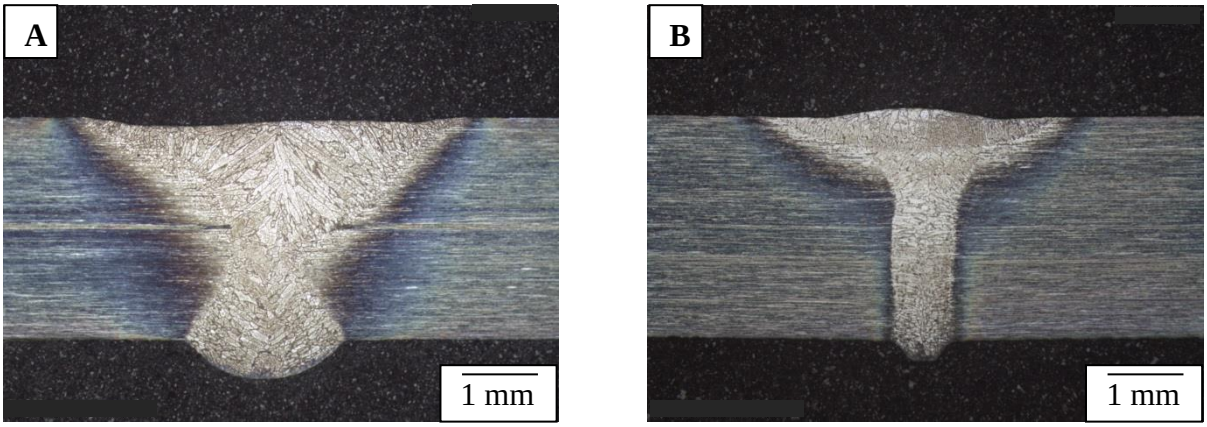

Figure 5.9: (A) BOP1 with a total power of 4.5 kW and (B) BOP5 with a total power of 2.5 kW

Table 5.8: Core parameters with different power

Weld		Dimension (mm)			Ferrite content (%)		
#	Power	Cap	Waist	Root	Cap	Waist	Root
BOP1	4.5 kW	5.20	2.03	2.12	57.4 ± 6.0%	56.9 ± 4.8%	54.6 ± 5.2%
BOP2	4 kW	4.96	1.59	1.90	63.3 ± 3.5%	60.8 ± 5.6%	54.9 ± 6.1%
BOP3	3.5 kW	4.77	1.29	1.80	66.5 ± 3.7%	60.1 ± 5.0%	55.5 ± 5.1%
BOP4	3 kW	4.60	1.10	1.47	67.0 ± 5.6%	62.6 ± 5.3%	55.0 ± 4.7%
BOP5	2.5 kW	4.19	0.89	0.85	73.9 ± 4.6%	60.5 ± 5.4%	62.8 ± 4.5%

The maximum undercut observed at the cap was 0.14 mm, and the maximum root excess (sagging) was 0.55 mm.

As power decreases, weld cap, waist and root dimensions shrink. Below a total power of 2 kW (1 kW × 2), full penetration was not achieved. At 2.5 kW (1.25 kW × 2), the root was too narrow (< 1 mm) which is not desirable for industrial applications such as nuclear waste

containers. Indeed, slight variations of the process parameters producing narrow roots can cause a lack of penetration and would be rejected as defective.

Single beam welding of 2.5 kW previously developed gave acceptable weld profile and therefore the total power was set at 5 kW (2.5 kW × 2), for all dual beam experiments. The welding parameters presented in Table 5.7 were then carried out to produce butt weld. Results are presented in the following sections.

5.3.2 Weld profile

Dual beam welds were compared to a single beam butt weld. A difference in weld profile can be noticed, as shown in Table 5.9. The attached measurements are presented in Table 5.10.

Table 5.9: Micrograph of single beam and dual beam welds

E9W2 - Single beam butt weld	**21 - Dual beam BOP**	**21B - Dual beam butt weld**
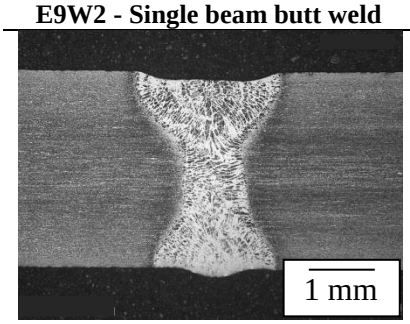	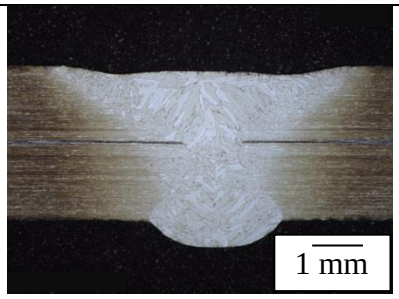	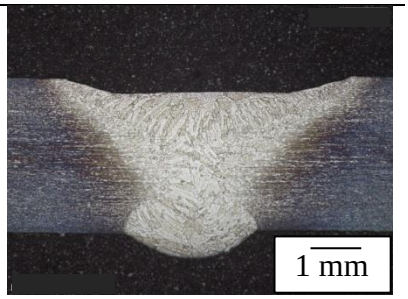
2.5kW, 1 m/min, -4 focus	2 x 2.5 kW, 1 m/min, -4 & +125mm focus, d 11mm	2 x 2.5 kW, 1 m/min, -4 & +125mm focus, d 11mm
16B - Dual beam butt weld	**17B - Dual beam butt weld**	**20B - Dual beam butt weld**
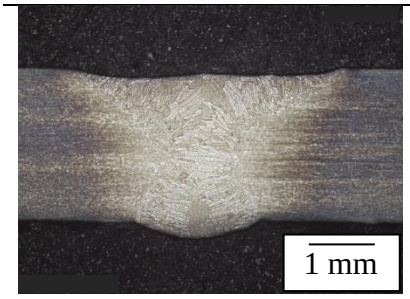	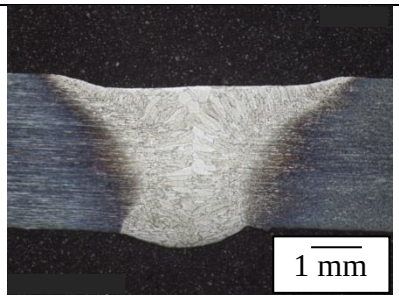	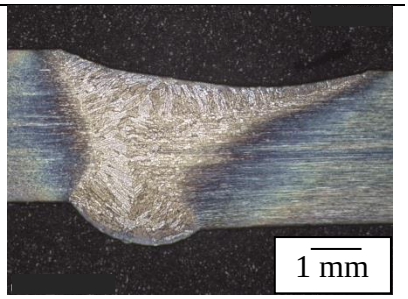
2.5kW, 1 m/min, -4 & +93 mm focus, d 8mm	2 x 2.5 kW, 1 m/min, -4 & +93 mm focus, d 10 mm	2 x 2.5 kW, 1 m/min, -4 & +93mm focus, d 9 mm

Table 5.10: Weld profile measurements of single beam and dual beam welds

weld	**Dimensions (mm)**				
	Cap	Undercut	Waist	Root	Root excess
E9W2	2.19	0.14	0.96	1.89	0.13
16B	6	0.80	5.30	1.93	0.15
17B	6	0.10	5.86	2.44	0.22
20B	8	0.90	6.11	2.26	0.47
21	5.53	0.14	2.31	2.55	0.52
21B	6.13	0.29	2.74	2.52	0.51

Bead on plate weld profile (weld 21) is similar to butt-weld profile (weld 21B) apart for a slightly larger top (+ 0.6 mm), probably due to the micrometric gap between the two butt-

welded plates that also widen slightly (+ 0.4 mm) the waist of the butt-welded sample. Dual beam 20B exhibit a slight mismatch default due to incorrect fitting. Single beam weld profiles are characterised by an hourglass shape, and in case of dual beam welding, the post-heating beam dramatically changes the shape of the weld, especially from the cap to the waist, making it looks like a V–shape. In the example taken, with dual beam approach, the cap and waist were almost three times larger and the root 75% larger when compared to a single beam.

5.3.3 Temperature measurement

Temperature change during welding of butt weld 21B was recorded with the parameter and compared with single beam welding measurement. Results are plotted in Figure 5.10.

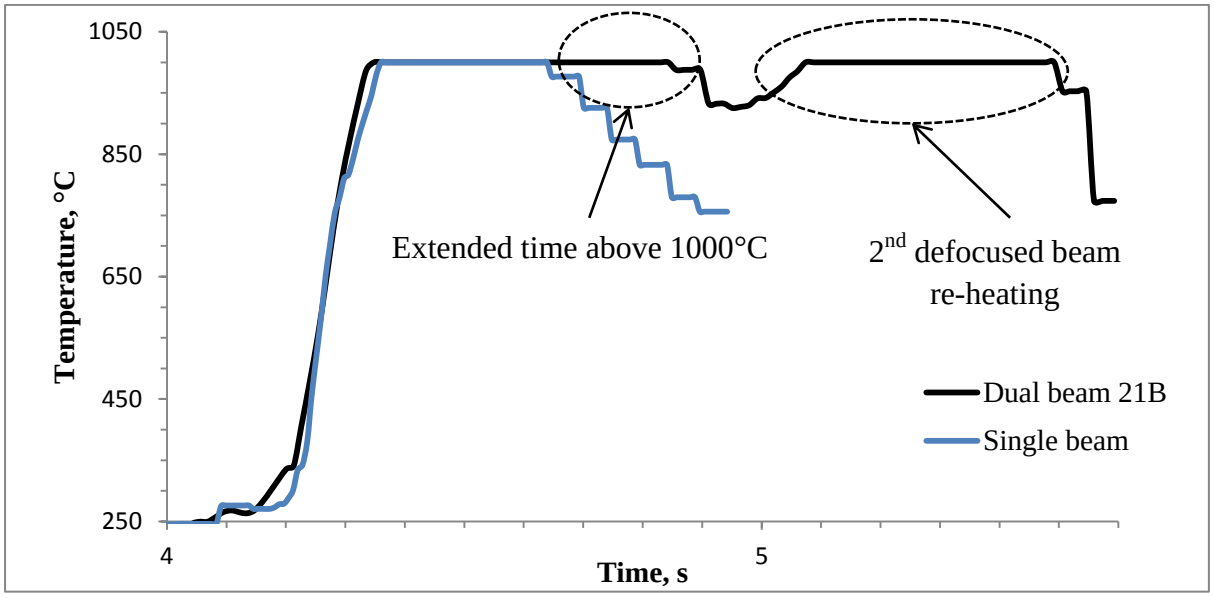

Figure 5.10: Single beam vs dual beam surface cool down

The material surrounding the weld pool is warmer due to the re-heating beam, explaining the extended time at which the molten material remains at a temperature above 1000 °C when compared to single beam welding. Table 5.11 presents the average cooling rate of 5 measured single beam welding (butt weld or melt run) made at 2.5kW at 1m/min at -4 mm focus and compared to dual beam welding. The cooling rate of dual beam welding was measured from the last temperature above 1000 ˚C generated by the first beam to the first temperature below 800 ˚C generated by the second beam.

Table 5.11: cooling rate

Weld	1st beam Power	2nd beam	Time in the 1000 -800˚C interval (s)	Cooling rate corresponding (˚C/s)
Average of 5 single beam	2.5 kW	-	0.28 ± 0.01	750 ± 50
21B dual beam	2.5	2.5 kW at +125 mm focus	0.82 ± 0.01	350 ± 50

5.3.4 Microstructure and phase balance results

Optical micrograph observed from 50 to 200× magnifications revealed a microstructure made of large ferrite grain with orientation following roughly the heat flow. Most of the austenite content appears to form in allotriomorphs mode at the prior-ferrite grain boundaries. These austenite grain boundaries are visibly thicker with dual beam compared to single beam welding (Figure 5.11). Widmanstätten growing from the allotriomorphs into the grain can also be observed in addition to intergranular austenite (Figure 5.12). A qualitative predominance of these intragranular austenite precipitates can be noted in the dual beam welded samples compared to single beam sample.

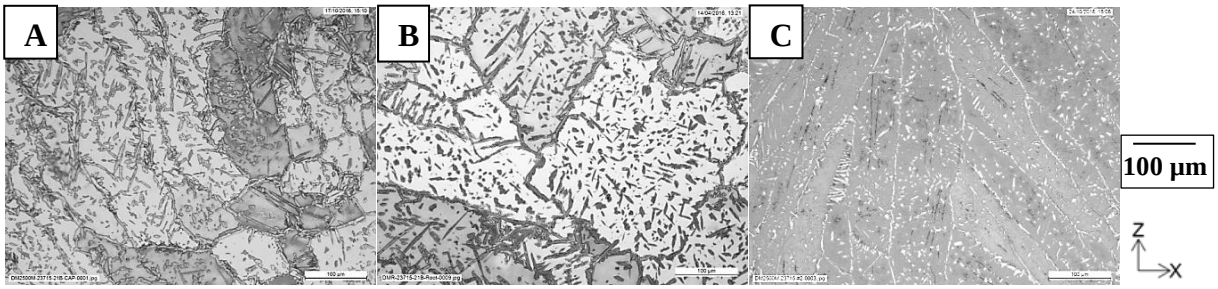

Figure 5.11: (A) Weld cap and (B) root of dual beam butt weld 21B compared to (C) cap of single beam weld E9W2 at 100× magnification

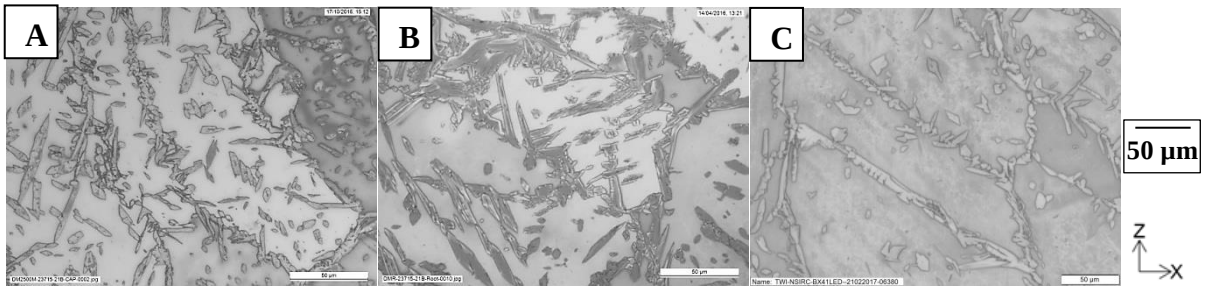

Figure 5.12: (A) Weld cap and (B) root of dual beam butt weld 21B compared to (C) cap of single beam weld E9W2 at 500× magnification

These observations are corroborated by quantitative ferrite measurements presented in Table 5.12. The ferrite content seems to be constant along the vertical direction of the weld (Z-axis). Welds ferrite content obtained with single beam (2.5 kW, 1 m/min) were averaged.

Table 5.12: Ferrite measurements

Weld	Type	2nd beam spot size (mm)	Gap (mm)	Cap	Waist	Root	Average
Average	Single beam	-	-	74.4 ± 3.5%	-	72.0 ± 4.1 %	
16B	Dual beam butt weld	6	5	63.9 ± 4.6%	62.0 ± 5.9%	58.5 ± 5.7%	61.5 ± 5.4%
17B	Dual beam butt weld	6	7	65.4 ± 4.0%	68.6 ± 3.8%	61.6 ± 4.3%	65.2 ± 4.0%
20B	Dual beam butt weld	8	5	58.8 ± 6.8%	60.0 ± 5.3%	59.3 ± 5.9%	59.4 ± 6.0%
21	Dual beam BOP	8	7	57.3 ± 5.3%	61.8 ± 5.7%	59.1 ± 6.8%	59.4 ± 5.9%
21B	Dual beam butt weld	8	7	58.8 ± 4.0%	67.9 ± 4.8%	61.3 ± 4.7%	62.7 ± 4.5%

These results can be correlated with the extended cooldown of the material observed with dual beam process. A reduction of the ferrite excess is observed when compared to single beam welding. The phase balance was around 60% with the dual beam technique when compared to 70% with a single beam. Nevertheless, the variation of parameters for the presented butt weld with dual beam technique seems to have no impact on the phase balance (i.e. phase balance results for 16B butt weld are similar to 21B butt weld). More significant variation of the defocus position and separation between the beams were then tested in Section 5.4 to have clearer and wider picture of the process, but first, a more in-depth analysis of the chemical composition changes between the phases of butt weld 21 along with a hardness test were carried.

5.3.5 Chemical composition

The micro-chemical composition of the phases present at the cap (0.5 mm below the surface), waist (1.5 mm below the surface), and root locations (2.5 mm below the surface) were determined by an EDX microprobe fitted to the scanning electron microscope (SEM). The resulting analysis of EDX at these locations and the parent material performed on γ-austenite and δ-ferrite islands are summarised in Table 5.13 and graphically presented in Figure 5.13. Results are given in %weight with the coefficient partition K.

Table 5.13: Chemical comparison by phase in mass %

	Phase	**Si**	**Mo**	**Cr**	**Mn**	**Ni**
Parent	γ	0.4	2.4	20.7	1.5	6.6
	δ	0.6	3.2	22.5	1.3	4.9
		K = 1.3	**K = 1.3**	**K = 1.1**	**K = 0.9**	**K = 0.7**
Dual beam						
Dual beam 0.5 mm from surface	γ	0.5	2.8	21.6	1.4	5.9
	δ	0.5	3.0	22.0	1.3	5.5
		K = 1.0	**K = 1.1**	**K = 1.0**	**K = 0.9**	**K = 0.9**
Dual beam 1.5 mm from surface	γ	0.5	3.0	21.9	1.4	6.3
	δ	0.4	2.9	22.3	1.3	5.2
		K = 0.8	**K = 1.0**	**K = 1.0**	**K = 0.9**	**K = 0.8**
Dual beam 2.5 mm from surface	γ	0.5	2.9	21.7	1.4	6.2
	δ	0.5	3.0	21.9	1.3	5.5
		K = 1.0	**K = 1.0**	**K = 1.0**	**K = 0.9**	**K = 0.9**

As explained before in Section 4.4.5.2, the elemental partitioning in the parent material is observed with a higher content of nickel and manganese in the austenite phase (austenite stabiliser elements) and a higher content of chromium and molybdenum in ferrite phase (ferrite stabiliser elements). For single beam laser welding, the rapid cooldown established in the previous chapter let no time for substantial partition between ferrite-stabilising and austenite-stabilising elements to occur in the weld metal. No substantial partitioning was observed either with the dual beam process although the partitioning coefficient for Si and Mn element stayed closer to the one of the parent material when compared to the single beam process.

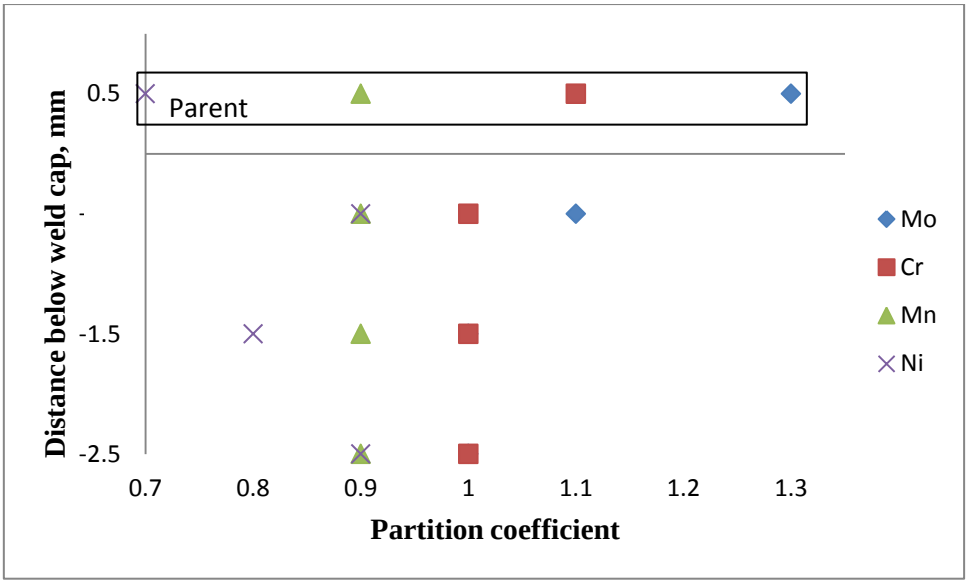

Figure 5.13: Chemical partition in parent material and butt weld 21B

5.3.6 Hardness

Changes in ferrite content and grain sizes usually translate to changes in hardness. Comparing with research elsewhere [28], [71], [118], [119] laser welded DSS tend to have an increased hardness at the weld location. Results obtained with the Vickers microhardness showed this trend, but a smaller increase in hardness can be noted for the dual beam process when compared to a single beam.

Table 5.14: Hardness result

	Hardness (HV)		
Location	Cap	Waist	Root
Parent metal	**258**	-	**268**
Parent metal	**255**	-	**278**
Parent metal	**268**	-	**268**
HAZ	**261**	-	**272**
Fusion boundary	**253**	-	**267**
Weld metal	**286**	-	**262**
Weld metal	**273**	**292**	**267**
Centre weld metal	**290**	**268**	**251**
Weld metal	**269**	**284**	**261**
Weld metal	**285**	-	**262**
Fusion boundary	**264**	-	**264**
HAZ	**264**	-	**278**
Parent metal	**260**	-	**281**
Parent metal	**268**	-	**275**
Parent metal	**264**	-	**267**
Average Weld	**Average cap**	**Average waist**	**Average root**
Dual beam: 274 HV Parent: 267 HV (std 7)	281HV (std 8)	281V (std 10)	260 HV (std 5)
Single beam: 288 HV Parent: 264 HV (std 12)	291 HV (std 11)	292 HV (std 4)	283 HV (std 6)

5.3.7 Corrosion

Results are presented in Table 5.15. For baseline comparison, the parent material, free of welds, was tested. Then, the samples of dual beam welding were tested. 21B butt-weld sample was first tested without preparation but presence of scale and spatter incursions around the weld contributed to weight loss and failed the tests. The sample was then retested with a prior polishing of the cap and root. Both butt welds (single and dual beam) qualify, but it is interesting to note that dual beam welded sample resulted in a corrosion rate equal to the one of the parent material while single beam welded sample's corrosion rate was five to ten times higher. Another important factor to consider is the size of the exposed weld area. Dual beam welded sample, with a cap almost three times larger than the single beam welded sample should have been more prone to corrosion if the two samples had the same ferrite balance or the dual beam welded sample, with a corrosion rate ten times lower compared with a single beam (prepared samples) account for a net improvement of the phase balance.

Table 5.15: Corrosion test of welded 3 mm grade 2205 DSS with dual beam

Description	Specimen size (mm)	Surface area (cm^2)	weight loss (mg)	corrosion rate in (mdd)	corrosion rate in ($mm.y^{-1}$)
Parent material – no weld					
Polished on both side	50.5 × 25.9 × 2.7	30.28	0.1	0.33	1.54×10^{-3}
Polished on both side	52.0 × 27.7 × 2.8	32.72	0.1	0.31	1.42×10^{-3}
Dual beam butt weld					
21B no preparation	50.5 × 27.0 × 3.0	29.70	4.5	14.10	6.56×10^{-2}
21B polished on both side	50.4 × 25.5 × 2.5	29.43	0.1	0.34	1.58×10^{-3}
21B polished on both side	47.9 × 27.0 ×2.6	29.76	0.1	0.34	1.56×10^{-3}
Dual beam melt runs					
E15P1W2 (1)	55.5 × 24.6 × 2.9	31.95	0.1	0.31	1.46×10^{-3}
E15P1W3 (2)	55.0 × 26.9 × 2.8	34.18	0.1	0.59	2.72×10^{-3}
E15P2W4 (3)	49.7 × 26.1 × 2.9	30.34	0.1	0.33	1.53×10^{-3}
E15P2W5 (4)	49.9 × 24.5 × 2.9	28.94	0.1	0.35	1.61×10^{-3}
E15P2W6 (5)	50.4 × 26.9 × 2.9	31.60	0.1	0.32	1.47×10^{-3}
E15P3W8 (6)	55.5 × 25.1 × 2.9	32.54	0.1	0.31	1.43×10^{-3}
E15P3W9 (7)	55.6 × 26.8 × 2.8	34.42	0.1	0.29	1.35×10^{-3}
E15P4W10 (8)	55.3 × 24.3 × 2.9	31.49	0.1	0.32	1.48×10^{-3}
E15P4W11 (9)	54.2 × 27.3 × 2.9	34.32	0.1	0.29	1.35×10^{-3}
E15P4W13 (10)	52.2 × 27.7 × 2.8	33.39	0.1	0.30	1.39×10^{-3}
E15P5W14 (11)	51.7 × 27.7 × 2.9	33.25	0.1	0.30	1.40×10^{-3}

5.4 Results and discussion of 6 mm plates experiments

After setting up the dual beam system, the focus position and distance from the first beam were varied until full penetration was achieved. Once found, the distance between the two beams was iteratively augmented till the cut-off point for full penetration. The next step was to defocus the second beam as much as possible within this separation interval.

5.5.1 Process window for full penetration

Power and welding speed were fixed during all the experiment. The beam splitter used provided a 50:50 power split thus the maximum power, 5 kW, was used.

Welding speed was set as 1 m/min as lower speed was not desired and higher speed would have reduced the cooldown and the chance to obtain full penetration. Dual beam welding at higher speed was not tested as it was already hard to achieve full penetration at 1 m/min.

The laser beam of the first spot stayed at a fixed -4 mm focus, choice having been made in the previous experiment. The second beam focus was either +26 mm or –4 mm leading to nominal spot size diameters of 1.7 and 0.45 mm, respectively. A significant positive defocus position results in a larger spot size at the surface, heating a wider area, and this was believed to be beneficial for extending the cooldown of the whole melt pool. Focusing inside the material was nevertheless used to obtain full penetration of the material.

Table 5.16 highlights the parameters that lead to a full penetration of the 6 mm plate.

Table 5.16: Parameters for full penetration

Run	Distance separation (mm)	Focus position of the 2nd beam (mm)	Penetration
E10W1	2	+26	NONE
E10W2	0 (overlap)	+26	NONE
E10W3	0 (overlap)	+26	NONE
E10W4	0 (overlap)	+26	NONE
E10W5	**0 (overlap)**	**-4**	**FULL**
E10W6	**1.2**	**-4**	**FULL**
E10W7	2	-4	PARTIAL
E10W8	**1.8**	**-4**	**FULL**
E10W9	**1.6**	**-4**	**FULL**
E10W10	**1.6**	**-4**	**FULL**

The highly defocussed beam (+26 mm) had not enough power density to help to achieve full penetration, even when overlapping the -4 mm focus beam (454 µm spot size at the material interface). When both beams were close to focus position (-4 mm), the power density was high enough to achieve full penetration, and then the maximum separation distance was found to be 1.8 mm. With this set-up, the keyhole was stable as the full penetration was consistent.

5.5.2 Cracking, porosity and weld quality

No welding defects or porosity were observed under radiograph and cross-section micrographs at 1000× magnification. This is partly due to the good crack resistance of the material and partly the welding conditions selected. X-ray analyses were done at 100 kV with an exposure time of 2 min as described in Section 3.6.2; a sample is given in Figure 5.14. Note that the dual beam technique resulted in heavy spatters, as seen in Figure 5.15.

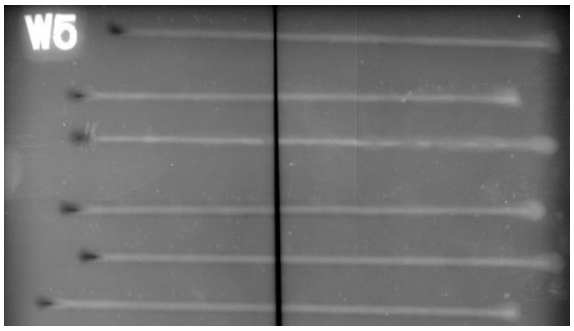

Figure 5.14: X-ray of dual beam welds

Figure 5.15: Heavy spatter caused by dual beam

The excessive spatter observed can be a cause of standard rejection according to BS EN ISO 17637:2016 [123].

5.5.3 Weld profile

Cross-sectioned weld were measured and compared to single welding beam process. Figure 5.16 shows (A) a typical single beam weld and (B) and (C) the resulting welds profiles made with the dual beam process. Cap, waist and root of the dual beam welds are significantly larger when compared to single beam weld. Measurements of dual beam welds profiles are presented in Figure 5.17.

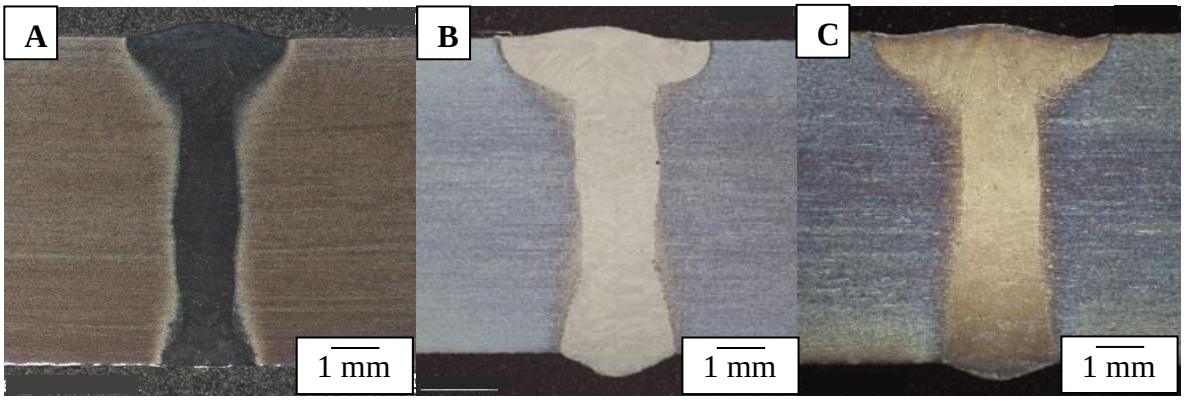

Figure 5.16: (A) Single beam at 4.5 kW, 1 m/min, 1 mm focus (B) Dual beam overlap and (C) Dual beam with 1.8 mm separation *d*

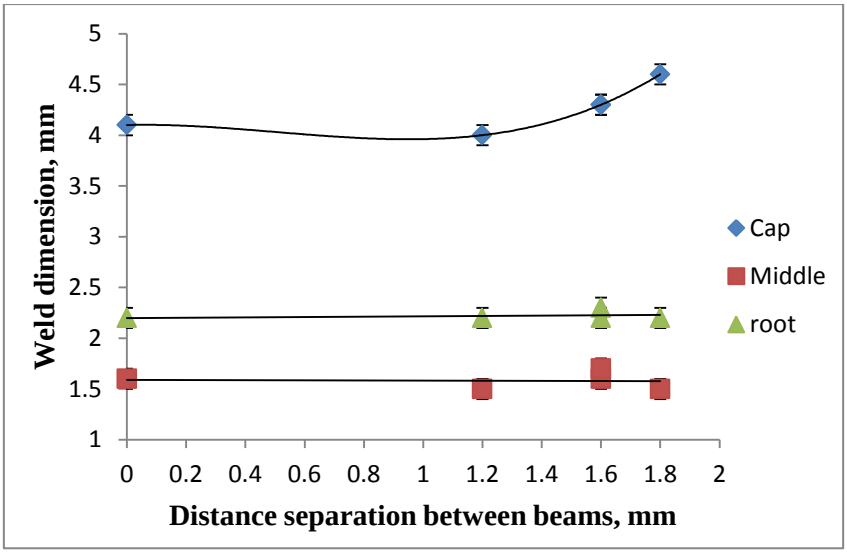

Figure 5.17: Distance separation influence on weld profile (measurements and linear regression)

It can be seen that distance separation between beams does not influence the root and waist profile. On the contrary, the greater the distance separation *d*, the wider the top bead (cap). For fully penetrating welds, top bead width (cap) varied from 4 mm to 4.6 mm. The average measurement of waist and root bead were found to be 1.6 and 2.3 mm wide respectively. In comparison with weld made with a 300 µm spot size single beam at 4.5 kW, with welding speed from 1 to 1.25 m/min and focused in the vicinity of the focal point, it was found that with the dual beam process:

- The bead width is up to 15% larger;
- and the waist is 23 to 65% larger;
- and the root bead is 50% larger in average.

The last result is the most significant as narrow root welds (< 2 mm) are usually not desired in the industry. The widening of the cap with an increasing distance separation between the two beams suggested an extended keyhole. An essential difference in weld profile regarding the waist and the root was observed when compared to single beam process. Waist and root are significantly larger (~ 50%) with dual beam welding. Although industrial application often required a root width superior at 2 mm, as obtained with dual beam process, standards BS EN 10088-2 does not indicate a minimum width [99]. It is not known if the wider waist and root are a result of a slight misalignment of the trailing beam or a broader keyhole. The latter supposition is nevertheless more likely as symmetric the weld profiles from the cross sections do not suggest any misalignment.

5.5.4 Temperature measurement

When compared to the cooling time of bead on plate obtained with single beam melt run made at 5 kW at the same speed and focus position (1 m/min; - 4 focus), Figure 5.18, it can be seen that:

- With the dual beam technique, the material stays twice longer over 1000°C compared to single beam welding.
- The cooling time in the 1000 – 800 °C is shorter with the dual beam (~0.2 s) than with a single beam (0.5 s).

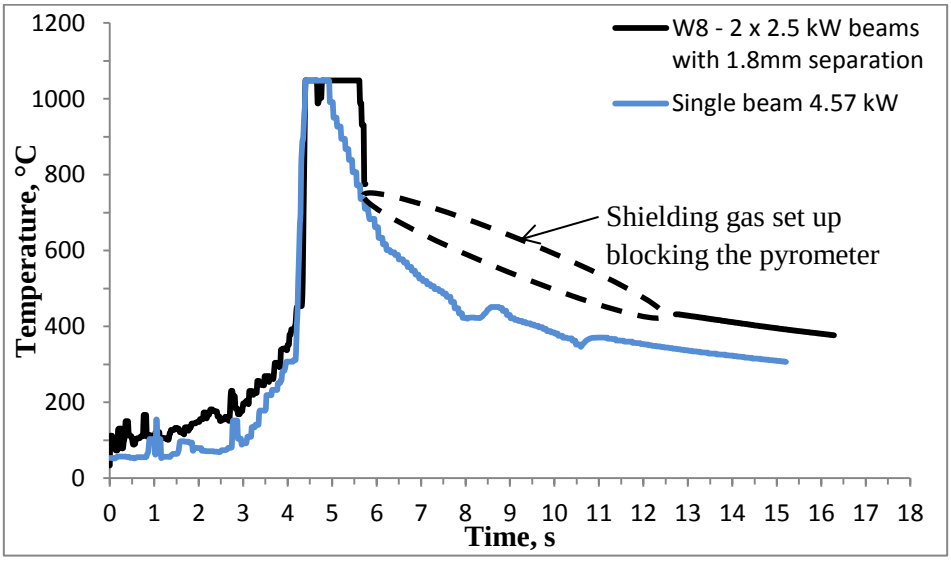

Figure 5.18: Dual beams Vs Single beam cooling rate comparison

The faster cooling rate from 1000 to 800 °C obtain with the dual beam process compared to single beam process can probably be explained by the wider weld profile (waist and root) obtain with this method. A greater volume of molten material dissipates more heat at constant heat input. On the other hand with the dual beam process, the extended time in which the material stays over 1000 °C might give rise to a significant increase of austenite depending on when the solidification of the material started. The limitation of the pyrometer for recording temperature from 1350 °C (grade 2205 DSS liquefaction point) and 1000 °C is an issue.

Austenite forms in the region 1350 to 800 °C. Therefore the longer the material stays in this temperature range, the better for austenite formation. Because of the distance separation between the two beams, the possible formation of a larger keyhole than with single beam process maintained the material for a longer time in the temperature range over 1000 °C. However, larger waist and root width accounted for a faster heat dissipation explaining a steeper cooling rate in the 1000 to 800 °C when compared to single beam process.

5.5.5 Phase balance

Point count results for dual beam process are presented in Table 5.17. The average uncertainty is ± 3.5%, and the maximum ferrite content difference from a weld to another (at constant area) is only 7%. Together with a 2.4% standard deviation between all the measurements, it can be concluded that there are no significant differences between all these results. As a reminder, the attached incertitude is calculated for the result to be given at 95% level of confidence. This means if the ferrite content is found to be 70.0% and the uncertainty is ± 3.0%, therefore there are 95% chances that the true ferrite content (the true population mean) is between 67.0 and 73.0%.

Table 5.17: Point count results for dual beam process

Run properties		Ferrite content (%)			
Weld	Distance separation (mm)	Cap	Waist	Root	Average
E10W5	0 (overlap)	74.4 ± 2.9%	78.6 ± 3.6%	74.0 ± 3.2%	**75.7 ± 3.2%**
E10W6	1.2	69.8 ± 3.5%	77.5 ± 3.9%	74.9 ± 3.5%	**74.1 ± 3.6%**
E10W8	1.8	75.0 ± 3.0%	74.5 ± 3.4%	78.0 ± 4.1%	**75.8 ± 3.5%**
E10W9	1.6	72.3 ± 2.8%	74.8 ± 3.5%	75.3 ± 4.2%	**74.1 ± 3.5%**
E10W10	1.6	71.8 ± 4.0%	71.0 ± 3.6%	75.0 ± 3.5%	**72.6 ± 3.7%**

Comparison with a ferrite content of bead on plates made with single beam welding at 1 m/min in the vicinity of the focal point (-6 to +2 mm), with 5 kW power shows that no improvement in ferrite reduction was made.

5.5.6 Corrosion

Following the same standard and methodology used before and presented in Chapter 3 (i.e ASTM A923 test method C), two samples and the parent material were tested. Results are presented in Table 5.18. Parent material passed the test (mdd value < 10) with the same results that were measured in previous chapter. The samples need to be polished to remove impurity or grease that can bias the weigh before the test and to reveal easily any oxidation or pitting that can result from the test. Here, no pitting crevices were observed after immersing the sample 24 h in the ferric chloride solution. Even with wider cap and root compare to single beam welding, the dual beam welded samples passed the test. The corrosion rate was similar to the one observed with single beam welding.

Table 5.18: Corrosion test of welded 6 mm grade 2205 DSS with dual beam

Description	**Specimen size (mm)**	**Surface area (cm^2)**	**weight loss (mg)**	**corrosion rate in (mdd)**	**corrosion rate in ($mm.y^{-1}$)**
Parent material – no weld					
Polished on both side	49.3 × 27.8 × 5.8	36.35	0.1	0.27	1.28×10^{-3}
Polished on both side	51.2 × 25.4 × 5.7	34.74	0.1	0.29	1.34×10^{-3}
Dual beam					
E10W5 polished on both side	54.4 × 21.5 × 5.7	32.04	0.3	0.94	4.35×10^{-3}
E10W10 polished on both side	49.9 × 23.0 × 5.7	31.26	0.2	0.64	2.97×10^{-3}

5.6 Concluding remarks

5.6.1 For the 3 mm plates dual beams experiments

A dual beam laser welding technique was proposed. It was found that at a fixed welding speed, the addition of a trailing defocused beam of ~ 8 mm diameter with a power density of 5 kW/cm^2 was able to bring the phase balance down to the accepted range of ferrite, which was not possible with a single beam process. Weld shapes of dual beam welded samples no longer look like an hourglass but rather like a V because of the effect of the post-heating beam. The significant increase in the length of the cap, waist and also the root can be seen as

positive as narrow waist and root are not desirable for the intended industrial application. Effects of the dual beam technique on the microstructural changes were investigated, and the ferrite content was found to be 10 to 15% lower when compared with single beam process. The lower content of ferrite was also associated with the lack of intermetallic precipitation revealed by the corrosion test. No significant changes in hardness were found. Also, further studies are required to fine tune the technique, the potential of dual beam welding with laser fibre to overcome ferrite excess at the welds was demonstrated. Improved weldability of DSS at a relatively high welding speed was established.

5.6.2 For the 6 mm plates dual beams experiments

Feasibility of welding 6 mm thick plate of grade 2205 DSS with a dual beam system of 2×2.5 kW beam was demonstrated. Full penetration was achieved when focusing both beams close to their focus point and with a maximum distance separation of 1.8 mm. The weld's profiles were found to be wider (especially the waist and root bead) than welds made with a single 5 kW beam with a similar spot size at the same welding speed. This difference can be advantageous as narrow root weld are usually not wanted. Higher cooling rates than with single beam were observed, and ferrite content measurement showed no improvement in term of austenite formation. The wider resulting weld profile can be advantageous in industry as it offers slightly more tolerance of the welding process.

Chapter 6: Autogenous Yb:fibre laser welding of grade 2205 duplex stainless steel with diffractive optics

6.1 Background

After establishing the welding parameters with a single beam for grade 2205 duplex stainless steel on 3 and 6 mm thick plates, the results were used to develop a dual beam technique that led to a reduction of the excessive ferrite content a the weld. The dual beam technique nevertheless requires a bulky set-up that doubles the number of optical components for laser welding. Another approach is to use a standard single beam laser set up (collimator, focusing optics and cover slide) coupled with a diffractive optic inserted before the focusing lens to achieve a split energy distribution (multiple beams) in the focal plane. As dual beam results showed that a re-heating beam with a distance separation *d* of 8 to 11 mm and a power density around 5 to 9 W. mm^{-2} reduced the ferrite content, a commercially available 3-spots diffractive optical element (DOE) was then selected. It provided a pre and post-heating with a distance separation of 8.52 mm with the welding beam when used with the same optics from Chapter 4 (100 mm FL collimator and 200 mm FL focusing lens). The re-heating beam produced by the DOE was smaller (300 µm in diameter) than the one obtained with the beam splitter set up (6 or 8 mm), so the power density was higher than in the dual beam experiments (3×10^2 $W.mm^{-2}$ when 5 kW power was used and 2×10^2 $W.mm^{-2}$ when 3.5 kW where used). In this chapter, the off the shelf DOE was characterised and tested to carry out melt runs and butt welds on 3 and 6 mm thick grade 2205 DSS. Section 6.2 reviews the overall experimental approach and Section 6.3 presents the DOE used and its characterisations. Results for the 6 mm plates are presented in Section 6.4 and for the 3 mm plates in Section 6.5. Finally, section 6.6 presents the brief trial of another diffractive optics used, and the concluding remarks are stated in section 6.7.

6.2 Experimental programme

6.2.1 Approach

The 3-spots DOE was characterised in terms of power transmission efficiency and beam size measurements. Then for the welding of 3 and 6 mm thick plates of grade 2205 DSS, the core idea was to replicate the process parameters developed in Chapter 4 for the main welding beam and to have a post-heating beam with a similar power density and distance from the first beam as in Chapter 5.

The pyrometer was used to measure the cooling rate during welding. Samples were cross-sectioned for weld profile measurement and metallographic examination. The point count technique covered by ASTM E562 standard was used to measure the resulting phase balance at the weld location. Chemical analysis of austenite and ferrite phases at different weld location was carried out on selected samples using EDX semi-quantitative method. Grain orientation was observed using EBSD technique. ASTM A923 test method C was performed on selected samples to evaluate the corrosion resistance properties.

6.2.2 Equipment and material

In this entire chapter, the IPG YLS 5000 Yb:fibre laser was used and mounted on the Aerotech 3-axis table. The jig, clamps, pyrometer and Prometec beam profiler used are the ones described in chapter 3. The optics initially selected in Chapter 4 were used (Optoskand 100 mm FL collimator and 200 mm FL focusing lens) leading to the theoretical spot size of 300 µm. The focusing optics and the diffractive optic were held in the designed welding head presented in Chapter 3.

6.2.3 Experiments

Autogenous beam welding with a diffractive optic on the 6 mm thickness plate consisted of 15 melt runs with different process parameters. Power was set at 5 kW. The efficiency of the DOE for the zero order being 90%, this translates to 4.5 kW going to the main beam, making the experiment comparable with welding without DOE. Investigations focused on microstructural changes at the weld cap due to the re-heating beam. Cross-sections were point counted, and a sample was analysed with EBSD and EDS techniques to obtain more information on the grains orientation, phase distribution and elemental partition between the austenite and ferrite. A corrosion test was carried out for two selected samples.

Autogenous beam welding with a diffractive optic on the 3 mm thickness plates consisted of 10 melt runs and four butt welds performed with different process parameters. Temperature measurement highlighted the effect of the pre and re-heating beams and butt welds were cross-sectioned and point counted.

Finally, a 4-spots DOE was tested to perform some melt runs on the 3 mm thickness plates. Because of low material and laboratory availability, only two melt runs were analysed and point counted.

6.3 3-spots DOE characterisation

6.3.1 Beam profile

A 3-spots transmissive DOE made of fused silica and designed for a wavelength of 1070 nm was selected. The resulting pattern on the focal plane is shown in Figure 6.1. The grating period of the DOE was 25 µm which leads to a separation angle of 2.44° for the laser operating wavelength. With focusing optics of 200 mm focal length, the distance *d* between the diffracted orders was 8.52 mm. Spots were aligned to the welding direction, the first spot acted as pre-heating, the zero order as the welding beam and the last spot as re-heating.

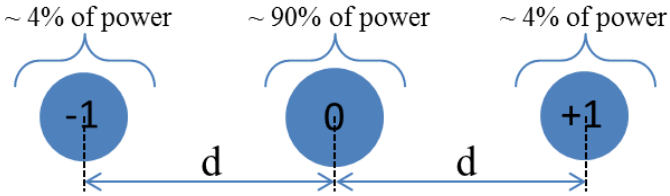

Figure 6.1: Pattern of 3-spots DOE

Both sides of the optic have an anti-reflective coating. Higher orders of diffraction redirecting less than 2% of the total power are not shown in Figure 6.1.

When using the DOE, the sensitivity of the beam profiler was not adequate to capture beams with a high discrepancy of energy distribution at the same time, as +1 and -1 order had just enough energy to be detected while the zero order saturated the beam sampler. The beam profile measurement is shown in Figure 6.2. All the diffraction orders (0, +1, -1) were characterised independently, by blocking the other beams. Figure 6.3 shows the 3D beam profile of the zero and first order taken separately. It was found that all these beams were a quasi-perfect replica of the beam without DOE, in terms of beam quality (M^2 = 15.5), spot size ($\omega 0$ = 0.155 mm), divergence (θ = 0.034 rad) and Rayleigh range (ZR = 4.59 mm) as summarised in Table 6.1.

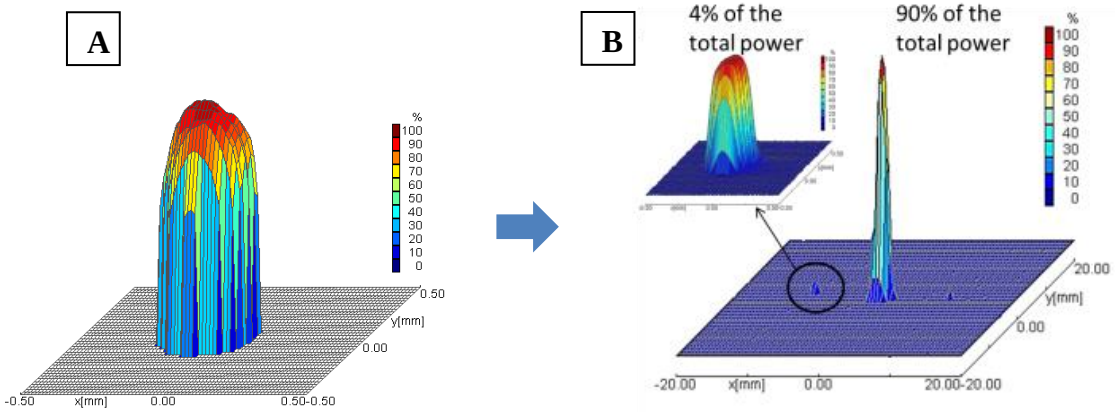

Figure 6.2: 5 kW laser beam (A) without and (B) with 3-spots DOE.

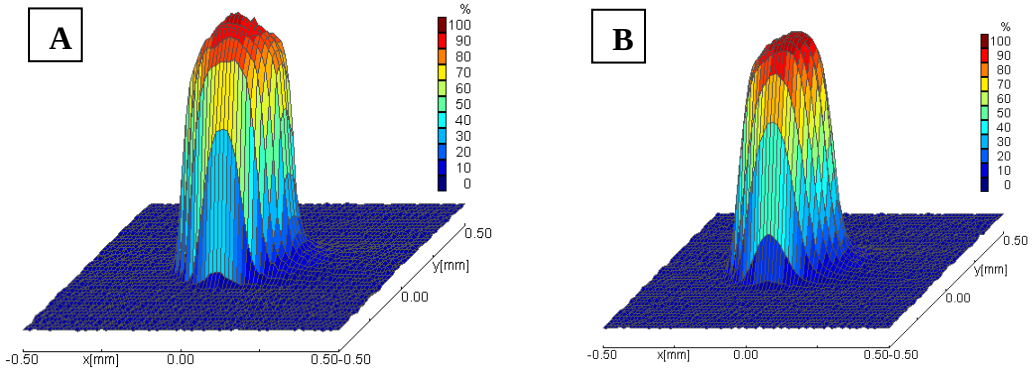

Figure 6.3: (A) Zero-order beam (welding beam) and (B) 1st order diffracted beam (reheating beam) in focus

Table 6.1: Measurements of the zero order beam (welding beam) and 1st order diffracted beam:

Parameters	**Zero-order** Value (86% def)	**1st order** Value (86% def)	**Unit**
ω_0	0.155	0.157	mm
θ	0.034	0.034	rad
Z_R	4.59	4.700	mm
M^2	15.4	15.4	none

6.3.2 Power measurement

The laser power was measured with and without the DOE. The DOE had a 99.3% transmission efficiency expected (manufacturer data sheet) and was measured to be 95.3 ± 5%. The DOE was not cooled, but heating of the optic's housing was not observed. Nevertheless, welds in the laboratory were short and separated by long periods of time. For industrial applications where the laser is required to remain on for longer periods of time, active cooling of the DOE is recommended to avoid overheating.

6.3.3 Temperature measurement of the side beam

The temperature changes caused by the reheating beam on its own were measured. The DOE was rotated by 90° so that the first order of diffraction was sideways to the welding beam and not trailing it. Power was set at 5 kW, with 200 W going to the first order diffracted beam. The welding speed was 1.25 m/min, and the focus position was set at – 4 mm. The pyrometer recorded a fixed point on the parent material surface while being visited by the reheated beam. Temperature measurements are presented in Figure 6.4. The material, initially at room temperature, was raised at 700 °C when heated by the first order diffracted beam. This did not vaporise the metal but melted the surface. For the reheating during welding, it is important that the metal does not get in liquid phase again as it will re-solidify in ferrite phase instead of being kept in a molten phase where austenite can form.

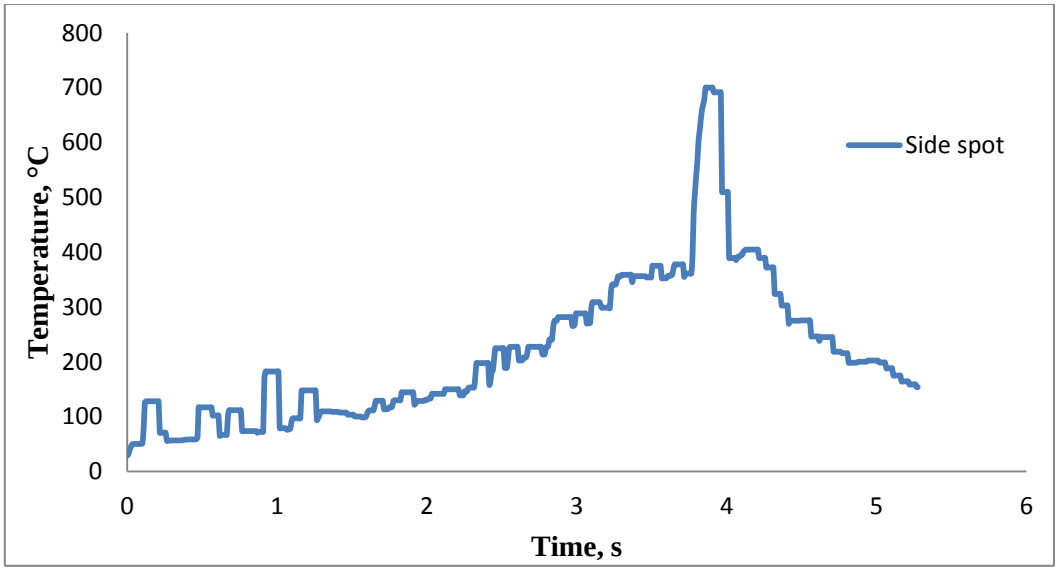

Figure 6.4: Side spot (+1 order) temperature measurement

6.3.4 General observations when using DOE

For alignment, the guide laser pointer (λ ~680 nm) built in the laser system is useful, but it shows a different pattern as the spacing between spots (*d*) is wavelength dependent. As the laser guide's wavelength is around half the wavelength of the IPG Yb:fibre laser the distance between zero and ±1 orders is half as well. Figure 6.5 shows the diffracted pattern from the laser guide's light.

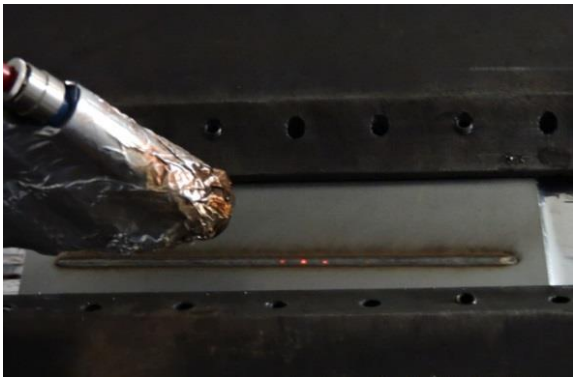

Figure 6.5: 3-spots DOE

Welding was made with power going up to 5 kW during 7.5 seconds without damaging the DOE. Laser damage threshold of fused silica is the same as the focusing optic used for laser welding with 5 kW. Higher order of diffractions that redirect a meagre amount of power should also be taken into account as over an extended time they can melt items in their path. The DOE manufacturer provides the full range of angles (θf) for all orders of diffractions.

6.4 Results and discussion for 6 mm plates

6.4.1 Process window for full penetration

The processing power was set at 5 kW for all the experiments. As a result, 4.5 kW was redirected in the central beam (zero order diffraction) initiating the keyhole. The power used for the welding process was therefore equal to the power used in Chapter 4 for the entire autogenous laser welding experiments on 6 mm plates. The process window for full penetration is the same as before, the post-heating and pre-heating beams of 200 W each were not contributing to broaden the process in terms of penetration.

6.4.2 Weld profile

As before, no welding defects or porosity were observed under radiograph and cross-section micrographs at 1000× magnification. Weld surfaces were shiny, and very few spatters were observed. Porosity check with x-ray was not undertaken as none were observed in all previous experiment, including the dual beam process.

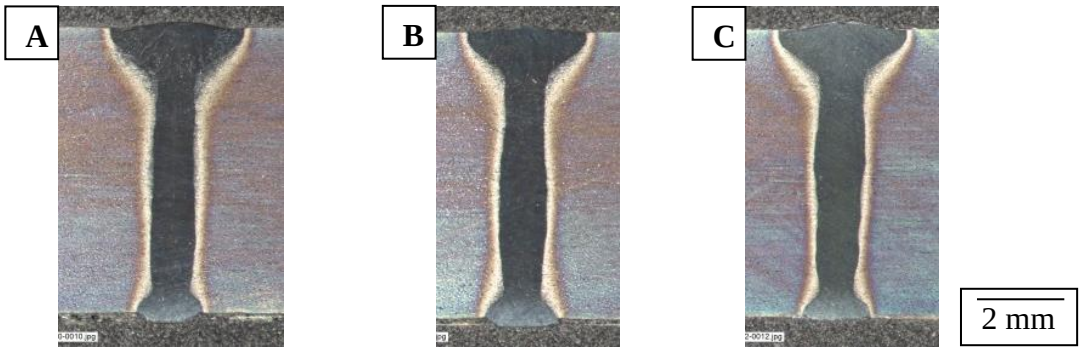

Figure 6.6: Welds with DOE at (A) -4 mm focus (B) -2 mm focus and (C) 0 mm focus (all at 1.25 m/min at 5 kW)

Melt runs performed with the DOE were made at a welding speed of 1.25 m/min and tree different focus positions. Melt runs without the DOE were made with the same setting but at 4.5 kW. Weld profiles were measured and are summarised in Table 6.2. Full penetrating welds were achieved with the typical shape that can be observed in Figure 6.6, and the welds made with and without DOE were almost identical in shape and dimension. The DOE did not introduce any weld profile modification higher than 0.35 mm. Slight cap reinforcement and root sagging of maximum 0.3 mm were observed with and without the DOE.

Table 6.2: Weld profile measurements with and without DOE welding of 6 mm plates

Weld parameters			Dimension (mm)			Area (mm^2)	
DOE	Power (kW)	Focus position (mm)	Cap	waist	root	Cap area	DOE area
no	4.5	-4	3.01	1.24	1.45	2.9	x
no	4.5	-2	2.49	1.20	1.62	1.8	x
no	4.5	0	2.56	1.05	1.61	2.0	x
yes	5	-4	2.72	1.08	1.61	2.3	0.3
yes	5	-2	2.79	1.09	1.64	2.4	0.4
yes	5	0	2.91	1.10	1.56	2.5	0.4

The cap area affected by the second re-heating beam can be seen under micrograph of cross-sectioned weld polished and etched with sulfuric acid as depicted in Figure 6.7. The slight change of colour from the etching that reveals the re-heated area (named DOE area) might be due to a local change of microstructure, either in elemental composition or phase balance ratio compared to the surrounding weld area.

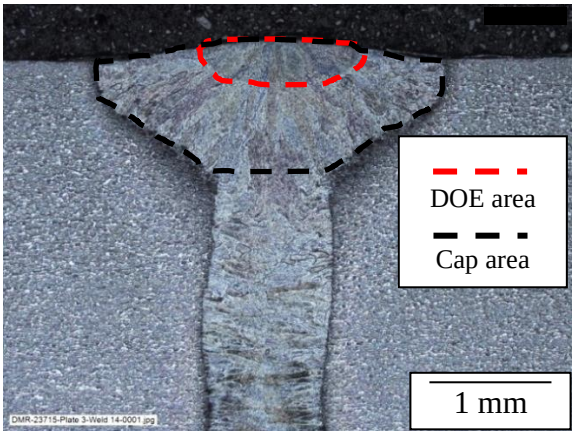

Figure 6.7: Weld made with the DOE at 1.25 m/min and -4 mm focus position

6.4.3 Temperature measurement

A pyrometer measuring temperatures from 400 to 2000 ˚C (Optris CT XL 3MH) was selected to observe the effect of the re-heating beam. After technical, alignment and set up issues that could not be resolved during the available time for the experiments, the same pyrometer mentioned in previous chapters was used to estimate the cooling rate. Few measurements reported in Table 6.3 were obtained, and the cooling rates in the 1000 -800˚C temperature interval were marginally improved compared to the one reported in Chapter 4 and done with

a single beam. No dip or peaks in the measurements were caused by the re-heating beam, and it is assumed that the effect of the re-heating beam took place above the pyrometer saturation.

Table 6.3: Cooling rate for 6 mm plates

Welding speed (m/min)	Heat input (J/mm)	Time in the 1000 -800˚C interval	Cooling rate (˚C/sec)
1	300	0.39 ± 0.01	500 ± 50
1.25	240	0.34 ± 0.01	550 ± 50

6.4.4 Microstructure change and phase balance

The material solidified primarily in the ferrite phase, and the welds were mostly ferritic, similarly to previous observations made in Chapter 4 and 5. An electron backscatter image obtained with the procedure and setting described in Chapter 3 revealed the phase balance (Figure 6.8 A) and the grain orientation (Figure 6.8 B) of the weld cap. The weld is the one presented in Figure 6.7 (performed with the 3-spots DOE at 5kW, 1.25 m/min and -4 mm focus position). The grain arrangement in the crystal orientation map presented in Figure 6.8 B is similar to the one observed with the single beam process (Figure 4.19). The ferrite grains form existing crystals and grow away from the heat sink, following the gradient from high to low thermal conductivity and are much larger and longer than in the parent material. The effect of the re-heating beam does not seem to create smaller ferrite grain and even when looking at the phase mapping no apparent higher austenite phase density (blue phase) was noticed. When taking a closer look at the phase mapping and getting the statistical austenite content in the DOE area (estimation of the area based on the darker shade that can be seen in Figure 6.7) and the surrounding cap, a difference is noted. Figure 6.9 shows the EBSD phase mapping analysis of two different selected areas. Phases content of ferrite and austenite does not add up to 100% because of the presence of 7 to 6% unidentified point. The Ferrite content is higher than the when measured with point counting method, but it is only indicative as point count was the chosen method to evaluate the ferrite across all the welds produced for this research.

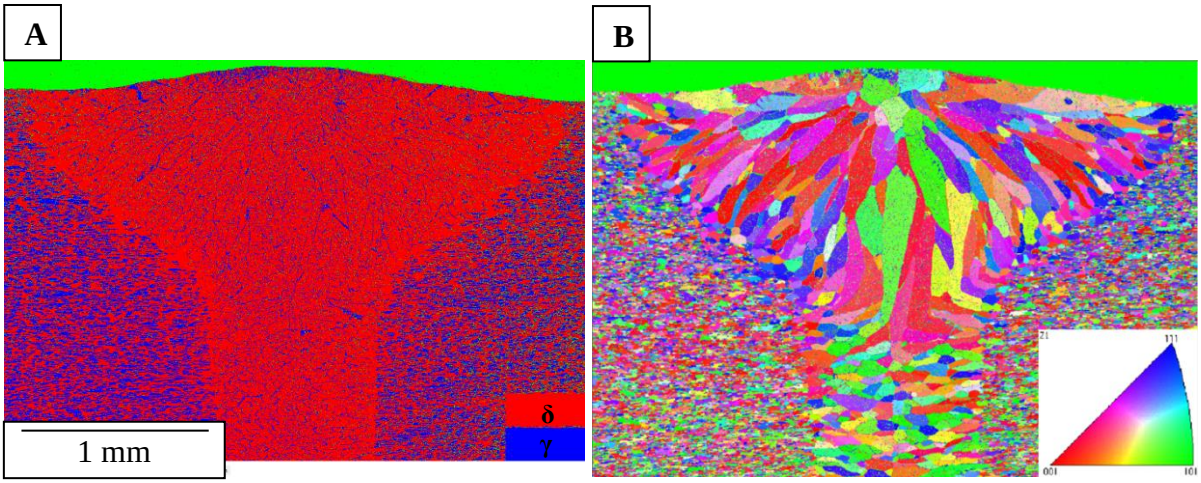

Figure 6.8: EBSD (A) phase imaging and (B) crystal orientation map

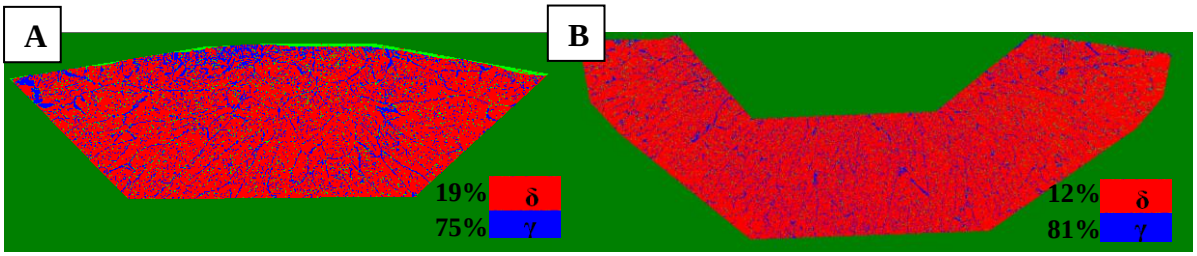

Figure 6.9: Phase mapping from EBSD (A) DOE area and (B) surrounding cap

The deposited energy in the just-solidified weld led to a coarsening and further growth of already nucleated austenite. The coarsening of the austenite, especially in its allotriomorph form at the prior grain boundary, is depicted in Figure 6.9 which shows austenite out of the area affected by the DOE, and inside this area. In Figure 6.9 A, allotriomorph austenite widths were measured and ranged from 2.1 to 3 µm In Figure 6.9 B, allotriomorph austenite widths were measured and ranged from 2.5 to 5.6 µm. This phenomenon might account for the slightly darker shade in Figure 6.7, which reveals the DOE affected area. Evaluation of the ferrite content by point counts, presented in Table 6.4, shows a reduction of the ferrite volume fraction in the DOE reheated area compared to the rest of the weld cap.

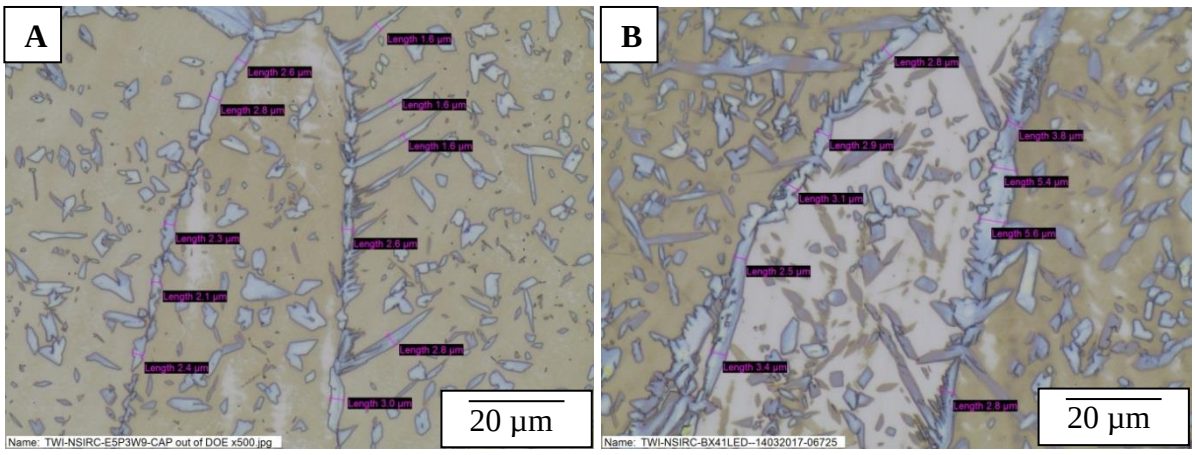

Figure 6.10: (A) Cap out of the DOE affected area and (B) reheated area at the cap

Table 6.4: Ferrite content of welded 6 mm grade 2205 DSS with the 3-spots DOE

Parameter	**Ferrite content (%)**			
Focus position (mm)	Cap	Cap DOE	Waist	Root
-4	73.7 ± 3.7%	60.3 ± 4.0%	75.4 ± 3.3%	61.1 ± 4.4%
-4	68.6 ± 4.3%	59.6 ± 3.7%	74.3 ± 3.9%	58.4 ± 4.2%
-4	68.8 ± 4.4%	57.8 ± 3.3%	76.4 ± 3.5%	58.4 ± 3.6%
-4	70.2 ± 5.2%	57.9 ± 6.3%	73.4 ± 3.8%	62.8 ± 4.1%
Avg.	**70.3 ± 4.4%**	**58.9 ± 4.3%**	**74.9 ± 3.6%**	**60.2 ± 4.1%**
-2	65.9 ± 3.9%	57.5 ± 4.3%	73.0 ± 3.8%	62.0 ± 4.7%
-2	69.6 ± 3.6%	60.3 ± 3.5%	73.1 ± 4.6%	59.6 ± 5.2%
Avg.	**67.8 ± 3.8%**	**58.9 ± 3.9%**	**73.1 ± 4.2%**	**60.1 ± 5.0%**

Both the cap and the root are covered by the shielding gas having a low thermal conductivity. The root being typically narrower than the cap, heat is, therefore, more concentrated. This

probably leads to a slower cool down at this location, giving more time for austenite to grow and accounting for the discrepancy in ferrite content with the cap**.**

6.4.5 Chemical composition

Following the same procedure and using the same equipment as reported in the previous chapters, the micro-chemical compositions of the δ-ferrite and γ-austenite phases were measured at different depth along the central vertical axis of the weld and are presented in Table 6.5. Again, the elemental compositions are given with the partition coefficient K ([element weigh % in δ] / [element weigh % in γ]). As observed in previous chapters, the elemental partition is not as developed in the weld as in the parent material. Nevertheless, in the parent material, elements are already quite close in proportion in each phase. At least, no major changes in composition are observed nor supersaturation of an element in one phase.

Table 6.5: Chemical analysis

	Phase	**Si**	**Mo**	**Cr**	**Mn**	**Ni**
Parent	γ	0.4	2.3	21.3	2.1	6.7
	δ	0.4	3.2	23.4	1.8	5.1
		K = 1.0	**K = 1.4**	**K = 1.1**	**K = 0.9**	**K = 0.8**
0.2 mm from surface (DOE area)	γ	0.3	3.0	22.9	1.8	5.2
	δ	0.4	3.0	22.9	1.8	5.1
		K = 1.2	**K = 1.0**	**K = 1.0**	**K = 1.0**	**K = 1.0**
0.8 mm from surface	γ	0.4	3.1	22.9	1.8	5.2
	δ	0.4	3.0	23.0	1.8	5.2
		K = 1.0	**K = 1.0**	**K = 1**	**K = 1.0**	**K = 1.0**
3 mm from surface	γ	0.3	3.1	22.8	2.0	5.3
	δ	0.4	3.0	23.0	1.9	5.3
		K = 1.3	**K = 1.0**	**K = 1.0**	**K = 1.0**	**K = 1.0**
beam 5.5 mm from cap surface	γ	0.5	3.3	23.0	2.0	5.4
	δ	0.5	3.2	22.9	1.9	5.3
		K = 1.0	**K = 1.0**	**K = 1.0**	**K = 1.0**	**K = 1.0**

6.4.6 Corrosion

ASTM A923 test method C was used one last time to test the corrosion resistance of two melt runs made with the 3-spots DOE. Both were made at 1.25 m/min with a - 4 mm focus position. Results are presented in Table 5.18. Both samples passed the test (mdd < 10) and no pitting crevices were observed after immersing the sample 24 h in the ferric chloride solution. The corrosion rate was similar to the one observed with dual beam welding presented in Chapter 5.

Table 6.6: Corrosion test of welded 6 mm grade 2205 DSS with the 3-spots DOE

Description	**Specimen size (mm)**	**Surface area (cm^2)**	**weight loss (mg)**	**corrosion rate in (mdd)**	**corrosion rate in ($mm.y^{-1}$)**
Parent material – no weld	49.3 × 27.8 × 5.8	36.35	0.1	0.27	1.28×10^{-3}
Both polished on both side	51.2 × 25.4 × 5.7	34.74	0.1	0.29	1.34×10^{-3}
3-spots DOE	50.0 × 18.7 × 5.6	26.40	0.2	0.76	3.52×10^{-3}
Both polished on both side	50.9 × 22.4 × 5.6	31.01	0.2	0.64	3.00×10^{-3}

6.5 Results and discussion for 3 mm plates

6.5.1 Process window for full penetration

The processing power was set at 2.5 or 3.5 kW for all the experiments, the total heat input of 150 or 210 J/mm were therefore identical to single beam experiments. As a result, 2.25 or 3.15 kW was redirected in the central beam initiating the keyhole. The process window for full penetration was the same as before, the post-heating and pre-heating beams of 100 or 140 W each were not contributing to broaden the process in terms of penetration.

6.5.2 Weld profile

No welding defects or porosity were observed under radiograph and cross-section micrographs at 1000× magnification. Weld surfaces were shiny and very few spatters were observed.

Full penetrating welds were achieved with the typical hour-glass shape that can be observed in Figure 6.11 (welds at 1 m/min and - 4 mm focus position). Weld profile measurements are summarized in Table 6.7. The area affected by the re-heating beam is revealed in the micrograph by a darker shade.

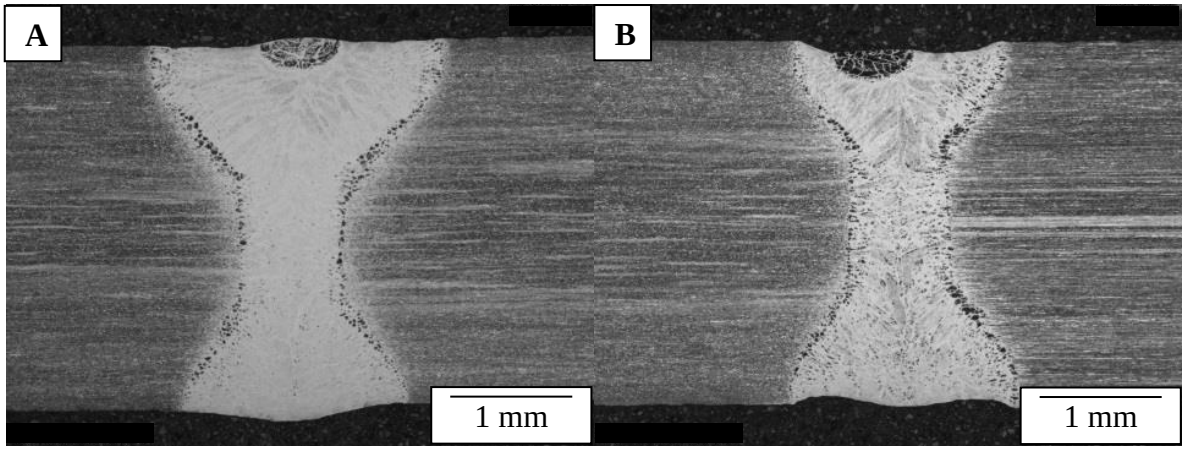

Figure 6.11: Weld made with the DOE at a processing power of (A) 2.5 kW and (B) 3.5kW

Table 6.7: 3 mm with DOE weld profile dimensions

Parameters			**Dimension (mm)**		
Power (kW)	Welding speed (m/min)	Focus position (mm)	Cap	Waist	Root
2.5	1	-2	2.93	0.93	1.56
2.5	1	-4	2.76	0.93	1.79
3.5	1	-2	3.00	1.3	1.99
3.5	1	-4	1.75	0.83	1.86
3.5	1.5	-2	2.27	0.84	1.53
3.5	1.5	-4	2.77	0.91	1.53

When compared with welds made with the single beam process, the 3-spots DOE welds were almost identical in shape and dimension. The DOE did not introduce any weld profile

modification higher than 0.5 mm. Slight cap reinforcement and root sagging of maximum 0.20 mm were observed with and without the DOE.

6.5.3 Temperature measurement

The same pyrometer mentioned in previous chapters was used to estimate the cooling rate. Four butt welds were carried out. All were done at 1 m/min at -4 mm focus position. Processing powers tested were 2.5 and 3.5 kW. Each butt weld was carried out with and without the 3-spots DOE with the same exact optical set up for reliable comparison. Figure 6.12 shows the temperature measurement recorded.

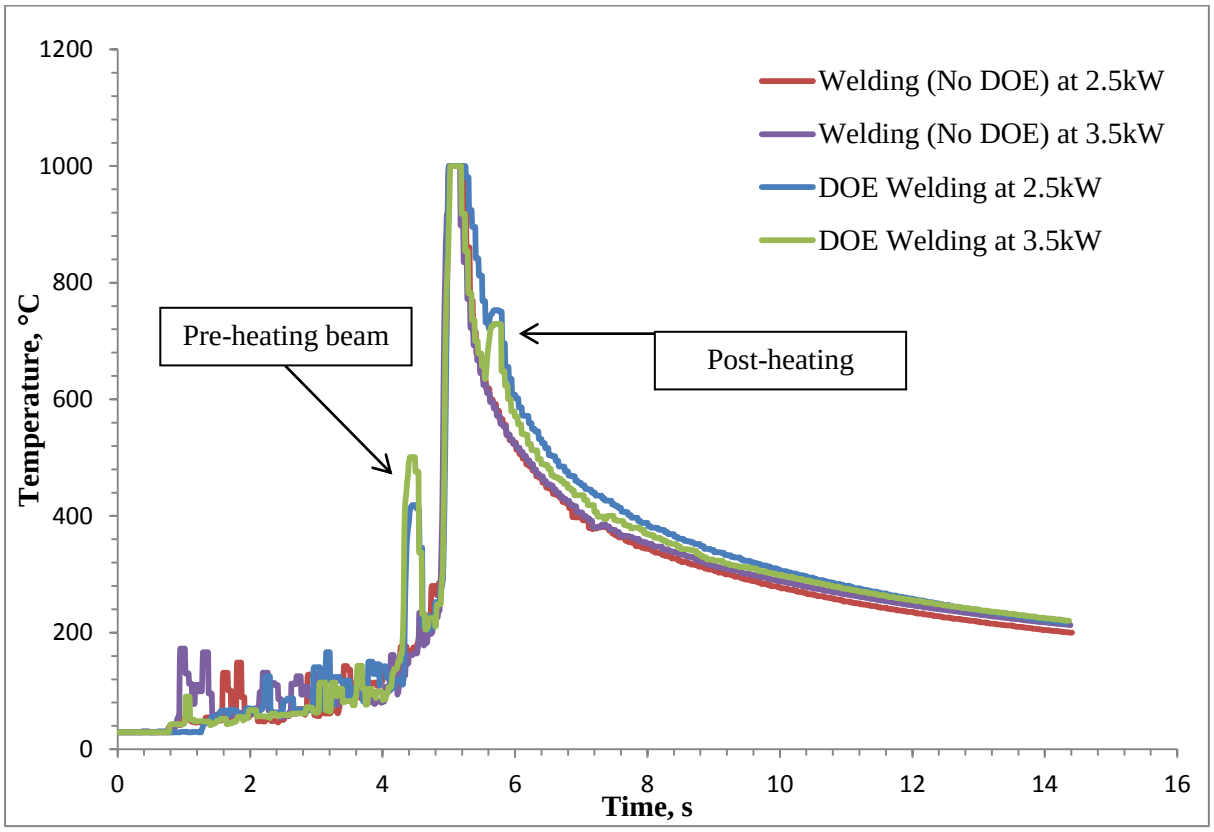

Figure 6.12: Laser welding of 3 mm grade 2205 DSS with and without 3-spot DOE

Measurements of the cooling rates in the 1000-800˚C temperature interval are given in Table 6.8. Cooling rates were calculated and averaged using two or three measurements of the recorded temperature of welds made with the same processing parameters.

Table 6.8: Average cooling rate of welded 3 mm grade 2205 DSS with DOE

Parameters Power (kW)	Welding speed (m/min)	Heat input (J/mm)	Average time in the 1000 -800˚C interval (s)	Average cooling rate corresponding (˚C/s)
2.5	1	150	0.24 ± 0.01	**700 ± 50**
2.5	1.5	100	0.11 ± 0.01	**950 ± 50**
3.5	1	210	0.20 ± 0.01	**850 ± 50**
3.5	1.5	140	0.24 ± 0.01	**800 ± 50**

In weld temperature measurement presented in Figure 6.12, the post-weld heating did not happen soon enough for the weld to extend the material in the 1200-800˚C range, which is where most of the austenite forms. With the 3-spots DOE, post-weld heating only took place approximately 680 ms after welding. To promote the austenite formation in the weld, post-weld heating should have taken place after around 300 ms following the welding beam. At 1 m/min (or 16.667 mm/s) welding speed, the time interval translates to about 5 mm spacing between the two beam spots. The current tri-spot DOE produced spots at 8.5 mm apart.

6.5.4 Phase balance

Evaluations of the ferrite content by point counts are presented in Table 6.12. The re-heated areas revealed by the etching were too small to be appropriately point counted. The whole cap area was, therefore, point counted, but no reduction of the ferrite content was observed when compared to single beam welding. Table 6.10 shows the ferrite content of the four butt welds mentioned in the previous section.

Table 6.9: Ferrite content of welded 3 mm grade 2205 DSS with DOE

Parameter			**Ferrite content (%)**	
Power (kW)	Welding Speed (m/min)	Focus position (mm)	Cap	Root
2.5	1	-4	73.1 ± 5.9%	70.4 ± 4.5%
2.5	1	-4	73.8 ± 5.5%	71.5 ± 4.7%
2.5	1	-4	75.3 ± 5.3%	70.6 ± 4.8%
2.5	1	-2	74.9 ± 5.8%	76.0 ± 4.2%
2.5	1	-2	71.8 ± 5.1%	69.1 ± 5.2%
3.5	1	-2	69.0 ± 5.2%	62.6 ± 5.5%
3.5	1	-4	71.1 ± 5.1%	66.8 ± 5.5%
3.5	1	-4	70.1 ± 5.2%	64.7 ± 5.5%
2.5	1.5	-2	74.9 ± 5.5%	76.3 ± 4.9%
3.5	1.5	-4	74.8 ± 4.6%	72.3 ± 5.2%

Table 6.10: Ferrite content of 3 mm plates butt welds performed with and without 3-spots DOE

Parameter	**Ferrite content (%)**			
	Single beam		3-spots DOE	
Power (kW)	Cap	Root	Cap	Root
2.5	74.4 ± 4.0%	72.0 ± 4.1%	73.8 ± 5.5%	71.5 ± 4.7%
3.5	71.6 ± 3.4%	70.0 ± 3.9%	70.1 ± 5.2%	64.7 ± 5.5%

6.6 4-spots DOE

A 4-spots transmissive DOE made of fused silica and designed for a wavelength of 1070 nm was selected. The resulting pattern on the focal plane is shown in Figure 6.13. The grating period of the DOE was 53.5 µm which leads to a separation angle of 1.146° for the laser operating wavelength. With the focusing optics of 300 mm focal length, the distance *d* between the diffracted orders was 6 mm. Spots were aligned to the welding direction, the first spot (zero order) was the welding beam, and the three following spots acted as the re-heating.

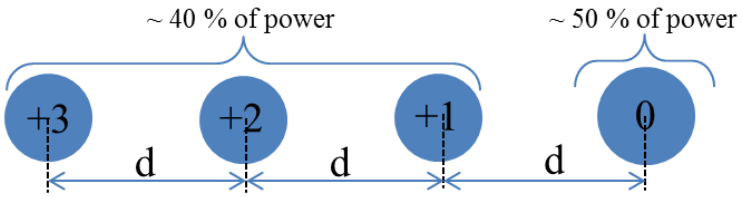

Figure 6.13: Pattern of 4-spots DOE

Both sides of the optic have an anti-reflective coating. Higher orders of diffraction redirecting almost 10% of the remaining total power are not shown in Figure 6.13.

6.6.1 4-spots diffractive optics characterisation

The Prometec UF-100 equipment was used in a defocus position with a 500 µm sampling needle to visualize the beam profile generated by the DOE. Unfortunately, because of the great disproportion in term of power distribution between the different orders (0 order: ~50% and +1, +2 and +3 orders are each ~13%) it was only possible to observe the higher diffraction order when the zero order beam was saturated as shown in Figure 6.14 (A). By reducing the scanning window and dropping the power, it was possible to observe the 0 order beam, followed 6 mm behind by the first order of diffraction without saturation, as shown in Figure 6.14 (B).

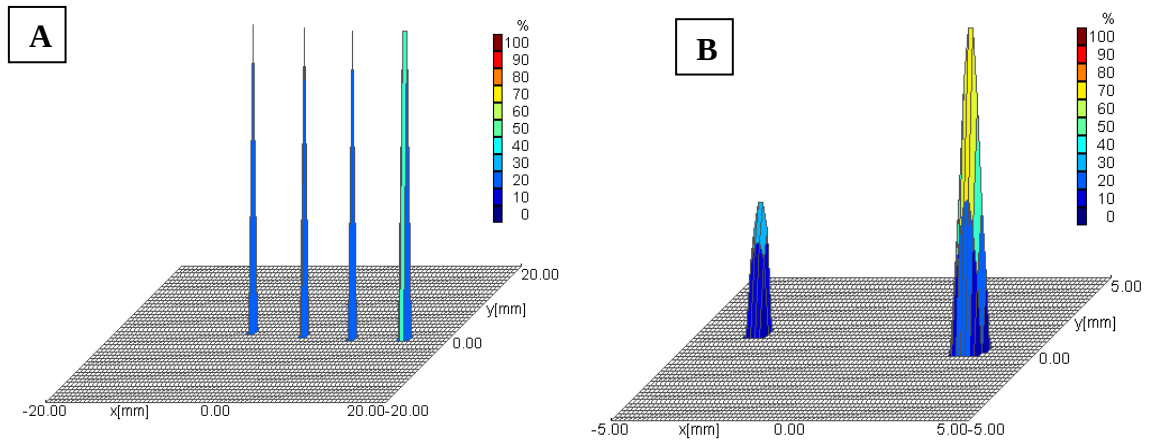

Figure 6.14: Intensity of (A) zero order and higher order of diffraction and (B) zero and first order of diffraction

To observe the pattern generated with the Yb:fibre laser, a 1 kW short pulse of 0.5 s was fired on a painted plate of aluminium to imprint it. The result is presented in Figure6.15. The -3, -2 and -1can just be observed, and the distance between the spot was measured and found to be 6 mm as predicted.

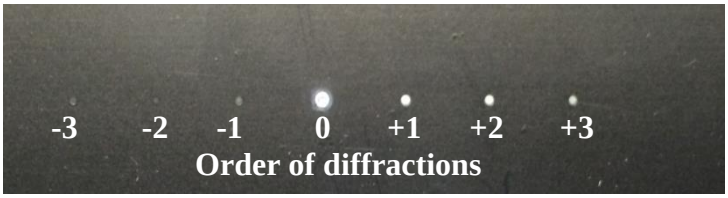

Figure 6.15: Marking of the 4-spots DOE

When the diffractive optic was used during welding at high power (2.5 to 5 kW) the power directed in the unwanted higher order of diffraction (-2, -1, +4 and above) turned out to be difficult to handle. Higher order diffraction spots distributed along the weld, preceding or following the keyhole, are not an issue for the intended application. Preheating spot will merely make a difference while additional post heating spots are desired to extend the cooldown. Nevertheless, they had a noticeable effect on accounting for the melting of the shielding gas pipes trailing the weld. A total of four distinctive spots can be seen, corresponding to the +4, +5, +6, +7 order of diffraction as seen in Figure 6.16.

Figure 6.16: Burnt shielding gas nozzle

6.6.2 Results on 3 mm plates

The DOE was tested to perform melt runs on the 3 mm plates only, as not enough power was available to weld the 6 mm plate with the 4-spots DOE. With this optic, the zero order (welding beam) can reach a maximum of 2.5 kW with the 5 kW Yb:fibre laser.

Welding speed was kept at 1 m/min and focus position at -4 mm like in most of the previous experiments. Welds made using 2.5 kW resulted in incomplete penetration while 3.5 kW was enough for full penetration even with only 1.75 kW for the main beam. Two welds carried out with 3.5 kW are presented in figure 6.17. Their dimensions are given in Table 6.13. With marginally smaller cap and root and a waist marginally wider, the welds had similar profile compared to single beam and 3-spots DOE welding.

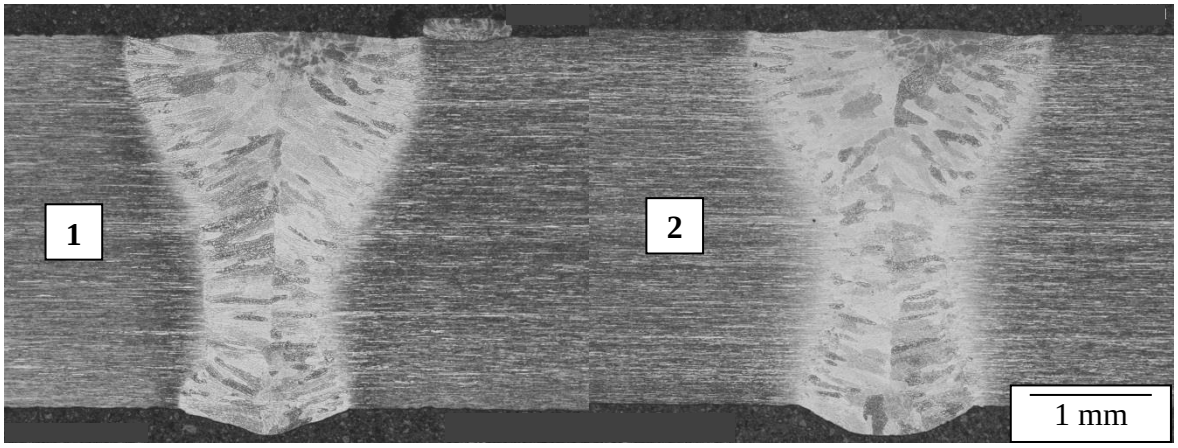

Figure 6.17: Welds with 4-spots DOE

Table 6.11: Welds profile measurements with 4-spots DOE welding of 3 mm plates

weld	Dimension (mm)		
	Cap	Waist	Root
1	2.37	1.20	1.38
2	2.39	1.06	1.46
Average	2.38	1.13	1.42

The resulting ferrite volume fraction was measured through manual point count at different areas of the cap. The results are given in Figure 6.18 and 6.19.

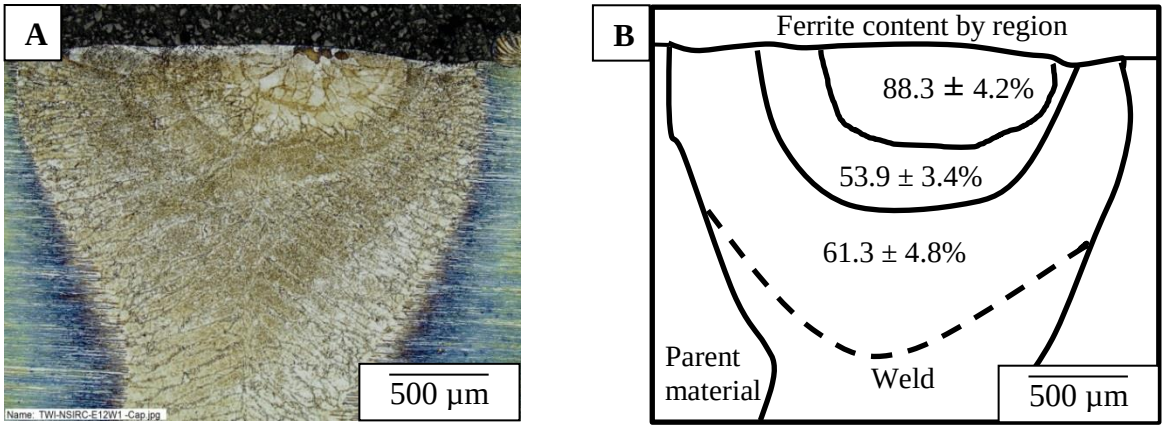

Figure 6.18: Ferrite content by region in a weld performed with the 4-spots DOE (1)

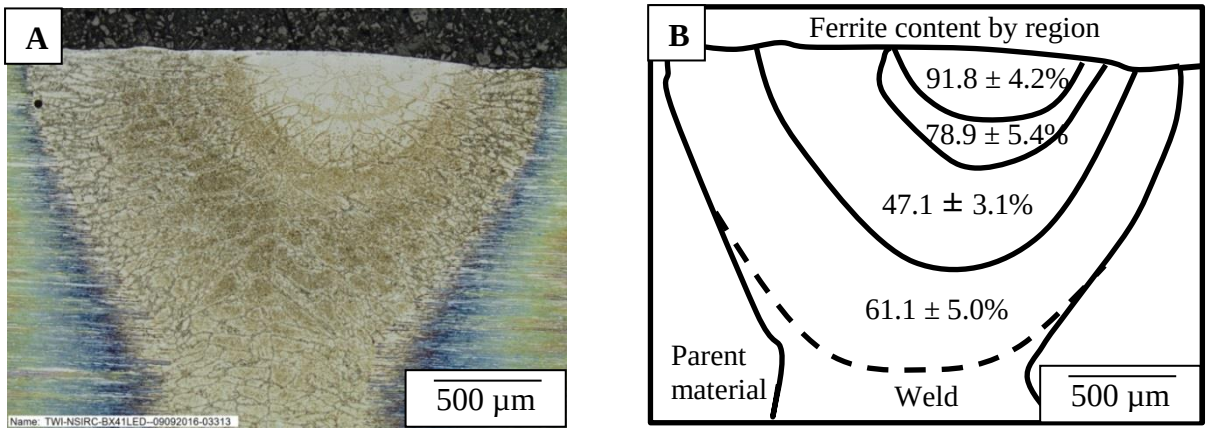

Figure 6.19: Ferrite content by region in a weld performed with the 4-spots DOE (2)

The last post-heating beam at the cap location probably led to a re-melting of the material followed by a very high cooling rate, as an area containing around 90% of ferrite phase was observed. Deeper in the weld cap at about 0.6 mm, the ferrite content was found significantly reduced with a nearly equal phase balance of ferrite/austenite.

6.7 Concluding remarks

The same set of optics selected in Chapter 4 was used except for the 4-spots DOE where the 300 mm FL focusing lens was used. Shielding gas, welding speed, processing power and focus position established in Chapter 4 served as a reference point for the experiments presented. The dual beam welding energy distribution developed in Chapter 5 established the baseline for the selection of two DOE. The 3-spots DOE was characterised and used with a welding head designed for this particular purpose. The optic withstood high power, and the diffracted spots were a perfect replica of the main beam.

6.6.1 For the 6 mm plates DOE experiments

Welding of the 6 mm thick plates with the 3-spots DOE led to a local reduction of the ferrite content at the cap. The austenite growing along the grain boundaries of the ferrite phase was observed to be a few micrometres thicker, and a higher density of intragranular austenite was revealed through point count. No substantial element partition was observed between the austenite and ferrite phase along the weld when carrying out semi-quantitative EDX measurements. All the welds made with the 3-spots DOE passed the corrosion resistance test (ASTM A923 Test method C).

6.6.2 For the 3 mm plates DOE experiments

Butt welds of the 3 mm thick plate with and without the 3-spots DOE were carried out with the same set-up and material to allow reliable comparison. The temperature measurement of the butt weld showed the effect of post and pre-heating beam, but the cooling rate was not decreased in the right range of temperature. Interaction time with the post-heating beam was probably too short due to the small size (300µm) of the beam when compared to dual beam welding (post-heating of 6-8 mm). Point count of the whole cap area revealed no improvement in ferrite reduction when compared to single beam welding.

The 4-spots DOE was then tested on the 3 mm thick plates. The succession of 3 reheating beams led to a local re-melting of the cap area. Part of the upper cap resulted in high ferrite content of around 90%, but below, the phase balance was restored (close to the parent material phase content). More fine tuning of the tailored energy is needed to achieve an acceptable ferrite content below 70% at 1 to 1.5 m/min processing speed and the results presented in this chapter led to think that it is possible.

Chapter 7: Summary and conclusion

7.1 Introduction

This chapter begins with a review of the objectives presented at the end of Chapter 2, followed by a summary of the experiments reported in this thesis that lead to the achievement of these objectives.

Finally, conclusions of the work carried out, and considerations for further research are discussed.

7.2 Summary

The research motivation was to determine the feasibility to remove filler materials during the Yb:laser welding process of grade 2205 duplex stainless steel (with thicknesses of 3 and 6 mm that are typically used in the nuclear sector) to decrease the cost and reduce the complexity of the process.

The research objectives were to:

- Establish the feasibility of autogenous single beam welding of grade 2205 DSS with thicknesses of 3 and 6 mm that are typically used in the nuclear sector. Determine the effect of the key process parameters on the resultant weld quality and the dynamic behaviour of the welding process.
- Determine the feasibility of dual beam laser welding to reduce the ferrite phase excess at the weld location.
- Select and characterise a diffractive optical element (DOE) that emulates an optimised dual laser beam.
- Confirm the possibility of using DOE during keyhole laser welding.
- Determine whether the DOE based approach can reduce the ferrite excess at the weld location.

The first stage of this research was to evaluate the single beam Yb:fibre laser welding process of grade 2205 DSS without the use of filler wire (i.e. autogenous welding). The benchmarking of the process provided the basis for comparison with dual beam and DOE welding. Autogenous Yb:fibre laser welding process was developed for the two mentioned thickness of grade 2205 DSS, and the process parameters were optimised in terms of spot size, welding speed, processing power and focus position. Results showed that the high cooling rate, mostly influenced by the welding speed, hindered the growth of austenite and promoted a ferrite excess at the weld especially at the cap. Consequences of the high ferrite content were translated into a hardness increase at the weld and higher corrosion rate of the material. The feasibility of autogenous single beam welding of grade 2205 DSS was established, but the excessive ferrite at the weld location remains an issue that could not be solved without reducing the welding speed to an undesired level.

Using the process parameters developed in the single beam trials, further investigation was performed using the dual beam laser welding technique to reduce the high cooling rate and reduce the ferrite excess at the weld while maintaining the welding speed. Dual beam was achieved using two laser welding heads; the first head produced a focussed beam for welding, and the second head was in a highly defocused position to produce a trailing re-heating beam with a lower power density. Due to limited flexibility in the optic set-up, the resulting spot size of the welding beam was 375 μm (compared to 300 μm in single beam experiment). Point count results showed that a re-heating beam with a distance separation *d* of 8 to 11 mm and a power density around 5 to 9 W. mm^{-2} restored the ferrite content at the weld location for the 3 mm thick plates. The dual laser beam technique was successfully used to reduce the ferrite excess at the weld location on 3 mm thick plates of grade 2205 DSS, but a bulky set up that doubled the number of optical components for laser welding that was required. As the beam splitter could only provide an equal split of the total available power, the 6 mm plates could be welded only with the two beams in focus and at close proximity (< 2mm) to each other. Resulting welds were significantly wider, but no reduction of the ferrite content was observed.

Final approach to tailor the energy distribution was achieved using a DOE placed between the collimator and the focusing optic. When using DOE, only one welding head was needed. A commercially available 3-spots DOE was then selected. Using the same set of optic as selected in the first experimental chapter, the DOE produced a re-heating beam 8.52 mm apart from the main welding beam. The welding beam obtained with the 3-spots DOE had the same properties (diameter, BPP and intensity) to the one described in single beam experiments. The 3-spots DOE successfully reduced the ferrite content at the weld cap. Nevertheless, as the re-heating beam was the same size of the welding beam, it had a short interaction time with the material. Longer re-heating beam interaction time was needed to re-heat the weld beyond the surface. Therefore, a 4-spots DOE was selected for further weld trials. Due to limited resources, the 4- spots DOE was briefly tested but was found to produce promising results. In some part of the resulting weld cap, the ferrite content was brought close to 50%.

The possibility of using DOE during autogenous keyhole laser welding was confirmed. In current work, laser welding utilising the DOE approach could not entirely reduce the ferrite excess in the weld to the acceptable range of 30-70% ferrite, and further investigation and optimisation are necessary to achieve an improved weld quality.

7.3 Conclusion

The work conducted during this document has resulted in several conclusions listed below:

- Grade 2205 DSS is readily weldable (no subject to crack or porosity) with a high power Yb:fibre laser providing a small spot size (< 600μm) and a shielding gas set up on both side of the weld.

- The use of pure nitrogen shielding gas when compared to argon shielding gas was confirmed to be essential to promote the growth of austenite at the weld location.
- The resulting phase balance at the weld location is dependent on the heat input, and acceptable ferrite content can be obtained autogenously providing a slow welding speed (< 0.5 m/min) that are usually is desired in the industry.
- On 3 and 6 mm thick plates, when using a 5 kW Yb:fibre laser and a processing speed of 1 m/min, the phase balance at the weld location exceeded the recommended 70% ferrite content threshold. The ferrite threshold was established by research showing that the detrimental reductions in toughness, pitting resistance and SCC resistance are less significant within the range of 30 to 70% of ferrite at the weld location. This range is also stipulated in offshore standards for submarine pipelines [31].
- Weld resulting in excessive ferrite content of around 80% significantly failed the ASTM A923 test Method C [107], while welds with around 70% of ferrite qualified. The test consisted of measuring the sample mass losses after a 24 h immersion in a ferric chloride solution at a controlled temperature. The corrosion rate can then be calculated in mdd and $mm.y^{-1}$. This cost-effective testing method is used for evaluating the corrosion resistance of the welded panel for nuclear waste containers.
- An autogenous dual beam technique achieved with two welding heads was able to influence the weld ferrite content on the 3 mm thick plates. The ferrite content was brought back to a volume fraction close to 50% when compared to the 70% and over obtained with single beam welding. This technique allows to match the ferrite requirement for a specific application without using filler wire material and without compromising the welding speed (1 m/min).
- Diffractive optic in the form of DOE gratings can efficiently produce multi-beams with different intensity. The DOE made of fused silica can withstand high power (5 kW in the presented experiments) and a custom welding head to allow quick access to the optic was designed, fabricated and successfully tested during this experimental programme.
- The selected 3-spots DOE produced a re-heating beam that locally reduced the ferrite content within the recommended range of 30-70% at the weld location on the 6 mm thick plates.

This experimental programme demonstrated the feasibility of using tailored energy distribution via dual beam or DOE welding to reduce the resulting ferrite content at the weld location without using filler wire and with a welding speed of 1 and 1.25 m/min. This can have an implication for specific applications requiring a relatively high welding speed ($\geq$ 1 m/min) and the requirement to pass ASTM A 923 Test method C [107] or meet the offshore standards (DNV-OS-F101) [31]. Although the selected DOEs were not entirely suitable as the re-heating beam did not cover the whole weld cap, the feasibility was demonstrated.

For future work, the diffracted pattern developed with the dual beam technique for the 3 mm thick plate of grade 2205 DSS can be implemented with a computer-generated hologram (CGH) diffractive optic type, designed with an IFTA method and manufactured with a direct

writing technique. This would allow the welding with a single processing head and with a resulting ferrite content in the same proportion as the parent material. For the welding of 6 mm thick (and thicker) plate of grade 2205 DSS, the use of a Yb:laser source higher than 5 kW would be necessary to develop a dual beam welding approach.

Appendix 1

A1. 1Quantum physic of photon-electron interactions

Bhor's postulate (1913) explains that the total energy of an atom can only have discrete values [124]. This means that the electrons orbiting around the nucleus can only have discrete orbits in function of their specific energy level. Quantum jumps, or the change of an atom's energy level to another one, happen mainly through the absorption or emission of a photon. A photon is a particle of light that has energy but no mass or charge and has the properties of both a particle and a wave. The emitted or absorbed photon's energy has to be equal to the difference of energy between the two sub-mentioned levels (ΔE). There are three primary photon related electron transitions explained below. Principles are explained with an electron, but atom and also molecule can also absorb or emit a photon. In case of molecules, their discrete levels of energy are associated with molecular rotation or vibration. For a thoughtful quantum understanding of these interactions, a knowledgeable or brave reader can refer to "Optical Spectroscopy of Inorganic Solids" from Henderson and Imbusch [125], otherwise clear and more descriptive information can be found in "Introduction to laser technology" by Hecht [126].

A1.1.1 Absorption

One of the ways an electron can gain energy is to absorb a photon. Considering the quantification of energy level and the conservation of energy, the energy of the photon must correspond to the energy difference between two energy levels of the electron. For instance let's consider an electron at rest, i.e. in its ground state of energy E_0. To jump to a higher level of energy E_1, the electron must absorb a photon having an energy equal to $\Delta E = E_1 - E_0$ as shown in Figure A1.1.

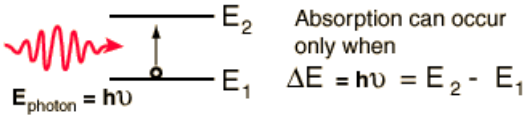

Figure A1.1: Photon absorption

A1.1.2 Spontaneous emission

An excited electron will naturally relax to a lower level of energy and ultimately to its ground state. This relaxation process is accompanied by the emission of a photon having an energy corresponding to the difference in energy between the two levels as depicted in Figure A1.2. The photon is emitted with a random direction and polarization. Spontaneous emission is also called fluorescence. The rate of spontaneous emission (and thus the lifetime of the excited level) is typically a few nanoseconds (~10^{-8}s) if there are allowed transitions to lower levels [125].

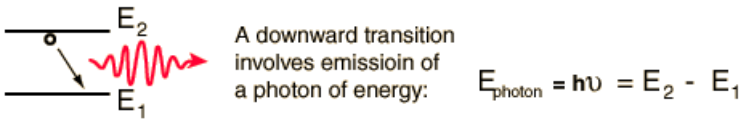

Figure A1.2: Spontaneous emission

The frequency (ν) and therefore the wavelength (λ) of the emitted electromagnetic radiation are directly related to the photon energy (ΔE), and it is given by the Equation A1.1:

$$\Delta E = h\nu = hc/\lambda \qquad \text{Equation A1.1}$$

Where "h" is the Plank's constant (4.1×10^{-15}eV.s) and "c" the celerity (speed of light, 3.0×10^{8}m.s^{-1}).

A1.1.3 Stimulated emission

The relaxation of an electron to a lower energy level can also be induced by an incoming photon for which the quantum energy is equal to the energy difference between its present level and a lower level. In this particular case, the emitted photon released by the atom (electron's atom) has the same phase and direction of the incident one (see Figure A1.3).

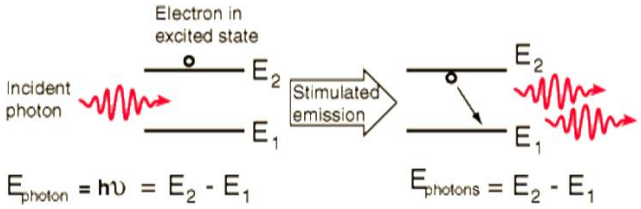

Figure A1.3: Stimulated emission

A1.1.4 Population's inversion

Let's consider a gain medium with two levels of energy.

Let's name N_1 the number of atoms in laying in the energy level E_1 and N_2 the number of atoms in laying in the energy level E_2. For material in thermal equilibrium at temperature T the ratio of N_2 / N_1 is given Equation A1.2:

$$\frac{N_2}{N_1} = e^{\left[\frac{-(E_2-E_1)}{kT}\right]} \qquad \text{Equation A1.2}$$

Where *k* is Boltzmann's constant, equal to 8.617×10^{-5} eV.K^{-1}. At room temperature T is roughly equal to 300K so *k*T worth around 0.026eV. Taking an emission of λ=1μm (Fibre and Nd:YAG laser emit around this wavelength), the energy difference $E_2 - E_1$ can be easily calculated (ΔE = hc/ λ) and found to be 1.241eV. This leads $e^{-(\frac{1.241}{0.026})}$ to be incredibly small (~10^{-20}) meaning that almost no atoms are in exited state. At thermal equilibrium we have $N_1 >> N_2$. Since most of the atoms are in a low level of energy and that every photon that's created by stimulated emission, another photon disappears by absorption, the amplification of light cannot happen.

For a laser to operate, one requires a non-equilibrium situation, when the number of atoms in a higher energy level is greater than the number in a lower energy level. This situation is called a population inversion.

From the Equation A1.2, rising infinitely the temperature of the system cannot achieve a population inversion as shown by Equation A1.3:

$$\lim_{T\to\infty} e^{\left[\frac{-(E_2-E_1)}{kT}\right]} = 1\,. \qquad \text{Equation A1.3}$$

At best, half of the atoms will be excited and the other half at the ground state. Consequently, atoms need to be excited by an external input of energy, a stimulation that can be in an optical or electric form. However, as absorption and spontaneous emission are competitive processes, it is impossible to obtain a population inversion with only a two-level system. Indeed, the probability of absorption and the probability of spontaneous emission, calculated by Einstein and referred as Einstein A & B coefficient, are the same.

Hence laser systems must have three or four level of energy with the upper level of the lasing emission being metastable. This means the atoms (electrons) in this level have a relatively long lifetime (for instance around 1-2ms for ytterbium-doped gain medium) in order to increase the probability to undergo a stimulated emission. The highest energy level has a short lifetime and electron decay rapidly to the upper metastable level. The energy released when they decay to a lower level is radiationless, i.e., it does not release a photon, but energy is dissipated in the form of heat or vibration.

In reality, the gain medium of any laser has many more levels of energy, but only three or four are involved in the laser effect. Different level systems are shown in Figure A1.4.

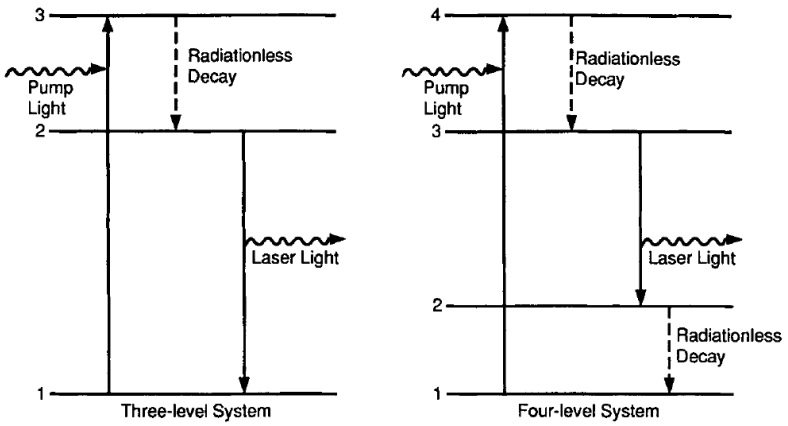

Figure A1.4: 3 and 4 level systems [127]

Three level-system emits between a metastable level (level 2) and the ground state (level1) while in a four-level system, the ground state is not involved in the lasing transition. The main issue with a three level system is that atoms are naturally in the ground state thus they require an intense pumping to maintain a population inversion between level 2 and level 1. With a four-level system, the population inversion is easier to achieve as it takes place between level 3 (metastable level with a long lifetime) and level 2 (not metastable level with

a short lifetime). Level 2 rapidly get empty thus supporting the population inversion condition.

It can be interesting to mention that the model presenting an individual electron jumping to well defined level of energy is not correct, though sufficiently realistic to understand the photon-electron interaction. In quantum physic, the electron does not orbit around the nucleus with a well-defined energy level but has rather a higher presence probably to be found at a certain distance from the nucleus at certain energy level. Also gain medium of actual working laser have a far more complex number of energy level and the upper or lower level of energy often consist of a closely spaced group of energy level. Although these groups of energy level are very close and can be reduced to one level for the sack of understanding, they account for more than one wavelength being emitted hence broadening the bandwidth of laser emission slightly.

Appendix 2

A2.1 Manufacturing diffractive optics

Several techniques are used to manufacture grating, binary and multilevel diffractive optics. It is either by lithography or direct writing.

A2.1.1 Lithography

Choosing the material on which to perform the lithography (i.e. the material for the optic) is usually the first task when deciding to produce a diffractive optic. The material of choice for Diffractive optics at visible wavelengths, near-UV, and near-IR is fused silica (wavelength range around 150 nm to 3µm with a refractive index around 1.5). GaAs (wavelength range around 1.5 to 18 µm with a refractive index around 3.3) and Si (wavelength range around 1 to 7 µm with a refractive index around 3.5) are also suitable for infrared optics, but Si high refractive index is subject to tight tolerances on depth control. Commonly used with CO_2 lasers is ZnSe and other substrates like BK7, InP or CaF_2 that are interesting for UV to IR but can be challenging to process [128]. The lithographic process then consists of the following steps summarised in Figure A2.1.

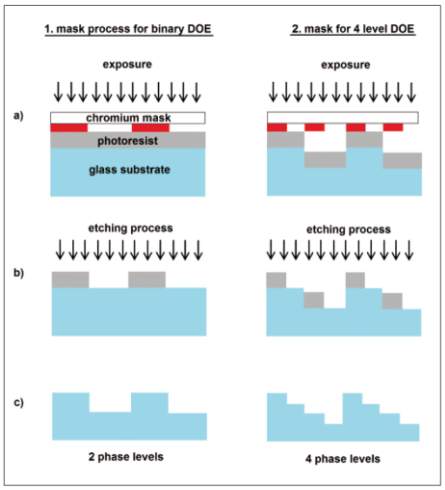

Lithographic processing of diffractive optical elements: (a) Structure of chro- mium (red) mask will be transferred into photoresist; (b) Structure of photoresist will be etched into glass substrate; (c) Resulting phase profile.

Figure A2.1: Lithographic processing of DOE [78]

The mask is usually written in chromium by the electron beam. UVs are usually used for the exposure, transferring the mask' structure into a photoresist on top of the substrate. Ion etching process, usually RIE (Reactive Ion Etching) is followed to engrave the photoresist shape in the substrate. With single mask processing, binary diffractive elements can be manufactured. A multilevel DOE requires further processing steps. The multilevel technique is suitable for a low number of phase levels, from 2 to 8 or 16 but it should be noted that even small residual alignment errors between consecutive masking steps can cause significant efficiency losses [129]. Also, greater number of phase level (>16) does not make sense, regarding performance or fabrication costs.

A2.1.2 Direct writing

Direct writing does not require mask, and several techniques are available, namely diamond tool machining, direct dosage modulation in real time and multi-pass exposure technique.

A2.1.2.1 Diamond tool machining

It consists of an arm with a diamond tip (~µm) with a specific shape which is controlled by a CNC device to carve the substrate directly. However, such elements are limited to circularly symmetric elements such as on-axis symmetric lenses, with smallest fringes several times greater than the diamond tool.

A2.1.2.2 Direct dosage modulation

In the dosage modulation technique, the writing beam (laser or e-beam) is directly modulated to the appropriate dosage when writing the desired shape.

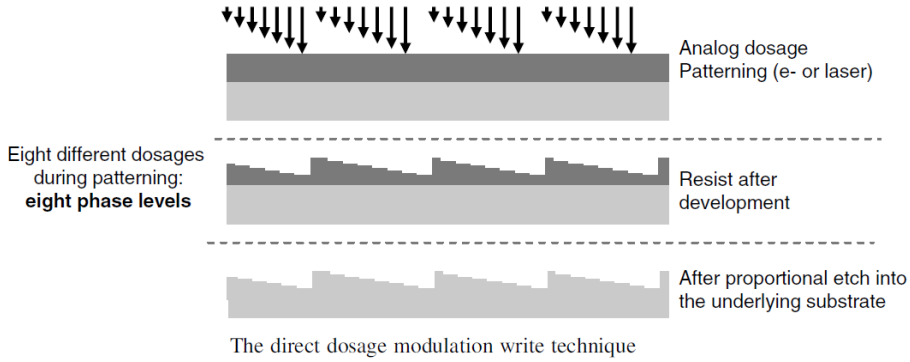

Figure A2.2: Direct dosage modulation

A2.1.2.3 Multi-pass exposure

In the direct write multi-pass exposure technique, the same writing strategy is used as for traditional multilevel exposure, but this time using direct binary write. Each exposure is made with a different dosage (lower at each pass). The advantage is that the dosage is not changing during the writing.

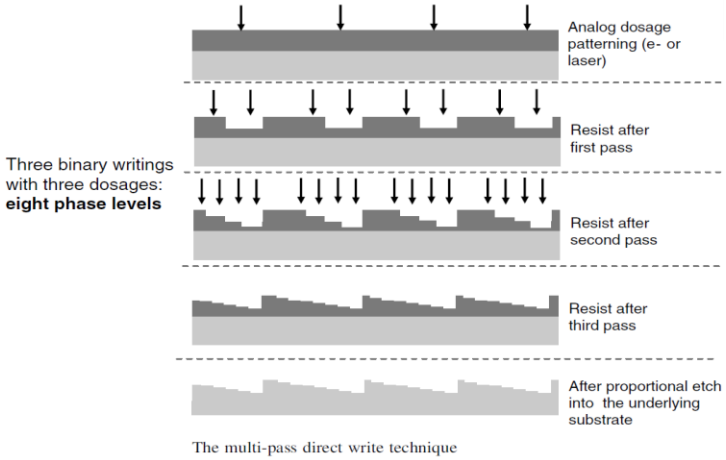

Figure A2.3: The multi-pass direct write technique

The disadvantage of this technique is that it needs to register N times to a pre-written pattern (or sets of etched alignment marks), and therefore it produces systematic misregistrations due to the limited accuracy of such alignment techniques.

A2.1.3 Grayscale lithography

Two main techniques to produce quasi-analogue surface-relief profiles in the resist (and subsequent transfer to the substrate by proportional etching) have been presented: multilevel binary lithography with N masks for 2^N levels and direct multilevel write in resist either multi-pass or single pass (direct modulation).

The main drawback of direct writing is that no masks are created hence no replication of the element can be made. Also, there is a limit on shape accuracy and roughness for laser beam direct writing that is due to the spot size of the laser beam and a limit on the depth of the structure for electron-beam direct write from wide scattering of the electron beam. Also, the two methods have in common the problems of high cost and deformation of the mould by humidity and heat [130].

Lithography binary profile leads to diffraction efficiency under 40%, and while multilevel lithography is better, it remains a lengthy, complicated and costly solution. While the price of a multilevel DOE decreases when mass produced, the complexity and length of the process remain the same.

An alternative to these techniques is grayscale lithography: a single step process with one mask to keep replication possible and with excellent diffraction efficiency. The idea is shown in Figure A2.4.

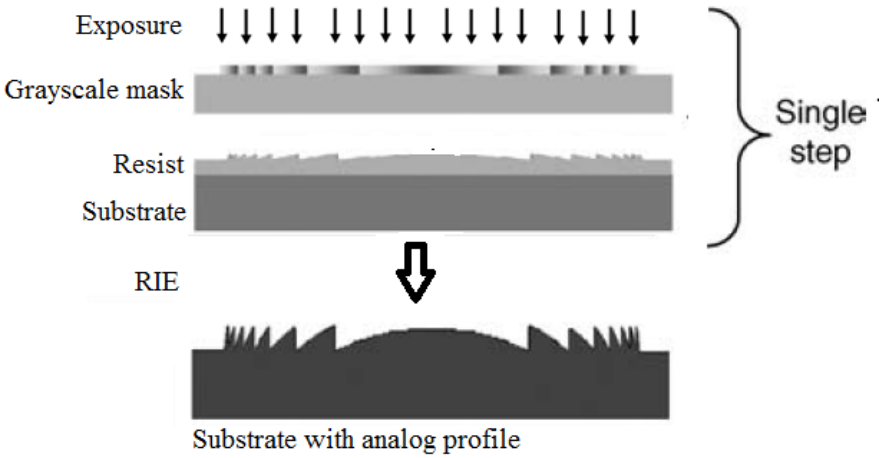

FigureA2.4: Single step lithography

Below, Figure A2.5 compares the diffraction efficiency between single-step grayscale lithography and conventional lithography:

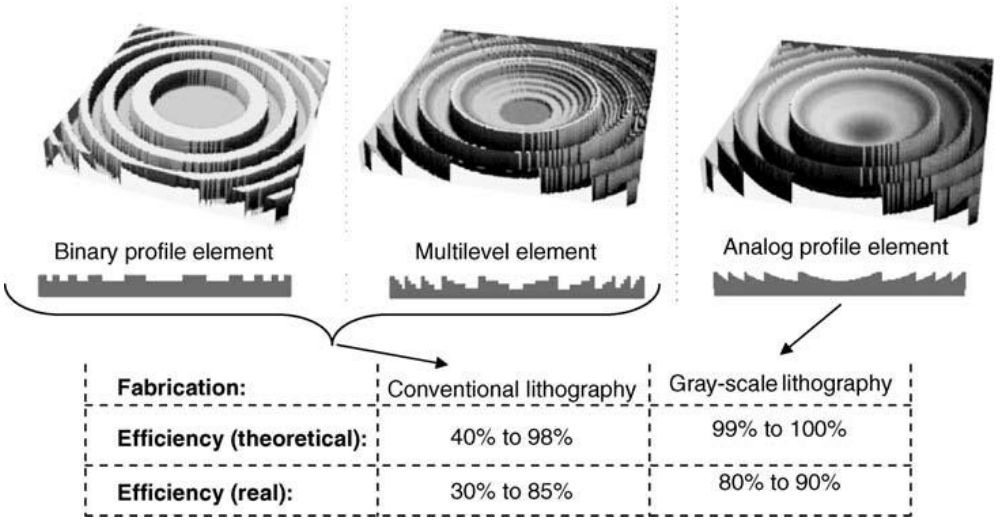

FigureA2.5: Efficiency of different lithography techniques

Several grayscale lithography techniques have been reported since the mid-1990s. The different techniques to make such a grayscale mask are presented.

First, one can think of printing directly the phase pattern generated by the IFTA algorithm in a photographic emulsion (photographic film). This has been done by Suleski on a holographic film to be used with a laser operating in the visible region [131]. Nevertheless, this technique is outdated as the resolution is too low. Other techniques to produce a grayscale mask presented in the next paragraphs.

A2.1.3.1 The inorganic GeSe resist masking technique

This technique is somewhat complicated because it uses inorganic resist and dry development.

A2.1.3.2 The HEBS glass masking technique

This technique reviewed by Daschner [132] consists of exposing a modulated electron beam to a High Energy Beam Sensitive Glass (HEBS) to change locally is optical density. The steps are shown in Figure A2.6.

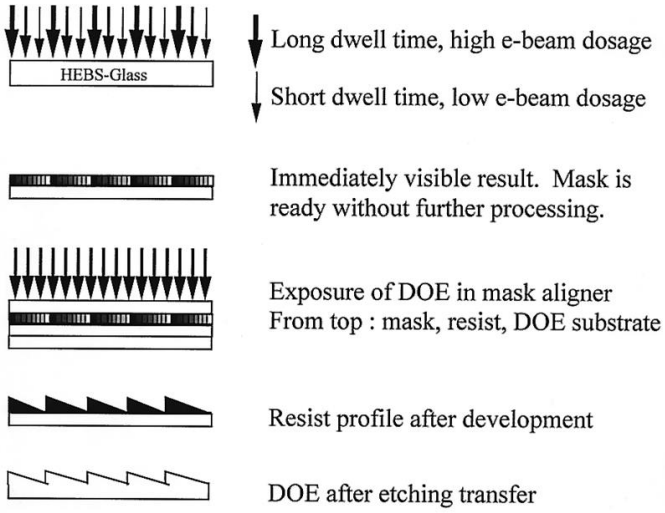

Figure A2.6: The HEBS Glass Masking Technique

References

[1] T. H. Maiman, “Stimulated optical radiation in ruby,” *Nature*, vol. 187, pp. 493–494, 1960.

[2] P. T. Houldcroft and A. B. J. Sullivan, “Gas-jet laser cutting,” *Br. Weld. J.*, p. 443, 1967.

[3] R. G. Gould, “The LASER Light Amplification by Stimulated Emission of Radiation,” *Ann Arbor Conf. opti. Pump.*, vol. 128, 1959.

[4] H. Schwarz and A. J. DeMaria, “Electron, ion, and light beams as present and future material working tools,” *Nat. Electron. Conf.*, pp. 351–365, 1962.

[5] C. J. Bahun and R. D. Eng-Quist, “Metallurgical applications of lasers,” *Nat. Electron. Conf.*, pp. 607–619, 1962.

[6] J. L. Bromberg, *The Laser in America, 1950-1970*. MIT press, 1991.

[7] J. Ion, *Laser Processing of Engineering Materials: Principles, Procedure and Industrial Application*, 1st ed. Oxford: Elsevier, 2005.

[8] L. Quintino, A. Costa, R. Miranda, D. Yapp, V. Kumar, and C. Kong, “Welding with high power fiber lasers – A preliminary study,” *Mater. Des.*, vol. 28, pp. 1231–1237, 2007.

[9] F. Vollertsen and C. Thomy, “Welding with Fiber Lasers From 200 To 17000 W,” *Proc. ICALEO*, p. paper 506, 2005.

[10] D. Belforte, “Fibre lasers continue growth streak in 2014 laser market,” *Industrial Laser Solutions*, 2015. [Online]. Available: http://digital.industrial-lasers.com/industriallasers/20150102?#pg7.

[11] D. Belforte, “Industrial lasers continue solid revenue growth in 2016,” *Industrial Laser Solutions*, 2017. [Online]. Available: http://www.industrial-lasers.com/articles/print/volume-32/issue-1/features/industrial-lasers-continue-solid-revenue-growth-in-2016.html.

[12] G. Overton, A. Nogee, D. Belforte, and H. Conard, “Annual Laser Market Review & Forecast : Where have all the lasers gone ?,” *laser focus world*, no. 1, pp. 1–24, 2017.

[13] J. Ki Lai Leuk, C. Hung Shek, and K. Ho Lo, *Stainless Steels: An Introduction and Their Recent Developments*. Hong Kong, 2012.

[14] J. Charles and P. Chemelle, “The history of duplex developments,nowadays DSS properties and duplex market future trends,” *World Iron Steel*, no. 6, 2011.

[15] M. Liljas and F. Sjöholm, *Duplex Stainless Steels*. Hoboken, NJ, USA: John Wiley & Sons, 2013.

[16] International Molybdenum Association (IMOA), *Practical Guidelines for the Fabrication of Duplex Stainless Steels*, 3rd ed. London, UK: IMOA, 2014.

[17] T. G. Gooch, “Weldability of duplex ferritic-austenitic stainless steels,” in *Duplex Stainless Steels*, R. A. Lula, Ed. Metals Park, Ohio, 1983, pp. 573–602.

[18] T. Wegrzyn, “Delta ferrite in stainless steel weld metals,” *Weld. Int.*, vol. 6, no. 9, pp. 690–694, 1992.

[19] R. N. Gunn, *Duplex Stainless Steels - Microstructure, properties and applications*. Abington

Publishing, 1997.

[20] L. F. Svensson and B. Gretoft, “Properties-Microstructure Relationship for Duplex Stainless Steel Weld Metals,” *Proc. Int. Conf. Duplex Stainl. Steel*, p. Paper 22, 1986.

[21] H. Hwang and Y. Park, “Effects of Heat Treatment on the Phase Ratio and Corrosion Resistance of Duplex Stainless Steel,” *Mater. Trans.*, vol. 50, no. 6, pp. 1548–1552, 2009.

[22] A. Sedriks, *Corrosion of stainless steels*, 2nd ed. John Wiley & Sons, 1996.

[23] J. Potgieter, P. Olubambi, L. Cornish, C. Machio, and S. Sherif, “No Influence of nickel additions on the corrosion behaviour of low nitrogen 22% Cr series duplex stainless steels,” *Corros. Sci.*, vol. 50, no. 9, pp. 2572–2579, 2009.

[24] H.-Y. Ha, M.-H. Jang, T.-H. Lee, and J. Moon, “Interpretation of the relation between ferrite fraction and pitting corrosion resistance of commercial 2205 duplex stainless steel,” *Corros. Sci.*, vol. 89, pp. 154–162, 2014.

[25] Y. Guo, J. Hu, J. Li, L. Jiang, T. Liu, and Y. Wu, “Effect of annealing temperature on the mechanical and corrosion behavior of a newly developed novel lean duplex stainless steel,” *Materials (Basel).*, vol. 6, no. 9, pp. 6604–6619, 2014.

[26] H. Tan, Y. Jiang, B. Deng, T. Sun, J. Xu, and J. Li, “Effect of annealing temperature on the pitting corrosion resistance of super duplex stainless steel UNS S32750,” *Mater. Charact.*, vol. 60, no. 9, pp. 1049–1054, 2009.

[27] Nuclear Decomissioning Authority, “Packaging of Sellafield Ltd Generic 3m 3 Box Design (Interim stage) Summary of Assessment Report,” 2012. [Online]. Available: https://rwm.nda.gov.uk/publication/sellafield-ltd-generic-3m3-box-design-interim-stage/?download.

[28] A.-M. El-Batahgy, “Effect of Laser Beam Welding Parameters on Microstructure and Properties of Duplex Stainless Steel,” *Mater. Sci. Appl.*, vol. 2, no. 10, pp. 1443–1451, 2011.

[29] D. H. Kang and H. W. Lee, “Study of the correlation between pitting corrosion and the component ratio of the dual phase in duplex stainless steel welds,” *Corros. Sci.*, vol. 74, pp. 396–407, Sep. 2013.

[30] R. A. Walker and T. G. Gooch, “Pitting Resistance of Weld Metal for 22Cr-5Ni Ferritic-Austenitic Stainless Steels,” *Br. Corros. J.*, vol. 26, no. 1, pp. 51–59, 1991.

[31] Det Norske Veritas AS, “DNV-OS-F101: Submarine pipeline systems,” *Det Norske Veritas*. 2013.

[32] T. Amman, “Gas-shielded Arc Welding of Duplex Steels,” North Ryde, Australia, 2010.

[33] K. Chan and S. Tjong, “Effect of Secondary Phase Precipitation on the Corrosion Behavior of Duplex Stainless Steels,” *Materials (Basel).*, vol. 7, no. 7, pp. 5268–5304, 2014.

[34] C.-C. Hsieh and W. Wu, “Overview of Intermetallic Sigma () Phase Precipitation in Stainless Steels,” *ISRN Metall.*, vol. 2012, no. 4, pp. 1–16, 2012.

[35] R. Magnabosco, “Kinetics of Sigma Phase Formation In a Duplex Stainless Steel 2 . Experimental Procedure,” *Mater. Res.*, vol. 12, no. 3, pp. 321–327, 2009.

[36] A. J. Ramirez, J. C. Lippold, and S. D. Brandi, “The Relationship between Chromium Nitride and Secondary\nAustenite Precipitation in Duplex Stainless Steels,” *Metall. Mater. Trans. A*, vol. 34A, no. August, pp. 1575–1597, 2003.

[37] E. Bettinia, U. Kivisäkkb, C. Leygrafa, and P. Jinshan, “Study of corrosion behavior of a 22% Cr duplex stainless steel: influence of nano-sized chromium nitrides and exposure temperature,” *Electrochim. Acta*, vol. 113, pp. 280–289, 2013.

[38] J. Verma and R. V. Taiwade, “Effect of welding processes and conditions on the microstructure, mechanical properties and corrosion resistance of duplex stainless steel weldments — A review,” *J. Manuf. Process.*, vol. 25, pp. 134–152, 2017.

[39] D. Howse and S. Baclet, “Evaluation of Welding Processes for S32205 Duplex Stainless Steel Plate,” 2010. [Online]. Available: http://www.twi-global.com/technical-knowledge/industrial-member-reports/evaluation-of-welding-processes-for-s32205-duplex-stainless-steel-plate-957-2010/.

[40] A. Vandewynckèle, E. Couso Vaamonde, J. Arias Otero, M. Pérez de Lama, and G. Quintáns Rodríguez, “Laser-arc welding of duplex stainless steel,” in *Proceedings of ICALEO*, 2007, p. Paper 603.

[41] E. Westin and A. Fellman, “Laser hybrid welding of a lean duplex stainless steel,” *Proc. ICALEO*, pp. 335–344, 2007.

[42] E. Westin and A. Fellman, “Fiber laser hybrid welding of stainless steels,” *Proc. ICALEO*, pp. 545–553, 2008.

[43] V. Muthupandi, P. Bala Srinivasan, S. K. Seshadri, and S. Sundaresan, “Effect of weld metal chemistry and heat input on the structure and properties of duplex stainless steel welds,” *Mater. Sci. Eng. A*, vol. 358, no. 1–2, pp. 9–16, 2003.

[44] J. Pekkarinen and V. Kujanpää, “The effects of laser welding parameters on the microstructure of ferritic and duplex stainless steels welds,” *Phys. Procedia*, vol. 5, no. PART 1, pp. 517–523, 2010.

[45] D. J. Richardson, J. Nilsson, and W. A. Clarkson, “High power fiber lasers: current status and future perspectives,” *J. Opt. Soc. Am. B*, vol. 27, no. 11, pp. B63–B91, 2010.

[46] T. Taira, S. JOLY, and R. BHANDARI, “Passive q-switching type solid-state laser device,” Patent: WO2012160801 A1, 2012.

[47] Coherent®, “Understanding Laser Beam Parameters Leads to Better System Performance and Can Save Money.” [Online]. Available: https://cohrcdn.azureedge.net/assets/pdf/Understanding-Beam-Parameters_FORMFIRST.pdf. [Accessed: 29-Sep-2017].

[48] W. M. Steen and J. Mazumder, *Laser Material Processing*, 4th ed. London: Springer, 2010.

[49] IPG, “YLS, 1-120 kW,” 2018. [Online]. Available: http://www.ipgphotonics.com/en/products/lasers/high-power-cw-fiber-lasers/1-micron-3/yls-1-100-kw.

[50] E. Shcherbakov, V. Fomin, A. Abramov, A. Ferin, D. Mochalov, and V. P. Gapontsev, “Industrial Grade 100 kW Power CW Fiber Laser,” *OSA Tech. Dig.*, 2013.

[51] A. Kaplan, “Analysis and modeling of a high-power Yb:fiber laser beam profile,” *Opt. Eng.*, vol. 50, no. 5, pp. 54201–54206, 2011.

[52] International Organization for Standardization, “11146-1: Lasers and laser-related equipment — Test methods for laser beam widths, divergence angles and beam propagation - Part 1: Stigmatic and simple astigmatic beams.” 2005.

[53] International Organization for Standardization, “11146-2: Lasers and laser-related equipment -- Test methods for laser beam widths, divergence angles and beam propagation ratios -- Part 2: General astigmatic beams.” 2005.

[54] G. Verhaeghe and P. Hilton, “The effect of spot size and laser beam quality on welding performance when using high-power continuous wave solid-state lasers,” *Proc. ICALEO*, pp. 264–271, 2005.

[55] Chaturvedi, Ed., *Welding and joining of Aerospace materials*. Woodhead Publishing, 2012.

[56] W. Duley, *Laser Welding*. Wiley, 1998.

[57] Y. Kawahito, N. Matsumoto, M. Mizutani, and S. Katayama, “Characterisation of plasma induced during high power fibre laser welding of stainless steel,” *Sci. Technol. Weld. Join.*, vol. 13, no. 8, pp. 744–748, 2008.

[58] M. Sokolov and A. Salminen, “Improving laser beam welding efficiency,” *Engineering*, vol. 6, pp. 559–571, 2014.

[59] D. Bergström, J. Powell, and A. F. H. Kaplan, “The absorptance of steels to Nd:YLF and Nd:YAG laser light at room temperature,” *Appl. Surf. Sci.*, vol. 253, no. 11, pp. 5017–5028, 2007.

[60] Z. Gao, P. Jiang, G. Mi, L. Cao, and W. Liu, “Investigation on the weld bead profile transformation with the keyhole and molten pool dynamic behavior simulation in high power laser welding,” *Int. J. Heat Mass Transf.*, vol. 116, pp. 1304–1313, 2018.

[61] S. Katayama, Y. Kawahito, and M. Mizutani, “Elucidation of laser welding phenomena and factors affecting weld penetration and welding defects,” *Phys. Procedia*, vol. 5, pp. 9–17, Jan. 2010.

[62] E. Beyera, A. Mahrleb, M. Lütkeb, J. Standfussa, and F. Brücknera, “Innovation in high power fiber laser applications,” in *Proceedings of SPIE*, 2012.

[63] S. Iqbal, M. M. S. Gualini, and A. ur Rehman, “Dual beam method for laser welding of galvanized steel: Experimentation and prospects,” *Opt. Laser Technol.*, vol. 42, no. 1, pp. 93–98, 2010.

[64] M. Harooni, B. Carlson, and R. Kovacevic, “Dual-beam laser welding of AZ31B magnesium alloy in zero-gap lap joint configuration,” *Opt. Laser Technol.*, vol. 56, pp. 247–255, 2014.

[65] J. Shen, B. Li, S. Hu, H. Zhang, and X. Bu, “Comparison of single-beam and dual-beam laser welding of Ti–22Al–25Nb/TA15 dissimilar titanium alloys,” *Opt. Laser Technol.*, vol. 93, pp. 118–126, 2017.

[66] V. Avilov, A. Fritzsche, M. Bachmann, A. Gumenyuk, and M. Rethmeier, “Full penetration laser beam welding of thick duplex steel plates with electromagnetic weld pool support,” *J. Laser Appl.*, vol. 28, no. 2, 2016.

[67] N. A. McPherson, H. Samson, T. N. Baker, and N. Suarez-Fernandez, “Steel microstructures in autogenous laser welds,” *J. Laser Appl.*, vol. 15, no. 4, pp. 200–210, 2003.

[68] R. Sołtysiak, “Effect of laser welding parameters of DUPLEX 2205 steel welds on fatigue life,” *Solid State Phenom.*, vol. 223, pp. 11–18, 2015.

[69] F. Mirakhorli, F. Malek Ghaini, and M. J. Torkamany, “Development of weld metal microstructures in pulsed laser welding of duplex stainless steel,” *J. Mater. Eng. Perform.*, vol. 21, no. 10, pp. 2173–2176, 2012.

[70] M. Keskitalo, K. Mäntyjärvi, J. Sundqvist, J. Powell, and A. F. H. Kaplan, "Laser welding of duplex stainless steel with nitrogen as shielding gas," *J. Mater. Process. Tech.*, vol. 216, pp. 381–384, 2015.

[71] E. Capello, P. Chiarello, B. Pre, and M. Vedani, "Laser welding and surface treatment of a 22Cr-5Ni-3Mo duplex stainless steel," *Mater. Sci. Eng. A*, vol. 351, pp. 334–343, 2003.

[72] E. M. Westin and A. Fellman, "Effect of laser and laser hybrid welding on the corrosion performance of a lean duplex stainless steel," *J. Laser Appl.*, vol. 22, no. 4, pp. 150–158, 2010.

[73] F. M. Dickey, L. S. Weichman, and R. N. Shagam, "Laser beam shaping techniques," *Proc. SPIE*, vol. 4065, 2000.

[74] R. J. Beck, A. J. Waddie, J. P. Parry, J. D. Shephard, M. R. Taghizadeh, and D. P. Hand, "Adaptive laser beam shaping for laser marking using spatial light modulator and modified iterative fourier transform algorithm," *Phys. Procedia*, vol. 12, no. PART 2, pp. 468–472, 2011.

[75] E. Beyer and J. Standfuss, "Innovations in laser welding using high brightness lasers," in *James Watt Institute – Innovative Manufacturing Research Centre Conference*, 2012.

[76] S. Katayama, M. Hirayama, M. Mizutani, and Y. Kawahito, "Deep Penetration Welds and Welding Phenomena with Combined Disk Lasers," *Proc. ICALEO*, pp. 661–668, 2011.

[77] A. Laskin, V. Laskin, A. Gmbh, and R. Chaussee, "Refractive beam shapers for material processing with high power single mode and multimode lasers," *SPIE Conf. Proc.*, vol. 8600, pp. 10–11, 2013.

[78] U. Umhofer, E. Jäger, and C. Bischoff, "Refractive and diffractive laser beam shaping optics High end components for material processing," *Opt. Components*, no. 3, pp. 24–27, 2011.

[79] F. M. Dickey, S. C. Holswade, and D. L. Shealy, *Laser Beam Shaping Applications*. Boca Raton: CRC Press Taylor & Francis Group, 2006.

[80] L. Mrna, M. Šarbort, Š. Rerucha, and P. Jedlička, "Adaptive optics for control of the laser welding process," *EPJ Web Conf. 48*, vol. 17, pp. 1–7, 2013.

[81] R. Völkel and K. J. Weible, "Laser Beam Homogenizing: Limitations and Constraints," *Proc. SPIE*, vol. 7102, p. 71020J–71020J–12, 2008.

[82] Hamamatsu, "Hamamatsu develops the spatial light modulator with the world's highest power handling capability for wavefront control of high-power lasers," 2017. [Online]. Available: http://www.hamamatsu.com/eu/en/news/news2/20170413000000.html. [Accessed: 19-May-2017].

[83] S. Noden, "Applications of diffractive optical elements with high power lasers (Doctoral dissertation)," Loughborough University, 2000.

[84] K. S. Hansen, "Multispot fiber laser welding (Doctoral dissertation)," Aalborg University, 2015.

[85] B. C. Kress and P. Meyrueis, *Applied digital optics from micro-optics to nanophotonics*. John Wiley & Sons, Ltd, 2009.

[86] D. C. O. Shea, T. J. Suleski, A. D. Kathman, and D. W. Prather, *Diffractive Optics: Design Fabrication and Test*. Bellingham, Washington, 2004.

[87] "An in-depth look at axicons," *Edmund Optics*, 2010. [Online]. Available:

https://www.edmundoptics.co.uk/resources/application-notes/optics/an-in-depth-look-at-axicons/.

[88] J. M. Moran, “Compensation of Aberrations due to a Wavelength Shift in Holography,” *Appl. Opt.*, vol. 10, no. 8, pp. 1909–1913, 1971.

[89] O. Ripoll, V. Kettunen, and H. Herzig, “Review of iterative Fourier-transform algorithms for beam shaping applications,” *Opt. Eng.*, Nov. 2004.

[90] M. Leung, H. Man, and J. Yu, “Theoretical and experimental studies on laser transformation hardening of steel by customized beam,” *Int. J. Heat Mass Transf.*, 2007.

[91] J. Kell, “Melt pool and microstructure manipulation using diffractive holographic elements in high power conduction laser welding,” 2007.

[92] K. S. Hansen, M. Kristiansen, and F. O. Olsen, “Beam Shaping to Control of Weldpool Size in Width and Depth,” *Phys. Procedia*, vol. 56, pp. 467–476, 2014.

[93] M. Gibson, R. Higginson, J. Tyrer, and M. Blackmur, “Control of the grain size using holographic beam shaping,” in *Proceedings of ICALEO*, 2009, no. Paper 1505.

[94] Hilton, “Diffractive optical elements for manipulation of CO2 laser radiation - a feasibility study,” *TWI core Res.*, 1996.

[95] Hilton, “Laser materials processing using tailored heat sources,” *TWI core Res.*, 1999.

[96] R. Higginson, M. Gibson, J. Kell, and J. Tyrer, “Weld pool shaping and microstructural control using novel computer generated holographic optic laser welding of steel and stainless steel,” *Mater. Sci. Forum*, 2010.

[97] J. Hammond, E. Johnson, C. Koehler, J. Stack, and T. Suleski, “Diffractive optics for laser welding and bonding,” . *Proc. SPIE*, no. 3633:206–213, 1999.

[98] B. Victor, “Custom beam shaping for high-power fiber laser welding (Doctoral dissertation),” The Ohio State University, 2009.

[99] British Standards Institution, “10088-2: Stainless steels. Technical delivery conditions for sheet/plate and strip of corrosion resisting steels for general purposes.” 2014.

[100] International Organization for Standardization, “6947: Welding and allied processes - Welding positions.” 2011.

[101] PicoTechnology, “PicoLog 5.25.3.” [Online]. Available: https://www.picotech.com/downloads.

[102] International Organization for Standardization, “17636-1: Non-destructive testing of welds -- Radiographic testing -- Part 1: X- and gamma-ray techniques with film.” 2013.

[103] International Organization for Standardization, “19232-1: Non-destructive testing -- Image quality of radiographs -- Part 1: Determination of the image quality value using wire-type image quality indicators.” 2013.

[104] National institute of health, “ImageJ.” [Online]. Available: https://imagej.nih.gov/ij/.

[105] British Standards Institution, “13919-1: Welding — Electron and laser beam welded joints — Guidance on quality levels for imperfections.” 1997.

[106] ASTM International, “E562-02: Standard test method for determining volume fraction by systematic manual point count,” 2002.

[107] ASTM International, “A923-14: Standard Test Methods for Detecting Detrimental Intermetallic Phase in Duplex Austenitic/Ferritic Stainless Steels,” 2014.

[108] British Standards Institution, “6507-1: Metallic materials. Vickers hardness test. Test method.” 2005.

[109] R. Lai, Y. Cai, Y. Wu, F. Li, and X. Hua, “Influence of absorbed nitrogen on microstructure and corrosion resistance of 2205 duplex stainless steel joint processed by fiber laser welding,” *J. Mater. Process. Technol.*, vol. 231, pp. 397–405, 2016.

[110] A. Mourad, A. Khourshid, and T. Sharef, “Gas tungsten arc and laser beam welding processes effects on duplex stainless steel 2205 properties,” *Mater. Sci. Eng. A*, vol. 549, pp. 105–113, 2012.

[111] W. Suder, “Study of fundamental parameters in hybrid laser welding (Doctoral dissertation),” Cranfield University, 2012.

[112] S. Williams and W. Suder, “Use of fundamental laser material interaction parameters in laser welding,” *Laser Sci. to Photonic Appl.*, no. July, pp. 1–2, 2011.

[113] M. Hashemzadeh, W. Suder, S. Williams, J. Powell, A. F. Kaplan, and K. T. Voisey, “The application of specific point energy analysis to laser cutting with 1 μm laser radiation,” *Phys. Procedia*, vol. 56, no. C, pp. 909–918, 2014.

[114] Outokumpu, “2205 Datasheet,” 2013. [Online]. Available: http://www.outokumpu.com/sitecollectiondocuments/datasheet-2205-code-plus-two-hpsa-imperial-outokumpu-en-americas.pdf.

[115] J. Liao, “Nitride Precipitation in Weld HAZs of a Duplex Stainless Steel.,” *ISIJ Int.*, vol. 41, no. 5, pp. 460–467, 2001.

[116] S. Weissman and N. G. Anderson, “Design of Experiments (DoE) and Process Optimization. A Review of Recent Publications.,” *Org. Process Res. Dev.*, vol. 19, no. 11, pp. 1605–1633, 2015.

[117] H. Zitter, G. Mori, G. Hochortler, and H. Wieser, “Evaluation of CPT values determined by ASTM G48 practice,” *Mater. Corros.*, vol. 53, no. 1, pp. 37–43, 2002.

[118] E. Taban and E. Kaluc, “Welding behaviour of Duplex and Superduplex Stainless Steels using Laser and Plasma ARC Welding processes,” *Weld. World*, vol. 55, no. 7–8, pp. 48–57, 2011.

[119] Z. Sun, M. Kuo, I. Annergren, and D. Pan, “Effect of dual torch technique on duplex stainless steel welds,” *Mater. Sci. Eng. A*, vol. 356, no. 1–2, pp. 274–282, 2003.

[120] S. Brahimi, “Fundamentals of hydrogen embrittlement in steel fasteners,” *IBECA Technologies Corp.*, 2014. [Online]. Available: http://www.boltcouncil.org/files/HydrogenEmbrittlementInSteelFasteners-Brahimi.pdf.

[121] N. Bailey, F. Coe, T. Gooch, P. Hart, N. Jenkins, and R. Pargeter, *Welding steels without hidrogen cracking*. Cambridge: Woodhead Publishing, 2004.

[122] “Conversation with Stuart Dutton at Graham Engineering.” Nelson Lancashire BB9 8SY, 2016.

[123] British Standards Institution, “17637:2016: Non-destructive testing of welds. Visual testing of fusion-welded joints.” 2016.

[124] N. Bohr, “On the constitution of atoms and molecules,” *Philos. Mag.*, vol. 26, no. 6, pp. 1–25,

1913.

[125] B. Henderson and G. Imbusch, *Optical Spectroscopy of Inorganic Solids*. Oxford: Clarendon Press, 1989.

[126] J. Hecht, B. Hitz, and J. J. Ewing, *Introduction to laser technology*, Third ed. New York: IEEE Press, 2001.

[127] J. F. Ready, *Industrial Applications of Lasers*, 2nd ed. San Diego: Academic Press, 1997.

[128] D. C. O. Shea and T. J. Suleski, "Chapter 6: Making a Diffractive Optical," in *Diffractive Optics: Design Fabrication and Test*, pp. 115–132.

[129] M. B. Stern, M. Holz, S. S. Medeiros, and R. E. Knowlden, "Fabricating binary optics: process variables critical to optical efficiency," *J. Vac. Sci. Technol.*, pp. 3117–3121, 1991.

[130] J.-S. Sohn, M.-B. Lee, W.-C. Kim, E.-H. Cho, T.-W. Kim, C.-Y. Yoon, N.-C. Park, and Y.-P. Park, "Design and fabrication of diffractive optical elements by use of gray-scale photolithography.," *Appl. Opt.*, vol. 44, no. 4, pp. 506–511, 2005.

[131] T. J. Suleski and D. C. O'Shea, "Gray-scale masks for diffractive-optics fabrication: I. Commercial slide imagers.," *Appl. Opt.*, vol. 34, no. 32, pp. 7507–7517, 1995.

[132] W. Däschner, P. Long, R. Stein, C. Wu, and S. H. Lee, "Cost-effective mass fabrication of multilevel diffractive optical elements by use of a single optical exposure with a gray-scale mask on high-energy beam-sensitive glass.," *Appl. Opt.*, vol. 36, no. 20, pp. 4675–4680, 1997.